Nanostructured Materials for Advanced Electrochemical Energy Storage Applications

A DISSERTATION
SUBMITTED TO THE FACULTY OF
THE UNIVERSITY OF MINNESOTA
BY

Benjamin E. Wilson

IN PARTIAL FULFILLMENT OF THE REQUIREMENTS
FOR THE DEGREE OF
DOCTOR OF PHILOSOPHY

Advisor: Andreas Stein

March 2016

Dedication

To Lindsay, for always being there.

Abstract

This dissertation discusses work aimed at developing and improving nanostructured materials for electrochemical energy storage, specifically electrochemical double layer capacitors (EDLCs) and lithium-ion batteries (LIBs). This was achieved through a combination of templating, precursor selection, and heteroatom doping to control the morphology and composition of the materials for improved performance in both types of energy storage.

The first part of the thesis discusses EDLCs. First, a new method to produce soft-templated carbon materials is described. This process allows for improved production of mesoporous carbon made through soft templating. The work continues with using ionic liquids to dope nitrogen into hard templated mesoporous carbon. This led to a 40% improvement in specific capacitance due to improved conductivity. The section concludes with an investigation of physical and electrochemical properties of twelve ionic liquid electrolytes to determine which parameters are most important to achieve a high energy density.

The second part discusses my work on LIBs, starting with a design of a low-cost electrochemical cell for in-situ X-ray diffraction monitoring during galvanostatic cycling. It continues with the development of a novel cathode material, Li_8ZrO_6, with a high lithium content. In this material, the redox activity is localized on oxygen atoms. Li_8ZrO_6 displays initial capacities higher than those of commercial materials but has large polarization. The capacity is further improved with transition metal doping, leading to a final specific capacity of over 175 mAh/g after 140 cycles at a rate of C/5.

Table of Contents

List of Tables

List of Figures

List of Abbreviations

Listed in alphabetical order:

3DOm	Three-Dimensionally Ordered Mesoporous
A	Area
A	SI unit – amp
AC	alternating current
b	pore radius
BuMePyl	*N*-butyl-*N*-methylpyrrolidinium
Bu$_3$MeN	tributylmethylammonium
BuPyd	*N*-butylpyridinium
c-	SI prefix – centi-
C	capacitance
C	rate unit set at 1 Faraday constant per mol per hour
°C	SI unit – degrees Celsius
cal	SI unit – calorie
CCT	colloidal crystal template
CMC	carboxymethyl cellulose
CTA	Chain Transfer Agent
d	diameter/thickness
ΔG°	standard free energy of reaction
Da	Dalton
DCA	dicyanoamide

DEC	diethylene carbonate
DFT	Density Functional Theory
DI	deionized
DMC	dimethylene carbonate
DOS	density of states
ε_r	electrolyte dielectric constant
ε_0	dielectric constant of a vacuum
E	energy density
E°	standard cell potential
EC	ethylene carbonate
EDLC	Electrochemical Double-Layer Capacitor
EISA	Evaporation-Induced Self-Assembly
EMI	1-ethyl-3-methylimidazolium
EtMe$_2$Im	1-ethyl-2,3-dimethylimidazolium
F	Faraday constant (96485 A·s/mol)
F	SI unit – Farad
fcc	face-centered cubic
FFT	fast Fourier transform
F(R)	Kubelka-Munk remission function
g	SI unit – gram
GC	glassy carbon
h	SI unit – hour

HexMeIm	1-hexyl-3-methylimidazolium
HPLC	high pressure liquid chromatography
Hz	SI unit – Hertz
I	current
ICP-MS	inductively-coupled plasma mass spectroscopy
I_D	peak intensity (disordered)
I_G	peak intensity (graphitic)
IL	ionic liquid
J	SI unit – Joule
k-	SI prefix – kilo-
KST	Kohn-Sham theory
L	SI unit – liter
L_a	graphitic domain size
LIB	Lithium-Ion Battery
LFP	lithium iron phosphate
LZO	lithium zirconium oxide (typically Li_8ZrO_6)
μ-	SI prefix – micro-
m-	SI prefix – milli-
M-	SI prefix – mega-
m	mass
m	SI unit – meter
M	SI unit – molar

Me$_3$BuN	butyltrimethylammonium
min	SI unit – minute
n-	SI prefix – nano-
n	number of electrons involved
NMP	N-methyl pyrrolidone
OcMeIm	1-octly-3-methylimidazolium
P	power density
Pa	SI unit – Pascal
PDOS	partial density of states
PEO	poly(ethylene oxide)
PF	phenol-formaldehyde
PrMeIm	3-methyl-1-propylimidazolium
PrMePi	*N*-methyl-*N*-propylpiperidinium
ppm	parts per million
PS	polystyrene
PTFE	polytetrafluoroethylene
PVDF	polyvinylidene difluorode
PXRD	powder X-ray diffraction
QSDFT	Quenched Solid Density Functional Theory
R	reflectance
RAFT	Reversible Addition-Fragmentation chain Transfer
rpm	rotations per minute

S	SI unit – Siemens
SAXS	Small Angle X-ray Scattering
SBR	styrene butadiene rubber
SEI	solid-electrolyte interface
SEM	scanning electron microscopy
t	time
TDOS	total density of states
TEM	Transmission Electron Microscopy
TEOS	tetraethylorthosilicate
TFSI	bis(trifluorosulfonyl)imide
TGA	thermogravimetric analysis
THF	tetrahydrofuran
UV-vis	ultraviolet-visible
V	SI unit – volt
W	SI unit – watt
wt%	weight percent
XPS	X-ray photoelectron spectroscopy
XRD	X-ray diffraction
Ω	SI unit – Ohm

Chapter 1: Introduction to Rechargeable Electrical Energy Storage

As climate change becomes an ever increasing problem, due in large part to the increase in fossil fuel use during the last century, alternative sources of energy are being explored while improvements in the efficiency of existing technologies are also sought. Many energy sources, such as wind- and solar-based power sources, are variable, producing fluctuating and unpredictable outputs of electrical energy.[1] To balance the supply and demand needs on a grid-level scale, electrical energy must be stored and redistributed for better overall grid level efficiency. Another application needing improved electrical energy storage systems relates to hybrid and all-electric vehicles for commercial and personal transportation.[2] Therefore, a major challenge for the coming decades is improving electrical energy storage technology on multiple scales, from grid level to personal vehicles, and timeframes, from seconds to days.[3] This thesis work explores two primary technologies, electrochemical double-layer capacitors (EDLCs) and Li-ion batteries (LIBs), specifically developing materials for improved performance of these types of electrical energy storage devices.

1.1 Methods for Electrical Energy Storage

While multiple requirements must be met for rechargeable electrical energy storage devices, two primary parameters used typically used to determine performance: specific power and specific energy.[2] Specific power can be described as the rate at which the energy can be delivered, or how quickly one can charge and discharge a cell. This is proportional to the potential energy of the cell squared divided by the total resistance of

the cell. Specific energy can be described as the amount of energy that the cell can deliver and is proportional to the capacity of the cell times the potential energy squared. As can be seen from these relationships, the potential energy of the cell is of great importance for the final performance of the device, and will be discussed later for each device.

There are two primary devices to store electrical energy: capacitors and batteries. Figure 1.1 shows the relative range of power and energy densities of typical devices used to store charge.[4] Capacitors can be divided into two primary types – electrolytic capacitors and so-called supercapacitors, which are based on double-layer capacitance and/or pseudocapacitance.[5] These devices generally have a high power density but limited energy density, making them ideal for situations where rapid charging and discharging is desired, such as in regenerative braking for hybrid vehicles.[2] Specifically, EDLCs are currently used commercially in areas such as harbor cranes, flash photography, and emergency exits on Boeing airplanes.[6-8] On the other hand, batteries generally have much higher energy density but lower power density.[9-10] For high performance rechargeable batteries, LIBs are currently the technology used in common portable electronic devices due to their low weight and high energy density.[11-12]
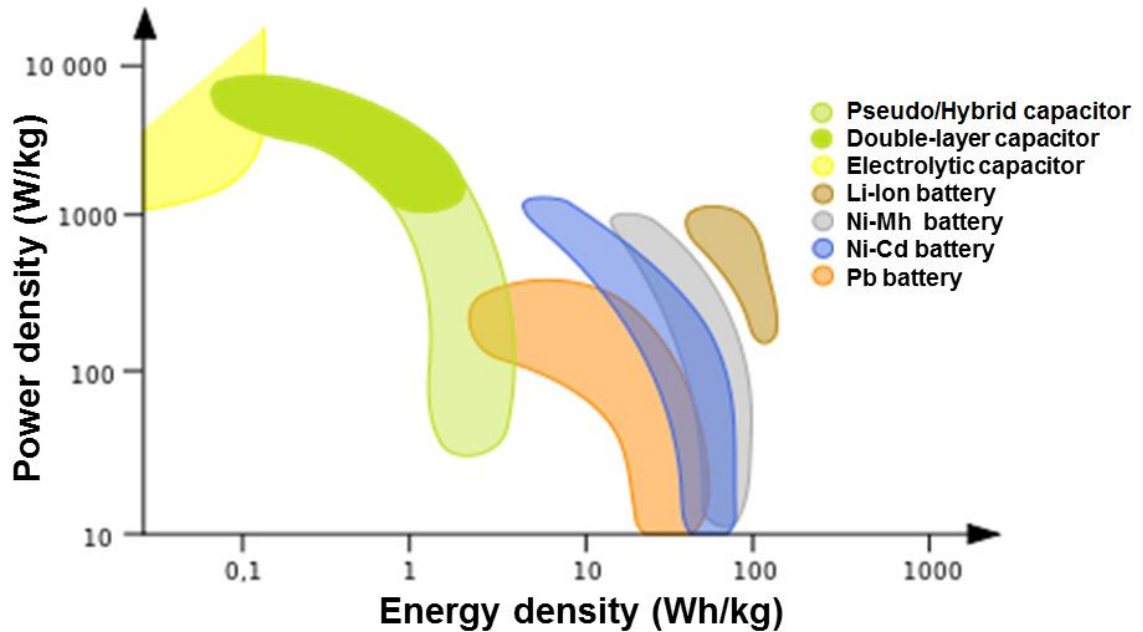
Figure 1.1. Ragone plot of typical electrical energy devices showing the relative energy and power density ranges of each type. Adapted with permission from reference 13. Copyright 2008 Nature Publishing Group.

1.2 Electrochemical Double-Layer Capacitors

EDLCs are a type of rechargeable electrical energy storage device that utilizes surface-based electrostatic adsorption of ions onto an electrode surface.[14] This phenomenon was first described by Helmholtz in 1853 when he proposed a system based on a double-plate capacitor in which charge separation occurred between the electrolyte and the surface of the electrode.[14] This differs from conventional capacitors where charge separation occurs between two parallel plates. However, it was not until 1957 when Becker et al. built the first large-scale experimental design that demonstrated the electrochemical double-layer.[15] This system was based on porous carbon electrodes derived from lampblack and an aqueous H_2SO_4 electrolyte. Unfortunately, this design

3

was unable to be commercialized due to limitations of the cell design and a high cost. The first commercial design was created by the Standard Oil Company in 1970 and was based on a carbon paste electrode and a similar sulfuric acid electrolyte.[16] This system was able to deliver 67 F/g and utilized a coin cell design (a standard cell design that aptly looks like a coin, both in size and shape); this was a much more practical alternative to Becker's cell. The first US mandate for improved EDLCs came in 1989 when the Department of Energy began a development program to promote advances in EDLCs.[14] This was done to boost development into battery or fuel cell power sources for hybrid vehicles and provide necessary power for acceleration and efficient energy recuperation during braking. Since that time, research has aimed to increase the specific surface area of the electrodes,[17, 18] develop novel electrolytes,[19, 20] and reduce the resistance within the electrode.[21, 22]

1.2.1 Mechanism of Charge Storage

As mentioned, the basic mechanism for charge storage within an EDLC is based on the reversible, electrostatic adsorption of electrolyte ions on the surface of an electrode.[14, 23-24] Figure 1.2 shows an idealized representation of a charged EDLC where the anions are adsorbed onto the positively charge cathode and the cations are adsorbed onto the negatively charged anode. The directly adsorbed ions and their solvation shell create what is known as the Inner Helmholtz Layer.[25] The capacitance derived from this behavior described by Helmholtz in 1853 and can be modeled by Equation 1.1:

$$C = \frac{(\varepsilon_r \varepsilon_0) A}{d}$$
(1.1)

4

where C is the capacitance of the electrode, A is the surface area of the electrode available for ion adsorption, ε_r is the electrolyte dielectric constant, ε_0 is the dielectric constant of a vacuum, and d is the effective thickness of the Inner Helmholtz Layer. However, this model does not accurately match experimental results, leading to Guy and Chapman proposing the Outer Helmholtz Layer, where more distant, less well-adsorbed ions can orient towards the charged electrode surface.[25] A unified theory was later described by Stern and Geary that combined the two theories to create the modern model of an EDLC.[25] The remainder of the volume is filled with the diffuse layer, or disordered electrolyte, that does not contribute significantly towards charge storage within the EDLC and does not typically exist within the confines of small mesopores on which this thesis work focuses.[24]
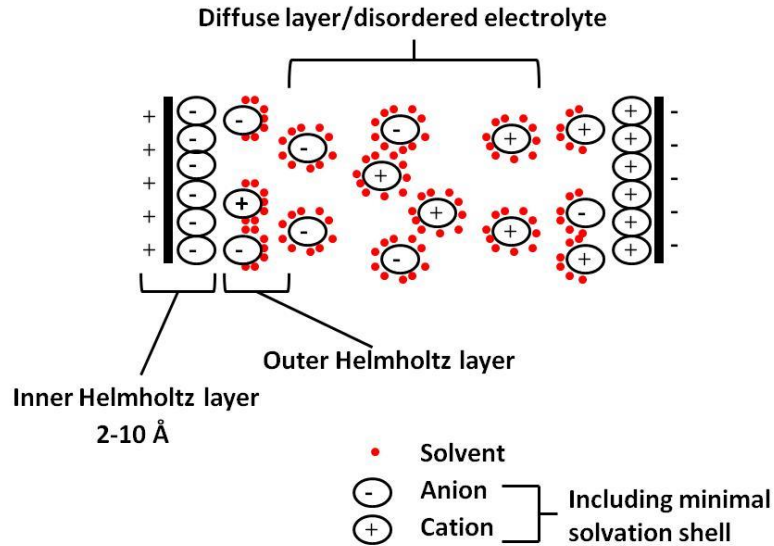
Figure 1.2. Schematic of the charge storage mechanism in an EDLC. The charge is stored primarily in the Inner Helmholtz Layer whose thickness is determined by the ions in the electrolyte and the level of solvent interaction. The Outer Helmholtz Layer helps stabilize the system. The diffuse layer consists of disordered electrolyte and does not contribute to the capacitance.

The Stern and Geary model can be used to accurately model infinitely parallel, *flat* surfaces, but as Equation 1.1 shows, the capacitance is proportional to the surface area available for electrode adsorption.[26] To attain higher capacitance, greater surface areas are needed, leading to the use of highly porous materials. As the pore sizes drop below 50 nm into the mesopores range (2-50 nm),[27] and especially below 5 nm, the Stern and Geary model breaks down significantly due to increased interactions between the ions on the highly curved surfaces.[26] Furthermore, the ions are unable to pack efficiently, and solvation shells are forced closer together, changing the interactions of the Inner Helmholtz Layer. Additionally, the Outer Helmholtz Layer has reduced volume in which to form, leading to a further breakdown in the model. The effect is that charge is stored in

6

cylindrical layers,[5, 28] rather than the parallel plates described by Helmholtz, and can be more accurately modeled by Equation 1.2:

$$C = \frac{(\varepsilon_r \varepsilon_0)A}{b \, ln\left(\frac{b}{b-d}\right)}$$

(1.2)

where d is the distance between the ions and the electrode, b is the pore radius, and the other variables remain the same as in Equation 1.1. In the case of organic and aqueous electrolytes (solutions of ions based on either organic solvents or water, respectively), a minimum pore diameter of around 2 nm is required for the double-layer, based on typical solvation shell diameters.[29]

However, in the case of electrolytes that do not require a solvation shell, such as ionic liquids (which are salts that remain a liquid at room temperature), even smaller pores can be utilized for double-layer capacitance.[30] In this case, the capacitance model does not involve a double-layer, as there is no room for this to occur; rather, the ions form a "wire" within the pores, leading to an ideal pore diameter based on each ionic liquid where the ions match the pore size for maximum capacitance. It has been shown that for the ionic liquid 1-ethyl-3-methylimidazolium bis(trifluoromethylsulfonyl)imide (EMI TFSI), the optimal pore size is similar to the ionic dimensions of the salt determined from X-ray crystallography (Figure 1.3).[30] Therefore, while double-layer capacitance occurs primarily in the mesopores of a structure, micropores can also contribute significantly to the total capacitance.
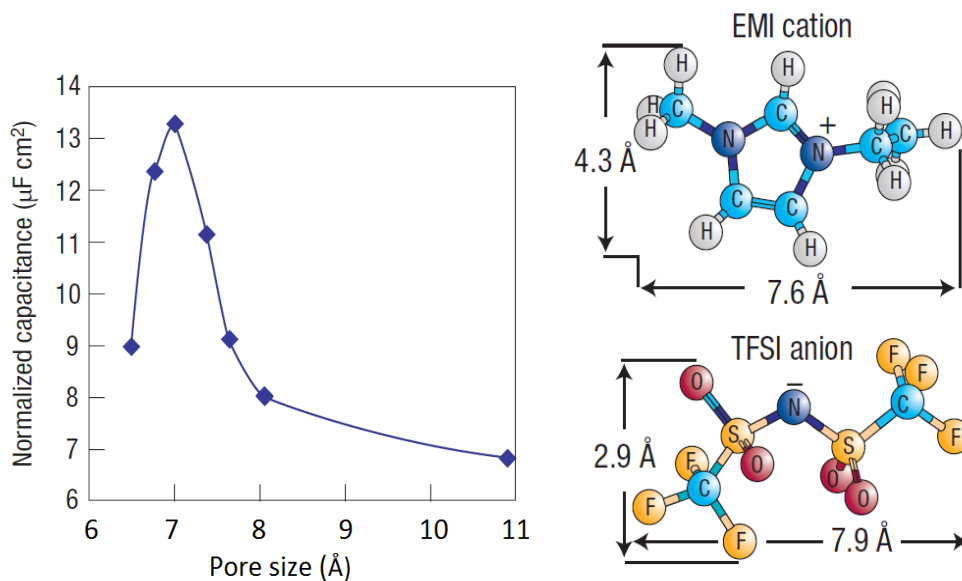
Figure 1.3. Results showing capacitance in micropores that are too small to form an EDL. The peak capacitance occurs at approximately the diameter of the ions used as the electrolyte. Adapted with permission from reference 30. Copyright 2008, American Chemical Society.

Beyond the double-layer capacitance described, EDLCs can exhibit what is known as pseudocapacitance.[5, 31] In double-layer capacitance, electrons are removed or added in a delocalized fashion, creating an overall charged surface with little formal oxidation state changes. However, in pseudocapacitance, which can occur in tandem with double-layer capacitance, a redox active material is included in the electrode leading to localized electron transfer and a formal oxidation state change.[32] This can add a significant amount of capacitance to a system, for instance, the capacitance of carbon nanofoams increases from 53 F/g to 110 F/g with the addition of a MnO_2 coating.[31] Figure 1.4 shows typical capacitance ranges of various EDLC materials, with carbons typically exhibiting only double-layer capacitance and polymers and metal oxides exhibiting pseudocapacitance.[33] While pseudocapacitance can significantly increase the specific capacitance of an

electrode material, there are several downsides, most notably, increased cost and limited lifespans.[34] While double-layer capacitors can be charged and discharged for hundreds of thousands to millions of cycles with little loss in performance, pseudocapacitors can be limited to fewer than 1000 cycles due to irreversible reactions on the surface of the electrodes.
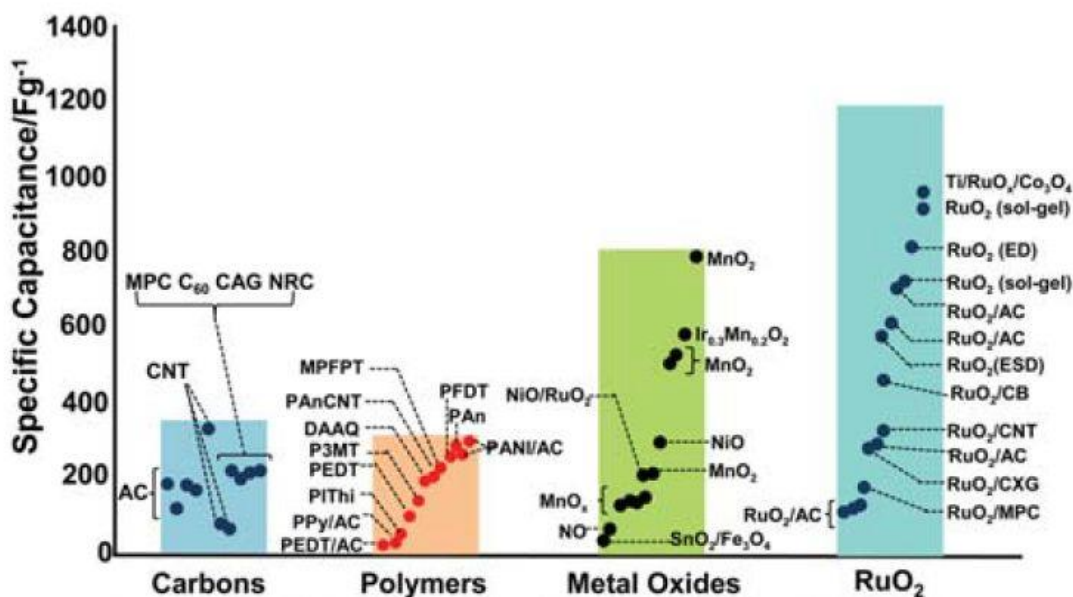
Figure 1.4. Comparison of various pseudocapacitive materials and their relative capacitances. RuO_2 has the highest capacitance; however its high cost makes it unattractive for widespread commercial use. Reprinted with permission from reference 33. Copyright 2010, Royal Society of Chemistry.

1.2.2 Components of an EDLC

EDLCs are composed of two primary components that limit their performance: the electrodes and the electrolyte.[35] The two electrodes need to be electrically separated; otherwise the device will short out because current can travel directly between the

9

electrodes, eliminating the stored potential energy. This can be done through either an electrically resistive spacer, such as porous polymers or glass, or spatially separated. However, the specific energy of the EDLC is determined by the specific capacitance of the electrode (generally reported in farads per gram) and the potential limit of the electrolyte.[24, 36]

In the case of double-layer capacitance, on which this thesis work focuses, most electrodes are made from porous carbon, as porous carbons are easily synthesized, low in cost, and possess high conductivity.[35-36] Activated carbon materials derived from biomass have been used extensively as electrode materials.[37-44] Typically, the carbon is heated under an inert atmosphere, such as nitrogen, to carbonize the material, followed by secondary treatment in an oxidizing solution to improve the surface area and specific capacitance of the material. The resulting materials can have high surface areas of over 2000 m^2/g with specific capacitances of over 300 F/g.[40, 45] However, these materials have a wide distribution of pore sizes, ranging from micropores of less than 2 nm to large textural mesopores in the 100s of nanometers. This disordered structure leads to many dead ends throughout the material, limiting the effectiveness of the high surface area.[46] Density functional theory (DFT) calculations combined with experimental work on commercial activated carbons suggests that surface areas above 1200 m^2/g do not significantly increase the specific capacitance of the electrode.[47-48]

The electrochemical performance can be improved by increasing external surface area, for example by using nanofibers,[49] or with internal surface area, such as with nanostructured materials.[35] Graphene, for instance, has a theoretical specific surface area

of approximately 2600 m^2/g, one of the highest in potential electrode materials.[50] However, due to agglomeration concerns and the readiness of graphene sheets to re-stack and form graphite nanocrystals, these materials are typically used in composites, such as with nanofibers.[51-53] Additionally, composites of carbon nanotube-graphene can been used to create an open 3-D porous structure with large surface area.[54] Such a composite showed a high capacitance of nearly 200 F/g in the ionic liquid electrolyte 1-ethyl-3-methylimidazolium tetrafluoroborate. One of the advantages to using an ionic liquid electrolyte is the higher potential limits within which the cell can cycle due to the lack of a solvent.[55]

The other component of the supercapacitor cell that primarily limits the overall performance of the device is the electrolyte. There are four primary classes of electrolytes; aqueous, organic, ionic liquids, and solid electrolytes. Aqueous electrolytes were the first type of electrolyte used in the development of EDLCs.[15] They are the least expensive option and are composed of ionic species in water, commonly strong acids or bases.[56, 57] Aqueous electrolytes have higher capacitances than organic- or ionic liquid-based electrolytes due to the smaller size of the ions[58-59, 60] and have higher conductivity than organic electrolytes.[61] However, aqueous electrolytes are limited to a working potential around 1 V due to the decomposition of water at higher voltages,[58] although this can sometimes be extended to 2 V with some pseudocapacitive electrodes.[62]

Organic electrolytes are organic salts, such as tetraethylammonium tetrafluoroborate, dissolved in an organic solvent, like ethylene carbonate or acetonitrile.[22, 63, 64] These electrolytes have a larger attainable working potential, up to around 3.5 V,[58] with some

systems reaching 4.8 V at room temperature.[63] They also typically exhibit lower capacitance than aqueous electrolytes in similar systems,[65] but the increase in working potential produces an EDLC with a higher specific power.[64] Organic electrolytes are also water sensitive; capacitor failure occurs at higher operating voltages due to the decomposition of residual water within the electrode.[66] Additionally, the use of organic solvents raises health and safety concerns for organic electrolyte-based EDLCs.[20]

Ionic liquids are salts that are liquid at or below room temperature[19] and provide a high maximum working potential of up to 6 V.[20] There are many commercially available ionic liquids, providing a wide range of options to use in an EDLC.[19] Ionic liquids are safer than organic electrolytes because they are not flammable and generally less toxic.[20] Also, these electrolytes have a larger maximum potential window than aqueous or organic electrolytes.[20, 67] Additionally, most ionic liquids are able to operate at a wider temperature range than aqueous or organic electrolytes,[68] and they can be synthesized from a number of renewable and recyclable sources, making them a more environmentally friendly option.[69, 70] However, ionic liquids are more expensive than aqueous or organic electrolytes, limiting their usage in commercial applications.[19, 71]

Solid electrolytes are also used in EDLCs, usually in the form of a conductive polymer mixed with an active electrode material.[72, 73] Pseudocapacitive materials, such as NaI/I_2 or polyaniline, are also often added to improve the capacitance.[72, 73] The primary benefit of solid electrolytes is the ability to synthesize an all solid-state capacitor that is lightweight and mechanically robust.[74] Using a carbon nanotube ink and a polyethylene terephthalate electrolyte, Hu *et al.* produced micrometer-thick EDLCs with capacitances

of 140 F/g within a 3 V potential window.[74] These flexible capacitors are suitable for wearable energy storage devices and other technologies that require flexibility and durability. Additionally, to make an entirely self-contained system, gold current collectors have been decorated onto the active material.[73]

1.3 Lithium-Ion Batteries

Lithium-ion batteries (LIBs) are another type of rechargeable electrical energy storage device that is more prevalent in modern personal electronics, such as cell phones and laptops.[11-12] LIBs have a higher energy density than EDLCs, but generally lower power density.[9, 14] The first widespread commercial success of LIBs occurred in 1991 based on a carbon anode, non-aqueous electrolyte, and a lithium cobaltate ($LiCoO_2$) cathode.[75] The primary advantage of LIBs over other battery technologies is the much higher energy density available, typically over 250 Wh/kg, compared to lead-acid batteries which are usually around 30 Wh/kg.[76] This high energy density is a result of the mechanism for charge storage and the lightweight materials that are used to produce the battery.

LIBs are composed of four primary components: an anode, cathode, electrolyte, and a porous spacer to separate the anode and cathode, as seen in Figure 1.5.[76-77] The cathode is made from a material that has a high lithium content by weight, such as $LiCoO_2$ or $LiFePO_4$. The anode is made from a material that can accept lithium ions during cycling, typically a layered material, such as graphite,[76] or a metal or semiconductor that can form a solid solution with lithium, such as silicon.[78] The electrolyte is a solution of a lithium salt, such as $LiPF_6$, in an organic solvent that usually consists of mixed carbonates such

as ethylene carbonate, dimethyl carbonate, and diethyl carbonate.[79] The spacer is used to eliminate an electrical short between the anode and cathode, similar to the spacer in EDLCs, while providing a pathway for electrolyte ions to freely pass between the electrodes.[79]
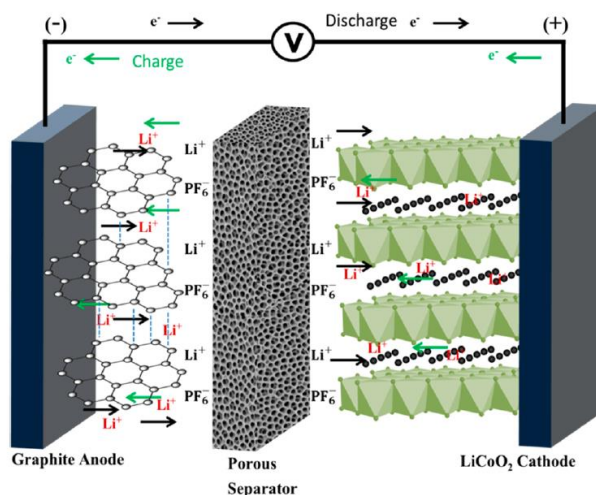
Figure 1.5. Schematic of a typical LIB composed of a graphite anode, $LiCoO_2$ cathode, $LiPF_6$ electrolyte, and porous separator. The direction of charge flow is shown in black for discharging the cell and in green for charging the cell. Reprinted with permission from reference 76. Copyright 2015, American Chemical Society.

LIBs store charge through a "rocking chair" mechanism where lithium ions travel between the electrodes while electrons travel through the circuit to balance the charge. When the cell is being charged, the electrons and ions travel from the cathode to the anode, with the reverse direction during discharge, as seen in Figure 1.5. In this case, the charge is stored through changing the composition of the electrode materials, and subsequently the chemical potential energy of each electrode. The standard cell potential

($E°$) is then related to the standard free energy of formation of the reaction between the electrodes according to Equation 1.3:

$$\Delta G_0 = -nFE \qquad (1.3)$$

where ΔG_0 is the standard free energy of the electrode reactions, F is the Faraday constant, and n is the number of electrons involved in the reactions.[76]

1.3.1 Contemporary Cathode Materials

LIB cathodes are made from materials that initially contain lithium in the crystalline structure. These lithium ions can be organized in 1-D, 2-D, or 3-D arrangements (Figure 1.6).[77] The first structure shown to work efficiently as a LIB cathode material was the $LiCoO_2$ layered structure, with two dimensional Li-ion diffusion paths. The first published use of this material was in 1980, when J. Goodenough's group showed that Li-ions can be electrochemically extracted from the parent $LiCoO_2$ material, giving a theoretical energy density of 1.11 Wh/kg.[80] In this structure, the oxygen atoms form a cubic close-packed array, with lithium and cobalt occupying alternating layers of octahedral holes.[77] During cycling, the cobalt atoms primarily provide the electrons for charge balance. At half an equivalent of lithium removed ($Li_{0.5}CoO_2$), cobalt tends to form an intermediate oxidation state of +3.5, which induces a crystalline change to a monoclinic structure, which prevents further cycling.[81] Furthermore, the cobalt can dissolve into the electrolyte solution during cycling, leading to oxygen release and structural breakdowns. To address this issue, surface oxide coatings have been used, such as ZrO_2, Al_2O_3, or TiO_2, providing an effective strategy to reduce cathode breakdown and allow for longer lifetimes of the battery.[82-83]
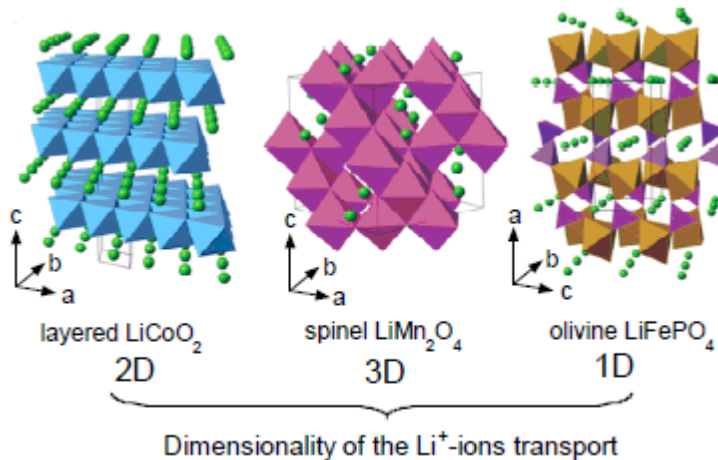
Figure 1.6. Crystal structures of three Li-ion cathode materials showing the different lithium ordering in one, two, or three dimensions. Reprinted with permission from reference 77. Copyright MDPI AG.

The next major composition shown to reversibly cycle Li-ions as a cathode material was $LiMn_2O_4$, which exhibits the spinel structure and has 3-D Li-ion diffusion paths.[84-85] This structure also has a cubic close-packed arrangement of oxygen atoms, with manganese occupying half of the octahedral holes, leading to a network of edge-sharing MnO_6 octahedra.[77] The lithium ions occupy tetrahedral holes that exist between empty octahedral holes, leading to the three dimensionality of the lithium diffusion. This material was first published in 1983 when it was shown that lithium ions could be inserted electrochemically into $LiMn_2O_4$.[84] In this case, a slight phase change was observed when above one stoichiometric equivalent of lithium was added. In 1984, a follow-up paper showed that the material could have up to 0.6 equivalents of lithium reversibly extracted, giving a total compositional range of $Li_{0.4}Mn_2O_4$ to $Li_2Mn_2O_4$.[85]

It wasn't until the late 1990s that a new cathode structure was shown to exhibit promising electrochemical behavior. In 1997, $LiFePO_4$ was shown to be able to reversibly extract and insert lithium ions.[86] This material has an olivine structure with orthorhombic symmetry.[77] It is similar to the naturally occurring mineral triphylate $(Li(Mn, Fe)PO_4)$, although the pure iron-containing phase that is useful as a cathode material is an artificial product.[87] In this case, the oxygen atoms form a hexagonally close-packed array, with Li-ions occupying half of the octahedral holes formed, the other half filled by iron. This creates the 1-D channels of Li-ions seen in Figure 1.6. When cycling, up to 0.8 Li-ions can be reversibly extracted and reinserted before irreversible crystalline changes occur.[86] One significant advantage of $LiFePO_4$ over $LiCoO_2$ and $LiMn_2O_4$ is the relatively low cost of the materials, because iron is significantly cheaper than the other two transition metals, making it a more attractive commercial material.[88]

Currently, most high-performance cathodes are made from $LiCoO_2$-based materials due to their higher capacity than the other materials, in spite of the higher cost. Typically, in the commercial versions of this material, some of the cobalt is replaced with nickel, which reduces the cathode breakdown and increases cell lifespans.[89] Pure $LiNiO_2$ cannot be used, because it exhibits exothermic oxidation of the electrolyte when the material begins to break down, leading to cell failure and potential fires.[90] Additionally, the realized specific capacity can be increased from 127 mAh/g to 180 mAh/g due to the higher structural stability allowed by the nickel atoms.[89] However, while the replacement of nickel reduces the cost of the cathode, the materials used account for approximately 80% of the cost of the final cell.[89, 91-92]

One of the most promising new cathode materials is $LiFePO_4$. It has a reasonably high theoretical capacity of 170 mAh/g, though typically only about 150 mAh/g is reached in devices due limitations resulting from low intrinsic conductivity.[91] It also exhibits increased structural stability due to strong covalent bonding between the oxygen and phosphorus atoms in the PO_4^{3-} units.[93] This stabilizes the antibonding Fe^{3+}/Fe^{2+} state through inductive effects. This structural stability also leads to increased thermal stability compared to $LiCoO_2$ and $LiMn_2O_4$.[86] Finally, $LiFePO_4$ is significantly cheaper than other alternatives, potentially reducing the cost of a final cell by between 10 and 50 percent while utilizing a more environmentally friendly transition metal compared to cobalt or manganese.[92]

However, there are three primary disadvantages to $LiFePO_4$: one, a low intrinsic conductivity of $<10^{-9}$ S/m;[94-95] two, low volumetric density compared to other cathode materials leading to low volumetric capacity;[96-97] and three, a low Li-ion diffusion coefficient limiting the rate performance of the material.[98] Of particular note is the low electric conductivity, as this thesis (chapters 6 and 7) describes the development of a new layered cathode material, Li_8ZrO_6, that also exhibits low electric conductivity. Therefore, the methods used to address this issue in $LiFePO_4$ are discussed as guidelines for how they were approached in the Li_8ZrO_6 system. There are three primary ways to reduce the effect of the low conductivity. The first is to reduce the active material grain size by altering the synthetic conditions.[93, 99] Secondly, secondary conductive phases can be added, such as carbon or metal nanoparticles, to increase the overall conductivity.[100-108]

And finally, dopants can be added to improve the electronic structure of the material, improving both the conductivity and lithium diffusion coefficients.[109-110]

In the case of LiFePO$_4$, it has been shown that the rate capability is mainly controlled by the specific surface area of the active material.[102, 111] One method to increase the specific surface area is to alter the synthetic parameters used to produce the material. Xia *et al.* prepared LiFePO$_4$ through a sol-gel method, creating a sample with a specific surface area of 24.1 m^2/g.[111] The sample was able to deliver a specific capacity of 115 mAh/g at a rate of 5C. For batteries, the C rate is defined as one Faraday constant per mole of the active material (or one stoichiometric equivalent of lithium) per hour. When using a polyol-based synthesis, homogenous nanoparticles of LiFePO$_4$ were produced, also giving excellent rate performance.[93] In general, results have shown that the smaller the particles, the better the electrochemical performance.[112] Another promising method to produce small grains of active material involves the use of a supercritical hydrothermal synthesis, though the samples tend to suffer from significant levels of impurity.[99]

Beyond changing the synthetic conditions, smaller grains can be achieved by the addition of carbon to the synthesis mixture, which has the further advantage of adding in a conductive element to the final composite. Ravet *et al.* coated LiFePO$_4$ particles with carbon and reached practical specific capacities approaching the theoretical value of 170 mAh/g.[113] This carbon coating accomplishes four primary functions.[91, 100] The first is to act as a reducing agent to minimize formation of trivalent iron ions during synthesis. It was shown that only 5% of added carbon can eliminate the formation of any Fe^{3+} phases during the synthesis.[104] Second, the carbon acts to spatially separate the particles,

reducing grain growth. Third, the carbon acts as an electronic bridge between particles to enhance the interparticle conductivity.[114] And finally, it helps avoid aggregation between particles, leaving pathways for lithium ions to easily travel through the composite during cycling.[108] As the carbon content increases during the synthesis, the particle size decreases, although the increased amount of the nonactive carbon phase reduces the volumetric energy density.[110] Utilizing an intermediate level of carbon gives a very small charge-transfer resistance and superior electrochemical performance.

Another way to gain the benefits of both reducing the grain size and providing excellent contact between carbon and the active material is to use a multiconstituent synthesis, along with templating to create excellent pathways for electronic diffusion. In 2011, Vu *et al.* published the synthesis of three-dimensionally ordered macroporous LiFePO$_4$/C composites.[115] By mixing both the active material and carbon precursors, followed by infiltration into a polymer template, an ordered structure was produced that provided spatial distribution of the active material inside the nodes of the structure (seen in Figure 1.7) with carbon connecting these nodes to provide electronic conductivity within the material. The open structure also allows for a high surface area contact between the composite and the electrode. This composite showed a specific capacity of 150 mAh/g at C/5 and was able to retain 64 mAh/g at the very high rate of 16C.
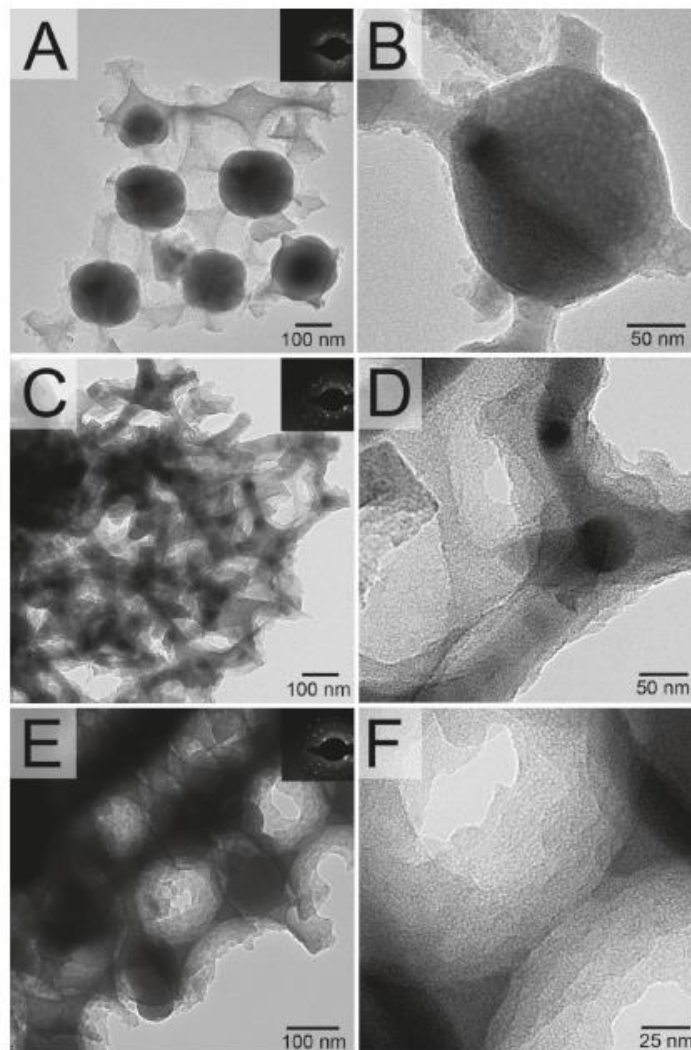
Figure 1.7. Transmission electron micrographs showing the structure of the hierarchically porous LiFePO$_4$/C composite synthesized at 600 (A and B), 700 (C and D), and 800 °C (E and F). The dark areas are the LiFePO$_4$ dispersed into the nodes of the structure. Reprinted with permission from reference 115. Copyright 2011, American Chemical Society.

1.3.2. Effect of Doping on Cathode Materials

As previously discussed, doping is another method for improving the performance of LiFePO$_4$. This can alter the electronic structure of the active material, increasing the

electronic conductivity and lithium ion diffusion. A large body of research has demonstrated the benefits of doping cathode materials for lithium-ion batteries.[88, 116-127] In the case of LiFePO$_4$, the introduction of Ti^{4+} or Zr^{4+} into the Fe^{2+} sites increases p-type semiconductivity within the cell.[117, 122] When Ni^{2+} is incorporated into the Fe^{3+} sites, the nickel doping increases the P–O bond strength, stabilizing the structure, reducing the Li-ion charge transfer resistance, and improving the capacity and rate performance of the cathode material.[124] Other dopant atoms, such as Mg, Ni, Al, and V have also been studied, generally leading to a decrease in the polarization resistance and an improvement in the capacity, with V^{5+} having the greatest effect.[123] Beyond doping the iron sites, the lithium sites can also be exchanged with supervalent atoms, such as Mg^{2+}, Al^{3+}, Ti^{4+}, and Nb^{5+}, which has increased the conductivity by a factor of 10^8 through the introduction of p- and n-type conductivity in the lithiated and delithiated states, respectively.

Other cathode materials also exhibit benefits from doping. Li$_3$V$_2$(PO$_4$)$_3$ has been doped with Fe,[121] Co,[127] and Cr.[125] When doped with Fe, the doped structure retains 71% of the initial capacity compared to 58% in the undoped sample. This improvement in performance is attributed to increased conductivity and structural stability deriving from the incorporation of the Fe^{3+} ions. Additionally, Fe has been used as a dopant in LiMn$_2$O$_4$ where an improved capacity was observed and correlated to the changing oxidation state of the doping atom.[116]

1.4 Synthesis of Nanostructured Materials

As discussed, nanostructuring materials gives many advantageous properties, from improving specific surface area and electrolyte wetting in supercapacitors[128-129] to

reducing grain size and increasing interfacial area in lithium ion batteries.[86, 93] Nanostructuring can be accomplished through a few strategies, such as through templating or textural structure resulting from synthetic conditions. Textural structure occurs naturally, based on the synthetic conditions and precursors used, making it an attractive alternative to templating, although only limited control over the final structure and be exercised.[130] The advantage of templating is that it forms a more ordered structure that can be optimized for a particular application. However, templating usually requires additional steps, creating a more complicated synthesis.[131-132] There are two primary methods of templating, soft templating and hard templating, which are discussed below.

1.4.1. Soft Templating of Materials

Soft templating utilizes a solution-based macromolecule, referred to as a structure-directing agent, and can be a block co-polymer[129, 133] or surfactant.[134-135] This agent creates the desired structure during the synthesis, and the shape and ordering of the pores are determined by the selection of the structure-forming agent and the ratio of precursor to agent. This method can be used to template a range of products, from carbon to silica, as well as composites of materials. For the purpose of this thesis, the following discussion will focus on soft templating of carbon products, because the thesis focuses primarily on templating carbon materials for EDLCs.

There are multiple synthetic strategies that utilize soft templating. The structure can be formed through a hydrothermal synthesis,[136-137] a multi-constituent synthesis.[136, 138] or thin-film-based evaporation-induced self-assembly.[129] The general synthesis involves creating a solution of a carbon precursor and the desired structure-directing agent. This

solution is then treated using the desired method, which involves some curing step to set the structure prior to final pyrolysis in an inert atmosphere to form the carbon product.[129, 139-140] If a multiconstituent synthesis is used, an additional etching step can be necessary to remove any other precursors, such as silica, to form the final product.[29, 136, 138]

This thesis work utilized evaporation-induced self-assembly (EISA) as the primary method of introducing diblock copolymers as a soft template. In this case, no additional precursors beyond the polymer and carbon precursor (a phenol-formaldehyde resol) were used in the initial solution. During EISA, the precursor solution is spread thinly over a substrate and allowed to dry.[129, 135-136] During this process, the structure-directing agent increases in concentration as the solvent evaporates and then forms micelles at what is known as the critical micelle concentration. This occurs because of the amphiphilic nature of the template. One portion interacts with the carbon precursor while the other phase separates into the interior of the micelle. As additional solvent evaporates, the space between the micelles is reduced, eventually ordering into the final structure.[141-142] This process is shown in Figure 1.8, showing the general mechanism of the formation of the formation of the intermediate ordered structure, in this case forming spherical micelles.[143]

Evaporation

| initial, solvated step | critical micelle concentration | ordered structure |
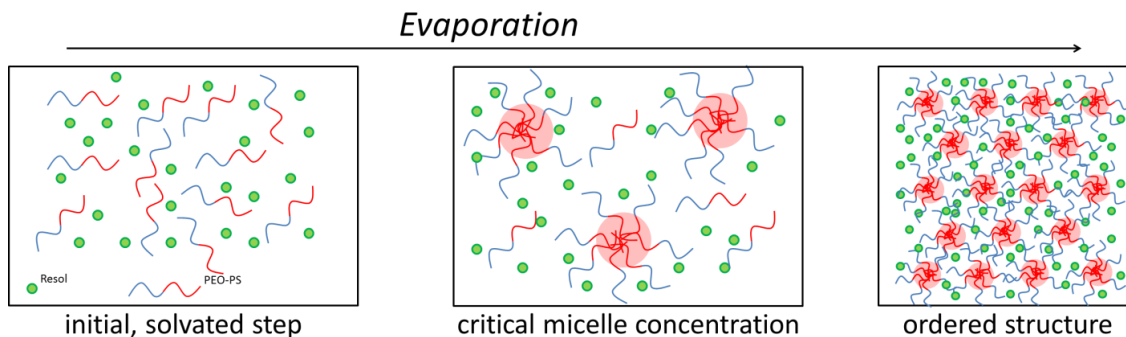
Figure 1.8. Schematic of the EISA process showing the formation of the micelles leading to the final ordered structure. Reprinted with permission from reference 143. Copyright 2014, Elsevier.

1.4.2. Hard Templating of Materials

Hard templating, for comparison, uses a pre-formed structure as a mold to create the final morphology. Template structures include microporous zeolites,[131, 144] mesoporous silica,[145-146] and silica or polymer spheres in a range of sizes.[115, 147] As the original structure, by necessity, is connected, the resulting inverse replica has interconnected pores, which is advantageous for applications such as in supercapacitors. Furthermore, the wide range of potential templates provides the basis for a wide range of morphologies, allowing for optimization of pore size and shape. In this thesis, hard templating using silica spheres was used to create three-dimensionally ordered mesoporous (3DOm) carbon electrodes for use in supercapacitors. In this case, the template was removed through the use of a hydrofluoric acid etch. Figure 1.9 shows the general synthesis scheme for producing 3DOm carbon.
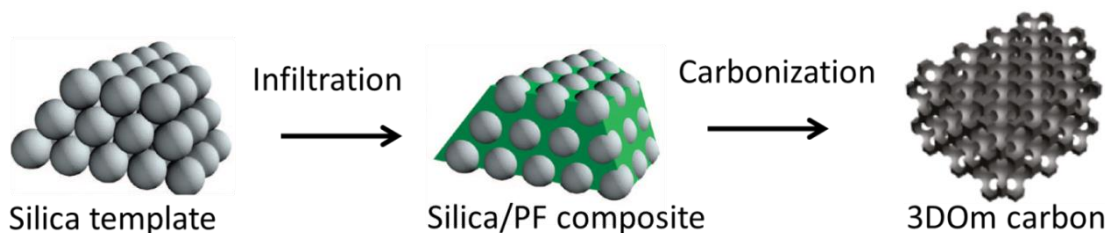
Figure 1.9. Schematic showing the process of forming 3DOm carbon using an ordered array of silica spheres as a hard template.

The final 3DOm structure is a face-centered array of spherical pores as a result of the ordered array of spheres used as the template.[148] The pores are well interconnected through windows that result from the interfaces between the silica spheres. This structure is ideal for the supercapacitor application, because the connected pores allow for easy electrolyte infiltration to access the high specific surface area of the material. In addition, the 3DOm framework is also well-connected, giving excellent electronic conductivity through the electrode material.[149]

1.5 Summary

This introduction has discussed the importance of improving rechargeable electrical energy storage and the general parameters used to determine their properties. The first half of the remaining thesis covers my work on supercapacitors. Chapter 2 focuses on soft templating of mesoporous carbon films, specifically using EISA. As mentioned, the precursor solution is spread thinly over a large area in order to get more even evaporation and a more ordered structure. However, this means that to isolate the product prior to carbonization, a tedious removal process must be used. In order for the film to spread evenly, the substrate must have a small contact angle with the solution. For phenol-

formaldehyde resol, the carbon precursor used here, a glass substrate is commonly used; however, the cross-linked phenol-formaldehyde resol adheres to the glass substrate. To isolate the product prior to carbonization, this involves manually scraping the films off the substrate. Chapter 2 discusses an alternate method that involves using a sacrificial layer between the glass and the phenol-formaldehyde resol. This does not significantly change the obtained product and eases the product isolation with a much higher yield.

Chapter 3 describes the use of a hard templated 3DOm carbon electrode in EDLCs and focuses on the electrolytes used in these devices. As discussed above, ionic liquids offer a higher potential window than many alternative electrolyte solvents, leading to a higher energy density. My work studied a selection of commercially available ionic liquids and compared measured physical and electrochemical properties, such as viscosity, ion size, and conductivity, to their potential window and specific capacitance. This was used to determine which properties lead to a better ionic liquid electrolyte.

Chapter 4 focuses on altering the electrode composition of 3DOm carbon synthesized in a similar method to Chapter 3. This was done to improve the specific capacitance of the electrode material in an ionic liquid electrolyte. To accomplish this, a nitrogen-containing ionic liquid, separate from the electrolyte, was used in the synthesis of the carbon, which resulted in nitrogen doping. By varying the ratio of phenol-formaldehyde resol to the ionic liquid, the level of nitrogen doping in the final product could be controlled. As the nitrogen level increased, the specific capacitance improved, especially at higher cycling rates. However, after the nitrogen increased beyond 7.6%, the interconnected pore structure that is important to electrode performance deteriorated,

27

leading to a significant loss in specific capacitance. This study shows that an optimal level of nitrogen doping is necessary for increased performance while maintaining the 3DOm structure.

Chapter 5 begins the work on lithium-ion batteries. One of the important areas to study is the mechanism of charge storage within the electrode, specifically any crystalline changes. While this can be modelled computationally, experimental in-situ observations help confirm the results and give additional insight. Specifically, monitoring the crystalline changes can be done with X-ray diffraction, but conventional methods can be cumbersome and require specialized equipment. To overcome these limitations, I developed a low-cost electrochemical cell that can be used for in-situ monitoring of crystalline changes of an electrode material while cycling. The work used $LiFePO_4$ as a model compound, as a significant amount of prior literature was available for comparison.

Chapter 6 begins the main portion of my involvement with the lithium-ion battery project, namely the development of a novel cathode material, Li_8ZrO_6. In this chapter, the initial work is outlined, along with some of the computational predictions and explanations of the performance of Li_8ZrO_6 as an electrode material. The chapter further describes the use of carbon as a secondary phase and yttria doping to reduce the active material grain size and create intimate contact with a conductive carbon phase. This material was able to reversible cycle over 140 mAh/g for 60 cycles, with initial specific capacities of over 200 mAh/g.

Chapter 7 continues this work, studying the effects of transition metal dopants on the specific capacity of Li_8ZrO_6, combined with additional computational modeling. Specifically, Mn, Fe, Co, Ni, Cu, and Ce were studied as potential dopant atoms, with all dopants resulting in improved specific capacities compared to an undoped control sample. Of these metals, Fe showed the highest specific capacity, with over 175 mAh/g maintained after 140 cycles, and over 80 mAh/g at a rate of 5C. This improvement in specific capacity is likely due to the dopant atoms lowering the band gap of the cathode material, allowing for a more favorable delithiation potential within the decomposition limits of the electrolyte.

Finally, the thesis concludes with closing thoughts and future directions for supercapacitors and lithium ion batteries. Overall, this thesis describes methods used to synthesize and characterize improved electrode materials used in rechargeable electrochemical storage devices.

Chapter 2: Use of a Sacrificial Layer for an Efficient EISA Synthesis of Mesoporous Carbon

Reproduced with permission from "Use of a Sacrificial Layer for an Efficient EISA Synthesis of Mesoporous Carbon" by Wilson, B. E.; Rudisill, S. G.; and Stein, A. in *Microporous and Mesoporous Materials*, **2014**, *197*, 174-179. Copyright 2014 Elsevier.

Contributions to this chapter were performed by Dr. Stephen Rudisill (TEM imaging).

2.1 Introduction

Evaporation-induced self-assembly (EISA) is a commonly used technique to create thin films of ordered, mesoporous materials with a variety of pore morphologies, such as cubic,[150-151] gyroid,[152] and hexagonal mesostructures.[151, 153-154] In general, an initial solution is made from the three main components (solvent, precursor material, surfactant template), followed by slow evaporation of the solvent, leading to liquid-crystal formation and an ordered structure (Figure 2.1, top).[155-156] This can be followed by additional curing steps and removal of the template (through pyrolysis or solvent extraction), leading to the final structure. This method has the advantage of in-situ structure formation (as opposed to hard templating where a pre-formed structure, such as silica, is used to create the pores), and the ease of template removal, which can often be combined with final structure formation in a single, thermal step.[150-151, 157-158] The block co-polymers commonly used as the template can provide larger pores than ionic surfactants, such as sodium dodecyl sulfate or long-chain alkylammonium salts,[159] while

being able to tune pore diameter and architecture through variation of block length and ratios of the different blocks.[157] Additionally, agents (such as short chain polystyrene),[157] other additives,[160] or mixed solvents can be used to further control the morphology.[152]
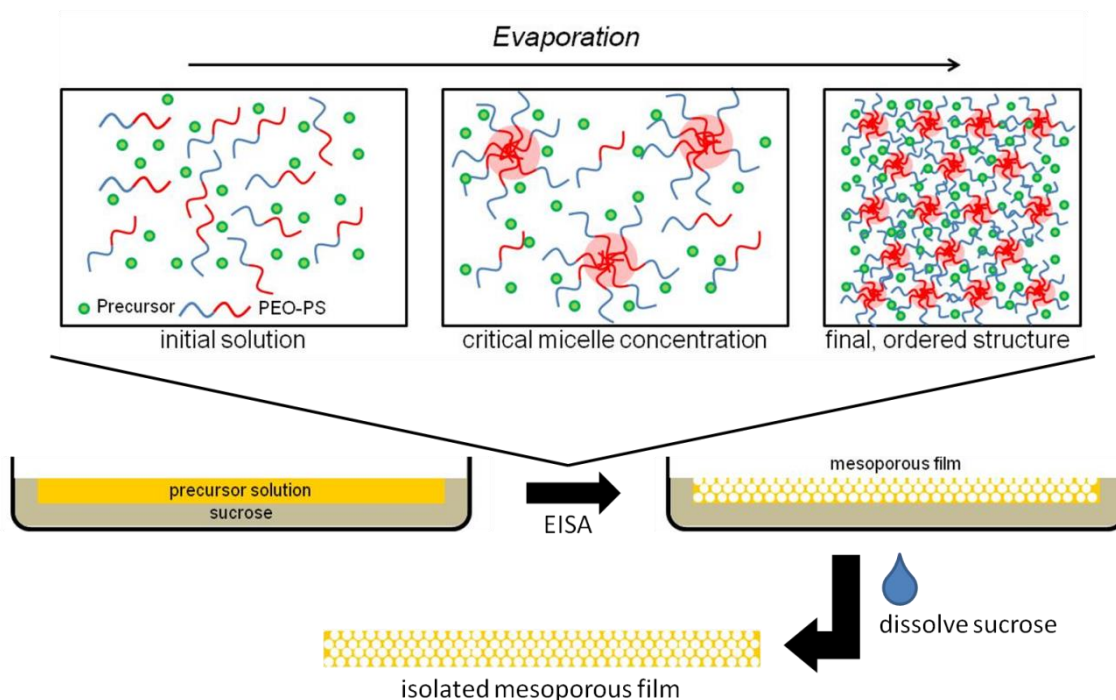
Figure 2.1. Schematic of the EISA process using a sacrificial sucrose interlayer and a diblock co-polymer as the template. A sucrose layer is deposited on a Petri dish, dried, and covered with the precursor solution for the mesoporous material. During the EISA process, the precursor solution begins to form micelles as the template concentration increases, eventually sedimenting into an ordered structure. The product film can be released from the substrate by dissolving the sucrose layer.

While EISA is a versatile and useful method for preparing mesoporous structures, it suffers from a significant drawback, namely tedious isolation and low yield of the product. Because the rate of evaporation and interfacial contact with a substrate are

31

important to creating a uniform structure, the precursor solution is commonly spread into very thin films, which usually demands a large number of substrates (such as glass Petri dishes) to obtain a reasonable amount of product.[17, 150-151] This then requires time-consuming removal techniques, such as mechanical scraping to isolate a very small amount of product, around 0.1–0.15 mg final product per cm^2 substrate for a typical carbon EISA synthesis. Some solutions to these issues involve the formation of hierarchical structures, for example, by performing EISA on polyurethane foams or silica spheres to provide the large substrate surface area.[158, 161-162] However, this either necessitates the removal of the substrate, requiring corrosive reagents such as KOH or HF, or leaving the substrate behind, thus reducing the mass content of the desired mesoporous material. Therefore, a better process to prepare EISA products that improves yield and ease of isolation is needed. As the most time consuming and arduous process during the EISA procedure is the isolation of the mesoporous film from the substrate, we focused on developing an easily removable substrate to improve the ease of film isolation.

Herein we report a technique of using a sacrificial layer to simplify the synthesis of extended, ordered, mesoporous carbon films using a block co-polymer template through EISA (Figure 2.1). Sucrose and KCl are low-cost, common, and environmentally friendly compounds, which are insoluble in THF (so as to not contaminate the precursor solution) and easily dissolved with water. For these reasons, they were chosen for the model layers on which the mesoporous carbon films were grown. The final carbon structures are compared between the three samples formed in glass Petri dishes; one with no sacrificial

layer, one with sucrose, and one with KCl, using gas sorption, small-angle X-ray diffraction (SAXS), and transmission electron microscopy (TEM).

2.2 Experimental

2.2.1 Materials

The quaternary ammonium salt Aliquat 336, 1-dodecanethiol (98%), carbon disulfide (ReagentPlus, >99%), oxalyl chloride (ReagentPlus, >99%), styrene (ReagentPlus, >99%; inhibited with 4-*tert*-butylcatechol), phenol (>99%), acetone (>99.5%), and sodium hydroxide (50% in water) were obtained from Sigma Aldrich. Chloroform (ACS reagent grade), methylene chloride (ACS reagent grade), and tetrahydrofuran (HPLC grade) were obtained from Fisher Scientific. Hydrochloric acid (concentrated in water) and isopropanol (ACS reagent grade) were obtained from Macron Chemicals. A solution of mixed hexanes (ACS reagent grade) was obtained from Pharmco-AAEPR. Polyethylene oxide (PEO, 20 kDa) was obtained from Alfa Aesar. Formaldehyde (37% in water) was obtained from J. T. Baker. Sucrose and potassium chloride were obtained from Mallinckrodt. All water used was deionized in-house to a resistivity of at least 18 MΩ·cm. All chemicals were used as received unless otherwise noted.

2.2.2 Preparation of Precursor Materials

The chain-transfer agent (CTA, 2-(dodecylthiocarbonothioylthio)-2-methylpropionic acid) was prepared according to a literature synthesis with no significant alterations.[163] Using the purified CTA, a PS-PEO block copolymer was prepared using a published RAFT polymerization described by He and Lodge with slight modifications.[164] Briefly,

the PEO-CTA macroinitiator was created by activating the CTA (1.2 g) with excess oxalyl chloride in anhydrous methylene chloride under Ar, followed by the addition of mono-hydroxy PEO (10.8 g). The PS-PEO copolymer was synthesized by reacting the PEO-CTA macroinitiator (5.0 g) with purified styrene (50.0 g) at 140 °C and 500 rpm using a Teflon-coated magnetic stir bar under Ar for 45 min, followed by quenching using liquid nitrogen following the literature preparation for all steps. The product was purified by precipitation from methylene chloride into mixed hexanes three times. A phenol-formaldehyde (PF) resol was synthesized following established methods.[150] Briefly, phenol (61 g) was melted at 50 °C in a 500 mL glass round-bottom flask, followed by the addition of a 20 wt% aqueous NaOH solution (13.6 g). An aqueous formaldehyde solution (37 wt%, 200 mL) was added dropwise while stirring. The solution was heated to 70 °C and left for 1 h while stirring at 300 rpm with a Teflon-coated magnetic stir bar to increase the extent of polymerization. The product was neutralized to pH ~7 using an aqueous HCl solution (0.6 M, ~30 mL). Water was removed through rotary evaporation at 40 °C, and the polymer was re-dispersed in THF to achieve a concentration of 50 wt%. After the NaCl precipitate was allowed to settle overnight, the solution was isolated by decanting. The resulting stock solution was stored in a refrigerator until use.

2.2.3 Preparation of Sacrificial Layers

First a stock solution was prepared; for KCl, a saturated solution was used, and for sucrose, a 2.0 M solution was used. The Petri dishes were then washed in a base bath (3 M KOH in isopropanol) for 1 h and rinsed with DI water to both clean the surface and

increase surface hydroxyls, improving the wettability of the solutions containing the desired layer. Once the Petri dishes were dry, the solutions of either sucrose or KCl were spread onto the bottom cover to achieve complete coverage, then dried at 70 °C. After the first layer was finished, a second layer was placed over any areas that had little or no coverage and dried again at 70 °C. In the case of the KCl, ten additions were required to completely cover the dish due to cracks that formed between the large growing crystals. With sucrose, usually two layers were sufficient, though occasionally three were required.

2.2.4 Preparation of Carbon Structure

The mesoporous carbon was synthesized using a modified procedure by Zhao et al.[157] First, a solution containing 5.0 g of 40 wt% resol and 0.3 g PS-PEO polymer in 14.7 g THF was prepared. This solution was spread over ten 10-cm diameter Petri dishes, either with or without a sacrificial layer. The covers were placed on the dishes and the solvent was then left to evaporate overnight under ambient conditions. The films were cured at 100 °C for 24 h to cross-link the PF resol. The mesostructured products that formed on the bare Petri dishes were then removed from the substrates by mechanical scraping using a razor blade, whereas the films formed on a sacrificial layer were removed by first submerging the dishes in boiling water for 30 min followed by gentle abrasion. The films that were removed from the sacrificial layer were then washed in 1.5 L of hot (~80 °C) water for 30 min and isolated by vacuum filtration. When using sucrose as the sacrificial layer, the initially isolated product was then soaked for an additional 30 min in another 1.5 L of hot water and re-isolated by vacuum filtration. In either case, the initial product

35

was washed three times with ~50 mL of water and vacuumed filtered to completely remove any residual sucrose or KCl. All products were then carbonized at 900 °C for 2 h, heating at 1 °C/min to 600 °C and 5 °C/min after under 0.5 L/min flowing nitrogen. The sample grown on bare glass is referred to as PS9.8, and the samples grown on sucrose and KCl as PS9.8S and PS9.8KCl, respectively.

2.2.5 Material Characterization

Nitrogen sorption was performed using a Quantachrome Autosorb iQ instrument. Samples were outgassed for 12 h at 200 °C prior to analysis. Total surface area and pore characteristics were calculated using the QSDFT adsorption model optimized by Quantachrome for mesoporous carbon materials with cylindrical/spherical pores.[165] Small-angle X-ray scattering (SAXS) measurements were carried out on a Rigaku RU-200BVH 2D SAXS instrument operating at 183 cm using a 12 kW, rotating Cu anode and a Siemens Hi-Star multiwire area detector. TEM images were obtained on an FEI Technai T12 microscope operated at 120 kV with a LaB_6 filament. Samples were prepared by suspending them in ethanol and bath sonicating for 15 min. Cu grids coated in Formvar were dipped into the resulting suspension and dried.

2.3 Results and Discussion

2.3.1 Preparation of Sacrificial Layer

The primary goal of this research was to develop a method that both simplifies the procedure and improves the yield of an EISA synthesis of mesoporous carbon. As the mechanical removal of the film from the glass substrate is the most time-consuming step

for the researcher, this step was the focus of the process optimization. The use of a sacrificial layer allows for easier removal (dissolution rather than mechanical scraping), better yield, and easier clean-up (as there is no resol remaining in the dish after removal of the template). In our case, a typical synthesis without a sacrificial layer gave approximately 100 mg of isolated mesoporous carbon, whereas with KCl, approximately 150 mg was obtained and with sucrose almost 200 mg was obtained, mostly due to better recovery of the sample from the Petri dishes. For the choice of a sacrificial layer, there are three main considerations: ease of use, negligible solubility in the EISA solvent, and lack of reactivity with the precursor (in this case the PF resol). Because THF was used as the solvent (due to solubility limitations of the polymer template), sucrose and KCl were chosen as model layers for the reasons outlined. Sucrose has a low solubility in THF of around 0.01 wt% at 60 °C,[166] while KCl is practically insoluble in THF.[167]

An important step in the preparation of the sacrificial layer is the cleaning and hydration of the glass substrates prior to depositing the sacrificial film. This causes the aqueous solutions to spread more evenly and leaves fewer defects that need to be repaired. Also, in the case of sucrose, if the film is deposited onto an untreated Petri dish, the solution beads up and does not form a coherent film. KCl, on both treated and untreated dishes, crystallizes and forms an inhomogeneous film, requiring many more layers to fully coat the bottom of the dish. Additionally, the concentration of the solutions is important for the quality of and ease of production for the final film. In the case of sucrose, a concentration lower than 2 M increases the number of defects in the sacrificial film with very low concentrations producing a visible "coffee-ring" effect. With higher

concentrations, solubility and viscosity make preparation and use of the solution more difficult, especially spreading and drying the film evenly, however, the final sacrificial film quality is similar to that obtained with a 2 M solution. As the concentration of the KCl solution is increased, the improvement in the film quality for each additional layer used is increased, and since there is little change in the viscosity of the film with higher concentrations, a saturated solution creates the highest quality film with the fewest number of layers.

2.3.2 Phenol-Formaldehyde Resol Films

The differences in the films can be easily seen in the dishes once the PF sol has been cross-linked. The PS9.8 film (Figure 2.2a) is glassy and mostly defect free (in terms of millimeter scale defects). In the case of PS9.8S (Figure 2.2b), the defects from the first deposition of the sucrose substrate can be seen in the bubbly areas, but these are completely covered by the second layer. For PS9.8KCl (Figure 2.2c), the granular structure resulting from crystallization of the KCl is evident by the rough appearance of the film, leading to a high level of millimeter-scale defects. A further advantage of using sucrose as a sacrificial layer is the ability to easily remove extended pieces of cross-linked polymer film. Figure 2.2d shows two large pieces of PS9.8S. Even larger pieces (>5 cm^2) can be removed under water, but due to the high aspect ratio of the films, upon removal to air, it is difficult to keep them from scrolling. Further, the pieces are limited by the centimeter-scale smoothness of the film, as cracks that can form create weak points where the film can easily separate. If a lower drying temperature (e.g. 40 °C for 48

h) combined with thinner coatings is used for preparing the sucrose films, fewer defects are created, and larger pieces can be isolated.
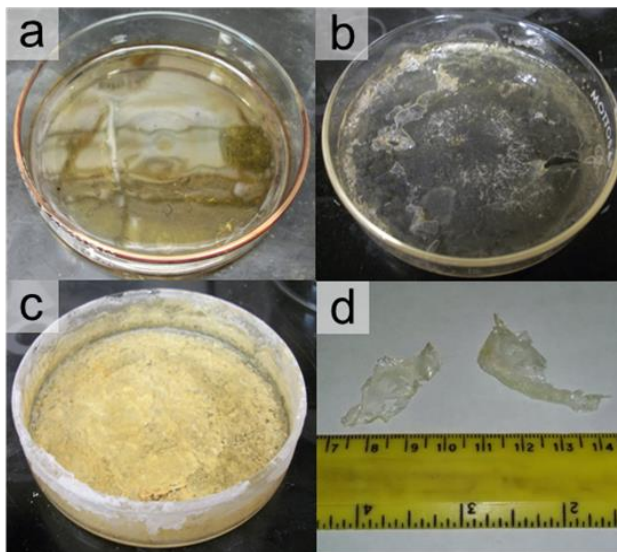
Figure 2.2. Images of cross-linked PF sol for (a) PS9.8, (b) PS9.8S on two layers of sucrose, (c) PS9.8KCl on ten layers of KCl and (d) an extended piece of PS9.8S. The defects seen on the sucrose film are from the first layer and are subsequently repaired with the second coat. In the KCl film, a granular structure can be seen. The diameter of the dishes is 15 cm.

The two primary advantages of using a sacrificial interlayer, beyond the ability to isolate larger fragments, are the reduction in active processing time (time the researcher is actively manipulating the samples) and increased yield. Without a sacrificial layer, the two most labor-intensive steps are the removal of the cross-linked film and cleaning the Petri dishes for reuse. Typically, the film is removed using mechanical scraping (such as using a razor blade). This process requires 10–15 minutes per 10 cm Petri dish, and yields an average of 10 mg per dish (0.12 mg/cm^2) of final carbon product. Beyond the safety

hazards of using such a technique, a large fraction of product is left in the corners of the dish that is exceedingly difficult to obtain. After isolation, cleaning the dishes completely requires the use of Piranha solution or similar corrosive liquids, which can dissolve the cross-linked polymer network. In all, the total active time for isolation and cleaning 10 dishes of product is around 3 hours. When using KCl, additional time is required to create the sacrificial layer, around 20 minutes of active manipulation, but the isolation time is reduced to less than 30 minutes; net active processing time is reduced approximately 75% compared to no sacrificial layer. In the case of sucrose, the creation of the sacrificial layer only takes 5 minutes of active manipulation to prepare 10 films (because fewer layers are needed than with KCl), with isolation time similar to KCl films, giving an over 80% reduction in active processing time. Further, the yield is almost doubled to nearly 20 mg/dish of final carbon product for KCl and sucrose, respectively, because of the greater efficiency of product isolation, which also leaves the dishes almost completely clean, and the KOH wash used prior to the next sacrificial layer preparation is sufficient to clean any residual surface impurities.

2.3.3 Analysis of Mesoporous Carbon Product

The mesoporous carbon products were studied using gas sorption to determine whether the different substrates affected their textural properties, including their pore diameters and total surface areas. The isotherms for all samples (Figure 2.3a) show the type-IV behavior typical for mesoporous carbon, with similar shapes and positions of the hysteresis. In all three cases, the sample isotherms almost completely overlap and show very similar pore size distributions (Figure 2.3b). Further, the samples exhibit very

similar total surface areas between 1020 and 1100 m^2/g, pore diameters (taken as the center of weight using a Gaussian peak fit for the primary mesopore peak) of 9 nm, and total pore volumes of 0.32 cm^3/g (Table 2.1). This shows that the use of these sacrificial templates does not significantly affect the pore texture. Even though the films displayed the millimeter-scale defects, the bulk nanostructure remains effectively unchanged.
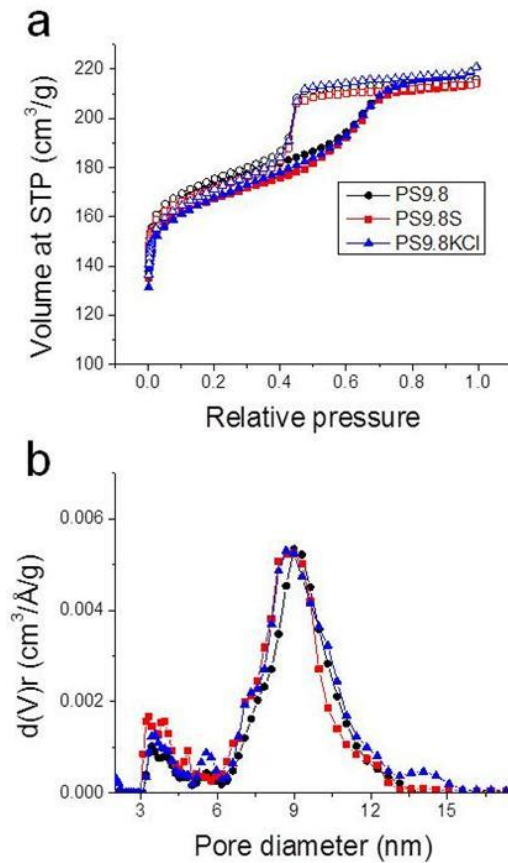
Figure 2.3. (a) Nitrogen sorption isotherms and (b) pore size distributions of PS9.8, PS9.8S, and PS9.8KCl.

Table 2.1. Summary of pore characteristics for PS9.8, PS9.8S, and PS9.8KCl.

	Surface area (m^2/g)	Pore diameter (nm)	Pore volume (cm^3/g)	d-spacing[*] (nm)
PS9.8	1100	9.0	0.32	14.9
PS9.8S	1020	3.9	0.32	14.7
PS9.8KCl	1040	8.9	0.32	14.1

[*] The d-spacing corresponds to the position of the main peak in the SAXS pattern.

A final important consideration is whether the change in substrate affects the order and geometry of the pores. SAXS patterns of the three materials are shown in Figure 2.4. The patterns are very similar for all three samples, showing one major peak attributable to a mesostructure with uniform pore spacing but irregular pore geometry. The position of this peak is not influenced by the sucrose interlayer and shifts only slightly when KCl is used as a sacrificial interlayer. This small change in the d-spacing with KCl could occur from changes in ionic strength of the solution surrounding the forming micelles, leading to differing spacing. However, because the change is small and the basic structure remains, both substrates would remain viable options as a sacrificial substrate for the formation of mesoporous carbon through EISA.
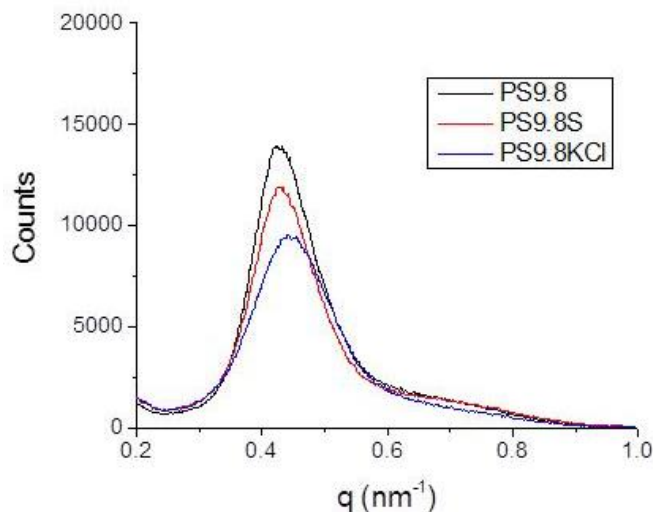
Figure 2.4. Small-angle X-ray scattering patterns of PS9.8, PS9.8S, and PS9.8KCl.

Based on the SAXS and gas sorption results, there is no significant change in the morphology of the pores, both in size and order. This indicates that the use of the sacrificial layer does not affect the solution-substrate interaction enough to change the mesostructure phase. This synthesis was optimized to obtain a cubic phase, which covers a large region in the phase diagram and may have contributed to the lack of a large morphological change.[129] In the case of other systems, the interaction between the sacrificial layer and the precursor solution may have a larger effect, and should be considered when used for syntheses where small changes have a large effect on the resulting structure.[168]

To visually investigate the pore morphology, TEM was used to directly observe the structure. Figure 2.5 shows representative images of the three samples. All of the samples show spherical mesopores approximately 9 nm in diameter, matching the gas sorption results, with no noticeable differences between the samples. The pores are spaced

43

approximately 12–15 nm apart, in agreement with the spacing determined from the peak in the SAXS patterns. PS9.8KCl has pores that are slightly more closely spaced than the pores in the other two samples. Beyond the small variation in pore spacing, the samples have no distinguishable differences, showing that the different sacrificial layers do not significantly affect the pore wall structure or geometry.
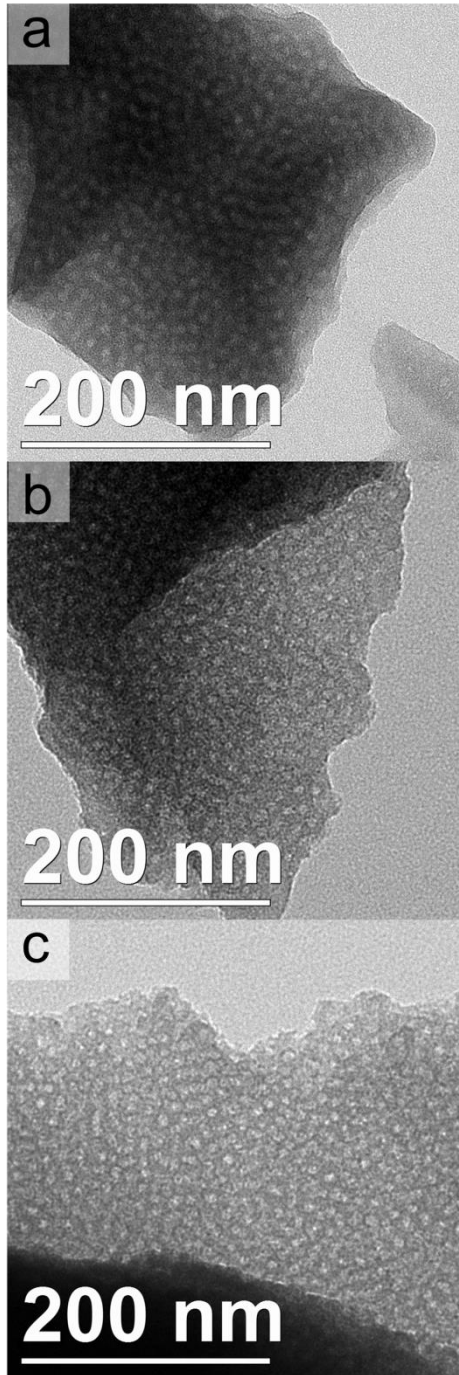
Figure 2.5. TEM images of (a) PS9.8C, (b) PS9.8S, and (c) PS9.8KCl, showing the nearly identical pore and wall structure of the three samples.

2.4 Conclusions

In summary, we have demonstrated a method employing sacrificial interlayers to facilitate EISA preparations of mesoporous carbon. It is easier to produce sacrificial layers on a lab scale with sucrose than with KCl because crystallization of KCl requires multiple coatings to create a cohesive film. Sucrose yields a much smoother, more defect-free PF film compared to the film produced on KCl, and yields a final carbon product similar to the film deposited on glass. KCl sacrificial layers, while more time-consuming to make, are easier to remove from the Petri dish, dissolving in a matter of seconds, rather than the 30 minutes required for sucrose. However, we observed an almost 1 nm decrease in the d-spacing of the mesoporous carbon with a KCl substrate, possibly due to the difference in ionic strength surrounding the forming micelles. Because the initial deposition of a KCl layer is relatively time consuming, it is not advantageous to use this substrate purely to save processing time. Regardless whether sucrose or KCl is used as a sacrificial layer, a higher mesoporous carbon yield is obtained, up to twice as much isolated, mainly due to easier recovery of the material from the Petri dish. Additionally, the product obtained is nearly identical in terms of small-angle X-ray scattering and gas sorption behavior, as well as visual observation through TEM imaging, indicating that the change in substrate and the subsequent interaction between precursors and the substrate do not affect the final carbon product. Therefore, because product isolation is significantly easier, the use of a sacrificial substrate significantly improves the viability of EISA as a scalable technique for the production of mesoporous carbon.

Chapter 3: Utilizing Ionic Liquids for Controlled N-Doping in Hard-Templated, Mesoporous Carbon Electrodes for High-Performance Electrochemical Double-Layer Capacitors

Contributions to this chapter were performed by Siyao He (TEM imaging), Keegan Buffington (synthesis assistance), and Dr. Stephen Rudisill (TEM imaging).

3.1. Introduction

3.1.1 Background to EDLCs

Electrochemical double-layer capacitors (EDLCs), or supercapacitors, are rechargeable electrical energy storage devices that offer a compromise between the high energy density of lithium-ion batteries (LIBs) and the fast rates available with dielectric capacitors.[6] In addition, the highly reversible storage mechanism allows for very long lifespans from hundreds of thousands to millions of charge and discharge cycles. Recently, EDLCs have begun to find their way into consumer devices, industrial products and vehicles, with applications ranging from memory back-up systems and cameras to harbor cranes and racecars.[6-8] Additionally, EDLCs can work synergistically with other

rechargeable electric storage devices, such as LIBs. EDLCs generally provide a higher specific power than LIBs, meaning they are better able to charge and discharge quickly. In applications such as regenerative braking, EDLCs would provide the primary storage during braking and power during acceleration,[8] with LIBs providing the power for continuous vehicle operation because of the larger amount of energy they are capable of storing.[2] The differences in the power and energy densities of EDLCs versus LIBs are due to the mechanism of charge storage. Rechargeable batteries store charge in the bulk of the electrode material through ion intercalation or conversion, whereas EDLCs store charge at the electrode/electrolyte interface, facilitating higher rates of charge and discharge.

The capacitance, energy, and power of EDLCs are defined by the following equations:

$$C = \frac{\varepsilon^* \varepsilon_0 A}{d} \tag{3.1}$$

$$E = \frac{1}{2} C V^2 \tag{3.2}$$

$$P = \frac{V^2}{4R} \tag{3.3}$$

where C is the capacitance of the cell, ε^* is the dielectric constant of the electrolyte in the double layer, ε_0 is the dielectric permittivity of a vacuum, A is the accessible surface area for ion adsorption, d is the effective thickness of the double layer, E is the cell energy, V is the maximum potential the cell is cycled at, P is the power of the cell, and R is the resistance of the cell. These equations show that for a given cell mass, the specific energy and power vary as the square of the cell potential. Further increases in the specific energy and power can be accomplished by increasing the capacitance, reducing the resistance of

the cell, and employing an electrolyte with a wider voltage window. To increase the capacitance, porous carbon electrodes are employed that significantly increase the area available for ion adsorption.[7-8] To achieve higher voltages, ionic liquids have shown promise as an electrolyte for supercapacitors.[169-172] They are stable at high temperatures while providing a significantly increased potential window compared to both aqueous- and organic-based electrolytes. As shown in Equations 3.2 and 3.3, increasing the potential window has a square-effect on both power and energy densities. However, ionic liquids tend to yield lower capacities than aqueous electrolytes,[173] in part due to their higher viscosities. To fully realize their benefits, it is therefore necessary to employ electrodes that facilitate efficient mass transport through their pore structure.

3.1.2 Materials Used for EDLCs

Activated carbon materials have been widely used as electrode materials due to their ease of synthesis, high surface areas (up to 2000 m^2 g^{-1}), and electrical conductivity.[40-44] However, these materials have a wide distribution of pore diameters from small micropores to large macropores with many underutilized dead ends throughout the structure.[130] Although it is known that micropores with optimized sizes can contribute to charge storage,[30] it has been demonstrated that with ionic liquid electrolytes, designed pore structures with well-interconnected, uniform mesopores can improve specific capacitance significantly compared to activated carbons, especially at high rates of charge and discharge.[149, 172]

Recent work has shown that the incorporation of heteroatoms into the carbon framework of EDLC electrode materials can significantly enhance the electrochemical

properties, both capacitance and rate performance.[174-179] Specifically, nitrogen-doped carbon has gained attention due to its improved conductivity and wettability with electrolytes.[176] Many N-doped carbon materials have been synthesized, such as graphene,[180] nanofibers,[181] and porous materials[176] through the post-treatment of carbon materials with ammonia, amines, and urea. However, this methodology can only give low loadings of nitrogen (<5 wt%) in the carbon matrix. Additionally, chemical vapor deposition can be used to incorporate nitrogen into the carbon material using acetonitrile or pyridine as precursors.[182-183] Another technique of incorporating nitrogen in a carbon matrix involves the synthesis and carbonization of nitrogen-containing polymers, such as polyaniline or polyacrylonitrile.[44, 175, 177, 184] Although this method allows for much higher nitrogen loadings (up to 16.7 wt%), it requires a complex synthesis involving expensive macro-initiators, limiting their widespread usability.

3.1.3 Incorporation of Heteroatoms into EDLCs

To create porous, templated N-doped carbon, a number of precursors have been used, including melamine,[178-179, 185] pyrazine,[186] complex dye molecules,[187] gelatin,[174] hexamine with resorcinol-furaldehyde,[176] amine-functionalized hard templates with furfuryl alcohol,[45] or treatment of the carbon product with a gaseous precursor, such as ammonia.[188] The resulting doped materials have shown a significant increase in capacitance compared to undoped carbon. For example, a nitrogen-doped carbon fiber material was prepared by coating carbon nanofibers with polypyrrole to achieve a maximum capacitance of 202 F/g in an aqueous electrolyte.[30, 189] Additionally, a porous nitrogen-doped carbon monolith was prepared through sintering a phenolic resol using

magnesium hydroxide and secondary thermal treatment under an ammonia atmosphere. When cycled using an aqueous electrolyte, the capacitance increased by a factor of 1.3 over a similar sample prepared under argon, up to a maximum capacitance of 245 F g^{-1}.[188] Typically, the capacitance of the nitrogen-doped carbons increases as the nitrogen content increases, up to between 8–10 wt%, and then decreases at higher concentrations.[174, 178, 182, 189-190]

Nitrogen-containing ionic liquids have also shown promise as precursors for nitrogen-doped carbon materials [191-194]. Ionic liquids are advantageous due to the large number of possible anion and cation combinations, enabling better control over the extent and type of heteroatom doping. Furthermore, ionic liquids can be made from renewable and green sources, making them a sustainable source for nitrogen doping.[195-196] As liquids, they are readily incorporated into existing solution-based syntheses and can also be used as reagents for nanocasting, using mesoporous silica as a hard template.[190]

3.1.4 3DOm Carbon as an Electrode Material

Recently, three-dimensionally ordered mesoporous (3DOm) carbon materials as EDLC electrodes showed a significant improvement in capacitance over commercial activated carbons when used with ionic liquid electrolytes due to the highly interconnected and uniform pore structure of the 3DOm carbon materials.[149] A 3DOm structure is created by first synthesizing a hard template made from sedimented silica spheres which naturally order into a face-centered cubic (fcc) array if they are sufficiently monodisperse.[148] This template is infiltrated with a precursor material, followed by thermal treatment to carbonize the precursor and yield a C/SiO_2 composite. The silica is

51

removed through etching, leaving an open, bicontinuous 3DOm structure, i.e., a continuous carbon structure with fully interconnected mesopore space. This allows the electrolyte to easily penetrate the mesopores and access the high surface area material while retaining a continuous structural backbone to maintain electrical contact. However, templating ordered structures directly using ionic liquid precursors has proven difficult, with only limited success at retaining the original pore morphology.[192] Therefore, additional techniques must be used to mesh the benefits of the nitrogen-doping abilities of the ionic liquid while maintaining the structural benefits of the well-interconnected 3DOm morphology.

Herein we report the use of a nitrogen-containing ionic liquid, 1-ethyl-3-methylimidazolium dicyanoamide (EMI-DCA, $C_8H_{11}N_5$), as a nitrogen and carbon source together with phenol-formaldehyde (PF) resols to improve the electrochemical performance of colloid-templated porous carbon electrodes for EDLCs in ionic liquid electrolyte systems. To my knowledge, this is the first mixed-precursor system to utilize ionic liquids for nitrogen doping with the second component providing structural stabilization to create an ordered, N-doped, porous carbon. By adjusting the ratio of the precursors, the amount of nitrogen incorporated in the carbon matrix forming the mesoporous structure can be controlled. The resulting N-doped carbon products show excellent electrochemical performance when low to moderate EMI-DCA precursor concentrations are used.

3.2 Experimental

3.2.1 Materials

Phenol (>99%), formaldehyde (aqueous solution, 37 wt%), tetrahydrofuran, polytetrafluoroethylene (PTFE, 60 wt% in water), tetraethylorthosilicate (TEOS, 99%), L-lysine (98%), hydrochloric acid (37 wt%), sodium hydroxide, and 1-ethyl-3-methylimidazolium dicyanoamide (EMI-DCA, >98%) were purchased from Sigma Aldrich, the ionic liquid 1-ethyl-3-methylimidazolium bis(trifluoromethylsulfonyl)imide (EMI-TFSI, >99 %, water content below 100 ppm) from IOLITEC, tetrahydrofuran (HPLC grade, >99.9%) and hydrofluoric acid (48–52 wt%) from Fisher Scientific. All chemicals were used without further purification. Water was deionized (DI) on-site to a final resistivity of >18.0 MΩ·cm, using a Barnstead Sybron purification system.

3.2.2 Preparation of Silica Spheres

Silica spheres were synthesized as previously described.[148] Briefly, a solution of L-lysine (70 mg) in water (70 g) was prepared in a 100 mL PFA round-bottom flask using a ¾ inch egg-shaped magnetic stir bar. While rapidly stirring, TEOS (5.4 g) was added dropwise and left to stir under ambient conditions for 1 h. This suspension was then heated in an oil bath at 90 °C while stirring at 500 rpm for 48 h under a condenser. TEOS (10.8 g) was added dropwise in five equal portions, each 1 h apart, and the suspension was left for an additional 48 h. This was repeated once more for a total of 28 g of TEOS over the synthesis. The suspension was dried in a Petri dish at 70 °C for at least 12 h, then calcined at 550 °C for 6 h in air to remove residual organic components and form the

colloidal crystal template. The final average silica sphere diameter was 17.4 ± 1.7 nm, determined by measuring over 300 separate spheres.

3.2.3 Preparation of Mesoporous Carbon

Mesoporous carbon samples were prepared by vacuum-infiltrating a precursor solution into the silica colloidal template (1:1 precursor:silica by weight) at 40 °C for 1 h, followed by aging the composite at 120 °C in a covered Petri dish. Samples were made with a series of ionic liquid (EMI-DCA) concentrations in the precursor solution, namely 100 wt%, 75 wt%, 50 wt%, 25 wt%, and 0 wt%, the balance being a solution of 50 wt% PF in THF (prepared as described in Chapter 2). After aging, the samples were pyrolyzed at 900 °C for 4 h (1 °C min^{-1} ramp rate to 600 °C, then 5 °C min^{-1} to 900 °C) under 0.5 L min^{-1} flowing nitrogen to carbonize them. The silica template was then removed through an HF etch by immersing the C/SiO$_2$ composite in 50 wt% HF in a sealed 125 mL HDPE bottle (~25:1 solution:composite by weight), and leaving the mixture for 24 h under ambient conditions, swirling it manually every hour for the first 6 h. (CAUTION: HF is highly toxic, corrosive, and a severe irritant − use with extreme care.) HF was then decanted and the carbon product was washed with DI water (100 mL), left to settle for 30 min, then decanted again. The washing procedure was repeated for a total of 8 times, the sixth wash being left for at least 16 h. The carbon product was then washed one more time in ethanol (100 mL) and dried at 70 °C for between 12 and 16 h. The final mesoporous carbon materials were designated "*X*_IL," where *X* refers to the content of EMI-DCA in the precursor solution, e.g., 0_IL contained 0% EMI-DCA and 100% PF solution, and 100_IL was made from 100% EMI-DCA and 0% PF solution.

3.2.4 Product Characterization

Scanning electron microscopy (SEM) was carried out on a JEOL-6700 microscope operating at 3.0 kV, with emission currents ranging from 18 to 20 μA. Because the carbon was sufficiently conductive, no metal coatings were used. Nitrogen sorption was performed using a Quantachrome Autosorb iQ instrument. Samples were outgassed for 12 h at 200 °C prior to analysis. Total surface area and pore characteristics were calculated using the quenched-solid-density-functional-theory (QSDFT) adsorption model optimized by Quantachrome for mesoporous carbon materials with spherical pores.[197-198] Small-angle X-ray scattering (SAXS) measurements were carried out on a Rigaku RU-200BVH 2D SAXS instrument operating with a pathlength of 183 cm using a 12 kW, rotating Cu anode and a Siemens Hi-Star multiwire area detector. Transmission electron microscopy (TEM) images were obtained on an FEI Technai T12 microscope operated at 120 kV with a LaB_6 filament. Samples were prepared by suspending them in ethanol and bath sonicating for 15 min. Cu grids coated in Formvar were dipped into the resulting suspension and dried. Elemental analysis was performed by Atlantic Microlabs (Norcross, GA) by combustion using automatic analyzers. Raman spectroscopy was performed with a Witec Alpha300R confocal Raman microscope using 514.5 nm incident radiation at 5–7 mW of power. Spectra were collected using a DV401 CCD thermoelectric-cooled detector and final spectra are the average of 100 scans, each with a 2 second integration over the spectral width centered at 1400 cm^{-1}. XPS was performed using a Surface Science SSX-100 spectrometer equipped with an Al anode operated at 10

kV potential and 20 mA current over a spot size of 0.64 mm^2. Peak positions were calibrated against the $C_{1s(sp3)}$ peak of (adventitious) carbon, set at 284.6 eV.

3.2.5 Cell Preparation and Electrochemical Tests

To prepare electrodes, the mesoporous carbon powder was mixed with binder (9:1:10 carbon:PTFE:water by weight) and extensively ground with a mortar and pestle to form a homogenous paste, as described previously.[149] The paste was rolled into a self-supporting thin film with a mechanical roller press and cut into 8 mm diameter circles, then dried overnight at 110 °C under vacuum to obtain final dried masses of 2.0–2.5 mg per electrode with thicknesses of approximately 150 μm, giving an electrode density of 27–33 mg cm^{-3}. To assemble an electrochemical cell, two electrodes of similar mass from the same film were wetted with the EMI-TFSI ionic liquid electrolyte and separated with a Celgard-3501 membrane, then packed into a reusable two-electrode cell body as previously described.[149, 199] All cell assembly was performed in a He-filled glove box.

Electrochemical tests were performed on an Arbin BT2000 electrochemical station. To measure the capacitance and test the cyclability, galvanostatic conditions were used. The cell was charged and discharged at different rates, then cycled at 1 A g^{-1} for 1000 cycles to measure the cell stability. The specific capacity of the electrode material was calculated using eq. 3.4, assuming that the masses and specific capacitances were identical for both of the electrodes in the symmetric cell.

$$C_{material} = \frac{4I \cdot \delta t}{m \cdot \delta V}$$

(3.4)

Here, *I* is the discharge current, δt is the discharge time, *m* is the total mass of carbon in the cell, and δV is the cell discharge voltage (3.5 V minus the voltage drop due to Ohmic resistance). Self-discharge tests were performed by first charging the cell to 3.5 V, then monitoring the potential change for 10 h, followed by a discharge and recharge back to 3.5 V and another rest step. After the fifth charge, the cell was left to rest for 48 h while the potential change was monitored. Electrochemical impedance spectroscopy was performed using a Solartron 1260 frequency analyzer from 100 mHz to 100 kHz at the open circuit potential and a 10 mV AC amplitude.

3.3 Results and Discussion

3.3.1 Product Structure

One of the primary benefits of 3DOm carbon is the bicontinuous structure of conducting walls and well-defined mesopores with open windows, allowing for efficient electrolyte infiltration and high capacitance. The pores are defined in part by the colloidal crystal template (CCT). In this study, the silica particles used to assemble the CCT are prepared by amino-acid assisted hydrolysis and have a regular spherical shape with an average diameter of 17.4 ± 1.7 nm (Figure 3.1a). Although larger colloids can be used to prepare CCTs with well-ordered fcc symmetry,[148-149] the 10% standard deviation of particle size here results in a sphere array with slightly reduced periodicity. Nonetheless, most colloidal particles are in direct contact with multiple neighboring spheres so that interconnecting windows form at these sites during the templating process. This sphere size was chosen for the current study of the effect of N-doping with ionic liquids because for undoped materials, a similar size yielded 3DOm carbon electrodes with the highest

specific capacities at both low and high current densities (for a range of materials made from 10 to 40 nm spheres).[149]
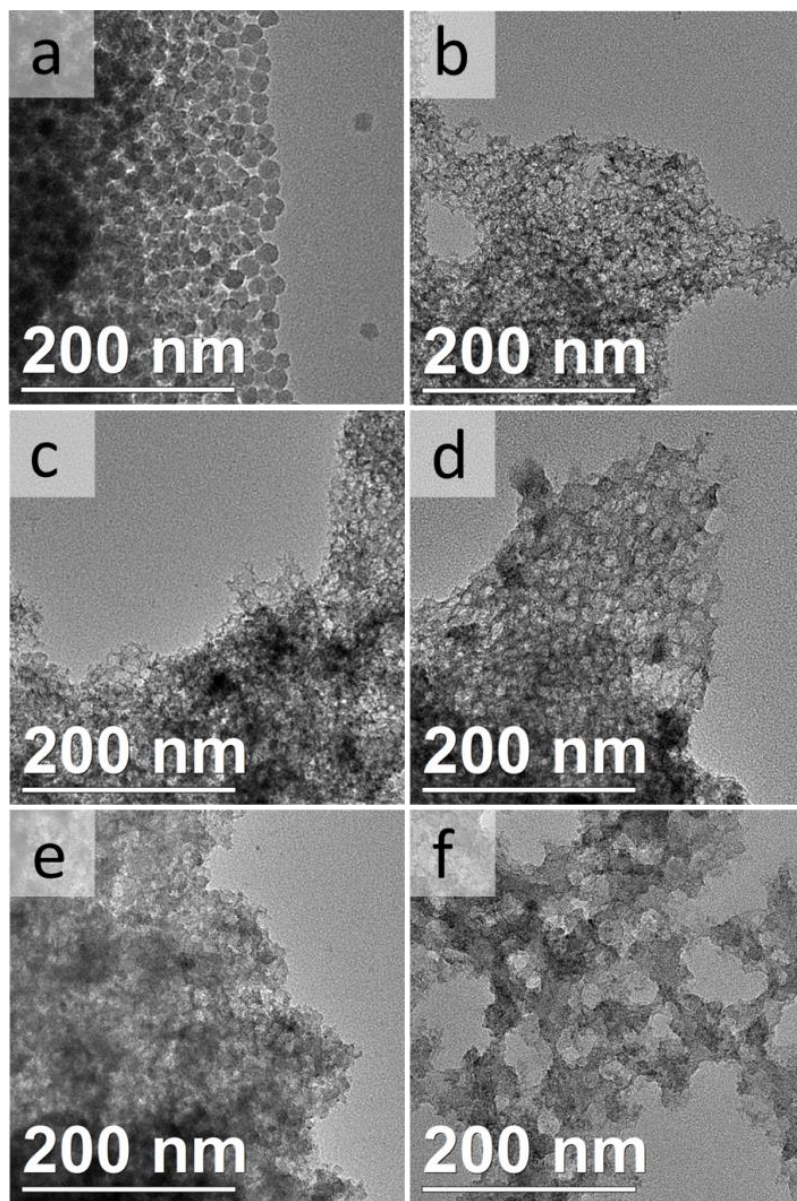
Figure 3.1. TEM images of (a) the colloidal silica template, (b) 0_IL, (c) 25_IL, (d), 50_IL, (e) 75_IL, and (f) 100_IL carbon materials.

TEM and SEM images provide information about wall and pore textures, including pore order, pore sizes and pore windows. Samples 0_IL, 25_IL, and 50_IL show well-defined mesopores of a similar size, approximately 20 nm in diameter (Figure 3.1b–d), close to the template sphere diameters. These pores can be seen throughout the structure and are well-connected, with open windows and a bicontinuous structure. When the ionic liquid precursor becomes the primary carbon source, the pore structure begins to deteriorate. 75_IL mostly retains mesopores of a diameter near 20 nm (originating from the silica template), though the pores are less well-defined (Figure 3.1e). Furthermore, the pores are interspersed with untemplated regions and large void spaces, showing additional structural collapse and lack of template replication. In 100_IL almost no spherical mesopores are visible and the structure is generally disordered (Figure 3.1f). These results demonstrate that the phenol-formaldehyde resol is important, providing a more rigid backbone for the inverse replication of the silica template, and it is necessary to maintain an open, bicontinuous structure for optimal electrochemical performance. SEM images reveal these pore textures over larger areas of the templated products.[200] In the case of the samples with low initial ionic liquid concentration (0_IL, 25_IL, and 50_IL), pores are clearly visible over the entirety of the sample. As the ionic liquid concentration in the precursor increases further, the templated mesopore structure begins to deteriorate, with less interconnectedness between pores, consistent with the TEM observations.

A major focus of this work is control over the incorporation of nitrogen into the mesoporous carbon framework. Elemental analysis data reveal that as the percentage of

ionic liquid in the precursor solution increases, the amount of nitrogen in the templated products also increases as expected (Table 3.1). The nitrogen content reaches a maximum of 12.0 wt% in 100_IL with a baseline of 0 wt% in 0_IL. The consistent increase in nitrogen content with increasing ionic liquid concentration in the precursor solution indicates that neither the ionic liquid nor the PF precursor is preferentially excluded during mixing, templating, and pyrolysis. Prior studies indicated that the largest capacitance and conductivity would occur between 5 and 8 wt% nitrogen,[174, 176-177, 179] and this synthesis technique therefore covers the desired range for EDLC applications. For other applications, the nitrogen content can be easily tuned between 0 and 12 wt% to achieve optimal performance based on the concentration of the ionic liquid used.

Table 3.1. Nitrogen content and nitrogen sorption data for carbon samples.

Sample name	Nitrogen content (wt%)	Total surface area ($m^2\,g^{-1}$)	Cum. surf. area for pores 10–25 nm in diameter ($m^2\,g^{-1}$)	Pore volume ($cm^3\,g^{-1}$)	d_{111} (nm)
0_IL	0.0	1393	204	4.50	14.6
25_IL	5.0	1380	241	3.58	13.4
50_IL	7.6	1070	196	1.49	12.8
75_IL	9.6	911	161	1.44	~12.5
100_IL	12.0	1040	36	1.03	~12.5

Pore characteristics were further studied using nitrogen sorption data and applying a QSDFT model designed for mesoporous carbon with spherical pores.[197-198] The sorption

isotherms and pore diameter distributions are shown in Figure 3.2, and relevant structural characteristics are given in Table 3.1. The primary feature of the pore size distribution for 0_IL is a peak centered at 17.5 nm, matching the diameter of the silica spheres used as a template. This peak is well preserved in 25_IL, which has a similar overall pore size distribution. As the concentration of the IL in the precursor solution continues to increase, this peak decreases in intensity and eventually disappears. It is still visible in 50_IL, but 75_IL and 100_IL do not have a clearly discernable feature at this point, though some hysteresis is still observed in the isotherms indicating the presence of mesopores. Further, the total pore distribution for 100_IL consists almost completely of small mesopores (<10 nm) and micropores, verifying that there is little structural retention from the silica sphere template. In this interpretation, it should be noted that the QSDFT model assumes a carbon surface, and the presence of nitrogen could affect the adsorption characteristics. However, the expected surface area from the mesopores would be approximately 165 m^2 g^{-1} in an idealized structure (assuming 17.5 nm spheres and a carbon density of 2.0 g cm^{-3}), which matches well with the cumulative surface area for pores between 10 and 25 nm of 196 m^2 g^{-1} for 50_IL, indicating that the model can still accurately model bulk pore characteristics for these carbon materials. With increasing ionic liquid content the total pore volume decreases. The sample prepared without any PF (100_IL) has less than 25% of the total pore volume of the sample prepared from only PF precursor, further showing the loss of templated microstructure. These observations confirm that the addition of phenol-formaldehyde resol in the initial precursor solution helps to maintain a templated structure with ionic liquid precursors for nitrogen-doped

carbon and that a minimum amount of PF is needed to achieve this stabilization. For the system and conditions used in this study, the minimum amount of PF in the precursor solution is approximately 25%.
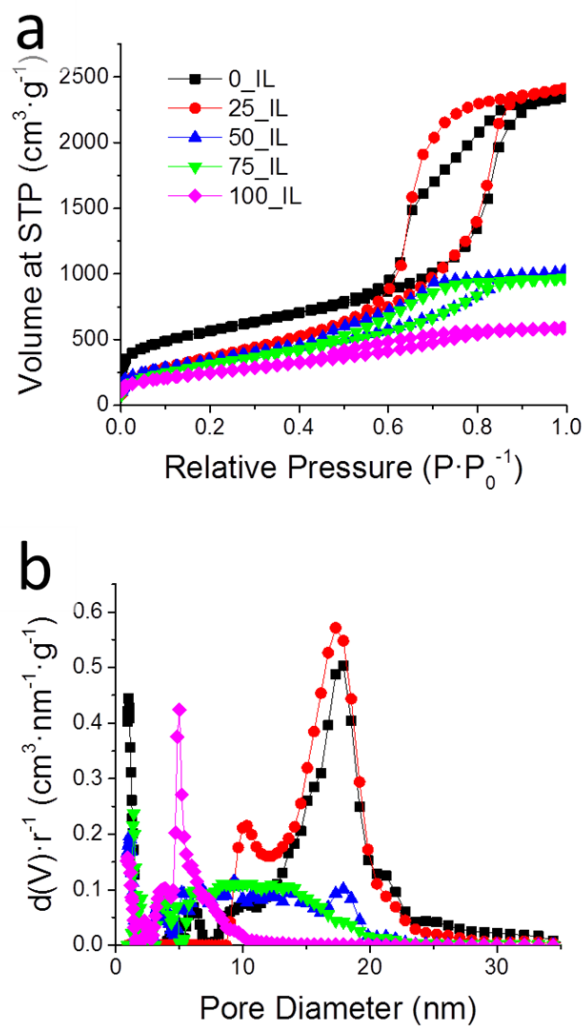
Figure 3.2. (a) Nitrogen sorption isotherms of the mesoporous carbon samples synthesized using various ionic liquid concentrations in the precursor solution and (b) the corresponding pore size distributions determined using the QSDFT adsorption model.

From SAXS data, the pore order and *d*-spacings of the mesoporous materials were determined (Figure 3.3). Overall, the samples with a low initial ionic liquid content show moderate levels of order, as indicated by two discernable scattering peaks and a shoulder corresponding to the [111] reflection, all of which match a face-centered cubic (fcc) lattice of spherical pores. Values for spacings of the d_{111} peaks are given in Table 3.1. These values decrease with increasing ionic liquid content in the precursor. In addition, as the ionic liquid concentration in the precursor increases, the peaks broaden and become less prominent, consistent with the observed decrease in order of the pore structure.
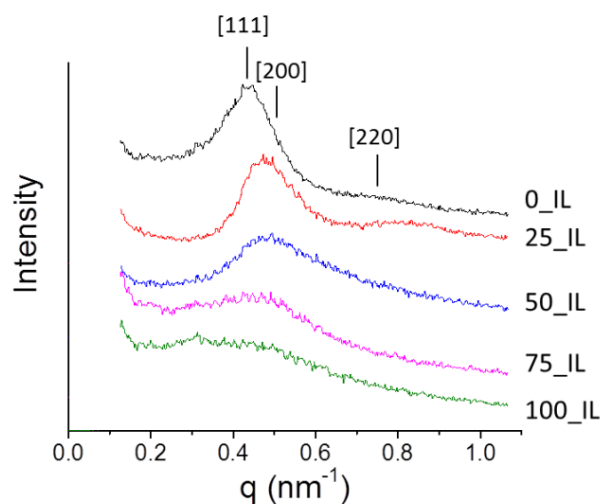
Figure 3.3. Small-angle X-Ray scattering patterns of the mesoporous carbon samples.

Raman spectroscopy was used to determine the relative graphitic nature of the carbon samples (Figure 3.4). The spectra show two primary peaks commonly observed in hard carbons with turbostratically disordered graphene sheets;[201] the G-band at 1597 cm^{-1} originating from the E_{2g} in-plane stretching motion of pairs of sp^2 carbon and the D-band

at 1350 cm^{-1} originating from the A$_{1g}$ breathing mode which is only polarizable in the presence of disorder.[202-203] The spectra were fit with two additional peaks, at 1190 and 1518 cm^{-1}, which are associated with the sp^3 carbon atoms found in glassy carbon to improve the accuracy of the fit.[204] From fitting these four peaks using Gaussian peak shapes, the graphitic domain size was determined using Equation 3.5:

$$\frac{I_D}{I_G} = \frac{C(\lambda)}{L_a}$$

(3.5)

where I_D is the peak intensity at 1350 cm^{-1}, I_G is the peak intensity at 1597 cm^{-1}, $C(\lambda = 514.5\ nm) = 4.4$ nm, and $L_a =$ is the graphitic domain size. The domain sizes, along with the peak intensities, are given in Table 3.2. With high ionic liquid content in the precursor, the grain sizes diminish slightly, and the extent of disorder at the atomic level increases within graphitic domains by replacement of carbon atoms with nitrogen dopant atoms. For all porous products in this study, the graphitic domain size is between 3 and 4 nm, typical for carbon materials derived from resols.[115, 149]
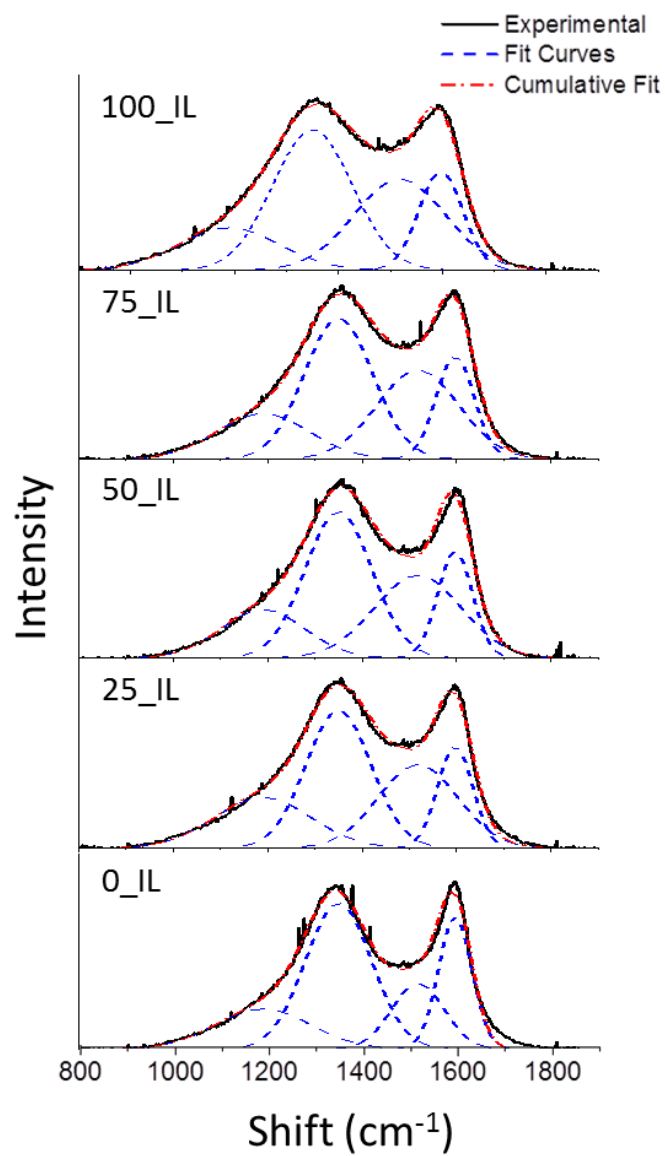
Figure 3.4. Raman spectra of the mesoporous carbon samples, showing the D and G bands typically observed for resol-derived, hard carbon materials with turbostratically disordered graphene sheets.

Table 3.2. Relevant parameters from the peak fitting of the Raman spectra.

Sample	I_{1190}	I_{1350}	I_{1518}	I_{1597}	L_a (nm)
0_IL	11.4	41.1	18.5	37.1	3.97
25_IL	15.5	42.2	25.6	31.3	3.27
50_IL	12.4	37.4	21.2	27.2	3.20
75_IL	14.0	43.2	27.3	31.7	3.22
100_IL	12.0	39.5	25.6	27.6	3.08

To examine the nitrogen functionalities contained within the carbon framework, XPS was performed on 50_IL as a representative sample (Figure 3.5). The N_{1s} peak can be deconvoluted into four distinct peaks, at 398.4, 400.3, 402.1, and 404.5 eV. The peaks can be assigned to pyridine-like nitrogen, graphitic nitrogen, oxidized nitrogen, and chemisorbed nitrogen, respectively.[205-208] The pyridine-like and graphitic nitrogen should contribute to the conductivity of carbon-based electrodes.
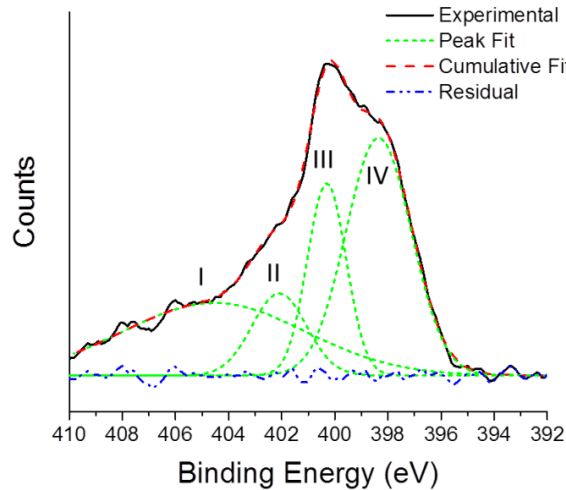
Figure 3.5. Deconvoluted XPS spectrum of the N_{1s} peak of 50_IL. Relative peak areas: I (31.2% of the cumulative area), II (11.2%), III (18.7%), and IV (38.9%).

3.3.2 Electrochemical Performance

After forming the carbon materials into an electrode and assembling an electrochemical cell as described above, the materials were cycled with a constant current over a range of current densities, from 0.1 to 10 A g^{-1}, based on the total mass of carbon in the cell. The cells were cycled between 0 and 3.5 V vs. the open circuit potential of the cell. During the initial few cycles, the charging half of the cycle is curved above 2.5 V (Figure 3.6a; 0.1 A g^{-1}), which is attributed to irreversible reactions between the electrolyte and reactive oxygen surface functional groups.[149] This feature becomes indiscernible by at least the fifth cycle, but usually by the third charging step. As the cell is cycled further, this feature diminishes and a symmetric, triangular-shaped profile emerges, typical of pure double-layer capacitance.
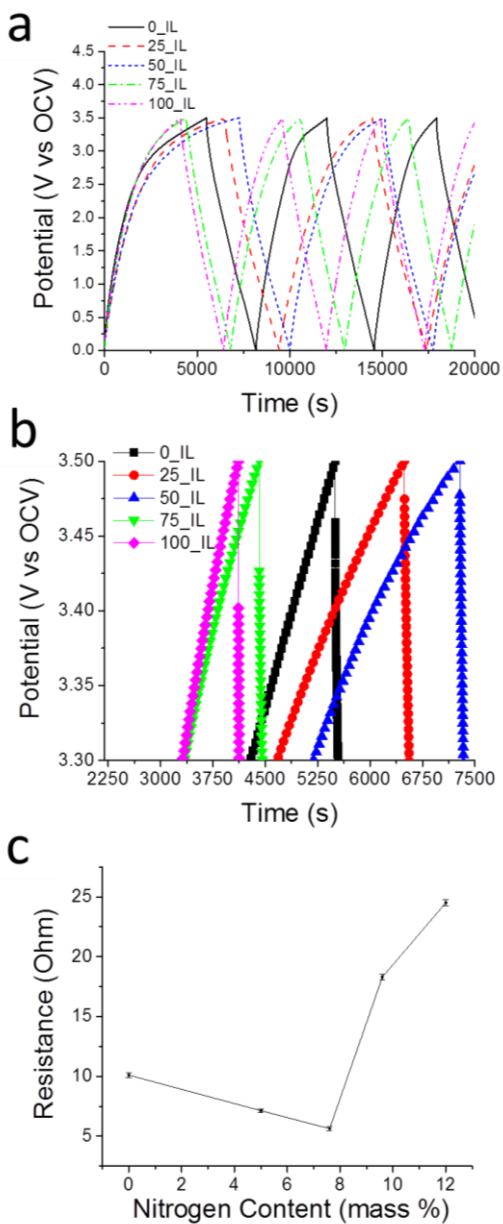
Figure 3.6. (a) The first few charge and discharge cycles of electrodes made from the templated carbon materials at 0.1 A g^{-1}. (b) Close-up of the initial discharge from the first cycle for each sample, showing the Ohmic drop of the samples (nearly vertical lines between adjacent data points after the peak). (c) Cell resistance calculated from the Ohmic drop of each cell correlated to the nitrogen content. The lines in (c) are intended to guide the eye.

A notable feature of each cycle is the Ohmic drop, or the instantaneous drop in potential when the cycle changes from charging to discharging and the current switches from positive to negative. The combined resistance of all of the components of the cell leads to an additional measured potential, separate from that due to electrochemical charging, following Ohm's Law. Because the components of the cell are all the same (cell body, separator membrane, and electrolyte) except the electrodes themselves, the Ohmic drop is proportional to the relative resistances of the electrode films. Figure 3.6b shows the Ohmic drop from the initial discharge; this Ohmic drop is consistent over all cycles. As the nitrogen content in the carbon material increases up to 7.6 wt%, the Ohmic drop decreases, with the smallest electrode resistance occurring for IL_50. This is due to the effect of nitrogen acting as an *n*-type dopant within the carbon structure, leading to improved electrical conductivity, specifically by introducing the pyridine-like and graphitic nitrogen seen in the XPS spectra. At higher nitrogen content, the resistance increases significantly (Figure 3.6c), which could be due to the loss of the bicontinuous structure and the smaller graphitic domains. As the structure becomes less continuous, additional internal resistance occurs from the increased interfacial contacts, leading to the larger Ohmic drop. To further test the effect of nitrogen moieties within the electrode materials, self-discharge tests of 0_IL and 50_IL were performed (Figure 3.7). 50_IL shows a smaller initial drop due to the previously mentioned Ohmic drop. Both samples show a small level of self-discharge, leveling off quickly to less than 1.0 mV/h in the last 40 h of rest, comparable to other templated carbon supercapacitors.[209] There are no significant differences between the rate of potential drop of the two samples showing the

additional nitrogen functional groups are not significantly redox active, and thereby not increasing the rate of self-discharge.[210]
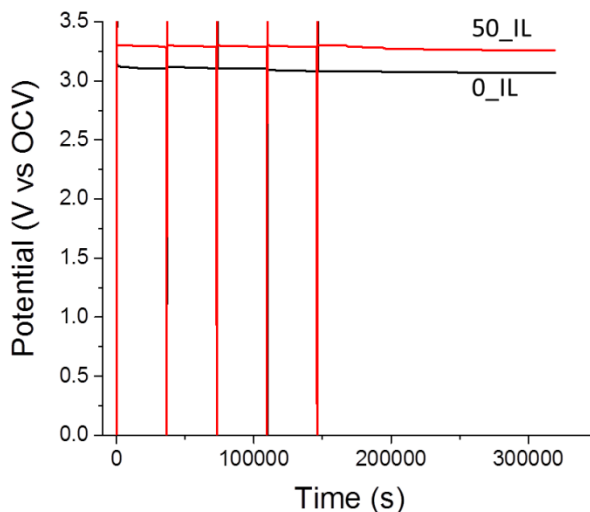
Figure 3.7. Self-discharge tests for 0_IL and 50_IL, showing similar rates of potential drop for both samples.

Electrochemical impedance spectroscopy was used to further study the electrical and ionic resistances within the cell. The Nyquist plots (Figure 3.8) all show an intersection with the real axis below 12 Ω in the high frequency region, which is typically the combined resistance of all of the cell components, including the ionic liquid electrolyte, which is a significant contributor to the overall resistance. These resistance values show a similar trend to the resistances measured from the Ohmic drop where increasing nitrogen content up to 7.6 wt% decreases the resistance, then increases it again at higher nitrogen content. In the moderate frequency region, a depressed semi-circular shape composed of two overlapping semi-circles is present, indicating at least two different charge or mass transfer resistances within the cell. The total charge-transfer resistance follows the same

70

trend as the series resistance, signifying more facile charge transport throughout the material and on the surface. Furthermore, the high charge-transfer resistance in 75_IL and 100_IL likely results from the degradation of the organized mesopore structure, causing a more tortuous path for the electrolyte ions. Finally, the low frequency region shows a nearly vertical slope, indicative of capacitive behavior.
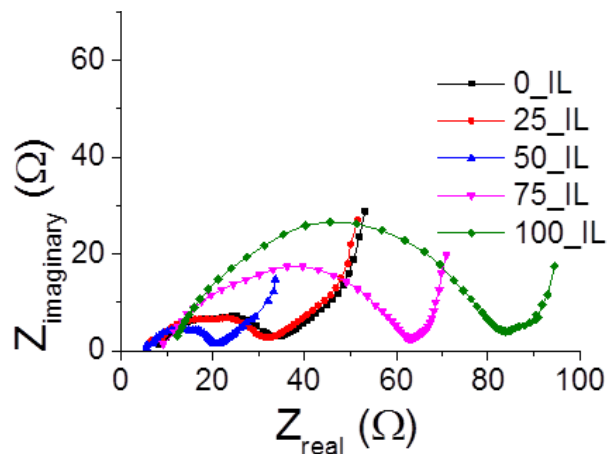
Figure 3.8. Nyquist plots of the mesoporous carbon samples, showing the decreasing resistance with increasing nitrogen content up to 50_IL, followed by increasing resistance to 100_IL.

To measure the specific capacitance of the porous carbon materials, galvanostatic cycling was performed from 0.1 to 10 A g^{-1}. At low rates, all of the materials yield high capacitance values of over 175 F g^{-1} (Figure 3.9a). A maximum capacitance of 237 F g^{-1} is reached with 50_IL at 0.1 A g^{-1}, an 18% improvement over the undoped 0_IL sample. At higher current densities, the lower porosity samples, 75_IL and 100_IL, begin to lose capacitance as a result of the less well-connected pore structure. However, the electrode materials that preserve the interconnected mesopore structure maintain high capacitance. At 10 A g^{-1}, the improvement due to N-doping becomes even more pronounced: the

71

capacitance is increased by 22% from 106 F g^{-1} for 0_IL to 130 F g^{-1} for 25_IL and by 42% to 151 F g^{-1} for 50_IL.
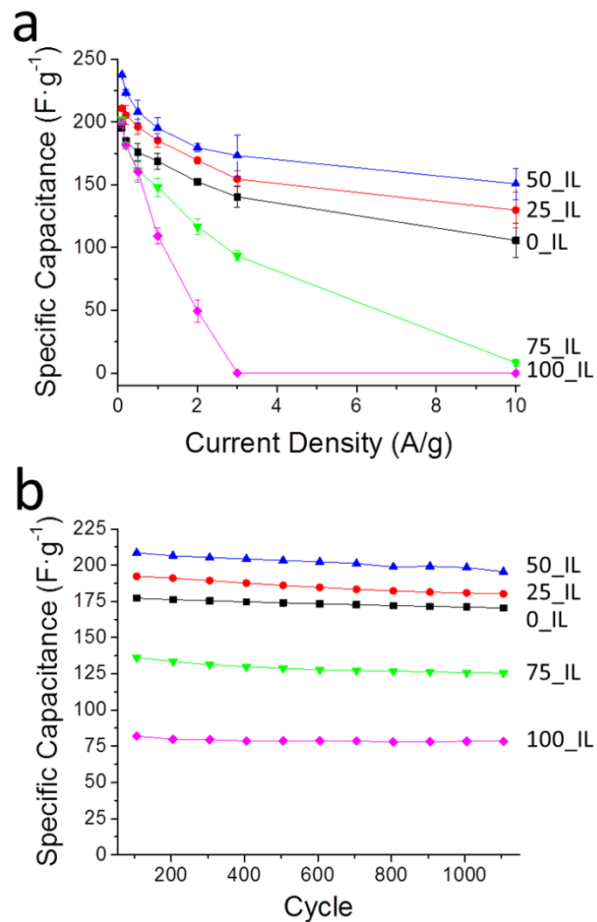
Figure 3.9. (a) Average specific capacitance of the carbon materials over a range of rates. (b) The specific capacitance of the carbon materials over ca. 1100 cycles at 1 A g^{-1}.

Beyond the increased rate performance, the increased specific capacitance is maintained over more than 1100 cycles at 1 A g^{-1}, the 50_IL material having an average specific capacitance of 202 F g^{-1}, which represents a 16.5% increase over the average specific capacitance of 0_IL (Figure 3.9b). The specific energy of a cell made from two

identical 50_IL electrodes is over 83 Wh kg^{-1} (unpackaged) for all 1100 cycles at 1 A g^{-1}, which would correspond to a specific energy of 25 Wh kg^{-1} in a commercial-style, packaged device, which typically contains 30 wt% active material. This is a 30% improvement over previous 3DOm carbon samples tested in a similar manner with ionic liquid electrolytes,[149] and comparable to the performance of related systems in aqueous electrolytes (Table 3.3). The similar specific capacitance to other N-doped carbon is even more remarkable due to the use of an ionic liquid electrolyte here, which typically yields lower capacitance values compared to aqueous electrolytes. The advantage of the ionic liquid electrolyte is that it offers a significantly increased potential window for cycling, leading to a large increase in the specific energy of an assembled cell, as shown in Table 3.3.

Table 3.3. Capacitance values for various N-doped carbon electrodes reported in the literature.

Material	Electrolyte	Specific Capacitance ($F\ g^{-1}$)	Current Density ($A\ g^{-1}$)	Specific Energy ($Wh\ kg^{-1}$) [a]	Reference
50_IL	EMI-TFSI	195	1.0	83	This work
50_IL	EMI-TFSI	237	0.1	101	This work
SBA-15 templated mesoporous carbon	6 M KOH	210	1.0	7.2	190
Carbon nanofibers	6 M KOH	202	1.0	7.0	189
Nanocrystalline graphene	6 M KOH	282	0.1	9.8	211
Nanocrystalline graphene	1 M $(C_2H_5)_4N\ BF_4$	224	0.1	31	211
Activated carbon ($870\ m^2\ g^{-1}$)	EMI-TFSI	51	Not reported	22	212
Activated carbon ($2600\ m^2\ g^{-1}$)	EMI-TFSI	180	Not reported	77	212
Carbide-derived carbon	EMI-TFSI	160	0.33	68	30

[a] Unpackaged, per kg of carbon.

3.4 Conclusions

Nitrogen-doped, mesoporous carbon samples were synthesized by templating from a silica colloidal crystal using PF resol and EMI-DCA as precursors. The amount of nitrogen incorporated into the structure could be controlled in the range from 0 to 12 wt% by varying the ratio of ionic liquid to PF in the precursor solution while maintaining a highly interconnected mesopore structure in the resulting electrode material up to an ionic liquid content in the precursor of 50% by mass. Although the cost of the ionic liquid component may currently limit scale-up of the method, the incorporation of the ionic liquid remains attractive for tuning the heteroatom content within the electrode material and hence its electrochemical properties. The deterioration of the template-defined mesopore structure with higher ionic liquid concentrations in the precursor points at the importance of the resol components in providing a robust structural backbone for the electrode, especially when non-aromatic ionic liquids are used as precursors.[213] The increase in nitrogen content in the well-templated electrodes led to a reduction in the Ohmic drop and an improved capacitance in ionic liquid electrolyte based systems. The specific capacitance increased from 195 F g^{-1} at 0.1 A g^{-1} and 170 F g^{-1} after 1100 cycles at 1 A g^{-1} in a sample prepared with a pure PF resol precursor to 237 F g^{-1} at 0.1 A g^{-1} and over 190 F g^{-1} after 1100 cycles at 1 A g^{-1} in a sample prepared with 50% EMI-DCA in the precursor. These capacitance values are comparable to those of other nitrogen-doped carbon systems cycled in an aqueous electrolyte, but were obtained with a high-potential ionic liquid electrolyte that provides a large electrochemical window. This shows that a PF resol can be used in an ionic-liquid-based synthesis to help maintain a templated

structure, and the inclusion of a moderate amount of the ionic liquid precursor improves the conductivity and specific capacitance of the mesoporous carbon material, enabling high specific energies.

Chapter 4: Ionic Liquids as Electrolytes for Electrochemical Double-Layer Capacitors

Contributions to this chapter were performed by Dr. Maral Mousavi (potential limit measurements), Sadra Kashefolgheta (DFT calculations), Eric Anderson (conductivity measurements), and Siyao He (TEM imaging).

4.1 Introduction

Electrochemical double-layer capacitors (EDLCs), or supercapacitors, are rechargeable energy storage devices with many applications in the transportation, consumer electronics, and communication sectors.[6, 214-216] EDLCs are comprised of two high surface area electrodes separated by an electrolyte solution. Charge separation is achieved upon charging of the device, and the energy is stored by the double layer at the interface between the electrode and the electrolyte. Because the energy is stored by a reversible physical phenomenon at an interface rather than a chemical reaction within a bulk material, EDLCs have rapid charging and discharging rates, high specific power, and long lifespans of thousands to millions of cycles.[6] Due to these characteristics, there

has been growing interest in EDLCs, and much research has been devoted to improving the performance and specific energy of these devices.[6, 217-220]

4.1.1 Specific Energy of EDLCs

The specific energy of an EDLC is proportional to the capacitance of the cell multiplied by the square of the operating potential; therefore, maximizing both the cell capacitance and the potential window of the device is crucial for engineering high-energy-density EDLCs.[220] The cell capacitance has been significantly improved by maximizing the accessible surface area of the electrodes through application of highly porous materials, primarily porous carbon, as the electrode materials. For example, a double-layer specific capacitance as high as 282 F/g has been achieved in nanocrystalline graphite.[217, 221-223] Such a value is exceeded only when pseudocapacitive mechanisms are also active. The maximum accessible potential window of such devices is usually limited by electro-decomposition of the electrolyte or solvent, and these devices should not be charged beyond a voltage that can cause degradation of these components. Since electrolytes bear localized charges, they often have lower electrochemical stability than neutral solvent molecules. Therefore, the choice of electrolyte determines the potential window of EDLCs.[224]

4.1.2 Ionic Liquids as Electrolytes

Four primary classes of electrolyte solutions have been used in EDLCs: aqueous,[225] organic,[64] polymeric,[226] and ionic liquid (IL) electrolytes.[171] Among these, ILs have the largest potential windows, exceeding 5 V,[169] compared to aqueous and polymer electrolyte solutions, which typically are limited to 1 V, and organic electrolyte solutions

(typically based on acetonitrile or cyclic carbonates such as propylene carbonate) that are limited to 3.5 V due to decomposition of the solvent.[64, 225] Additionally, ILs typically have a high decomposition temperature, allowing for a wider range of applications where high temperatures (exceeding 100 °C) are expected.[227-228] Despite these advantages, there has not been a comprehensive and systematic study of the effect of IL structure on the performance of IL-based EDLCs, and the few reports found in the literature investigated only a small selection of ILs or studied ILs diluted in solvents, which affect the electrochemical properties of the ILs.[229-232]

The structure of an IL affects the double layer capacitance, C, and also the accessible potential window, V, of an EDLC, both of which determine the specific energy of the device (proportional to CV^2).[220] A change in the structure of an IL that can increase the EDLC double-layer capacitance does not necessarily improve the electrochemical stability of the IL, and, therefore, it is critical to investigate the combined effects of double layer capacitance and electrochemical stability on the specific energy of a device. Unfortunately, most studies focused on either the double layer capacitance or the electrochemical stability.[171, 219, 226, 230] For example, Sato et al. showed that at room temperature, an EDLC with *N,N*-diethyl-*N*-methyl-*N*-(2-methoxyethyl)ammonium tetrafluoroborate as the electrolyte has a wider potential window but lower discharge capacity than an EDLC with 1-ethyl-3-methylimidazolium tetrafluoroborate as the electrolyte.[219] Incrementing the chain length of alkyl substitutes was reported to enhance the electrochemical stability of *N*-alkyl-*N*-methylimidazolium bis(trifluoromethylsulfonyl)imide ionic liquids[233] and to enlarge the potential window of

N-alkyl-*N*-methylpyrrolidinium bis(trifluoromethylsulfonyl)imide.[234] However, the same structural change (increasing the alkyl chain length) was reported to shrink the potential window of *N*-alkyl-*N*-methylpyrrolidinium bis(trifluoromethylsulfonyl)imide.[231] Sedev et al. showed that the double layer capacitance (at 100 °C) of 1-alkyl-3-ethylimidazolium chloride at glassy carbon electrodes decreases when the alkyl chain length is increased.[235] Similarly, 1-ethyl-3-methylimidazolium tetrafluoroborate was shown to yield a larger double layer capacitance than 1-butyl-3-methylimidazolium tetrafluoroborate at room temperature[221] and tetraalkylammonium tetrafluoroborate (alkyl: ethyl, propyl, butyl, and hexyl) was shown to give a size-dependent double layer capacitance.[236] In contrast to all these studies that suggest an effect of the cation structure, Yuyama and co-workers showed that the double layer capacitance of a quaternary ammonium salt with a methoxyalkyl group on the nitrogen atom depends more on the nature of the anion than on the cation structure.[229] Clearly, comparisons made between only a few ionic liquids do not allow for the determination of meaningful trends.

Moreover, the double layer capacitance of a given IL is strongly affected by the choice of electrode material.[237-240] In addition, the criterion used for quantification of electrochemical stability strongly influences the reported IL potential window.[224, 228, 241] Because of the diverse range of electrode materials and potential window quantification criteria, a direct comparison between many reports in the literature is not feasible. For meaningful comparisons, it is necessary to study the effect of the IL structure on the specific energy of EDLCs made of the same electrode materials and characterized with the same potential window quantification method. In this work, the electrochemical

stabilities of several room-temperature ionic liquids with common types of core structures of the cation and anion and various alkyl substituents in the cation were investigated. Using three-dimensionally ordered mesoporous (3DOm) carbon electrodes as a model system because of the uniformity and high degree of interconnectedness of their mesopores,[242] we studied the effect of the IL structure on the double layer capacitance of EDCLs, allowing us to determine IL characteristics that yield EDLCs with optimum energy densities.

4.2 Experimental

4.2.1 Materials

The ionic liquids butyltrimethylammonium (Me$_3$BuN) bistrifluorosulfonylimide (TFSI), tributylmethylammonium (Bu$_3$MeN) TFSI, 1-ethyl-3-methylimidazolium (EtMeIm or EMI) TFSI, 3-methyl-1-propylimidazolium (PrMeIm) TFSI, 1-hexyl-3-methylimidazolium (HexMeIm) TFSI, 3-methyl-1-octylimidazolium (OcMeIm) TFSI, 1-ethyl-2,3-dimethylimidazolium (EtMe$_2$Im) TFSI, *N*-methyl-*N*-propylpiperidinium (PrMePi) TFSI, *N*-butyl-*N*-methylpyrrolidinium (BuMePyl) TFSI, *N*-butylpyridinium (BuPyd) TFSI, EMI triflate, and EMI BF$_4$ all with a purity of 99% and a water content below 100 ppm were purchased from IoLiTec, phenol (>99%), formaldehyde (aqueous solution, 37 wt%), tetrahydrofuran, polytetrafluoroethylene (PTFE, 60 wt% in water), tetraethylorthosilicate (TEOS, 99%), L-lysine (98%), hydrochloric acid (37 wt%), potassium hydroxide, and sodium hydroxide were purchased from Sigma Aldrich, tetrahydrofuran (HPLC grade, >99.9%) and hydrofluoric acid (48–52 wt%) from Fisher Scientific. All chemicals were used without further purification. Water was deionized

(DI) on site to a final resistivity of >18.0 MΩ·cm, using a Barnstead Sybron purification system.

4.2.2 Preparation of Three-Dimensionally Ordered Mesoporous (3DOm) Carbon

The phenol-formaldehyde (PF) resol was prepared in the same manner as described in Chapter 2 and the silica sphere template in the same manner as described in Chapter 3. 3DOm carbon was prepared following a literature procedure.[149] Briefly, the PF resol solution was vacuum infiltrated into the silica template (1:1 w:w) for 1 h at 40 °C, followed by cross-linking the resol at 120 °C for 24 h in a covered glass dish. The PF/silica composite was pyrolyzed under flowing nitrogen at 900 °C (1 °C/min ramp rate to 600 °C, then 5 °C/min to 900 °C). The silica template was removed through hydrothermal treatment in 6 M KOH for 48 h at 180 °C. The carbon product was isolated through vacuum filtration and washed repeatedly, then allowed to soak in DI water for 30 minutes, followed by additional washing until the pH of the effluent was ~7.

4.2.3 Material Characterization

Transmission electron microscopy (TEM) images were obtained on an FEI Technai T12 microscope operated at 120 kV with a LaB_6 filament. Samples were prepared by suspending them in ethanol and bath sonicating for 15 min. Cu grids coated in Formvar were dipped into the resulting suspension and dried. Viscosity was measured on a TA Instruments AR G2 rheometer using parallel steel plates separated by 300 μm. The shear rate was increased logarithmically from 1 to 100 rad/s, then decreased at the same rate with 5 s equilibration and 5 s integration per point. The viscosity was determined by averaging data points during the decrease in shear rate.

82

Nitrogen sorption was performed using a Quantachrome Autosorb iQ instrument. 3DOm carbon samples were outgassed for 12 h at 200 °C prior to analysis. The total surface area and other pore characteristics were calculated using the quenched-solid-density-functional-theory (QSDFT) adsorption model optimized by Quantachrome for mesoporous carbon materials with spherical pores. The 3DOm carbon material gives a type IV isotherm with a type H1 hysteresis (Figure 4.7A), typical for 3DOm and other mesoporous structures, indicating a well-formed bulk pore structure. A total surface area of 1074 m^2/g was measured. The pore size distribution plot showed two primary peaks (Figure 4.7A, inset), one at 37 nm and one at 29 nm. These values correspond to the observed sizes of the pores and the windows seen in the TEM images.

Small-angle X-ray scattering (SAXS) was used to determine the extent of pore ordering. The measurements were carried out on a Rigaku RU-200BVH 2D SAXS instrument operating with a pathlength of 183 cm using a 12 kW, rotating Cu anode and a Siemens Hi-Star multiwire area detector. In the SAXS pattern (Figure 4.4B), two clear peaks can be observed, at q = 0.21 and 0.36 nm^{-1}, along with a shoulder at q = 0.25, which index well to the expected face-centered cubic array of pores. Further, the d_{111} value is 30.5 nm, which would match an ideal pore array with diameters of 37.4 nm, consistent with the observed peak in the gas sorption pore size distribution

Conductivity was measured using a custom-made conductivity cell, consisting of two temperature-controlled stainless steel plates and a Teflon spacer to hold the sample. The cell temperature was allowed to equilibrate at 25 °C for 15 min prior to measurements. Impedance measurements were carried out using a two-electrode cell with a Solartron

1255B frequency response analyzer and a SI 1287 electrochemical interface from Solartron (Farnborough, Hampshire, U.K.). The frequency range for these measurements was from 1 MHz to 1 Hz with a constant AC amplitude of 100 mV. Conductivities were calculated from resistances obtained by fitting of impedance spectra with ZView software (Scribner Associates, Southern Pines, NC) in the 500 to 1 kHz range. The cell constant was measured using a 500 µS/cm^2 KCl conductivity standard. Each measurement was repeated five times.

4.2.4 Electrochemical Measurements

Potential Limit Determination. Linear sweep voltammograms were measured with a CHI600C Potentiostat (CH Instruments, Austin, TX), a three-electrode cell with a 3.0 mm-diameter glassy carbon (GC) disk working electrode (BAS, West Lafayette, IN), a 0.25 mm Pt wire coil (99.998%, Alfa Aesar, Ward Hill, MA) auxiliary electrode, and a Ag$^+$/Ag reference electrode, at a scan rate of 100 mV/s. The reference electrode was prepared as reported previously.[243] Briefly, a glass tube equipped with a Vycor glass plug was filled with an acetonitrile solution containing 10.0 mM AgNO$_3$ and 100 mM NBu$_4$ClO$_4$, and an Ag wire was inserted into the tube. All the potentials reported in this work are with respect to 10 mM Ag$^+$/Ag. For the observation of the cathodic and anodic decomposition currents, the potential was scanned from 0 to -5 V and from 0 to +4 V (vs. Ag$^+$/Ag), respectively. The working electrode was polished on Microcloth polishing pads using 5.0 µm Micropolish II deagglomerated alumina (both from Buehler; Lake Bluff, IL) and rinsed thoroughly, first with deionized water and then with ethanol, followed by drying under a stream of argon. Prior to measurements, all ionic liquids were purged with

84

argon for 15 min while stirring vigorously to remove dissolved oxygen. All measurements were performed in pure ionic liquids, and solvents were not used for diluting the ILs. Statistical analyses were based on a two-tailed *t*-test at the significance level of 0.95.

Calculation of Ion Volumes. The structures of the ions were optimized with the B3LYP[244-248] density functional at the 6-311++G(d,p) level. Frequency calculations were performed at the same level of theory to ensure that all ions were in a minimum energy conformation. All calculations were made using the Gaussian 03 package.[247] Ion volumes were calculated as superpositions of van der Waals spheres of atoms with Multiwfn software using the Monte Carlo method.[249]

Cell Preparation and Galvanostatic Tests. Electrodes were prepared by grinding the 3DOm carbon powder with a binder (19:1:10 carbon:PTFE:water) until a homogenous paste was formed, as previously described.[242] The paste was rolled into self-supporting films using a mechanical roller, cut into 8 mm diameter circles, and dried overnight at 110 °C under vacuum to obtain final dried masses of 1.8–2.0 mg per electrode and thicknesses of approximately 150 μm. Electrochemical cells were assembled by the following method. Two electrodes of similar mass were wetted with the desired ionic liquid electrolyte and held under vacuum for 1 h, followed by the removal of excess electrolyte. The wetted electrodes were layered between steel current collectors in a two-electrode configuration, separated by a porous polypropylene membrane within a cell body that was previously described.[242] All cell assembly was performed in a dry room maintained below 100 ppm H_2O to minimize contamination.

Galvanostatic tests were performed on an Arbin BT2000 electrochemical station. To measure the capacitance, various rates were used, followed by 1000 cycles to determine cell stability. All cells were cycled between 0 and 2.0 V vs. the open circuit potential to maintain a constant potential window for all electrolytes well within the decomposition limits for any of the selected ionic liquids. The specific capacitance of the 3DOm carbon was calculated using eq. 1, assuming that the contribution from each electrode is identical in the symmetric cell,

$$C_{material} = \frac{4I \cdot \delta t}{m \cdot \delta V}$$

(1)

where I is the discharge current, δt is the discharge time, m is the total mass of carbon in the cell, and δV is the cell discharge voltage.

4.3 Electrochemical Stability of ILs

The structures of the cations and anions of the ILs investigated in this work are shown in Figure 4.1. This selection covers the main categories of cations (pyridinium, imidazolium, pyrrolidinium, piperidinium, and ammonium) and anions (bistrifluoromethanesulfonylimide, tetrafluoroborate, and trifluoromethanesulfonate) that are used in room-temperature ionic liquids. The alkyl substituents of these cations can be readily modified to alter the electrochemical properties of the ions.[228, 234, 250] Therefore, in addition to the core cation structures, we also studied ILs with different alkyl substituents. Only saturated hydrocarbon groups were considered as alkyl substituents in this work because non-saturated or oxygenated alkyl groups were shown in prior work to lower the electrochemical stability of the cations without improving their contribution to

the double-layer capacitance.[232, 251-255] In this section, we will first discuss the electrochemical behavior and stability of these ILs and then follow with an analysis of the double-layer capacitance and specific energy of EDLCs incorporating these ILs.
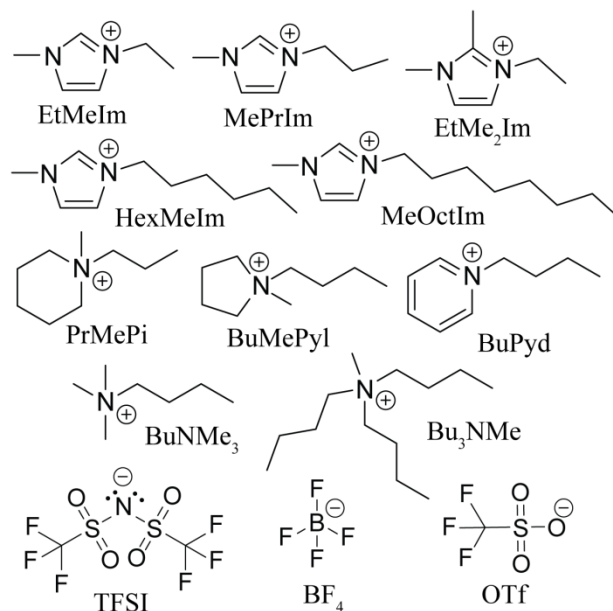
Figure 4.1. Structures and abbreviations of the cations and anions investigated in this study.

The electrochemical stability window of the ionic liquids was determined by a linear fit method described by the Bühlmann group.[224, 241, 256] This method has been shown to be more rigorous and is not affected as strongly as current cutoff methods by variables such as conductivity, concentration, and scan rate. However, because much of the previous literature uses a current cut-off method, those values are also given for comparison in the literature.[257] The potential limits are given in Table 4.1 with a visual representation of the linear fit method in Figure 4.2. A full discussion of the comparisons between the potential limits of the ionic liquids can be found in the paper from which this chapter is derived.[257] From the results, it was determined that saturated cations with quaternary ammonium

substituents generally provide the highest cathodic stabilities while aromatic cations are less stable towards reduction. Further, the type of cation has an effect on the anodic limit, consistent with previous literature, where the cation is responsible for both the oxidation and reduction limit.[254] Within the same class of cations, such as the imidazolium ionic liquids, an increase in the anodic stability is observed. Within the quaternary ammonium-based ionic liquids, Bu_3NMe TFSI has a significantly larger potential window, due to an increase in both the cathodic and anodic limit, while the other ion pairs have similar overall potential windows. In summary, the following trends were observed for potential windows of the ILs studied in this work: Bu_3NMe TFSI > BuMePyl TFSI ~ PrMePi TFSI > $BuNMe_3$ TFSI > EtMeIm TFSI ~ MePrIm TFSI ~ HexMeIm TFSI ~ MeOctIm TFSI ~ $EtMe_2Im$ TFSI > EtMeIm BF_4 > EtMeIm OTf > BuPyd TFSI.

Table 4.1. Electrochemical stability of room temperature ILs (V vs. Ag^+/Ag).

	cathodic stability			anodic stability		
	0.5 mA/cm^2	1.0 mA/cm^2	linear fit	0.5 mA/cm^2	1.0 mA/cm^2	linear fit
EtMeIm BF$_4$	-2.12 ± 0.19	-2.41 ± 0.04	-2.60 ± 0.01	1.12 ± 0.16	1.79 ± 0.13	1.99 ± 0.01
EtMeIm OTf	-2.27 ± 0.01	-2.49 ± 0.01	-2.60 ± 0.01	1.07 ± 0.28	1.52 ± 0.17	1.94 ± 0.01
EtMeIm TFSI	-2.38 ± 0.05	-2.47 ± 0.02	-2.56 ± 0.02	1.76 ± 0.04	1.97 ± 0.03	2.15 ± 0.00
MePrIm TFSI	-2.40 ± 0.07	-2.48 ± 0.01	-2.53 ± 0.01	2.05 ± 0.03	2.15 ± 0.01	2.19 ± 0.01
HexMeIm TFSI	-2.51 ± 0.01	-2.58 ± 0.01	-2.56 ± 0.01	2.10 ± 0.03	2.23 ± 0.01	2.17 ± 0.01
MeOctIm TFSI	-2.54 ± 0.01	-2.63 ± 0.01	-2.55 ± 0.00	2.12 ± 0.02	2.29 ± 0.01	2.14 ± 0.00
EtMe$_2$Im TFSI	-2.69 ± 0.01	-2.75 ± 0.01	-2.74 ± 0.01	1.96 ± 0.01	2.03 ± 0.01	1.99 ± 0.00
Bu$_3$NMe TFSI	-3.64 ± 0.05	-3.94 ± 0.05	-3.49 ± 0.05	2.75 ± 0.06	4.07 ± 0.61	2.58 ± 0.03
BuNMe$_3$ TFSI	-3.03 ± 0.03	-3.31 ± 0.01	-3.37 ± 0.02	2.27 ± 0.13	2.57 ± 0.02	1.98 ± 0.09
BuMePyl TFSI	-3.18 ± 0.03	-3.31 ± 0.01	-3.36 ± 0.02	2.23 ± 0.08	2.50 ± 0.03	2.36 ± 0.03
PrMePi TFSI	-3.26 ± 0.02	-3.40 ± 0.01	-3.34 ± 0.01	2.36 ± 0.11	2.62 ± 0.01	2.34 ± 0.03
BuPyd TFSI	-1.38 ± 0.10	-1.47 ± 0.01	-1.44 ± 0.04	2.24 ± 0.13	2.57 ± 0.02	2.43 ± 0.02

Glassy carbon as working electrode, scan rate 100 mV/s.
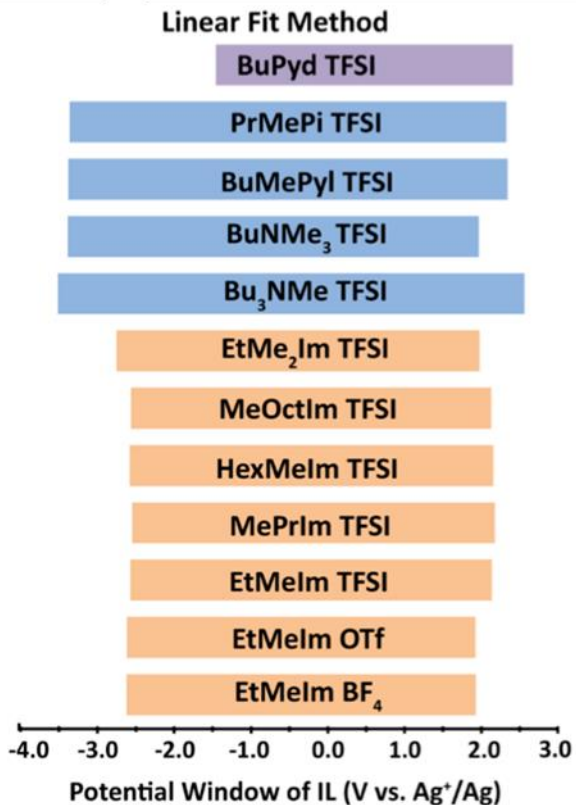
Figure 4.2. The solid bars represent the potential window in which the ILs are stable. The lower and higher ends of each bar indicate the cathodic and anodic limits of the IL, respectively. Both limits were measured with the linear fit method. Error bars are not shown because their values are too small to be readily visually recognizable.

4.4 Electrochemical Capacitance

4.4.1 3DOm Carbon Electrodes

For practical EDLCs, a critical parameter is the capacitance achieved with an IL electrolyte. To test the capacitance achieved with the various ILs, we utilized three-dimensionally ordered mesoporous (3DOm) carbon-based electrodes. 3DOm carbon was chosen as a model electrode material because it has a well-defined pore structure with

highly-interconnected pores and large pore windows, allowing for complete infiltration with the tested ILs (except for EtMeIm BF$_4$) and ready access to the large surface area delivered by the mesopores. High specific capacitance was demonstrated using this system with both organic and ionic liquid electrolytes.[242, 258] For this study, a large single batch of 3DOm carbon was prepared using as the template silica spheres of 38.4 ± 1.2 nm that were sedimented to form a close-packed array (Figure 4.3A). The final carbon product shows the characteristic 3DOm structure with well-defined pores and open windows (Figure 4.3B).
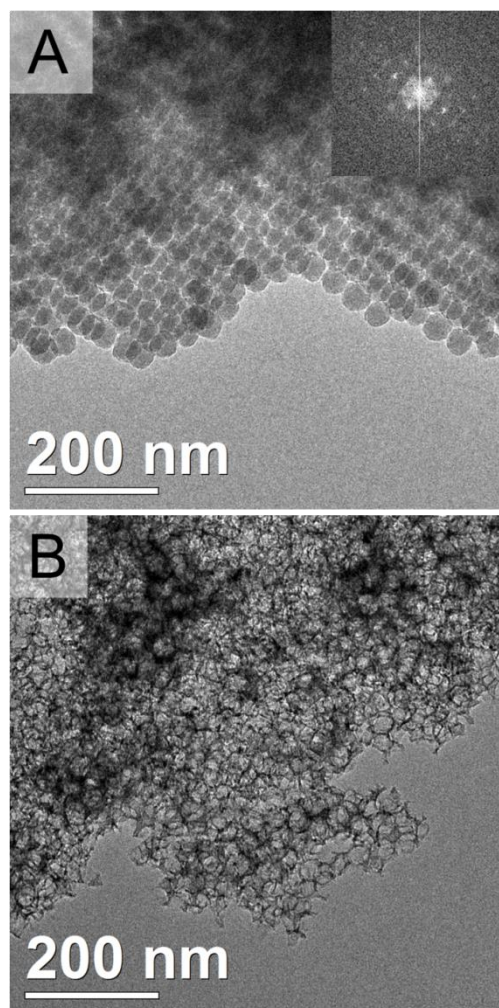
Figure 4.3. TEM images of (A) the silica colloidal crystal used as a template (FFT inset) and (B) the resulting 3DOm carbon used as an electrode material showing the open, interconnected pore structure.

Gas sorption analysis of the 3DOm carbon shows a type IV isotherm with a type H1 hysteresis, consistent with previously reported 3DOm carbon samples (Figure 4.4A). A total surface area of 1074 m^2/g was determined using a QSDFT model designed for mesoporous carbon samples.[197] The pore size distribution shows two major peaks, one at approximately 37 nm and one at 29 nm, corresponding to the pore diameter and pore windows, respectively. Small-angle X-ray scattering shows two well-defined peaks and a

shoulder that can be indexed to a face-centered cubic structure with a d_{111} spacing of 30.5 nm (Figure 4.4B).
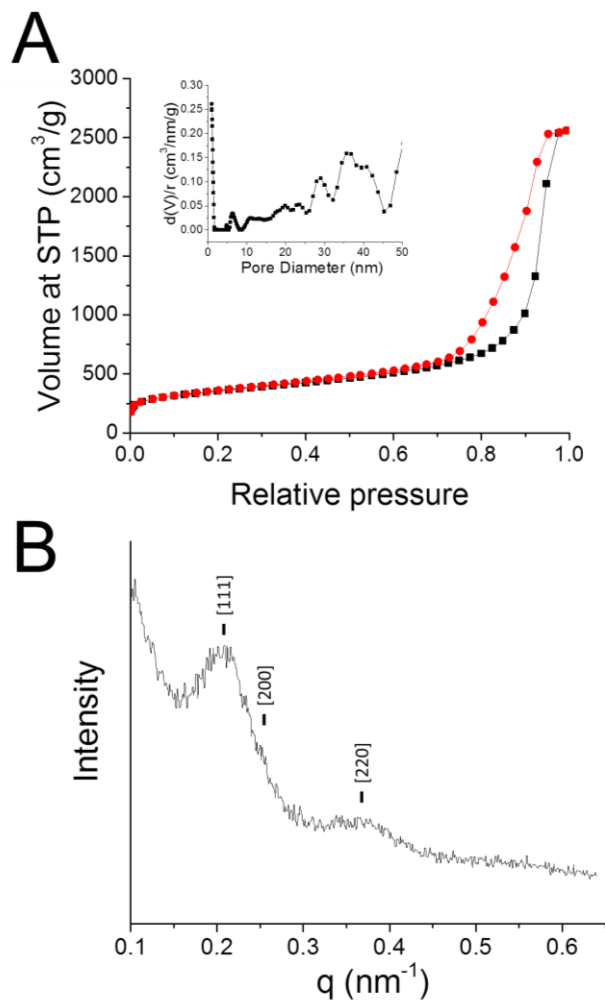
Figure 4.4. (A) Nitrogen sorption isotherm of the 3DOm carbon showing the characteristic type IV isotherms with type H1 hysteresis for mesoporous carbon and in the inset the QSDFT-modeled pore size distribution. (B) SAXS pattern for the 3DOm carbon.

4.4.2 Method for Quantifying the Specific Capacitance

The specific capacitance achievable with the various ionic liquids was measured in a symmetric, two-electrode cell employing the 3DOm carbon electrodes. The cells were charged and discharged at increasing current densities from 0.1 A/g to 20 A/g, followed by 1000 cycles at 1.0 A/g to determine the rate capabilities as well as capacitance retention (Figure 4.5). For most specific capacitance comparisons, the average value of the final 1000 cycles was used.
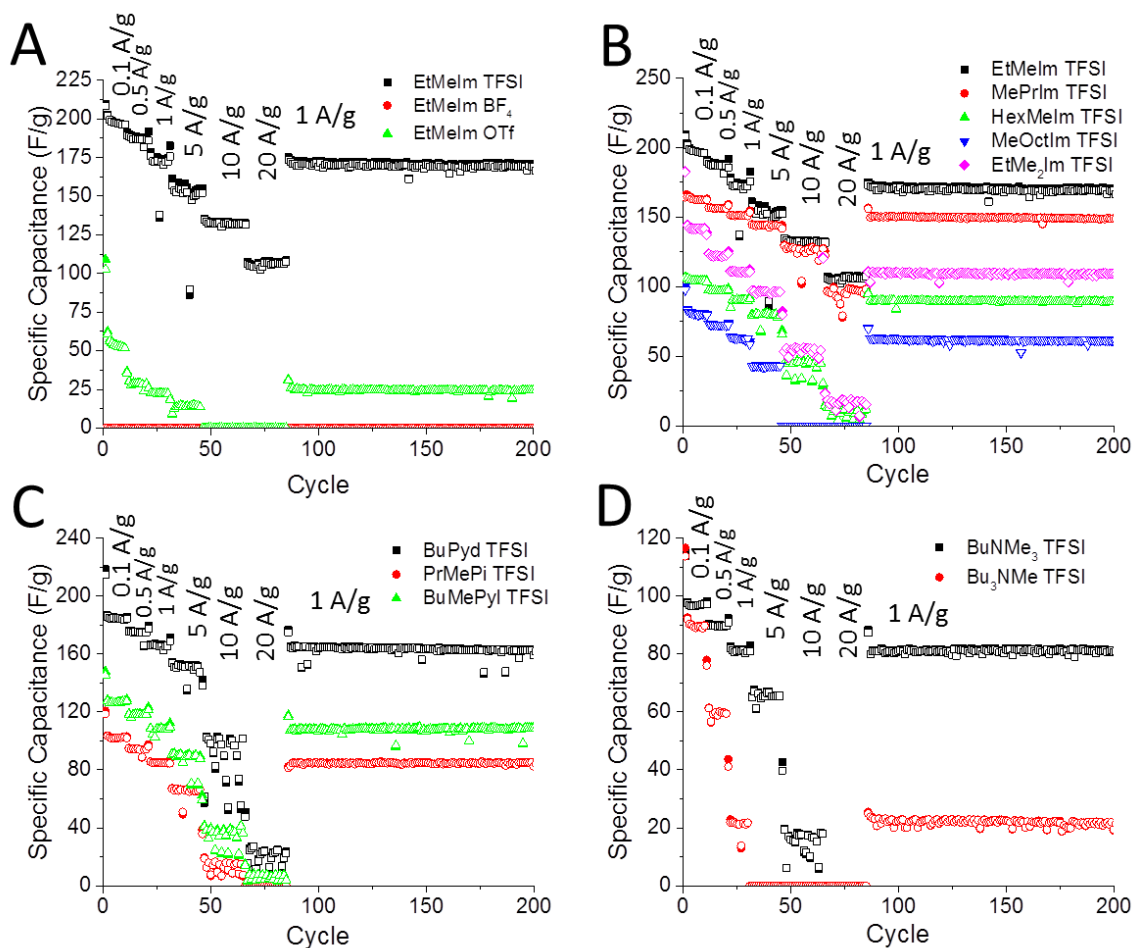
Figure 4.5. Specific capacitance values at various rates for 3DOm carbon electrodes using the IL electrolytes listed in the legends. Comparisons of (A) anion effects, (B) alkyl chain length effects, (C) cations with cyclic cores, and (D) cation volume effects.

The viscosity of the ionic liquids was also measured to compare this property with the observed electrochemical parameters. In general, the viscosity and the conductivity are inseparable, and the two properties match each other. This follows the Walden rule where the product of viscosity and conductivity in similar systems is equal to a constant.[259] The viscosity is shown in Figure 4.6 with the measured value given in Table 4.2.
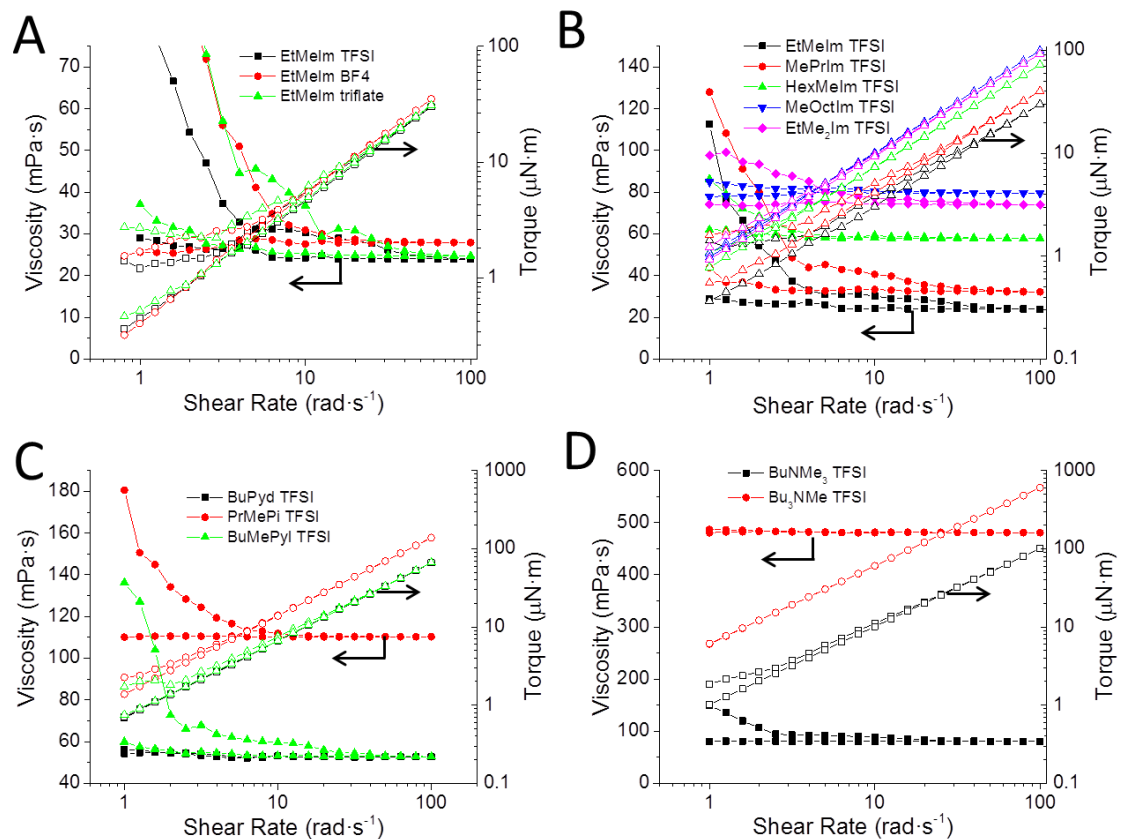
Figure 4.6. Viscosity and torque of ionic liquids sorted by (A) varied anions, (B) imidazolium-based cations, (C) nitrogen-containing cyclic cations, and (D) ammonium-based cations. The initial decrease in the measured viscosity with increasing shear rate is followed by level measurements as the shear rate was decreased again. This behavior is associated with shear ordering. The average of the data obtained during the shear rate decrease was used as the final reported number for viscosity.

Table 4.2. Physical properties of the ionic liquid electrolytes studied in this work.

	cation volume (nm^3)	anion volume (nm^3)	viscosity (mPa·s)	conductivity (S/m)	potential window (V)	specific capacitance (F/g @1 A/g)	specific energy (0.5 CV^2, J/g)
EtMeIm BF$_4$	0.118	0.049	27.9	1.44	4.60 ± 0.02	0	0
EtMeIm OTf	0.118	0.082	24.9	0.88	4.54 ± 0.02	24	246
EtMeIm TFSI	0.118	0.151	24.1	0.96	4.71 ± 0.02	160	1771
MePrIm TFSI	0.134	0.151	32.6	0.53	4.72 ± 0.01	148	1649
HexMeIm TFSI	0.185	0.151	57.5	0.22	4.73 ± 0.02	89	995
MeOctIm TFSI	0.219	0.151	79.5	0.13	4.69 ± 0.04	60	654
EtMe$_2$Im TFSI	0.134	0.151	74.1	0.26	4.73 ± 0.01	101	1128
Bu$_3$NMe TFSI	0.245	0.151	481	0.03	6.07 ± 0.06	21	384
BuNMe$_3$ TFSI	0.144	0.151	80.0	0.22	5.35 ± 0.09	81	1158
BuMePyl TFSI	0.167	0.151	53.0	0.30	5.71 ± 0.04	108	1763
PrMePi TFSI	0.183	0.151	110	0.17	5.68 ± 0.03	85	1373
BuPyd TFSI	0.149	0.151	52.6	0.33	3.87 ± 0.04	156	1166

4.4.3 Effect of Anion Type on Specific Capacitance

For the three anions tested (using the ILs EtMeIm TFSI, EtMeIm OTf, and EtMeBF$_4$), there was little correlation between the anion type, specific capacitance, and

97

any of the other variables tested. This is likely a result of different wetting behaviors of the three ionic liquids. EtMeIm TFSI, the IL with the highest specific capacitance, wets the electrode quickly with no observable beading on the surface. EtMeIm BF_4, on the other hand, forms a bead on the surface of the electrode that did not appear to wet the surface at all and, therefore, did not penetrate the mesopores. EtMeIm OTf spread out on the surface of the electrode, but more slowly than EtMeIm TFSI, indicating less favorable wetting behavior for that anion. The wetting behavior is a function of the type of carbon used for the electrode. In the present case, the carbon precursor, a phenol–formaldehyde-based resol, introduces oxygen functional groups, such as ketones, phenols, and carboxylic acids into the porous electrode and increases the polarity of the surface.[260] Similarly, oxygen groups are present in activated carbons, making these more hydrophilic. When used with more hydrophobic carbon electrodes, the less polar BF_4 and OTf-based ionic liquids may be able to provide higher specific capacitance values because they would wet the nonpolar electrode surface better and increase the interfacial contact area between the electrolyte and the electrode surface. Our observations show the importance of system-specific determination of electrolytes, especially with regards to the wetting behavior of the ionic liquid into the porous electrode. Because the ionic liquid with TFSI as the anion was most suitable for the model carbon system in this study, ionic liquids containing this anion were employed to determine the effects of different cations on electrochemical properties.

4.4.4 Effect of Cation Type on Specific Capacitance

To evaluate the effects of the cation type, ILs with different structures of the cation core but similar cationic volumes were compared. Specifically, BuPyd TFSI, BuNMe$_3$ TFSI, and MePrIm TFSI were compared because all have cationic volumes between 0.13 and 0.15 nm^3. In this set, the pyridinium-based IL electrolyte yields the highest specific capacitance at low to moderate current densities. The imidazolium-based cations provide slightly lower specific capacitance values and the ammonium-based cations the lowest values. The high performance of the BuPyd TFSI electrolyte, however, is reduced at higher current densities, for which the specific capacitance drops to 21 F/g at 20 A/g while MePrIm TFSI maintains 102 F/g at the same rate. This is likely due to the higher viscosity and lower conductivity of BuPyd, limiting the capacitance at the higher rates. The larger size appears to restrain charge carrier transport within the electrode pores, probably both due to the lower conductivity experienced in larger pores and due to wall interactions within the smaller pores. As a result, the formation of the electronic double layer requires a longer period of time, limiting the capacitance at higher rates.

4.4.5 Effect of Alkyl Substituents on Specific Capacitance of Imidazolium-Based ILs

To compare the effect of alkyl substituents on the specific capacitance of imidazolium-based cations, the chain length of the alkyl group in alkylmethylimidazolium cations was varied from two to eight carbon atoms (Figure 4.1). In this series, the specific capacitance decreases monotonically with increasing carbon chain length. Besides being related to increasing viscosity and decreasing conductivity of the IL, the decrease in specific capacitance can be explained by the smaller number of

ions that can be accommodated in the double layer when the ion volume is increased. However, when comparing two electrolytes with different numbers of alkyl substituents but identical cation volume, i.e., EtMe$_2$Im TFSI and MePrIm TFSI, the much higher specific capacitance for MePrIm TFSI is mainly explained by its lower viscosity, which results in higher conductivity. These effects are most pronounced at the higher current densities (Figure 4.5B) so that the specific capacitance of EtMe$_2$Im TFSI drops much more significantly as the current density is increased.

4.4.6 Effect of Alkyl Substituents on the Specific Capacitance of Quaternary Ammonium-Based ILs

To measure the effect of the alkyl substituents on quaternary ammonium-based ILs with TFSI as anion, both cyclic (PrMePi and BuMePyl) and noncyclic (BuNMe$_3$ and Bu$_3$NMe) cations were examined. At moderate current densities, the cyclic ammonium-based cations yield higher specific capacitances, even though they have larger ionic volumes and, in the case of PrMePi TFSI, lower conductivity than BuNMe$_3$ TFSI. This would indicate that the projection of these cyclic cations onto the electrode surface gives a smaller area, allowing a higher concentration of ions in the double layer. Within the set of cyclic and noncyclic cations, the trend of larger ions giving lower specific capacitance is maintained. Additionally, Bu$_3$NMe TFSI, which has the lowest conductivity of any of the ILs tested with the TFSI anion, shows the greatest drop in capacitance with increasing current density. It is unable to cycle at even 5 A/g even though it has a similar capacitance at low current densities as BuNMe$_3$ TFSI.

100

In summary, the ionic volume of the cations has the greatest effect on the maximum specific capacitance of the IL in a porous electrode, provided the electrolyte is able to fully wet the electrode pores. As the current density increases, the conductivity of the electrolytes limits the performance of the cell because of reduced mass transport within the pores during cycling. Therefore, based on specific capacitance, EtMeIm TFSI has the best overall performance as an IL electrolyte, which can be explained by its small ionic volume, low viscosity, and hence relatively high conductivity.

4.4.7 Specific Energy

As discussed above, the structures of cations and anions making up an IL affect the electrochemical stability and potential window of the IL, as well as the double layer capacitance of EDLCs in which the IL is used as an electrolyte. The specific energy of EDLCs is determined by both the specific capacitance and potential window of the IL electrolytes (0.5 CV^2). We showed that while ILs based on a quaternary ammonium cation offer wider potential windows than imidazolium based ILs, and yield much lower specific capacitance values in EDLCs. It is therefore important to balance both of these properties to identify the ILs that offer optimized energy densities. The maximum achievable energy densities were calculated from the potential window of the IL (determined with the linear fit method) and the specific capacitance (cycled at 1 A/g and from 0 to 2 V vs. open circuit potential) and are presented in Table 2. The following trend can be observed for the energy densities: EtMeIm TFSI ~ BuMePyl TFSI > MePrIm TFSI > PrMePi TFSI > BuPyd TFSI ~ BuNMe$_3$ TFSI > HexMeIm TFSI > MeOctIm TFSI > Bu$_3$NMe TFSI > EtMeIm OTf. It is interesting to note that Bu$_3$NMe TFSI, which

offers an exceptionally wide potential window, yields one of the lowest energy densities and is a poor choice for EDLCs. In contrast, even though EtMeIm TFSI does not have the largest potential window, the combination of an intermediate potential window and high capacitance makes it an excellent electrolyte choice for EDLCs. We realize that changing between different carbon materials as the electrode may slightly affect the magnitudes of both the potential window and the specific capacitance, yet, the observed trends should still apply if the electrolyte wets the electrode surface sufficiently. Therefore, these findings can provide insight into choosing the best IL to achieve high energy densities in a desired application.

4.5 Conclusions

This work has provided a systematic comparison of twelve ionic liquids as potential electrolytes for EDLC cells, relating structural features to trends in electrochemical properties. We showed that ILs based on quaternary ammonium cations and TFSI anion offer the widest potential windows. The ionic liquid Bu$_3$NMe TFSI offers an exceptionally wide potential window of 6 V. Increasing the length of the alkyl chain in 1,3-dialkyl-imidazolium TFSI ILs does not improve their stability towards reduction, yet, adding an alkyl group to the C2 position in the aromatic ring results in a significant improvement of cathodic stability. The highest capacitance was measured for EDLCs employing EtMeIm TFSI as an electrolyte, with an average specific capacitance of 162 mAh/g at 1 A/g during the final 1000 cycles. The specific capacitance and conductivity are both related to cation size and viscosity. The highest specific energy was achieved using EtMeIm TFSI and BuMePyl TFSI as electrolytes. On the basis of these results,

high performance ionic liquid electrolytes benefit from small sizes and low viscosity while maintaining the right polarity of the IL ions to sufficiently wet the electrode used in an EDLC.

Chapter 5: Design of a Low-Cost Electrochemical Cell for In-Situ XRD Analysis of Electrode Materials

Reproduced with permission from "Design of a Low-Cost Electrochemical Cell for In-Situ XRD Analysis of Electrode Materials" by Wilson, B. E.; Smyrl, W. H.; and Stein, A. in *Journal of the Electrochemical Society*, **2014**, *161*, A700-A703. Copyright 2014, The Electrochemical Society.

5.1 Introduction

In order to advance the understanding of the operation of electrode materials, to improve currently available materials, and to develop advanced electrode compositions, a better understanding of physical changes within the electrode materials during cycling must be obtained.[261-262] Many in-situ techniques are currently being used, including optical microscopy,[263-264] scanning electron microscopy,[265-267] transmission electron microscopy,[268] atomic force microscopy,[269] X-ray absorption spectroscopy,[270-272] Raman spectroscopy,[273-275] Fourier transform-infrared spectroscopy,[275] mass spectroscopy,[276-277] and nuclear magnetic resonance spectroscopy.[278-279] In addition to these, in-situ X-ray diffraction (XRD) is an important technique in the study of battery electrode materials as it allows for the simultaneous monitoring of the electrochemical processes and associated phase changes within an electrode material without the need for cumbersome ex-situ techniques that have the potential for unwanted side reactions during cell disassembly and possible exposure to the atmosphere.[280-281] The in-situ technique has been used

extensively in the past to study a variety of electrode materials, starting with Chianelli et al. in 1978 and Dahn's group in 1982.[282-283] Since then, additional cell designs have been created and tested, including cells based on coin cells.[284-288] However, these cells all use a beryllium window which is toxic, can decompose at higher potentials, and can suffer from signal attenuation due to varying path length with changing diffraction angle.[289]

To alleviate the problems associated with Be windows, polymer windows, such as polyimide, have been used as more practical X-ray transparent windows.[290-292] Since the polymers are non-conductive, a thin second layer of metal is typically coated on the polymer window to create a functional current collector. These components can be assembled into either a cell similar to cells with Be windows[290] or into a coin cell where part of the case is removed and replaced with a Kapton window. Commercially, there are several suppliers of coin cells with polyimide windows, generally coated with aluminum (see, for example, www.batteryspace.com and www.mtixtl.com). While polymer windows solve the problems associated with beryllium, the cells are not re-usable and cost more than US$20 per cell. Furthermore, both the coin cells and other bulkier cells require additional components to allow for an electrochemical hook-up within the XRD sample chamber,[288-289, 293] the use of a synchrotron to provide sufficient signal-to-noise,[288, 294-295] or complex procedures to eliminate undesirable side reactions.[296] Therefore, the development of a low-cost, easy-to-make, in-situ XRD electrochemical cell is needed.[281]

Herein we report a simple cell design that meets the above requirements while providing reasonable XRD signal and electrochemical performance. This cell was tested

using LiFePO$_4$ as a model cathode material due to its well understood phase transition during electrochemical cycling allowing for verification that the cell is capable of accurately following crystalline changes while performing galvanostatic tests.[270, 297-299] This in-situ XRD cell is based on a flexible fuel cell design previously developed by Smyrl and coworkers.[300]

5.2 Experimental

5.2.1 Materials

The chemicals used were obtained from the following sources: LiFePO$_4$ (LFP), electrolyte (1 M LiPF$_6$ in 1:1:1 ethylene carbonate:diethylene carbonate:dimethylene carbonate), Super P carbon, and styrene butadiene rubber (SBR, 40 wt% suspension in water) from MTI corporation; polypropylene films (PP2200) from 3M Corporation (Saint Paul, MN, USA); Parafilm from Pechiney Plastic Packaging Company (Chicago, IL, USA); quick-dry epoxy from LocTite Company; nickel mesh from Delker Corporation; lithium foil (0.38 mm thick) and carboxymethyl cellulose (CMC; 250 kDa) from Sigma Aldrich; microporous polypropylene membranes (Celgard 3501) from Celgard. All chemicals were used as received without further purification. All water used was purified in-house to a resistivity of greater than 18 MΩ·cm. The final cell assembly was carried out in a He-filled glove box.

5.2.2 Cathode Preparation

First, a measured amount of LFP was ball milled (SPEX SamplePrep 8000M mixer/mill using a ceramic zirconia vial/ball combination) for 5 min, followed by the

addition of Super P carbon to achieve a 84:10 LFP:C ratio by weight and another 5 min of ball milling. CMC as a 2 wt% suspension in water was added along with a 12.5 wt% SBR suspension in water, giving a final composition of 84:10:4:2 LFP:C:CMC:SBR by weight for the dry electrode components. The slurry was mixed for 10 min using a propeller-shaped blade at ~5000 rpm for 10 min. The slurry was allowed to dry for about 1 h under ambient conditions until it had reached a suitable viscosity. A piece of wire mesh was cut to dimensions of 1.3 cm × 5 cm, and a 1.3 cm × 1.3 cm section on one end of the mesh was coated with the prepared slurry using a spatula. The electrode and mesh were dried at 70 °C for 4 h, then at 110 °C under vacuum for 12 h. The electrodes were then pressed at 5 tons ram pressure and weighed to obtain an accurate electrode loading.

5.2.3 Cell Assembly

The various parts of the cell were cut into pieces with dimensions shown in Figure 5.1a. The cathode (including the active material) and anode halves (without the Li foil) were separately assembled outside the glove box using an edge sealer to melt the Parafilm layers and adhere the polypropylene sections together. Once the halves were made, they were transferred into a glove box, where the lithium, electrolyte, separator membrane, and final layer of Parafilm were added. A clamp (Figure 5.1b) was used to temporarily seal the cell while the cell was removed from the glove box, followed by a permanent seal with quick-drying 2-part epoxy around the edges. The clamp was removed after 1 h when the epoxy had cured and fully hardened. The cells were used immediately to minimize any oxygen or water permeating through the polymer layers, which typically begins to be noticeable in this system after 3–4 days. Additionally, two

bent paper clips were used to provide pressure on the electrodes and help maintain constant electrical contact throughout testing. A fully assembled cell with the clips attached is shown in Figure 1c.

5.2.4 Product Characterization

XRD was performed on a PanAlytical X'Pert Pro diffractometer using a Co source (λ = 1.790 Å) operating at an accelerating potential of 45 kV and a current of 40 mA and equipped with an X'Celerator detector. Each XRD scan used during an in-situ experiment scans from 40–45 °2θ, with a 0.002 degree step size and an integration time of 34 seconds per point with a total scan length of approximately 15 minutes. The cell was used in reflection mode. Galvanostatic tests were carried out using an Arbin BT2000 Electrochemical Station.
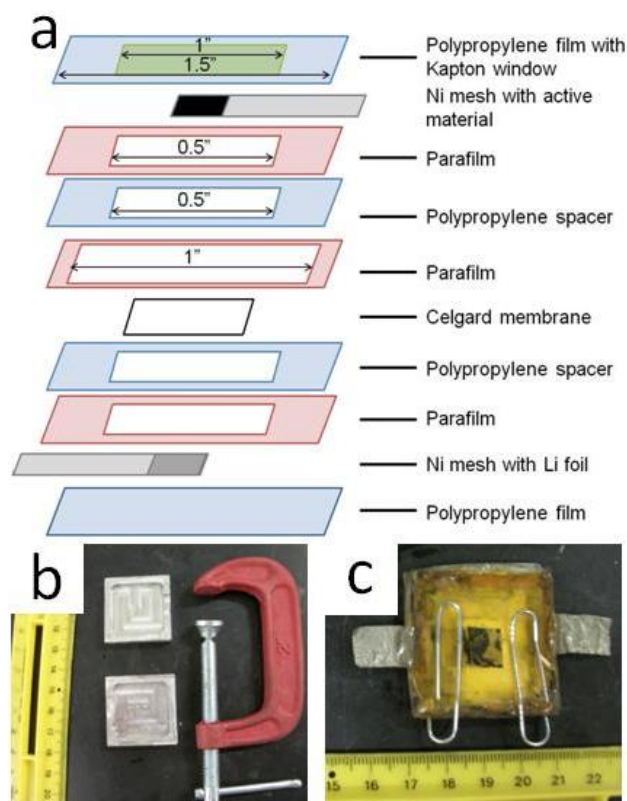
Figure 5.1. (a) Schematic diagram of cell components and assembly, (b) photograph of the clamp used to temporarily seal the cell for removal from the glove box prior to epoxy sealing, and (c) photograph of the fully assembled cell with clips used to maintain contact within the cell during cycling.

5.3 Results and Discussion

5.3.1 Cell Design

One of the benefits to this cell design is the low cost compared to other disposable cells, such as coin cells with Kapton windows, and also compared to the high initial cost of designing and constructing re-usable cells. Reusable cells are typically constructed using steel or aluminum bodies that have been machined into a proper shape, combined with an X-ray transparent window and additional components as needed.[282-283, 288, 290-292]

This results in a large up-front cost to the user, along with requiring sufficient knowledge to create a usable design. Using our design shown in Figure 5.1, a scientist can easily replicate cells with common, low cost materials and little additional equipment. Table 5.1 shows a cost break down of the components to each cell. The suppliers listed were chosen based on a simple product search and costs are representative for a reasonable laboratory scale production. The uses per amount purchased are based on the amount needed per total cell and are approximate. The Celgard membrane is not included as it is typically only sold on an industrial scale, which would lead to an inconsequential cost increase. The final cell only costs US$1.33; significantly less than commercial coin cells. Additionally, the design allows the cell to be used with a common clip-type sample holder for the XRD rather than the more complicated set-ups required for either coin cells or bulkier cells.

Table 5.1. Cost break-down of in-situ cell. Costs are based on a search for laboratory scale amounts and are typical of prices found. The uses per amount purchased are estimated based on minimal waste.

Component	Purchase amount	Cost (US$)	Supplier	Uses per amount purchased	Cost per cell (US$)
Kapton tape	Roll, 2" × 36 yards	65	www.uline.com	175	0.37
Ni mesh	1 sq. foot, 100 × 100 mesh	27	www.mcmaster.com	144	0.38
Polypropylene films	100 8.5×11 sheets	30	www.officeworld.com	3500	0.03
Parafilm	2" × 250 ft. roll	50	www.sigmaaldrich.com	4000	0.04
2-Component epoxy	8 25-mL tubes	22	www.buymbs.com	160	0.14
Li foil	23 mm × 0.38 mm, 100 g	273	www.sigmaaldrich.com	4200	0.07
Electrolyte	1 L	595	www.mticorp.com	2000	0.30
Total cell cost					1.33

This cell has several technical advantages over other cells, beyond the lower cost. Due to its simple design, it can be easily made, the hardest step being the final assembly in the glove box where all of the components are lined up. Because it is made out of clear and translucent polymers, after final assembly, the cell can be visually inspected for any major defects prior to cycling, and can potentially be viewed under an optical microscope if smaller-scale defects are a concern. Additionally, this cell can be used without modification to a clip-style XRD holder, common to most instruments. One inherent problem to a flexible cell design, such as this, is creating pressure between the electrodes to maintain good contact within the cell without blocking the X-ray beam. To address this

problem, bent paper clips placed on either side of the electrode (shown in Figure 5.1c) are used to create sufficient pressure. Without the clips, the capacity can fluctuate and the cell shows significantly lower overall capacities, with performance reduced over 75% compared to a cell with the clips.

5.3.2 Determination of PXRD Scan Window

Once the cell is assembled together with the electrode material, appropriate XRD scanning and potential windows need to be determined to optimize signal intensity and resolution of the diffraction pattern and to observe the relevant electrochemical events. One of the important steps in the cell assembly is the production of the electrode. The electrode thickness and composition are of particular importance as enough material is needed to produce a large XRD signal while balancing this with minimizing the electrode resistance from thick electrodes. Further, excess material on the backside of the electrode should be removed as this typically does not undergo electrochemical cycling, masking the phase changes within the rest of the electrode. A minor disadvantage of this cell design is a large background signal between 10 and 35° 2θ from the numerous polymer layers within the cell along with some background intensity in the XRD pattern from the conductive carbon (Figure 5.2a). Therefore, an appropriate window outside of this region should be selected which contains distinct and representative peaks for any expected phases. To determine a usable window, the cell was cycled at a rate of C/5 and paused at various points to determine the phases present and the potential at which phase transitions occurred. In the case of LFP, a window from 40–45° 2θ is shown, looking at the [131] peaks for both expected phases, specifically $LiFePO_4$ and $FePO_4$.[270, 298-299] The XRD

patterns (Figure 5.2c) confirm the expected transformation from $LiFePO_4$ to $FePO_4$ at approximately 4 V while charging, and the reverse transformation at approximately 3.2 V during discharge. The galvanostatic cycle can be seen in Figure 5.2b, during which the cell exhibited a discharge capacity of 129 mAh/g. A notable feature of the electrochemical data is the set of peaks seen in both the charge and discharge curves. These peaks originate from alternately applying a current to charge the cell and removing it to stop cycling and run the XRD scan. The change in potential is a result of the large polarization within the cell, resulting in an Ohmic drop that is brought on, in part, by the thickness of the electrode (~10 mg/cm^2). The relatively thick electrodes are required to obtain enough XRD signal to clearly discern any phase changes within the electrode material. A further consequence of this drop is a slight overestimation of the capacity of the cell. When the potential changes during cycling, the cell begins to leak current causing the same potential range to be scanned more than once, seen in the asymmetry of the Ohmic spikes.
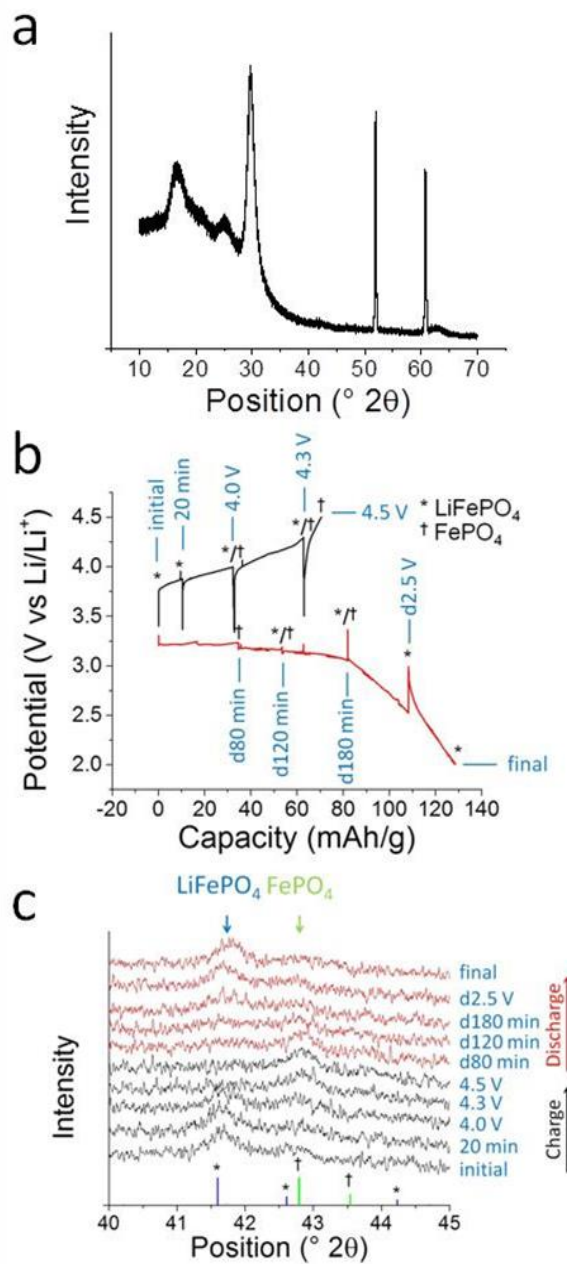
Figure 5.2. (a) XRD pattern for an in-situ cell containing no active material, (b) galvanostatic cycle of LFP cell (C/5) paused at various times for XRD analysis, and (c) XRD patterns for the LFP cell at the various times showing the phase transition from LiFePO$_4$ (*, PDF 00-040-1399) to FePO$_4$ (†, PDF 00-034-0134).

5.3.3 Continuous PXRD and Galvanostatic Scanning

One method to alleviate these Ohmic peaks and obtain a more complete understanding of the phase changes taking place is to continuously scan both the electrochemical and XRD window. Since the current is continuous, the Ohmic potential is also constant and no peaks are seen. This method requires a narrower XRD window so that the scan time is short enough obtain sufficient temporal resolution of the charging and discharging events. In this system, the cell was cycled at C/10 between 2.5 and 4.2 V (covering the entire voltage plateau where the phase change occurs) while continuously scanning between 40 and 45° 2θ for two full electrochemical cycles (Figure 5.3a). The corresponding galvanostatic curves (Figure 5.3b) show reasonable discharge capacities of 111 and 88 mAh/g for the first two cycles, respectively. The XRD patterns show the reversible phase transition between $LiFePO_4$ and $FePO_4$. Additionally, the electrochemical curves are smooth and do not show the Ohmic peaks from the previous cycling method, therefore providing a more accurate depiction of the electrochemical cycling behavior. By continuously scanning both the electrochemical and XRD window, a real-time depiction of crystalline phase changes within an electrochemical cell can be monitored without the effects of stopping and starting the current or cumbersome ex-situ techniques.
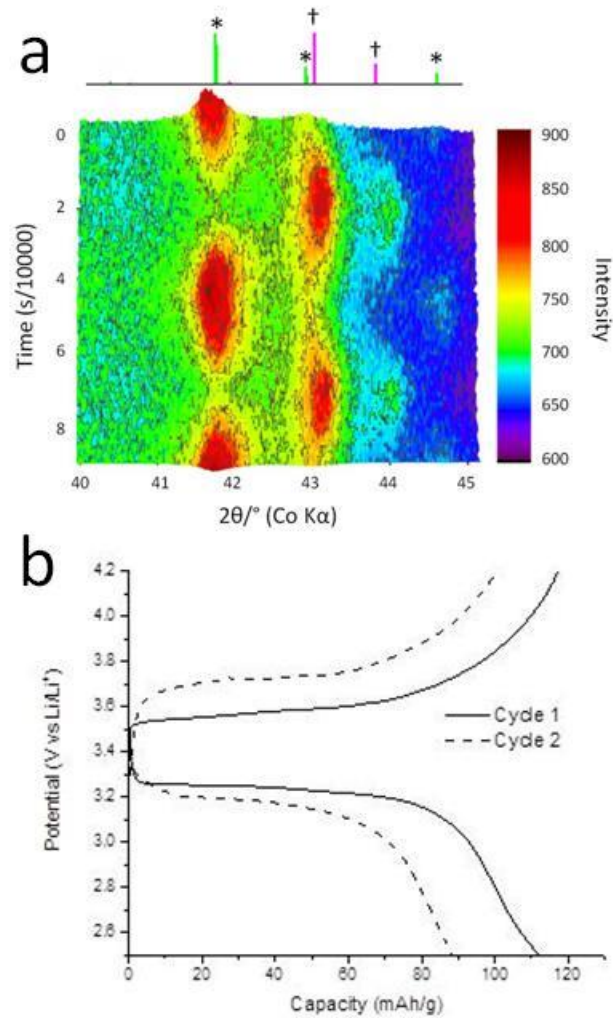
Figure 5.3. (a) In-situ XRD patterns for the first two cycles of an LFP electrode showing the reversible phase transition between $LiFePO_4$ (*) and $FePO_4$ (†) and (b) the first two galvanostatic cycles of the cell at C/10 with cycle 1 shown as a solid line and cycle 2 as a dashed line.

5.4 Conclusions

We have successfully developed a low-cost, disposable, in-situ XRD electrochemical cell that can be easily used with common XRD attachments. The cell is made using common pieces of equipment and easily available polymer materials that are generally

116

unreactive towards electrode materials, making it suitable for different types of battery chemistries. The cell was used to follow the known phase transition in a $LiFePO_4$ system to confirm both reasonable capacity (111 mAh/g at C/10) and discernible XRD peaks. The cell is resistant to oxygen and moisture penetration for up to three days under ambient conditions for the $LiFePO_4$ system, allowing sufficient time for analysis. By cycling the cell continuously through both the electrochemical and XRD windows, real-time crystalline phase changes can be observed and correlated with the galvanostatic profile.

Chapter 6: Y-doped Li$_8$ZrO$_6$: A Li-Ion Battery Cathode Material with High Capacity

6.1 Introduction

Rechargeable lithium ion batteries (LIBs) have proved useful for energy storage in small devices and transportation.[11-12, 301-303] Compared with most other kinds of batteries, LIBs have a higher output voltage and higher energy storage density, and they are more environmentally friendly. They have been widely used in portable electronic devices and are starting to be used in electric vehicles. A LIB has three major components, the anode, the cathode, and the electrolyte that transfers lithium ions between the two electrodes during the charging and discharging processes. The electrochemical reactions in the discharging step can be written as:

$$\text{anode:} \qquad \text{Li} \rightarrow \text{Li}^+ + \text{e}^- \qquad\qquad (6.1)$$

$$\text{cathode:} \qquad \text{Li}_x\text{M} + \text{Li}^+ + \text{e}^- \rightarrow \text{Li}_{x+1}\text{M} \qquad\qquad (6.2)$$

$$\text{total reaction:} \quad \text{Li}_x\text{M} + \text{Li} \rightarrow \text{Li}_{x+1}\text{M} \tag{6.3}$$
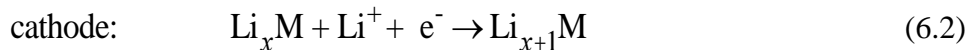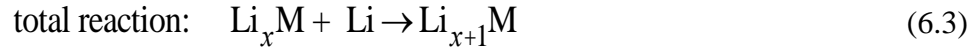
where "M" denotes a cathode host material in which the Li^+ can be reversibly inserted and extracted. Although written here simply as "Li", in practice the most widely used anodes are either lithium metal in half-cell tests or lithium metal intercalated into graphite in practical lithium ion batteries.[11]

The selection of the cathode materials affects the output potential and storage capacity of the battery, as well as the stability and the safety of the battery. Various kinds of cathode materials have been investigated and used in applications,[302-303] including layered structures, such as LiCoO_2 and LiNiO_2, spinel structures, such as LiMn_2O_4, and olivine structures, such as LiFePO_4. Considerable research has been devoted to exploring new materials and structures to improve battery performance, including the Li^+ diffusion rate, the electric potential and storage capacity, and how the number of cycles affects battery life. One example of progress is the improvement of the Li^+ diffusion rate in $\text{LiNi}_{0.5}\text{Mn}_{1.5}\text{O}_4$ through the control of disorder.[304] More sophisticated structures, such as nanostructured and porous electrodes,[305-307] are also promising for improving the performance of batteries.

Computational simulations provide a supplementary tool to understand lithium-ion battery properties at the atomic level, and they can be used to design and to optimize new materials for lithium batteries. Both classical calculations[308-310] and quantum mechanical calculations[311-317] have been carried out on lithium-ion batteries. In the latter, approximate solutions are obtained for the Schrödinger equation or the Kohn-Sham equations describing the electronic structure of the materials. Intercalation potentials,

structural changes during the charging and discharging processes, diffusion rates, and other properties can be derived from such studies.[311] Many promising materials, such as Li_xCoO_2,[318-320] $Li_2Ti_2O_4$,[321] $LiMn_2O_4$,[322] $LiTiS_2$,[323] $LiFePO_4$,[324] $LiMSiO_4$ (M = Fe, Mn, Co, Ni),[325-329] have been systematically studied.

In this chapter, I discuss density functional electronic structure calculations by Kohn-Sham theory (KST)[330] for a new cathode material, namely octalithium zirconate, Li_8ZrO_6 (LZO), to evaluate its feasibility for use in LIBs. These calculations were carried out by Dr. Shuping Huang in the Truhlar research group at the University of Minnesota and act to provide a fundamental understanding of the processes within the cathode material and as explanations for the experimental work discussed in the rest of the chapter. LZO has a layered structure suitable for intercalation and deintercalation of lithium and has a high theoretical specific capacity due to multiple lithium atoms in each formula unit. Given its high lithium content, it has been studied as a potential tritium breeding material in fusion reactors[331] and as a CO_2 absorbent.[332] Calculations indicate that it may have a redox potential vs. Li/Li^+ that is greater than 3.5 eV.[332-333] Compared with conventional cathode materials, LZO has a large band gap and low conductivity, it lacks a transition metal with multiple oxidation states, and it has a slow ion diffusion rate. However, the low conductivity may be overcome by synthesizing smaller particles since small dimensions increase the surface/volume ratio and shorten electron conduction and Li diffusion lengths. This has been demonstrated for other cathode materials with limited conductivity, such as $LiFePO_4$, which is now a commercial cathode material for LIBs.[305] The production of LZO with small enough grains sizes – in the 30–50 nm range – for

efficient delithiation and re-lithiation was achieved in the present work by the development of a method for producing yttrium-doped LZO/carbon composites, in which nanoparticles of doped LZO are in intimate contact with a conductive carbon phase.

This chapter concentrates on structure and energetics of LZO and yttrium-doped LZO with experimental support for some of the theoretical predictions. This includes voltage and volume change as the intercalated Li are removed, charge flow during reactions, and the stability of the delithiated compounds. This chapter also presents galvanostatic data that demonstrate the prospect of yttrium-doped LZO as a high capacity cathode material for LIBs.

6.2 Methods

6.2.1 Materials

Lithium nitrate (99%), zirconium oxynitrate hydrate (99%), yttrium nitrate hexahydrate (99%), lithium benzoate (98%), zirconium acetate hydroxide [$Zr(C_2H_3O_2)_x(OH)_y$, x + y ≈ 4], phenol (>99%), formaldehyde (aqueous solution, 37 wt%), tetrahydrofuran (THF, HPLC grade), *N*-methyl pyrrolidone (NMP, anhydrous, 99.5%), sodium hydroxide, and hydrochloric acid (~37 wt%) were purchased from Sigma Aldrich. Lithium acetate dihydrate was purchased from Johnson Matthey Company. Concentrated nitric acid was purchased from Macron Chemicals. Super P carbon, electrolyte (1 *M* $LiPF_6$ in 1:1:1 ethylene carbonate, dimethyl carbonate, and diethyl carbonate (EC-DMC-DEC) by volume), and polyvinylidene diflouride (PVDF) were purchased from MTI Corporation. Carbon-coated aluminum foil was obtained from ExoPack. Celgard 3501 polypropylene membrane films were obtained from Celgard.

Nitrate precursors were dried in an oven at 110 °C for at least 4 h prior to use to obtain a consistent mass. Deionized water was produced on site using a Barnstead Sybron purification system (final resistivity >18 MΩ·cm).

6.2.2 Preparation of LZO

The synthesis of LZO was accomplished by the thermal decomposition of nitrate precursors, following a procedure slightly modified from a previous published synthesis;[334] this yields LZO as a microcrystalline powder. Zirconium oxynitrate (4.2 mmol) and lithium nitrate (42 mmol) were ball-milled in a zirconia ball and cup set for 5 min and then calcined in a covered alumina crucible at 2 °C/min to 600 °C, followed by a 3 h isothermal step, further heating at 2 °C/min to 800 °C, and an additional 2 h isothermal step at 800 ˚C. (Molar calculations were performed using the anhydrous basis for the lithium and zirconium nitrate precursors, and 243.22 g/mol was used for zirconium acetate hydroxide [$Zr(C_2H_3O_2)_x(OH)_y$, $x = y = 2$], below.) The as-made product was ground to a fine powder using an agate mortar and pestle prior to further analysis.

6.2.3 Preparation of LZO/C Composites

To intimately mix the active material with a conductive phase, a more complex composite synthesis was used. First, zirconium acetate hydroxide (4.1 mmol), lithium acetate dihydrate (41 mmol), and Super P carbon (0.25 g) were ball milled for 5 min, followed by the addition of 0.25 g of stock PF solution (prepared in the same manner as described in Chapter 2). The composite was mixed well prior to curing the resol at 120 °C for 24 h. The dry powder was briefly ground using an agate mortar and pestle prior to pyrolysis under 0.5 L/min N_2 following the same thermal parameters as for the

bulk LZO. The final product was found to be 22.1 wt% carbon, as determined by combustion-based analysis, performed by Atlantic Microlabs, Norcross, GA.

Additionally, Y-doped samples were prepared starting from yttria-doped ZrO_2 nanoparticles on the surface of conductive carbon, made through a synthesis adapted from Jiang *et al.*[335] In this synthesis, carbon black mitigates agglomeration of ZrO_2 nanoparticles, and the yttrium is believed to reduce grain growth by lowering the surface energy of ZrO_2 grains or decrease the concentration of mobile species on the grain surface.[336] Briefly, zirconyl nitrate (3.24 mmol) and yttrium nitrate (0.207 mmol) were dissolved in a solution of nitric acid (0.2 g) and DI water (15.8 g). The solution was added in four parts to Super P carbon (1.66 g), with each part thoroughly mixed with a mortar and pestle, then dried before adding the next portion. After the final addition, the mixture was dried at 110 °C for 1 h, heated to 400 °C under static air at 2 °C/min, then cooled naturally to ambient temperature. The nanoparticles were converted to LZO by ball milling the ZrO_2/C with lithium benzoate at 10:1 Li:Zr (based on residual mass from thermogravimetric analysis) for 5 min, then carbonizing the composite at a maximum temperature (700, 750, 800, 850, or 900 °C) with a 1 °C/min ramp to 600 °C, followed by a 2 h hold, then 2 °C/min to the target temperature, followed by another 2 h hold, all under 0.5 L/min N_2 flow. The product was allowed to completely cool to room temperature before being removed from the inert atmosphere because partial self-combustion can occur at temperatures exceeding ~35 °C in the presence of air. The final products contained between 55–60 wt% carbon, as determined by combustion-based analysis, performed by Atlantic Microlabs, Norcross, GA, and are referred to as Y-

Li$_8$ZrO$_6$/C or Y-LZO-T, where the value of T refers to the maximum heating temperature in ˚C.

6.2.4 Battery Assembly

Electrodes were made from the LZO/C composites by first grinding Super P carbon (26.0 mg) and the composite (154 mg) using an agate mortar and pestle for 5 min to create a uniform mixture. A 10 wt% solution of polyvinylidene diflouride (PVDF) in N-methylpyrrolidone (NMP) (200 mg solution) was added, followed by additional NMP (~1 mL). The solution was mixed for 5 min to create a viscous slurry with a final dry composition of 60:30:10 Li$_8$ZrO$_6$:C:PVDF by weight. Because the yttrium-doped sample contained a significant amount of carbon in the composite, a slurry of this material was prepared without additional carbon, using a 90:10 weight ratio of composite:PVDF. The slurry was then cast onto carbon-coated aluminum foil using a doctor blade and dried at ambient temperature in a dry room maintained below 80 ppm H$_2$O, or 1% relative humidity during active use. The dried film was pressed using a roller press to approximately half of its original thickness (final thickness ~250 μm) and 0.5-inch diameter disks were punched out. Active material loading was between 2 and 2.5 mg/cm^2. The electrodes were assembled into CR2032 coin cells in a half-cell configuration with metallic lithium as the counter electrode. A Celgard 3501 polypropylene membrane was used as the separator and 1 M LiPF$_6$-EC-DMC-DEC as the electrolyte. A wave spring was used behind the current collectors to maintain pressure and electrical contact within the cell. All assembly was done in a He-filled glove box. Following the usual convention for reporting battery charging and discharging rates, I

define 1 C as a rate of one Faraday constant per mol of Li_8ZrO_6 per hour; this yields 1 C equal to 110.5 mA/g. All galvanostatic cycling was performed between 1.3 and 4.5 V vs Li/Li^+.

6.2.5 Product Characterization

Powder XRD of the microcrystalline Li_8ZrO_6 powder was performed on a PANalytical X'Pert PRO diffractometer using a Co anode at 45 kV and 40 mA and an X'Celerator detector. Rietveld refinement was performed using PANalytical X'Pert Hi-Score Plus software to a final *R*-value of 4.39 and a goodness-of-fit of 10.1. Ex-situ powder XRD analysis was performed on composite electrodes by attaching the discs to an oriented Si wafer using Kapton tape to maintain a uniform sample height for all samples.

XPS was performed using a Surface Science SSX-100 spectrometer equipped with an Al anode operated at 10 kV potential and 20 mA current over a spot size of 0.64 mm^2. XPS peak positions were calibrated against the $C_{1s(sp3)}$ peak of (adventitious) carbon, set at 284.6 eV.

Elemental analysis was performed using a Thermo Scientific iCAP 6500 dual view inductively coupled plasma optical emission spectrometer (ICP-OES), operated at 1200 W with a nebulizer flow of 0.7 L/min, cooling gas at 12 L/min, and auxiliary gas at 0.5 L/min. An integration time of 8 s was used for each measurement, and 5 replicate measurements were carried out per sample. Ultraviolet-visible spectroscopy (UV-vis) spectra were collected with a Thermo Scientific Evolution 220 spectrometer. Data were collected in the 190–800 nm range. UV-vis spectra were obtained and a Kubelka-Munk

transformation[337] was performed on the UV-vis spectrum of LZO using the following equation

$$F(R) = \frac{(1-R)^2}{2R} \tag{6.4}$$

in which $F(R)$ is the Kubelka-Munk remission function, and R is reflectance.[338] The UV-vis spectrum of semiconductors near the absorption edge is described by the following equation

$$F(R)hv = B(hv - E_g)^n \tag{6.5}$$

in which hv is the energy of a photon, B is a coefficient, and E_g is the band gap. Our computational results show that LZO has an indirect band gap, so we set n equal to 2, which is the appropriate value for allowed transitions with an indirect band gap. Therefore, the optical band gap was determined by plotting $(F(R)hv)^{1/2}$ against hv (which is known as a Tauc plot[339]), and E_g was obtained by extrapolating the linear part to $F(R) = 0$.

6.2.6 Density Functional Calculations

Parameters and methods used for the computational portion can be found in the original paper that forms the basis for this chapter.[340]

6.3 Results and discussion

6.3.1 Structures of LZO and Y-LZO/C

Six density functional methods were used to optimize the structure of LZO, and the optimized unit cell parameters are shown in Table 6.1. It was found that M06-L and PBE+U give the most accurate lattice parameters, and HSE06 and PBE0[341] also give

accurate geometries compared with experiment. The XRD pattern was simulated using the M06-L optimized structure and compared with both the experimental pattern from microcrystalline LZO and the pattern of the Rietveld-refined structure (Figure 6.1a). The computational pattern matches very well with the observed and refined patterns in both peak intensities and positions. Furthermore, the atomic positions obtained by Rietveld refinement of the experimental pattern and M06-L and HSE06 computational methods are nearly identical, further verifying the functionals. The lattice parameters of the unit cell in space group 148 ($R\bar{3}$) are also very similar for the refined structure and both of these functionals.[340] Overall, the close match between the computed and experimental parameters directly validates the ability of the M06-L and HSE06 functionals to accurately model the LZO crystal structure. In addition, this work confirms the structure of LZO that was previously only established by analogy to the powder pattern of Li_8SnO_6.[342-343]

Table 6.1. Lattice parameters of Li_8ZrO_6 determined from Rietveld refinement and optimized by various density functionals.

	$a = b/\text{Å}$	$c/\text{Å}$	volume/Å^3
Literature[a]	5.48	15.45	402
Rietveld refinement (this study)	5.49	15.47	404
PBE	5.51	15.58	410
N12	5.43	15.38	393
M06-L	5.46	15.46	399
HSE06	5.46	15.39	397
PBE0	5.45	15.43	398
PBE+U	5.47	15.46	400

[a] ref. 344
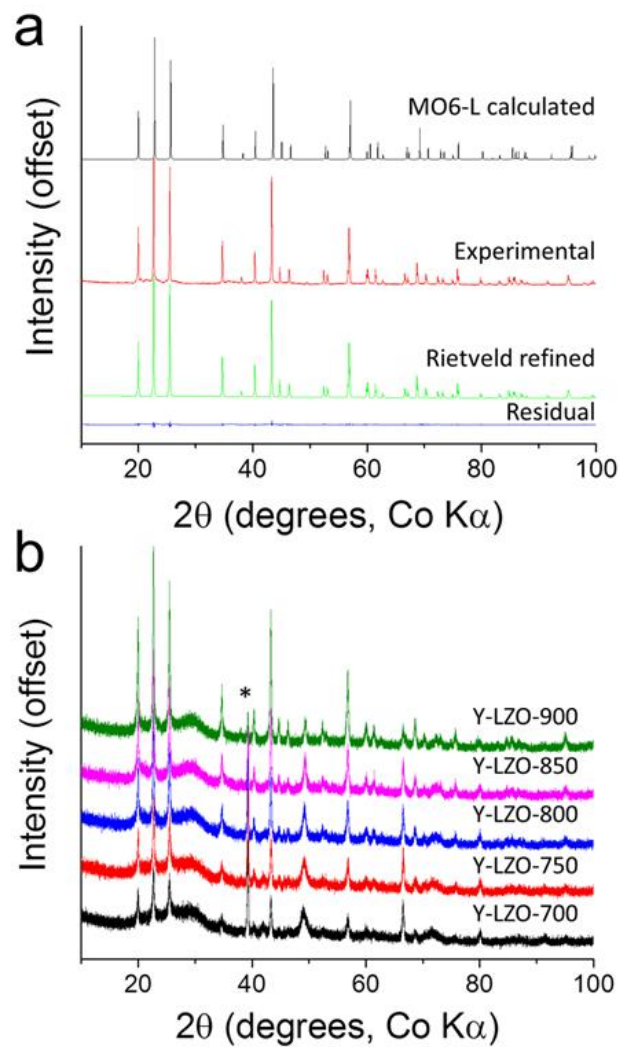
Figure 6.1. (a) Comparison of the calculated XRD pattern of LZO as determined from the M06-L functional to the experimental pattern and the pattern of the Rietveld-refined structure. The residual trace confirms the close match between the experimental and Rietveld patterns. (b) Experimental XRD patterns for the Y-Li$_8$ZrO$_6$/C composite material used for galvanostatic charging/discharging. The asterisk marks a reflection corresponding to a minor Li$_2$O secondary phase.

128

The powder patterns of the Y-LZO/C composites also match the primary peaks in the Rietveld refined pattern (Fig. 6.1b), indicating that the yttrium doping does not significantly alter the crystal structure. The broad peak at ~30 °2θ is a result of the large carbon component in the composite. The formation energy of oxygen vacancies is highly reduced in Y-LZO compared with LZO. The stability of two Y atoms at different layers and different distances were compared, showing that the two Y atoms prefer to be in the same layer and to be close to each other (d_{Y-Y} = 5.50 Å). Additionally, the O vacancy prefers Y coordination, different from Y-doped ZrO_2, in which O vacancy prefers Zr coordination.[345] The calculated lattice constants for Y-LZO are very slightly increased compared with the undoped material, and this small shift is also observed in the experimental XRD patterns (Table 6.2), determined from peak shifts.

Table 6.2. Comparison of lattice parameters of $Li_{96}Zr_{12}O_{72}$ and $Li_{96}Y_2Zr_{10}O_{71}$ from the HSE06 functional and experimental data.[a]

	$a\,(Å)$	$b\,(Å)$	$c\,(Å)$	Volume ($Å^3$)
$Li_{96}Zr_{12}O_{72}$	5.45	5.45	15.41	396
$Li_{96}Y_2Zr_{10}O_{71}$	5.47	5.47	15.49	402
Experimental	5.497	5.497	15.48	405
(for Y-Li_8ZrO_6/C, 900 ˚C)				

[a] Although the calculations are based on the 2×2×1 supercell, lattice parameters are reported here for the conventional cell for easier comparison with the experimental data. Because only the Γ point was used in the supercell calculations, the lattice parameter of pure LZO is slightly different from that in Table 6.1.

6.3.2 Electronic structure

To determine band structure, different functionals were first tested with ZrO_2, and their performance was compared with experimental results.[340, 346] It was found that in the case of ZrO_2, the calculated lattice constants and gap by HSE06 are in good agreement with experimental results. M06-L underestimates the band gap. The gap with N12-SX is within the range of experimental ones. A band gap calculation was then performed on Li_8ZrO_6 with the band gaps from various functionals shown in Table 6.3. The band structure of Li_8ZrO_6 shown in Fig. 3a was calculated with a local functional, M06-L, and has an indirect band gap of 5.3 eV. It is well known that local functionals underestimate semiconductor band gaps significantly,[347-349] but their predictions are still of interest because they can be used conveniently for exploratory work on trends, which they predict more accurately than they predict absolute values. Among the functionals used, HSE06 and N12-SX hybrid functionals, which include Hartree-Fock exchange, have the smallest error (0.3 eV) in predicting the gaps of 31 semiconductors.[348-349] The calculated LZO gap by HSE06 and N12-SX is 6.8 and 6.5 eV, respectively.

Table 6.3. Band gap of Li_8ZrO_6 as calculated using various methods.

	PW91	PBE	N12	M06-L	N12-SX	HSE	PBE0	PBE+U
band gap of Li_8ZrO_6	4.7^a	4.9	5.0	5.3	6.5	6.8	7.5	5.1
mean |error| [b]	1.1	1.0	1.0	0.7	0.3	0.3		

[a] ref. 332

[b] for 31 semiconductors found in ref. 349

The density functional calculations indicate an indirect band gap (Fig. 6.2a). Experimentally, the band gap of LZO was determined from the diffuse reflectance UV-vis spectrum (shown in Fig. 6.2b) by applying a Kubelka-Munk transformation and Tauc plot, as discussed in the methods section. This indicated a band gap of 5.75 eV. The HSE06 and N12-SX functionals overestimate the gap by about 0.7 and 1.0 eV, respectively. The large band gap signifies that LZO has poor electronic conductivity, which needs to be compensated by forming a nanocomposite with a conductive phase to allow the use of LZO as active material in an electrode, preferably with very small particle sizes. The density of states (DOS) and partial density of states (PDOS) that show the computationally derived orbital energy gap can be found in the original paper.[340]
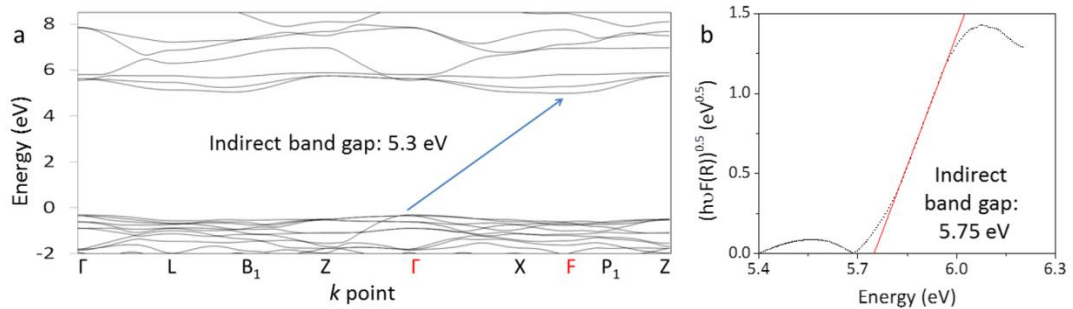
Figure 6.2. (a) Band structure of LZO calculated using M06-L, showing an indirect band gap of 5.3 eV. (b) The optical band gap of LZO was determined to be 5.75 eV using the Tauc plot obtained from a UV-vis spectrum.

6.3.3 Structures and energies of delithiated Li$_x$ZrO$_6$

To understand the charging and discharging process at the atomic scale, delithiated Li$_x$ZrO$_6$ structures from the Li$_8$ZrO$_6$ structure were generated. Table 6.4 shows the optimized volumes for the lowest-energy delithiated configurations of Li$_x$ZrO$_6$ with $x =$ 7, 6, and 5; more detailed information about the relative energies of various configurations can be found in the original paper.[340] The frequencies of the lowest-energy configurations for the range of compositions from Li$_8$ZrO$_6$ to Li$_5$ZrO$_6$ were calculated, and no imaginary frequency was found at the Γ point. The M06-L, N12, PBE, PBE+U, and HSE06 functionals all predict the same most stable delithiation configurations.

Table 6.4. Volume (Å^3) per formula unit of the lowest energy Li$_x$ZrO$_6$ configurations found. [a]

x	Label[b]	PBE	N12	M06-L	HSE06
8	Li8	411	393	399	397
7	Li7_x1	408	393	396	399
6	Li6_x12	408	384	396	399
5	Li5_x157 (Li5_x234)[c]	426 (369)[c]	408 (348)[c]	414 (363)[c]	417 (369)

[a] These volumes refer to the conventional unit cells.

[b] The label refers to the number of lithium atoms per formula unit (e.g. Li7_x1 refers to Li$_7$ZrO$_6$) with "_x#" referring to a specific atom label used in the original paper (ref. 340)

[c] Li5_x157 has much lower energy (~30 kcal/mol) than Li5_x234, but the layered structure is not maintained and an O−O bond is formed. Li5_234 is the most stable layered structure and is shown in parenthesis.

In the cases of Li$_7$ZrO$_6$ and Li$_6$ZrO$_6$, it is easier to remove Li atoms from tetrahedral interstitial sites than to remove them from octahedral sites, based on the computed delithiation energies. The volume of the unit cell and the structure both change very little

when x is decreased to 7 and to 6 in Li_xZrO_6; however, the distortion is very large when x is decreased to 5. The lowest-energy configuration is labeled Li5_x157, in which two tetrahedral Li atoms and one octahedral Li atom are removed, and the layered structure of the compound is destroyed. The smallest O−O distance becomes 1.34 Å in Li5_x157, and this is much shorter than the shortest distance, 2.96 Å, in LZO, and it is a typical distance for the superoxide O_2^-. The layered structure can be maintained in the case of Li5_x234 where three tetrahedral Li atoms are removed, but the volume is decreased by 10% compared with LZO, and this structure has an energy that is about 1 eV higher than that of Li5_x157. This indicates that two Li atoms may be topotactically removed without destroying the structures, while the extraction of the third Li atom may destroy the layered structure of LZO or greatly change the geometry.

Consistent with computational predictions,[340] the experiments showed very little change in structural dimensions after partial delithiation of Li_8ZrO_6 to approximately $Li_{7.62}ZrO_6$ (based on the measured discharge capacity) and subsequent relithiation, as shown in the powder XRD patterns obtained for Li_8ZrO_6/C composite electrodes (Fig. 6.3). Focusing on the characteristic (003), (101), and (012) peaks, no significant shift is observed during electrochemical cycling, confirming that the structure is maintained. The region of the XRD pattern in which reflections from a ZrO_2 phase would be observed does not show any evidence of crystalline ZrO_2. This indicates that ZrO_2 is not formed during cycling, which in turn indicates a topotactic delithiation reaction.
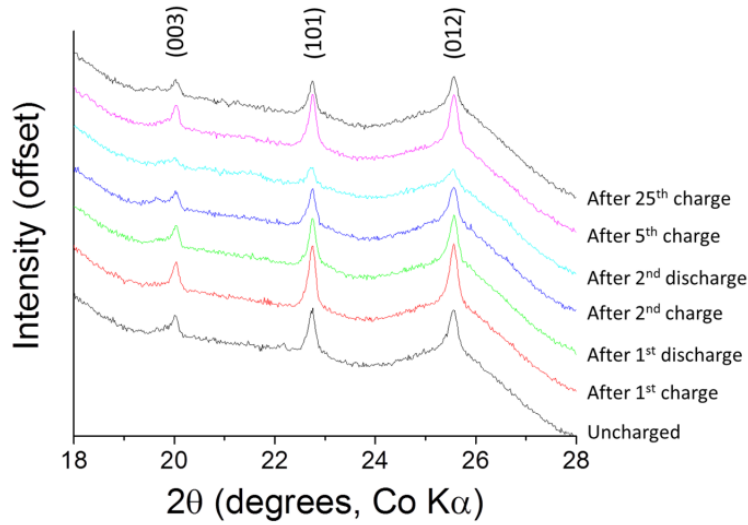
Figure 6.3. Partial ex-situ powder XRD patterns of electrode films made from a Li_8ZrO_6/C composite before charging and after the charge and discharge cycles indicated.

The average voltage of the electrochemical cell was derived using:

$$V = -\frac{1}{F}\frac{E(Li_xM) - E(Li_{x-\Delta x}M) - \Delta x E(Li)}{\Delta x} \tag{6.6}$$

where E is the total energy, and F is the Faraday constant. These are average potentials over the range of x from $x-\Delta x$ to x. For the undoped material, "M" denotes "ZrO_6." The average voltages of the electrochemical cell for integer x are shown in Table 6.5. From the lowest-energy configurations, the reaction energy was calculated for

$$Li_xZrO_6(s) \rightarrow Li_{x-1}ZrO_6(s) + Li(s) \quad (x = 8, 7, 6) \tag{6.7}$$
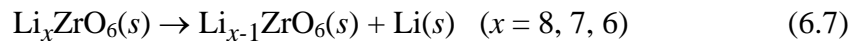
and the results are shown in Table 5. Although M06-L and HSE06 yield qualitatively different pictures of the delithiated structures, as already discussed, they predict the same voltages of 4.0 and 3.8 eV vs. Li/Li$^+$ for the extraction of the first and second lithium

134

atoms, respectively. PBE+U generates similar geometric structures as HSE06, but it underestimates the voltage compared to HSE06 and experiment.

Table 6.5. Reaction energy (kcal/mol) for $Li_xZrO_6(s) \rightarrow Li_{x-1}ZrO_6(s) + Li(s)^a$.

x	PBE	N12	M06-L	HSE06	PBE+U
8	85.0 (3.7)	84.4 (3.7)	92.5 (4.0)	92.9 (4.0)	71.1 (3.1)
7	82.2 (3.6)	79.3 (3.4)	87.0 (3.8)	88.1 (3.8)	66.9 (2.9)
6	53.7 (2.3)	54.9 (2.4)	58.8 (2.6)	56.8 (2.5)	70.8 (3.1)

^{a}A positive energy corresponds to an endoergic reaction. The lowest energy states from Table 6.4 are used. The numbers in parenthesis are the corresponding average voltages (V) of the cell vs. Li/Li^+.

The second and third lithium atoms are easier to remove from the Li_8ZrO_6 structure than is the first lithium atom, indicating that the oxygen hole polaron is energetically more favorable at high lithium vacancy concentrations. This is similar to the result found previously for Li_2MnO_3.[350] Table 6.6 shows the results of a different delithiation path, in which the LZO is completely decomposed into ZrO_2 (s), Li (s), and O_2 (g). The voltage for this path is significantly lower than that of reaction 6.7; therefore, this decomposition path is more thermodynamically favorable. This indicates that the topotactic reaction path does not involve the most stable structures. Kang et al.[351] have studied the voltage profile for the delithiation of Li_2O_2, and compared two paths, one being the delithiation path from Li_2O_2 to xLi and $Li_{2-x}O_2$, and the other being decomposition of Li_2O_2 into 2Li and O_2. They found that the latter does not correspond to topotactic delithiation, and the first path may be kinetically more favorable although the thermodynamic energy of reaction is less favorable. Similarly, the relative energy of the topotactic delithiation path and the equilibrium path for LZO can be compared by considering:

$$\Delta E = E_{Li_xZrO_6} - \frac{x}{8}E_{Li_8ZrO_6} - \left(1 - \frac{x}{8}\right)E_{ZrO_2} - \left(2 - \frac{x}{4}\right)E_{O_2} \tag{6.8}$$

Assuming that the entropies of the solid phases and the pressure-volume contributions to the free energy are negligible, we consider only oxygen gas and the phonon free energy in calculating the difference between free energy and the energy. This approximation has been successfully applied for the Li-Fe-P-O phase diagram.[352]

Table 6.6. Reaction energy (kcal/mol) for $1/8Li_8ZrO_6(s) \rightarrow 1/8ZrO_2(s) + Li(s) + 1/4O_2(g)$.[a]

PBE	N12	M06-L	HSE06
66.6 (2.9)	63.5 (2.8)	67.3 (2.9)	69.2 (3.0)

[a]The numbers in parenthesis are the corresponding voltages (V) of the cell vs. Li/Li$^+$.

There are multiple off-stoichiometric Li_xZrO_6 configurations with relatively low energy above the equilibrium state, all of which have the Li vacancies at tetrahedral sites. The structures become more and more unstable as x decreases in Li_xZrO_6. The calculated voltages for the topotactic delithiation path $Li_8ZrO_6 \rightarrow (8 - y)Li + Li_yZrO_6$ are shown in the original paper.[340] The predicted voltage for $y = 7.0$–7.92 is 4.02–4.18 V, consistent with the experimentally observed charging step at 4.3 V, indicating that these off-stoichiometric Li_yZrO_6 configurations are accessible in the charging process. The experimental galvanostatic charge curve for Li_8ZrO_6 at a charging/discharging rate of C/5 is given in Fig. 6.4 and shows two very small step-like features in the range from 3.9 to 4.3 V during delithiation that may be associated with removal of the first and second lithium atoms in a part of the material. The first discharge cycle showed a step near 2.6 V, which could be the re-formation of Li_8ZrO_6 from the Li_xZrO_6 formed during the

delithiation. Because of the low conductivity of Li_8ZrO_6, the full sample (average grain size 108 nm) was likely not accessed during galvanostatic cycling, so that the observed capacity was still much below the theoretical value. Considering the high voltage requirements for delithiation and no ZrO_2 observed after cycling experimentally, it is most likely that the topotactic path in reaction (7) is kinetically favorable.
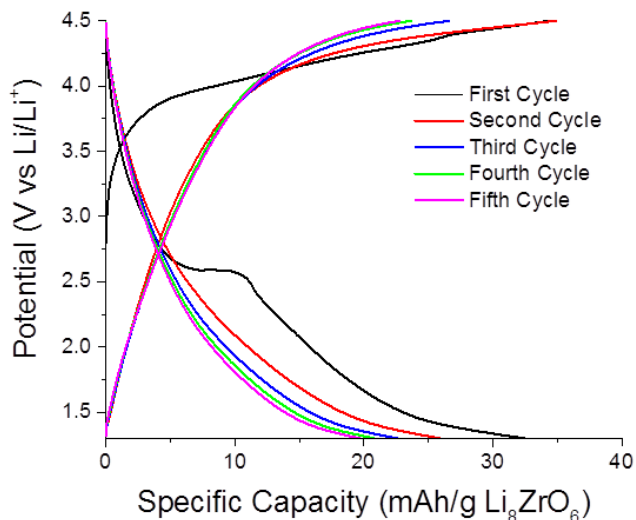
Figure 6.4. Galvanostatic charge/discharge curves of the coin cell used for the ex-situ PXRD analysis. A current density corresponding to C/5 (per gram composite material) was used. This corresponds to 0.57C per gram LZO.

6.3.4 Use of Yttrium Doping to Improve Specific Capacity

To increase the utilization of the cathode material, Y-doped ZrO_2 nanoparticles were employed as the LZO precursor, which together with the Super P carbon and the carbonization product from the lithium benzoate reduced the grain size to 51 nm at 900 °C calcination temperature and 31 nm at 700 °C calcination temperature. These grain

sizes were estimated by applying the Scherrer equation to the full-width-at-half-maximum of the (101) peak at 22.8 °θ corrected for instrumental broadening (Table 6.7). The smaller grain size, along with the additional carbon, was desirable to provide more intimate contact with the conductive carbon. These factors have been shown in other battery electrode materials to significantly improve electrochemical performance.[115, 353-354] Besides influencing grain sizes, increases in the calcination temperature cause some changes to the elemental composition, most notably reducing the amount of a residual Li_2O impurity (Table 6.7).

Table 6.7. Elemental composition (mass%) and grain sizes of the Y-doped Li_8ZrO_6/C composite materials as a function of calcination temperature.

temperature (°C)	Li	Y	Zr	C	H	N	O	calculated formula	grain size (nm)
700	10.8	0.22	10.5	57.7	0.62	0	20.1	$Li_8Y_{0.02}Zr_{0.98}O_{5.99}$ + 2.6 Li_2O + $C_{40.7}H_{5.2}N_0O_2$	31
750	11.2	0.21	10.7	60.3	0.56	0.32	16.6	$Li_8Y_{0.02}Zr_{0.98}O_{5.99}$ + 2.7 Li_2O + $C_{41.8}H_{4.6}N_{0.2}O_0$	35
800	10.0	0.12	9.74	55.6	0.83	1.10	22.6	$Li_8Y_{0.01}Zr_{0.99}O_{5.99}$ + 2.7 Li_2O + $C_{42.8}H_{7.6}N_{0.7}O_{4.3}$	37
850	10.5	0.30	10.9	58.6	0.58	1.83	17.3	$Li_8Y_{0.03}Zr_{0.97}O_{5.98}$ + 2.1 Li_2O + $C_{39.6}H_{4.7}N_{1.0}O_{0.7}$	48
900	9.12	0.50	12.8	58.9	0.57	1.84	16.2	$Li_8Y_{0.04}Zr_{0.96}O_{5.98}$ + 0.5 Li_2O + $C_{33.5}H_{3.9}N_{0.9}O_{0.4}$	51

As the calcination temperature was increased for the yttrium-doped Li_8ZrO_6/C composite materials, some notable changes in the final elemental composition were seen. I note that each sample was prepared from the same homogenous mixture of $Li(C_5H_5COO)$ and yttria-doped ZrO_2, the only change being the final calcination temperature. Table 6.2 shows the measured elemental compositions, with the Li, Y, and Zr amounts determined by inductively coupled plasma optical emission spectrometry (ICP-OES) and C, H, and N content obtained through combustion analysis. The oxygen content was determined from the mass balance, and the calculated composition was

determined assuming unity for the sum of the yttrium and zirconium content, 8 lithium atoms per formula unit, Li_2O and carbonaceous material as the only impurities, and overall neutral charge for the composite phase. As the calcination temperature was increased, the level of the Li_2O impurity decreased, matching the decrease in the intensity of the associated PXRD peak at ~39.3 °2θ (Co Kα). Furthermore, a significant amount of nitrogen was incorporated into the composite as the calcination temperature increased, up to 1.84 mass percent. This could be due to a side reaction wherein a portion of the lithium was carbothermally reduced by the Super P carbon present in the ZrO_2/C composite, and then reacted with the nitrogen atmosphere used for the calcination. This reaction could form LiN_3, which would react with the water and oxygen in the atmosphere, causing the self-combustion reaction observed when the samples were removed from the furnace above room temperature. In addition, a small increase in the amount of incorporated yttrium was observed at higher calcination temperatures.

On the basis of Raman spectra, the nature of the carbon matrix also changes with increasing calcination temperature, becoming more graphitic on the basis of a decreasing ratio in the relative intensity of the D- and G-bands observed in the Raman spectra (Fig. 6.5). The capacity of the materials in the first few cycles rapidly decreases (Fig. 6.6) due to irreversible electrochemical reactions, probably related to cell conditioning such as formation of a solid-electrolyte interphase (SEI). After these cycles, significant capacity remains, with Y-LZO-900 showing a reversible capacity of over 175 mAh/g at C/5. The other samples also show reversible capacity higher than that of the undoped Li_8ZrO_6 sample. Furthermore, all samples can be cycled at rates as high as 5 C, with Y-LZO-900

showing a capacity of over 30 mAh/g. After 100 total cycles, Y-LZO-900 maintains over

100 mAh/g at a cycling rate of C/5, corresponding to almost a full Li^+ per formula unit.

Considering cycles 60–105, the specific capacities decrease with increasing grain size

(Table 6.7, 31–48 nm) as the synthesis temperature is increased. Therefore, the following

trend in specific capacities is seen: Y-LZO-700 ~ Y-LZO-750 > Y-LZO-800 > Y-LZO-

850. All of these samples contain similar amounts of Li_2O as an impurity phase (Table

6.7). However, for the sample heated at the highest temperature (Y-LZO-900), much of

this Li_2O phase is lost, and the estimated average grain size (51 nm) is similar to that of

Y-LZO-850 (48 nm). With less inactive Li_2O, the fraction of active material is greater,

hence the increase in specific capacity per gram of Y-LZO.
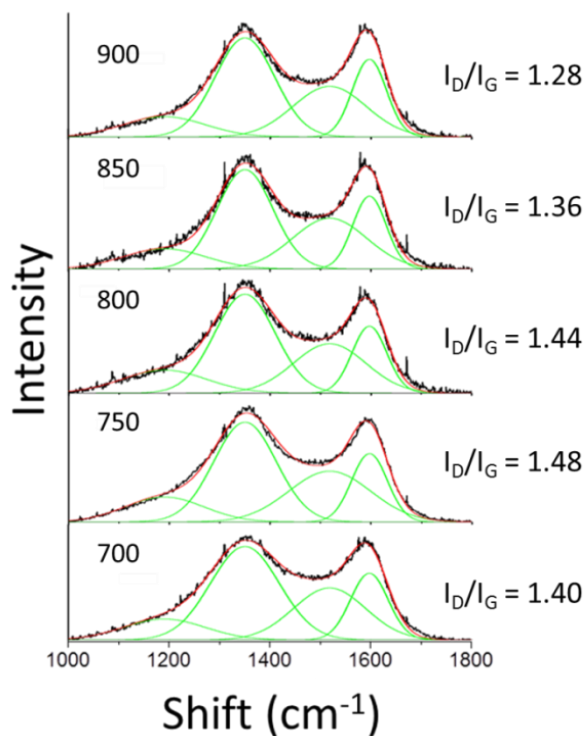
Figure 6.5. Raman data and associated I_D/I_G peak ratios showing a decrease in this ratio with increasing carbonization temperature (shown in ˚C). The Raman peaks were fit using four peaks, consistent with disordered carbon materials containing turbostratically disordered graphene sheets. The peaks at 1350 and 1597 cm^{-1} correspond to the D- and G-bands of graphitic carbon and the peaks at 1190 and 1518 cm^{-1} are associated with sp^3 carbon.
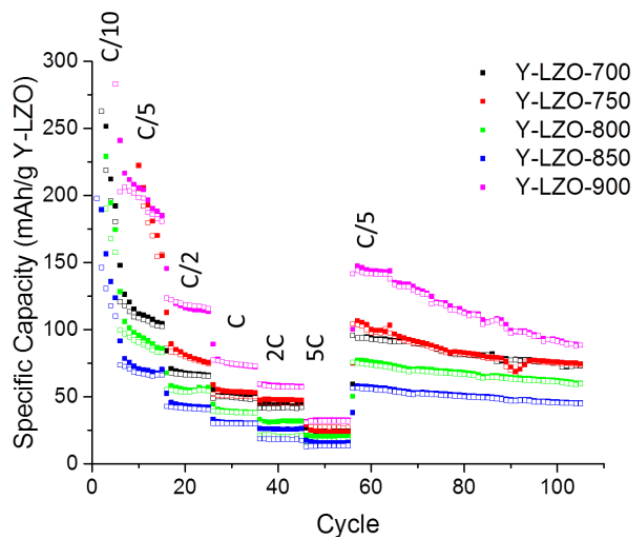
Figure 6.6. The specific capacity of the cell (per gram of Y-LZO) measured over 50 cycles at the indicated C-rates, with the C-rate calculated per gram composite. The corresponding rates per gram of Y-LZO are 0.27 C, 0.53 C, 1.3 C, 2.7 C, 5.3 C, 13 C and 0.53 C, respectively.

The first delithiation step for all of the Y-LZO samples showed the same general behavior as for the undoped samples, namely a rapid increase in the cell potential followed by a nearly asymptotical approach to the upper voltage limit. On the first discharge, a broad shoulder is observed that spans from 3.5 V to below 2.0 V as shown in Fig. 6.7. After the first cycle, the charging profile shows two shoulders, one at approximately 3.3 V and one above 4.0 V, corresponding to removal of the first and second Li^+ out of the material while the discharge profile is unchanged. The calculated delithiation energies for $Li_{96}Zr_{10}Y_2O_{71} \rightarrow Li_{95}Zr_{10}Y_2O_{71} + Li$ and $Li_{95}Zr_{10}Y_2O_{71} \rightarrow Li_{94}Zr_{10}Y_2O_{71} + Li$ are 4.05 and 4.16 eV, respectively, using the HSE06 functional, and 3.49 and 4.11 eV, respectively, with N12-SX. This is consistent with the experimental result: the voltage increases as more Li is removed, but it is different from the trend

143

shown in Table 6.5 for LZO. These features remain constant for all cycles tested indicating that the mechanism for delithiation and relithiation does not change as the material is cycled (cycles 8 and 60 are shown for Y-LZO-900 in Figs. 6.7a and 6.7b, respectively, as representative for all yttrium-doped samples). This behavior, along with the high capacities observed, shows that Li_8ZrO_6 is a promising novel cathode material for further study.
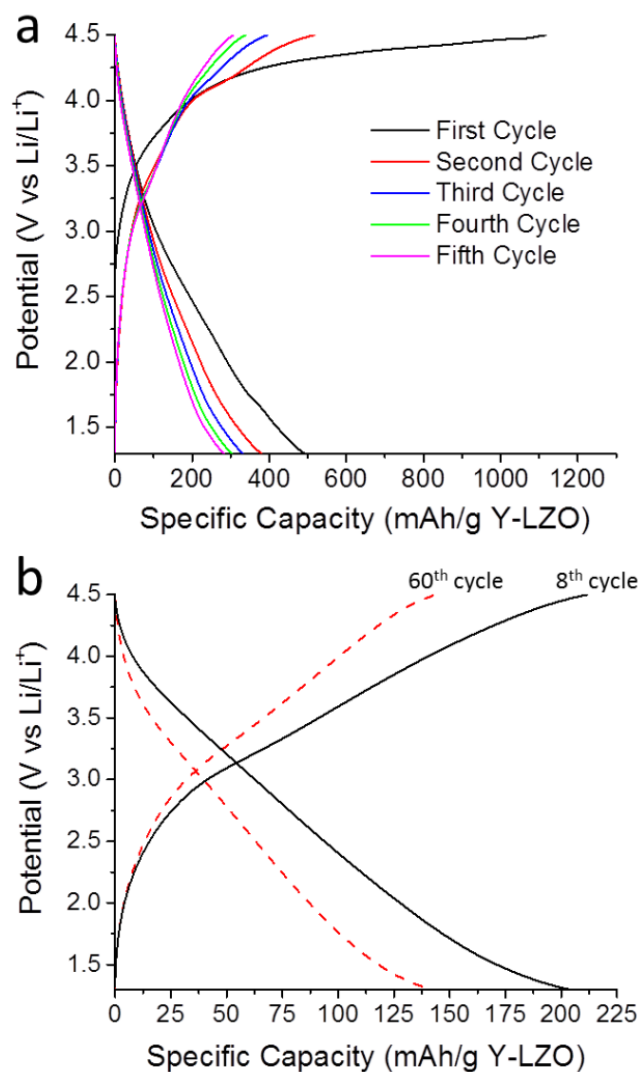
Figure 6.7. (a) Galvanostatic curves of the first five charge and discharge cycles for Y-LZO-900 carried out at C/10 (calculated per gram composite, 0.27 C per gram Y-LZO, see Fig. 6.6). (b) Galvanostatic curves of the 8th and 60th cycle for Y-LZO-900, showing the shoulders relating to the lithiation and delithiation events. Both of these cycles were carried out at C/5 (calculated per gram composite, 0.53 C per gram Y-LZO) and the capacity is shown per gram Y-Li_8ZrO_6.

The quantum mechanical calculations suggest the following explanation for the increase in voltage as more Li are removed from Y-LZO. The delithiation in LZO and Y-

LZO is associated with the oxidation of O^{2-} to O^-. In LZO and Li_2MnO_3, the voltage decreases as more Li ions are deintercalated, which was interpreted as indicating that the oxygen hole polaron is energetically more favorable at high lithium vacancy concentrations.[340] In Y-LZO, the substitution Y^{3+} for Zr^{4+} results in the creation of oxygen vacancies, so there is already a hole polaron at the oxygen vacancy before delithiation. Upon delithiation, there can be a repulsive interaction between the polaron at the void and the oxygen hole polaron, which results in the increase in voltage as more Li atoms are removed.

The density of states calculation with HSE06 shows that polaron hole states appear above the Fermi level for delithiated yttrium-doped LZO; they are located at the one of the oxygen atoms near the Li vacancy (Fig. 6.8). The calculated band gaps for the spin-down electrons of $Li_{95}Zr_{10}Y_2O_{71}$ and $Li_{94}Zr_{10}Y_2O_{71}$ are 1.90 and 1.53 eV, respectively. The band gap of yttrium-doped LZO decreases as more Li are removed, which is different from the case for pure LZO. During the delithiation process, the magnetic moments of the Zr, Li, and Y atoms remain approximately zero, while the magnetic moments of one of the oxygen atoms near the Li vacancy are ~ 0.7 μB. This trend shows that the O atoms, rather than the Zr atoms, are being oxidized during the delithiation process.
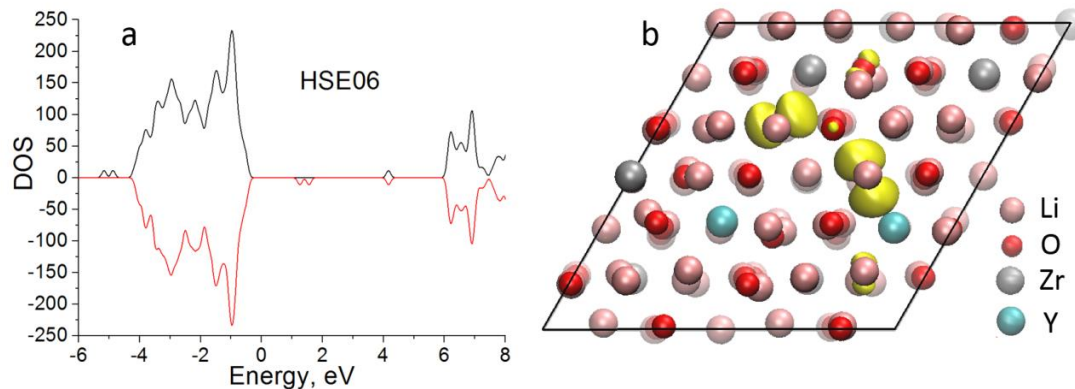
Figure 6.8. (a) The DOS of $Li_{94}Zr_{10}Y_2O_{71}$. The black curves are for the majority spin; by convention, this is the α spin (spin up). The red curves are for the minority spin; by convention, this is the β spin (spin down). (b) The charge density for the bipolaron of $Li_{94}Zr_{10}Y_2O_{71}$.

The partial oxidation of oxygen atoms was experimentally observed by X-ray photoelectron spectroscopy (XPS) of a Li_8ZrO_6-containing cathode after charging of the cell by delithiation. The O1s peak shifts from 530.3 eV in the uncharged (lithiated) electrode to a slightly higher binding energy of 530.6 eV after charging (partial delithiation to ca. $Li_{7.62}ZrO_6$) and then returns to 530.2 eV after discharge (Fig. 6.9). The shift to higher binding energy can be associated with an increase in oxidation state of the oxygen as a result of the delithiation.[355-356] It should be noted that the oxygen peak contains an envelope of oxygen contributions from both Li_8ZrO_6 and oxygen atoms from the PF-derived carbon phase in the composite cathode, so that the actual shift from partially delithiated Li_8ZrO_6 may, in fact, be larger.
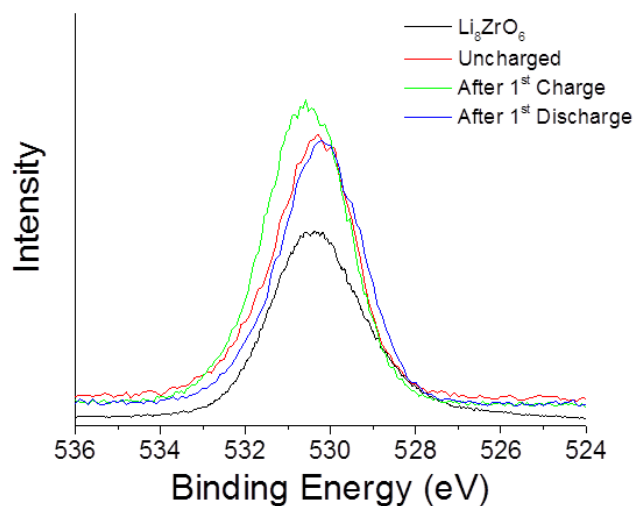
Figure 6.9. XPS spectra showing the position of the O_{1s} peak of a Li_8ZrO_6/C composite cathode before charging, after the first charge, and after the first discharge. A spectrum of neat Li_8ZrO_6 is included to demonstrate that the O_{1s} peak position is not affected by the composite preparation. The O_{1s} peak shifts to higher binding energy after partial delithiation, consistent with an increase in the oxidation state of oxygen.

6.3.5 Stability of Li_xZrO_6

The formation energy of Li_xZrO_6 is defined as

$$\Delta E = \left(\frac{1}{8}\right) E_{Li_xZrO_6} - \left(\frac{x}{8}\right) E_{Li} - \left(\frac{1}{8}\right) E_{ZrO_2} - \left(\frac{1}{4}\right) E_{O_2} \qquad (6.9)$$

The formation energy for the lowest-energy structure for each considered x is shown in Fig. 6.10. The formation energies of all structures in Fig. 6.10 are negative, indicating that Li_xZrO_6 is stable. The formation becomes less exoergic as x decreases in Li_xZrO_6.
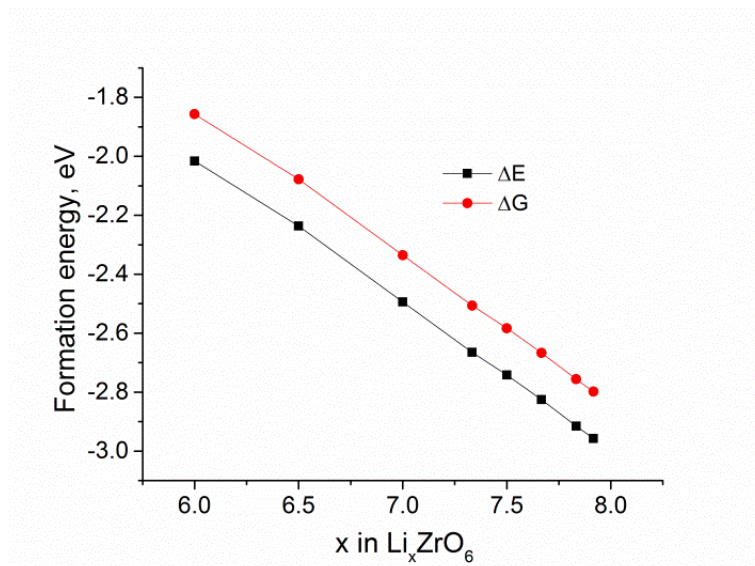
Figure 6.10. The formation energies for Li_xZrO_6 calculated with the HSE06 functional. At each x, multiple configurations are considered, and the formation energy of the lowest-energy configuration is given here.

To test the stability of the delithiated compounds with respect to releasing oxygen, an oxygen atom was extracted from Li_xZrO_6 and the reaction energy for $Li_xZrO_6(s) \rightarrow Li_xZrO_5(s) + 1/2O_2(g)$ was calculated. The PBE, N12, and HSE06 results are given in Table 6.8. The three functionals give the same trends of the reaction energy. When more lithium atoms are extracted from the crystal, it becomes easier to release oxygen in the form of O_2 gas. When $x = 8$, 7, and 6.5, the reaction has a positive energy change, while the reaction has a negative energy change for $x = 6$. Therefore, during the charging and discharging process, Li_6ZrO_6 may be only metastable, and the charging is kinetically controlled. For $x = 5$, the layered structure can release O_2 exothermically, while the oxygen release reaction is endothermic for the distorted structure, which is more stable.

149

Table 6.8. Reaction energy (kcal/mol) for $Li_xZrO_6(s) \rightarrow Li_xZrO_5(s) + 1/2O_2(g)$. calculated using PBE, N12, and HSE06.[a]

	O vacancy in		reaction energy		
x	Li_xZrO_6	Li_xZrO_5	PBE	N12	HSE06
8	Li8	10	153.5	151.0	161
7	Li7_x1	13	67.3	68.8	66.9
6.5			22.3		18.7
6	Li6_x12	10	−16.3	−17.5	-33.2
5	Li5_x157	11	6.8	3.9	6.2
5	Li5_x234	10	−28.5	−22.2	-33.3

[a]The numbers in the vacancy column correspond to specific lithium ions, the locations of which are discussed in the original paper (ref. 340) The lowest-energy configurations were used for calculations. A negative energy corresponds to an exoergic reaction. The oxygen atom that has the smallest Hirshfeld charge in Li_xZrO_6 was removed to form Li_xZrO_5. For $x = 6.5$, three Li atoms are removed from $Li_{16}Zr_2O_{12}$ cell, whereas for integer x, the primitive cell was used.

6.4 Conclusions

Theoretical and experimental studies on lithium-containing materials improve our scientific understanding of LIBs. In this chapter, Kohn-Sham density functional theory and a variety of experiments were used to study lithium-ion battery cathodes verify several predicted properties (band gap energy, structural and oxidation state changes during delithiation/relithiation, delithiation/relithiation potentials) experimentally. I have tested Li_8ZrO_6 as a new cathode material and showed that the Li_8ZrO_6 cathode has a large voltage of 4.0 eV vs Li/Li^+ for the delithiation of the first Li atom. The delithiation of Li_8ZrO_6 in a lithium-ion battery is predicted to follow a nonthermodynamic path through the 4.0 V plateau with the oxygen atoms being oxidized. The structure is maintained with

little volume change when one or two lithium atoms are extracted from Li_8ZrO_6, but the layered structure is greatly distorted when three lithium atoms are extracted. The delithiation product Li_6ZrO_6 is only metastable and may release O_2. Even if delithiation is limited to only two lithium atoms per formula unit, this material would have a theoretical capacity of 220 mAh/g, surpassing those of the current mainstream cathode materials $LiCoO_2$, $LiNiO_2$, $LiFePO_4$, and $LiMn_2O_4$. To achieve this capacity, it is necessary to overcome the low conductivity of Li_8ZrO_6. In electrode materials with similarly low conductivity ($LiFePO_4$, TiO_2), this has been achieved by nanostructuring, aliovalent doping, and forming intimate mixtures with conductive phases.[354] By doping the Li_8ZrO_6 with yttrium to reduce grain size and embedding the active material in a conductive carbon phase, it was indeed possible to achieve an initial specific capacity that nearly matched the theoretical capacity. Both HSE06 and PBE+U calculations show that Li removal creates a small-polaron hole on an oxygen atom near the Li vacancy for both LZO and yttrium-doped LZO. A challenge for future work is to achieve greater utilization of the lithium ion capacity and reduce the capacity fading in Li_8ZrO_6 as an active material for lithium-ion battery cathodes.

Chapter 7: Transition-Metal-Doped M-Li$_8$ZrO$_6$ (M = Mn, Fe, Co, Ni, Cu, Ce) as High-Specific-Capacity Li-Ion Battery Cathode Materials: Synthesis, Electrochemistry, and Quantum Mechanical Characterization

Reproduced with permission from "Transition-Metal-Doped M-Li$_8$ZrO$_6$ (M = Mn, Fe, Co, Ni, Cu, Ce) as High-Specific-Capacity Li-Ion Battery Cathode Materials; Synthesis, Electrochemistry, and Quantum Mechanical Characterizations" by Huang, S.; Wilson, B. E.; Smyrl, W. H.; Stein, A.; and Truhlar, D. G. in *Chemistry of Materials*, DOI: 10.1021/acs.chemmater.5b03554.

Contributions to this chapter were performed by Dr. Shuping Huang (computational calculations).

7.1 Introduction

Lithium-ion batteries (LIBs) are currently in high demand for portable energy storage for applications such as small electronics and transportation.[11-12] Compared to other secondary batteries, LIBs operate at a higher voltage and provide a higher energy-storage density. The performance of LIBs depends on multiple factors, including the properties of the anode, cathode, and electrolyte. While anode materials can reach high specific capacities of over 1000 mAh/g,[357] the practical capacity of traditional cathode materials (LiFePO$_4$, LiCoO$_2$) is limited to around 170 mAh/g,[115, 358-361] requiring a larger volume fraction of a packaged cell to be dedicated to the cathode than the anode for charge

balance within the battery. Therefore, an improvement in the capacity of a cathode material has a larger effect on the volume, and thus the energy density, of a packaged LIB.

Recently, the first use of Li_8ZrO_6 (LZO) as a cathode material in an LIB was reported, forming the basis for Chapter 6.[340] While not all of the lithium ions in the structure would be expected to reversibly intercalate and deintercalate, computational results predict that at least two lithium ions per formula unit can be topotactically exchanged, giving a theoretical capacity of 221 mAh/g. This represents an improvement of more than 10% compared to commercial electrode materials.[362-363] In Chapter 6, I showed that yttrium doping helps to reduce the grain sizes and this, along with the addition of conductive carbon, overcomes the otherwise-too-low electronic conductivity of the material; this, in turn, increases the specific capacity. Since the metal ions in LZO have generally fixed oxidation states, the charge on oxygen is modulated during delithiation and relithiation; this differs from the usual cathode materials that contain redox-active transition metals, but it was predicted by computation and experimentally observed through ex-situ XPS.[340] Therefore, the addition of elements with multiple common oxidation states could help balance the charge within the LZO framework during electrochemical cycling and thereby increase the specific capacity of the material.

A large body of research has demonstrated the benefits of doping cathode materials for lithium-ion batteries.[88, 116-127] In the case of $LiFePO_4$, a commercial cathode material with low intrinsic conductivity, the introduction of Ti^{4+} or Zr^{4+} into the Fe^{2+} sites increases p-type semiconductivity within the cell.[117, 122] When Ni^{2+} is incorporated into

153

the Fe^{3+} sites, the nickel doping increases the P-O bond strength, stabilizing the structure, reducing the Li-ion charge transfer resistance, and improving the capacity and rate performance of the cathode material.[124] Other dopant atoms, such as Mg, Ni, Al, and V have also been studied, generally leading to a decrease in the polarization resistance and an improvement in the capacity, with V^{5+} having the greatest effect.[123]

Other cathode materials have also exhibited benefits from doping. $Li_3V_2(PO_4)_3$ has been doped with Fe,[121] Co,[127] and Cr.[125] For example, in the case of Fe, the doping significantly increases the capacity retention over 80 cycles, with a retention of 71% compared to 58% for the undoped system. This improvement in performance is attributed to increased conductivity and structural stability deriving from the incorporation of the Fe^{3+} ions. Additionally, Fe has been used as a dopant in $LiMn_2O_4$ where an improved capacity was observed and correlated to the changing oxidation state of the doping atom.[116]

In Chapter 6, where I introduce Li_8ZrO_6, an initial discharge capacity of over 200 mAh/g was shown for Y-doped Li_8ZrO_6, with 142 mAh/g maintained over 60 cycles. However, the yttrium does not have a significant effect on the delithiation potential, the primary improvement in specific capacity being attributed to reduced grain size and more intimate contact with carbon. Here I show a general method of introducing multivalent transition metals as dopants into LZO by first incorporating them into ZrO_2/C nanocomposites as precursors. I demonstrate that such doping improves specific capacity and capacity retention for several of these materials. The experimental work is complemented by electronic structure calculations for the doped LZO materials that

154

predict the location of the dopant and the effects of doping on band gaps and delithiation energies.

7.2 Experimental

7.2.1 Materials

Nickel(II) nitrate hexahydrate (>97.0%), manganese(II) nitrate tetrahydrate (>97.0%), cobalt(II) nitrate hexahydrate (ACS grade, >98.0%), cerium(III) nitrate hexahydrate (99%), zirconyl nitrate (99%), lithium benzoate (99%), *N*-methyl-2-pyrrolidone (anhydrous, 99.5%), and Li foil (99.9%) were purchased from Sigma Aldrich; iron(III) nitrate nonahydrate (ACS reagent grade) was purchased from Baker Analytical; copper(II) nitrate trihydrate (analytical grade) was purchased from Mallinckrodt Chemicals; Super P carbon, battery electrolyte (1 M $LiPF_6$ in 1:1:1 ethylene carbonate (EC):dimethlyene carbonate (DMC):diethylene carbonate (DEC) by volume) and polyvinylidine difluoride (PVDF) were purchased from MTI Corporation; Celgard 3501 polypropylene separator was obtained from Celgard; carbon-coated aluminum foil was obtained from ExoPack. Zirconyl nitrate was dried at 110 °C for at least 18 h prior to use, and molar calculations for this compound were done on the anhydrous basis; all other chemicals were used without further purification.

7.2.2 Synthesis of Transition-Metal-Doped Li_8ZrO_2/C Composites

Samples were prepared using a modification of a previously reported synthesis of Y-doped Li_8ZrO_2.[9] First, zirconyl nitrate (1.90 mmol), the selected dopant metal nitrate (0.10 mmol), and Super P carbon (2:1 w:w C:nitrates) were ball-milled in a hardened

zirconia ball-and-cup set (SPEX SamplePrep) for 10 min. The nitrate/carbon composite was calcined under static air by ramping from room temperature to 400 °C at a ramp rate of 2 °C/min with no hold and then cooled naturally back to room temperature. The doped-ZrO_2/C composite samples are identified by "M-ZrO_2" where "M" is the dopant atom used, e.g., "Co-ZrO_2" for the cobalt-doped ZrO_2/C composite. The doped-ZrO_2/C composite was then ball-milled with lithium benzoate (either 8:1, 10:1, or 10.8:1 mol:mol Li:Zr based on residual mass after thermogravimetric analysis, assuming the molecular weight of the oxide is 123.2 g/mol) and pyrolyzed under N_2 (0.5 L/min) with a 1 °C/min ramp rate to 600 °C, followed by holding for 2 h, then 2 °C/min to 800 °C, followed by holding another 2 h. The sample was allowed to cool completely to room temperature before being removed from the inert atmosphere. The final LZO/C composites are identified by the dopant atom used in the synthesis and the Li:Zr molar ratio used, e.g., "Co-LZO-8" for the cobalt-doped Li_8ZrO_6/C composite synthesized with an 8:1 Li:Zr molar ratio. Additionally, an undoped sample was prepared by the same method using 10:1 Li:Zr, replacing the transition metal nitrate with additional zirconyl nitrate as a control sample; this is referred to as LZO-10.

7.2.3 Battery Assembly

Doped Li_8ZrO_2/C composites were ground with a solution of PVDF (10 wt% in NMP) in an agate mortar and pestle for 2–3 minutes, or until a completely homogenous paste was obtained. Additional NMP (~0.1 mL) was ground into the paste until a smooth slurry of the desired consistency was obtained. The slurry was cast onto carbon-coated aluminum foil using a doctor blade to create a thin film that was then dried for 18 h. The

dried films were pressed using a mechanical roller to a final film thickness of approximately 250 μm and cut into 0.8 cm diameter disks with an areal density of 2–4 mg/cm^2. The final composition of the electrodes was 90 wt% doped Li_8ZrO_2/C composite and 10 wt% PVDF binder. The disks were assembled into type-2032 coin cells in a half-cell configuration, using Li foil as the counter electrode, a Celgard 3501 membrane as the separator, and 1 M $LiPF_6$ in EC-DMC-DEC as the electrolyte. A wave spring was used behind the current collectors to maintain pressure within the cell after assembly. All film preparation was performed in a dry room maintained below 100 ppm H_2O when occupied and below 20 ppm otherwise. All cell assembly was performed in a He-filled glove box.

7.2.4 Electrochemical Measurements

Following the usual convention for reporting battery charging and discharging rates, I define 1C as a rate of one Faraday constant per mol of Li_8ZrO_6 per hour; this yields 1C equal to 110.5 mA/g. All galvanostatic cycling was performed between 1.3 and 4.5 V vs. Li/Li$^+$ using an Arbin BT2000 electrochemical workstation. Additional cycles were performed beyond what is shown in this chapter and can be found in the original paper from which this chapter is based.[364]

7.2.5 Product Characterization

Powder X-ray diffraction (PXRD) patterns were taken on a PANalytical X'Pert PRO diffractometer using a Co anode (λ = 1.789 Å) at 45 kV and 40 mA and an X'Celerator detector. The Scherrer equation[365] was used to estimate grain sizes based on peak broadening. Thermogravimetric analyses (TGA) were performed using a Netzsch STA 409 PC Luxx instrument to determine the residual mass of the ZrO_2/C composites. The

analyses were performed under dried air at a 10 °C/min ramp to a maximum temperature of 750 °C. The carbon content of the final products was determined through combustion analysis by Atlantic Microlab (Norcross, GA). Metal contents were determined through inductively coupled plasma mass spectroscopy (ICP-MS) after digestion in 1:1:1 (by volume, concentrated) HF:HCl:HNO$_3$ for 5 days in a Teflon-lined hydrothermal bomb at 150 °C.

7.2.6 Computational Methods

Computational work was performed by Dr. Shuping Huang, the details of which can be found in the original paper from which this chapter is based.[364]

7.3 Results and Discussion

7.3.1 Transition-Metal-Doped ZrO$_2$/C Composite Precursors

Because the target material, Li$_8$ZrO$_6$, has very low electrical and ionic conductivity, it is essential to achieve very small grain sizes when Li$_8$ZrO$_6$ is used as an electrode material for LIBs. This can be accomplished by employing ZrO$_2$ nanoparticles as precursors. One approach for obtaining ZrO$_2$ with small grain size involves synthesis within a carbon matrix combined with transition metal dopants.[340, 366-367] In ZrO$_2$, dopant atoms typically substitute for Zr up to a certain loading,[368-370] although interstitial sites may also be occupied in some cases with higher loadings of dopant.[366, 368] The powder X-ray diffraction (PXRD) patterns of the doped ZrO$_2$/C composite materials after calcination are shown in Figure 7.1. All samples contained primarily the tetragonal ZrO$_2$ phase with a small amount of monoclinic ZrO$_2$. The broad peak at approximately 29 °2θ

originates from the carbon present in the composites. Using the Scherrer equation and the primary peak of the tetragonal phase at 35.5 °2θ, grain sizes were estimated to be 8–10 nm for all samples.
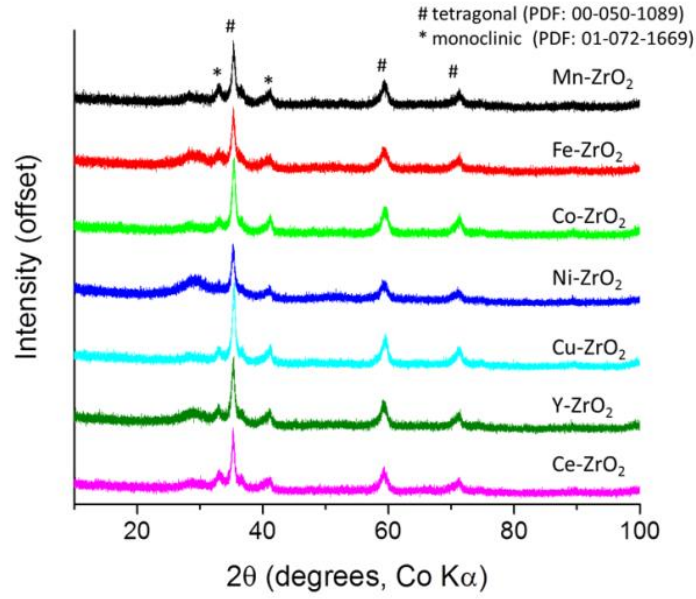
Figure 7.1. PXRD patterns of transition-metal-doped ZrO_2/C composite materials. The peaks corresponding to the tetragonal and monoclinic ZrO_2 phases are marked. For comparison, the trace for Y-ZrO_2/C is included; this material was used as the precursor for Y-LZO as described in Chapter 6.

In these composites, Super P carbon black was used as the confining matrix to prevent grain growth. The carbon content within the doped ZrO_2/C composite materials determined by thermogravimetric analysis varied widely in the materials containing different dopants (Figure 7.2), even though the initial carbon content in the synthesis was similar. Assuming that the difference between the original sample mass and the residual mass corresponds to the carbon content, the content ranged from 37.8 % for Cu-ZrO_2 to 78.7% for Ni-ZrO_2, compared to approximately 55% for yttria-doped ZrO_2 samples

presented in Chapter 6. The value for Ni-ZrO$_2$ is close to the expected carbon content if no carbon is lost during the synthesis, and the lower values indicate partial combustion of the carbon phase during heating of the composites containing the other transition metal ions, probably related to oxidation from the nitrate ions.
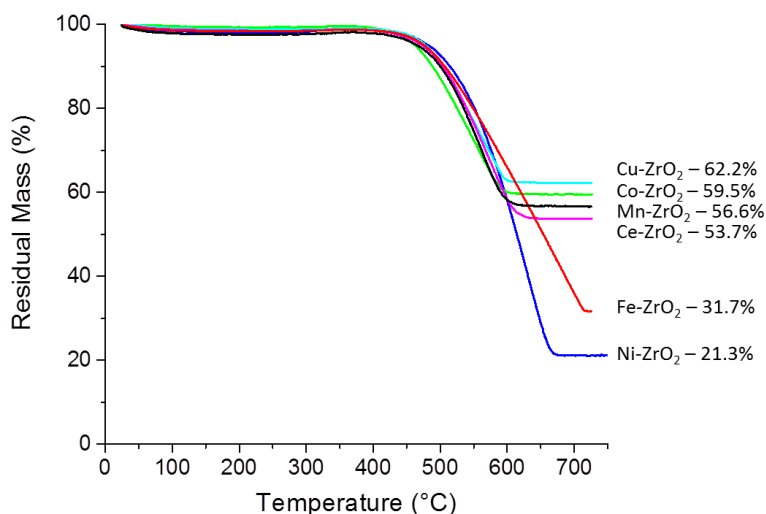
Figure 7.2. TGA curves of the transition-metal-doped ZrO$_2$/C composite materials combusted under dried air. Residual masses are listed for each sample.

7.3.2 Transition-Metal-Doped Li$_8$ZrO$_6$/C Composites (10.8:1 Li:Zr)

After reaction with a large excess of lithium benzoate, PXRD patterns of the samples all show the primary phase to be that of Li$_8$ZrO$_6$ (Figure 7.3), a layered structure suitable for lithium removal and reinsertion, except for Mn-LZO which only shows small peaks corresponding to the Li$_8$ZrO$_6$ phase with the primary peaks relating to Li$_2$O. The mole fraction of dopant relative to (dopant + Zr) in the final products (Table 7.1) is between 0.037 and 0.044, i.e., a little lower than the mole fraction in the synthesis mixture for the

M-ZrO$_2$ precursor (0.05). The final carbon content in these samples is lower than that in previously reported yttria-doped Li$_8$ZrO$_6$ (Y-LZO), except for Ni-LZO-10.8 due to its high initial content of carbon in the ZrO$_2$/C precursor composite (Table 7.1). Note that the carbon originates from both Super P carbon black and carbonization of lithium benzoate. In addition, Li$_2$O is observed as an impurity phase in the PXRD patterns, which was present due to the excess lithium precursor needed to minimize the formation of other lithium zirconate phases, such as Li$_6$Zr$_2$O$_7$ or Li$_2$ZrO$_3$. When the Li:Zr precursor ratio is reduced, as discussed later, the intensity of the Li$_2$O peaks is reduced, but the other lithium zirconate phases begin to appear. No visible reflections of the ZrO$_2$ precursor remain, indicating that all of the nanocrystalline ZrO$_2$ phase has reacted. These results demonstrate that the method of converting doped ZrO$_2$/C composites to Li$_8$ZrO$_6$ can be applied to a wide range of potential dopants.
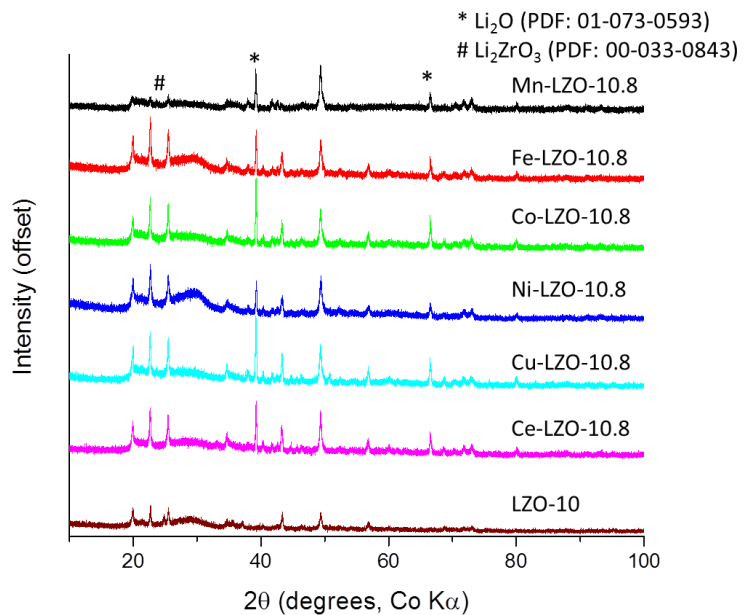
Figure 7.3. PXRD patterns of the transition-metal-doped Li_8ZrO_6/C composite materials made with a 10.8:1 Li:Zr precursor ratio and an undoped sample made with 10:1 Li:Zr precursor ratio with impurity peaks marked.

Table 7.1. Structural and compositional data for undoped and transition-metal-doped Li_8ZrO_6/carbon nanocomposites.

sample	grain size (nm)	carbon (mass%)	mole fraction dopant[a]	c (Å)	a,b (Å)
LZO-10	54.7	56.1	n/a	15.47	5.493
Y-LZO[b]	51.0	55.3	0.038	15.47	5.492
Mn-LZO-10.8	c	34.9	d	15.48	5.503
Fe-LZO-8	35.8	66.5	0.040	15.51[d]	5.497[e]
Fe-LZO-10	52.8	62.6	0.044	15.46	5.488
Fe-LZO-10.8	35.2	50.0	d	15.47	5.494
Co-LZO-8	66.8	40.4	0.037	15.47	5.483
Co-LZO-10	46.8	36.5	0.039	15.48	5.488
Co-LZO-10.8	42.3	34.5	d	15.46	5.493
Ni-LZO-10.8	39.9	57.3	d	15.44	5.498
Cu-LZO-8	61.4	38.6	0.038	15.48	5.488
Cu-LZO-10	49.1	37.3	0.039	15.48	5.483
Cu-LZO-10.8	43.8	34.9	d	15.46	5.497
Ce-LZO-10.8	45.2	38.9	d	15.46	5.493

[a] mol M/(mol M + mol Zr), where M refers to the transitional metal dopant

[b] From reference 340

[c] Grain size could not be determined due to low intensity of peaks.

[d] Elemental analysis was only performed for samples used for extended electrochemical testing.

[e] These values are less certain because of the broadness of the Li_2O reference peak position used as an internal standard.

Average grain sizes of the doped Li_8ZrO_6 phases were determined by applying the Scherrer equation to the [101] peak at 26.6 °2θ (except for Mn-LZO due to the lack of the strong peaks required for an accurate measurement). Grain sizes were similar for the doped samples, ranging in average from 35 nm for Fe-LZO to 45 nm for Ce-LZO (Table 7.1) prepared with a Li:Zr ratio of 10.8. These grain sizes are smaller than those in the previously reported yttria-doped Li_8ZrO_6 sample prepared under comparable conditions

at 900 °C, which had an average grain size of 51 nm.[340] With a lower Li:Zr ratio of 8, grain sizes increased for the Co-LZO and Cu-LZO samples.

Table 7.2 lists the radii of the cations we studied computationally; these radii are taken from the work of Shannon et al.[371-372] The radii of four-coordinate Ni^{2+}, Co^{2+} and Cu^{2+} are close to the radius of four-coordinate Li^+. For the six-coordinate metal ions, they are close to the radii of both six-coordinate Li^+ and Zr^{4+}. However, the radius of six-coordinate Ce^{3+} is much larger than either the radius of Li^+ or that of six-coordinate Zr^{4+}. The radii of four-coordinate or six-coordinate Fe^{3+} are 0.1 Å smaller than those of four-coordinate or six-coordinate Li^+, while the radii of four-coordinate or six-coordinate Mn^{2+} are 0.07 Å larger than those of four-coordinate or six-coordinate Li^+. In principle, doping at the Li ion site and at the Zr ion site are both possible. Both of these sites were considered in the calculations, and various configurations of dopants and vacancies and various spin states were examined to find the lowest-energy structure for each composition.

Table 7.2. Ionic radii (Å) of elements present in the M-LZO composites. The labels IV and VI represent fourfold and sixfold coordination, respectively. Only the radii for high-spin Mn^{2+}, Ni^{2+}, Co^{2+}, and Fe^{3+} are listed here.

Li^+	Zr^{4+}	Mn^{2+}	Ni^{2+}	Co^{2+}	Cu^{2+}	Ce^{3+}	Fe^{3+}
0.59(IV)	0.59(IV)	0.66(IV)	0.55(IV)	0.58(IV)	0.57(IV)		0.49(IV)
0.76(VI)	0.72(VI)	0.83(VI)	0.60(VI)	0.75(VI)	0.73(VI)	1.01(VI)	0.65(VI)

For M^{3+} doping at Zr ion sites, one oxygen vacancy was created to balance the charge, yielding $Li_{96}Zr_{10}M_2O_{71}$. Similarly to the previously studied Y^{3+} doping,[340] when

the two Fe^{3+} or Ce^{3+} ions are substituted for Zr^{4+} ions, they prefer to be in the same layer and close to each other, and the O vacancy prefers M coordination rather than Zr coordination.

For doping at Li ion sites, recall that LZO has two kinds of Li ion sites (Figure 7.4); one is a tetrahedral site, and the other is an octahedral site. From Chapter 6, we know that a vacancy at a tetrahedral site is more favorable than one at an octahedral site. For M^{2+} or M^{3+} doping at Li ion sites, we removed respectively one or two Li ions in tetrahedral positions for charge compensation; this forms $(M_{Li})^{+}$-$(V_{Li})^{-}$ and $(M_{Li})^{2+}$-$2(V_{Li})^{-}$ substitution–vacancy complexes with compositions $Li_{94}MZr_{12}O_{72}$ and $Li_{93}MZr_{12}O_{72}$. Then the PBE+U calculations predict that the substitution of M at the octahedral sites is more favorable than at the tetrahedral sites for Fe^{3+}, Mn^{2+}, Ni^{2+}, Cu^{2+}, and Co^{2+}. This is especially significant because doping at octahedral sites will not block the Li-ion diffusion between the tetrahedral layers. In addition, the Li vacancy at different positions was also considered; the structure with the Li vacancy in the tetrahedral layer close to M has the lowest energy. The most favorable spin state of the doping Fe^{3+}, Mn^{2+}, Ni^{2+}, and Co^{2+} was found to be the high-spin state.
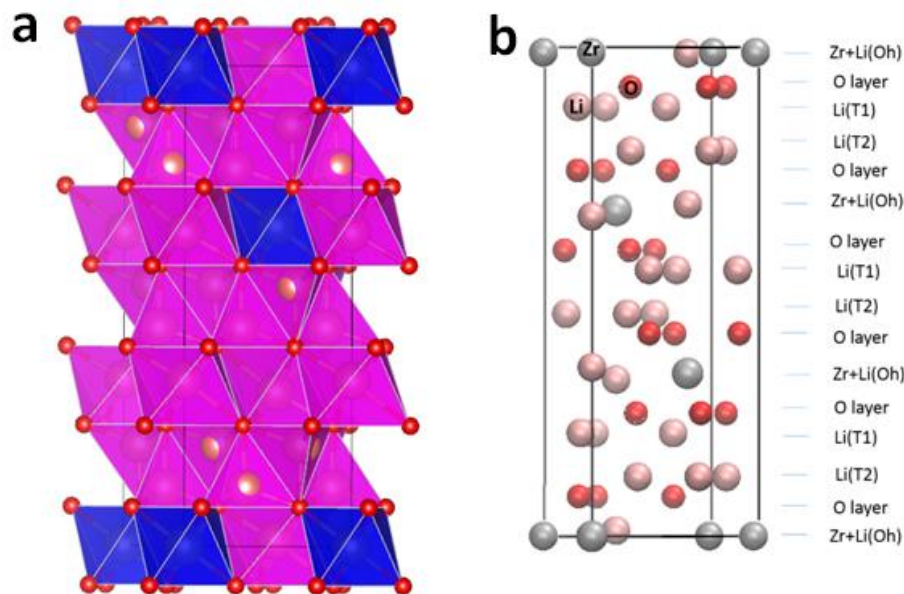
Figure 7.4. Conventional unit cell of LZO ($Li_{24}Zr_3O_{18}$). (a) Polyhedral representation with Zr-centered polyhedra shown in blue and the Li centered polyhedra in purple. (b) Atoms are shown as spheres with the layers labeled. The zirconium ions occupy octahedral sites in the oxygen hcp sublattice, and the lithium ions occupy tetrahedral sites (labeled as T1 and T2) and octahedral sites (labeled as Oh).

Table 7.3 lists the computationally predicted volumes, lattice constants c, delithiation energies (also called deintercalation energies), and energy gaps of LZO and doped LZO materials. The volume and lattice constant c increase significantly after Ce^{3+} doping at a Zr ion site, but less so after doping at a Li ion site. These values decrease slightly or are nearly the same as for undoped LZO after Fe^{3+}, Co^{2+} Mn^{2+}, Ni^{2+}, or Cu^{2+} doping. For all five of these dopants, the delithiation energy for dopants at the Zr ion site is about 0.5~1.1 eV lower than the delithiation energy for dopants at Li ion site, which means that the doping at the Li ion site is thermodynamically more favorable. All the cases of doping at a Zr ion site lead to a smaller delithiation energy compared to pure

166

LZO. For Ce^{3+} doped materials, the delithiation energy with substitution at a Zr ion site is smaller than with substitution at a Li ion site. PBE+U calculations show that doping with Ni^{2+} or Cu^{2+} at a Li ion site increases the voltage. In all cases examined, band gaps are decreased by doping.

Table 7.3. Calculations of the volume, lattice constant c, delithiation energy, and energy gap of LZO and doped LZO. Results are shown only for the lowest-energy lithiated and delithiated configurations. PBE+U calculations are shown for all cases, and HSE06 results are given in parentheses for selected cases. The majority spin and minority spin are denoted α and β, respectively.

	volume (Å^3)	c (Å)	Delithiation* energy (eV)	band gap (eV)	
				α	β
$Li_{96}Zr_{12}O_{72}$	1600.8	15.46	3.28	5.1	5.1
	(1583.7)	(15.41)	(4.09)	(6.8)	(6.8)
$Li_{96}CuZr_{11}O_{71}$	1599.3	15.45	2.43	3.2	2.4
	(1576.8)	(15.37)	(3.13)	(4.3)	(3.7)
$Li_{94}CuZr_{12}O_{72}$	1598.4	15.45	3.30	5.0	2.2
	(1576.4)	(15.38)	(3.74)	(6.6)	(3.3)
$Li_{96}Fe_2Zr_{10}O_{71}$	1591.7	15.41	2.63	3.1	2.8
	(1569.3)	(15.33)	(2.98)	(4.3)	(4.2)
$Li_{93}FeZr_{12}O_{72}$	1596.7	15.46	3.14	5.0	2.7
	(1573.6)	(15.38)	(4.15)	(6.6)	(3.9)
$Li_{96}CoZr_{11}O_{71}$	1601.0	15.46	2.10	2.8	2.9
	(1576.8)	(15.36)	(1.95)	(3.7)	(3.3)
$Li_{94}CoZr_{12}O_{72}$	1598.8	15.46	3.13	5.0	4.1
	(1576.0)	(15.38)	(3.08)	(6.4)	(4.6)
$Li_{96}NiZr_{11}O_{71}$	1599.8	15.45	2.40	3.0	3.1
	(1576.9)	(15.37)	(2.46)	(4.0)	(3.9)
$Li_{94}NiZr_{12}O_{72}$	1597.3	15.46	3.34	5.0	4.0
	(1574.2)	(15.38)		(6.6)	(5.3)
$Li_{96}MnZr_{11}O_{71}$	1603.7	15.47	1.02	1.7	3.4
	(1579.3)	(15.38)		(2.6)	(4.8)
$Li_{94}MnZr_{12}O_{72}$	1602.4	15.46	2.25	4.0	3.5
$Li_{96}Ce_2Zr_{10}O_{71}$	1631.0	15.56	0.33		
	(1607.4)	(15.52)	(0.42)	(1.1)	(4.6)
$Li_{93}CeZr_{12}O_{72}$	1616.2	15.47	0.36	0.3	4.6
	(1595.2)	(15.39)	(1.17)	(3.1)	(6.3)

*The delithiation energy is associated with removing only 1 Li atom from the lattice.

In order to further compare the relative energies of different doping sites, the reaction energies were calculated for

$$Li_{96}Zr_{12}O_{72}(solid) + M_2O_3(solid) \rightarrow Li_{96}Zr_{10}M_2O_{71}(solid) + 2ZrO_2(solid) \qquad (7.1)$$

$$Li_{96}Zr_{12}O_{72}(solid) + 1/2M_2O_3(solid) \rightarrow Li_{93}MZr_{12}O_{72}(solid) + 3/2Li_2O(solid) \qquad (7.2)$$

$$Li_{96}Zr_{12}O_{72}(solid) + MO(solid) \rightarrow Li_{96}Zr_{11}MO_{71}(solid) + ZrO_2(solid) \qquad (7.3)$$

$$Li_{96}Zr_{12}O_{72}(solid) + MO(solid) \rightarrow Li_{94}MZr_{12}O_{72}(solid) + Li_2O(solid) \qquad (7.4)$$

$$Li_{96}Zr_{10}M_2O_{71}(solid) + 2ZrO_2(solid) \rightarrow Li_{90}M_2Zr_{12}O_{72}(solid) + 3Li_2O(solid) \qquad (7.5)$$
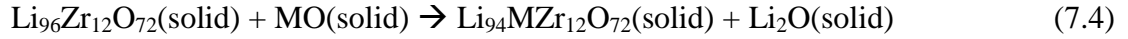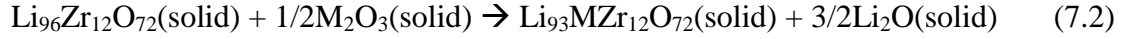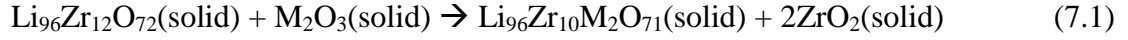
The results are in Table 7.4. The reaction energy of reaction 7.5 for Fe^{3+} is -1.89 (-1.76) eV by PBE+U (HSE06) calculations. The PBE+U or HSE06 calculations predict that the reaction energies of reaction 7.3 for Cu^{2+}, Ni^{2+}, Mn^{2+}, and Co^{2+} are more than 2.0 eV higher than those for reaction 7.4. These results indicate that doping at Li ion sites is thermodynamically more favorable than at Zr ion sites for Mn^{2+}, Fe^{3+}, Co^{2+}, Ni^{2+}, and Cu^{2+} dopants, in agreement with the conclusions drawn above from the delithiation energies. For Ce^{3+} doping, both reaction 7.1 and reaction 7.2 are endothermic, and the reaction energy of reaction 7.5 is -1.26 (-2.55) eV by PBE+U (HSE06) calculations, suggesting that Ce^{3+} doping is more favorable at Li ion sites.

Table 7.4. Calculated reaction energies (in eV per formula unit of $Li_{96}Zr_{12}O_{72}$) for reactions 1–5. PBE+U calculations are shown without parentheses, and HSE06 results are given in parentheses for selected cases.

	(1)	(2)	(3)	(4)	(5)
Fe^{3+}	(0.06)	(-0.64)			-1.89 (-1.76)
Ce^{3+}	3.86 (4.69)	1.67 (1.26)			-1.26 (-2.55)
Mn^{2+}			2.96 (2.46)	0.53	
Co^{2+}			2.56 (2.75)	0.36 (0.23)	
Ni^{2+}			2.92 (2.86)	0.49 (0.20)	
Cu^{2+}			2.83 (2.72)	0.76 (0.63)	

The experimental PXRD patterns of the undoped and doped materials show that doping at the levels used here has relatively little effect on the observed unit cell dimensions (determined using multiple peak positions and their respective Miller indexes, with Li_2O used as an internal standard), as shown in Table 7.1. This is consistent with the computed dimensions shown in Table 7.3. On the basis of the experimental data, it is not possible to distinguish between substitution of the transition metal dopants at either Zr or Li ion sites. Doping with Ce^{3+} had little effect on the *c*-dimension of Li_8ZrO_6 even though Ce^{3+} is larger than Zr^{4+}. This suggests that the Ce^{3+} is located in Li^+ sites in my experiments since the density functional results predict that a large increase should be observed when Zr^{4+} atoms are replaced. In the case of manganese-doped ZrO_2, the unit cell parameters were observed to have decreased,[373] which is different from what was observed for Mn-Li_8ZrO_6-10.8. However, in Fe-doped ZrO_2 the (111) interplanar spacing was observed to increase when the Fe^{3+} was in substitutional sites.[370] Computation predicts that the lattice parameter would decrease for Fe^{3+} substitution in the Zr^{4+} position, but remain similar for substitution at a Li^+ octahedral position (within the layer

170

containing the Zr^{4+}, Figure 7.4), indicating that the Fe^{3+} is more likely to occupy that position.

7.3.3 Electrochemical Testing of Transition-Metal-Doped Composites

The transition-metal-doped Li_8ZrO_6/C composite samples were tested in coin cells to measure their specific capacities and determine their electrochemical performance in delithiation/lithiation cycles (Figure 7.5a). Among the samples prepared with a Li:Zr ratio of 10.8, Cu-LZO exhibited the highest specific capacity, with an initial discharge capacity of 172 mAh/g. During the sixth cycle it showed a specific discharge capacity of 156 mAh/g, a significant improvement over the best sample in our previous publication synthesized at 800 ˚C (Y-LZO-800) which had a capacity of 100 mAh/g after the sixth cycle.[340] All other samples, except for Ce-LZO, also have higher specific capacities at the sixth cycle than Y-LZO-800, with Mn-LZO, Fe-LZO, Co-LZO, and Ni-LZO having specific capacities of 136, 120, 118, and 139 mAh/g, respectively, after correcting for the carbon content in the final composite (Table 7.1). After cycling each cell at C/5 (current based on the composite mass in the electrode) for 25 cycles, all samples maintain specific capacities between 85 and 118 mAh/g LZO, similar to those made with yttria doping. For comparison, undoped LZO-10 has a lower specific capacity than any of the doped materials. It is noteworthy that in these materials, the highest specific capacity (Cu-LZO) does not correlate with the smallest grain size (Fe-LZO) nor with the highest carbon content (Ni-LZO) in these samples. This implies that the dopant atoms themselves play the major role in enhancing the specific capacities.
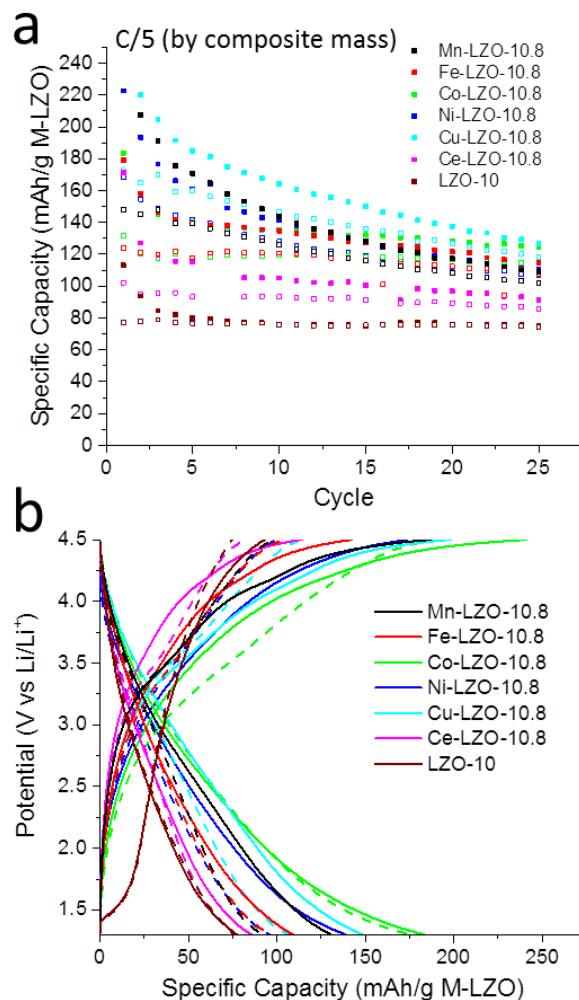
Figure 7.5. (a) Galvanostatic cycling capacities of doped Li_8ZrO_6 at a rate of C/5 (based on composite mass; charging is indicated by filled and discharging by open squares) and (b) cycles 2 (solid) and 25 (dashed) for each sample.

Similar to the observations in Chapter 6, there are no changes in the positions of the characteristic PXRD peaks during the first two charging steps of a Co-LZO sample, as measured by *ex-situ* analysis.[364] Because of the high levels of carbon in the final composites, a background cell was used to verify that the observed specific capacities of the M-LZO/C composites can be ascribed to M-LZO rather than to the graphitic carbon

components. Previously, PF_6^- has been shown to reversibly intercalate into graphitic carbon.[374-375] In the case of a mixture of graphite and a conductive additive, specific capacities as high as 147 mAh/g have been reported.[375] A background cell composed of a 4:6:1 mixture of silica:SuperP:PVDF (by mass) was cycled at C/5 based on the combined silica and carbon mass for five cycles. Results show that the specific capacity for this cell was negligible, with all cycles yielding a specific capacity of less than 5 mAh/g of silica.[364] Therefore, most of the specific capacity observed in the M-LZO/C composites can be attributed to the reversible delithation/lithiation reactions with M-LZO, not to the carbon component.

Capacity retention is an important variable in applications involving rechargeable batteries. One of the notable features in all of the Y-LZO samples previously reported is the significant negative slope of the capacity values with cycle number. Cu-LZO has a similar behavior, with a 32% capacity loss from the 1st to the 25th cycle. On the other hand, both Fe-LZO and Co-LZO have similar capacities at the 25th cycle to Cu-LZO, but have a much lower loss between the 1st and 25th cycles, corresponding to 13.5% and 12.5%, respectively. A notable feature visible in the individual charge curves (Figure 7.5b) is the emergence of an inflection point between 3.0 and 3.5 V. This inflection point corresponds to the expected delithiation potential for Fe^{3+}- and Co^{2+}-doped samples (Table 7.3), and it becomes gradually more pronounced with increasing cycle number, indicating that conditioning cycles are needed to obtain the full performance of the material. The charge and discharge curves of LZO-10 do not show such an inflection

point between 3 and 4 V due to the higher delithiation potential of the undoped material.[340]

7.3.4 Effects of Li:Zr Ratios in the Precursor

Samples of transition-metal-doped Li_8ZrO_6 with one of the following three dopant atoms were selected for further study: Fe and Co because of the improved capacity retention and Cu because of the higher specific capacity. Additionally, different ratios of Li to Zr were used to explore the effect of the different impurities. Specifically, either a stoichiometric amount of Li (8:1 Li:Zr) or a moderate excess (10:1 Li:Zr) were used. On the basis of the PXRD patterns (Figure 7.6), the stoichiometric precursor ratio introduces a smaller amount of the Li_2O impurity (lower relative peak intensity) compared to the 10.8:1 precursor ratio while a different lithium zirconate phase, $Li_6Zr_2O_7$, emerges (Table 7.5). When the Li:Zr precursor ratio is increased from 8:1 to 10:1, some of the $Li_6Zr_2O_7$ phase remains, but the impurity content shifts to a higher Li_2O concentration. Additionally, changing the Li:Zr precursor ratio affects the grain sizes (Table 7.1). As the ratio of Li:Zr is reduced, the grain size, in general, increases, with the exception of Fe-LZO-10.8, which has the smallest grain size of any of the samples prepared. Further, increasing the Li:Zr precursor ratio decreases the carbon content, indicating that the lithium benzoate addition leads to a net reduction in the final carbon content.
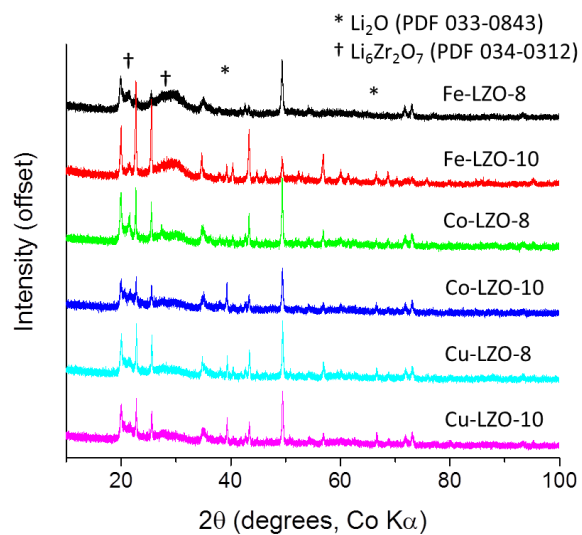
Figure 7.6. PXRD patterns of the transition-metal-doped Li_8ZrO_6/C composite materials made with either a 10:1 or 8:1 Li:Zr precursor ratio with Li_2O and $Li_6Zr_2O_6$ impurities marked.

Table 7.5. Relative mass percent of crystalline components in the M-LZO/C composites.[a]

Sample	Mass%		
	Li_8ZrO_6	Li_2O	$Li_6Zr_2O_7$
Mn-LZO-10.8	40	41	19
Fe-LZO-8	64	0	36
Fe-LZO-10	95	2	3
Fe-LZO-10.8	82	11	7
Co-LZO-8	85	1	14
Co-LZO-10	75	10	15
Co-LZO-10.8	75	19	6
Ni-LZO-10.8	80	10	10
Cu-LZO-8	87	4	9
Cu-LZO-10	79	8	13
Cu-LZO-10.8	77	17	6
Ce-LZO-10.8	80	14	6

[a] Mass percentages were calculated by a Rietveld refinement of the PXRD patterns in Figures 7.4 and 7.6. All refinement was done using X'Pert Highscore Plus software with the built-in refinement tools to a goodness-of-fit below 5.5 for all samples. Crystallography files were obtained from literature sources; Li_2O (Ref. 376), $Li_6Zr_2O_7$ (Ref. 377), and Li_8ZrO_6 (Ref. 340). The crystallographic information files were downloaded from the Crystallography Open Database Search (www.crystallography.net).

These transition-metal-doped samples were also galvanostatically cycled in the same manner as the previous composite materials (Figure 7.7). Most of the samples have comparable specific capacities and capacity retention to the 10.8:1 Li:Zr composite samples with two main exceptions. Co-LZO-8 has a much smaller capacity than all other samples and Fe-LZO-8 has a significantly higher specific capacity than any other Li_8ZrO_6 sample yet reported,[340] with a discharge capacity exceeding 2 Li per formula unit in early cycles and over 175 mAh/g at C/5 after 140 cycles. A large capacity is maintained at all rates tested, with 80 mAh/g specific discharge capacity at 5C. Fe-LZO-10 also shows a high capacity of 135 mAh/g after 140 cycles. The improved capacity of the Fe-LZO-8

over Fe-LZO-10 is probably due to the significantly smaller grain sizes, suggesting that further capacity improvements may be possible if even smaller grain sizes can be achieved.
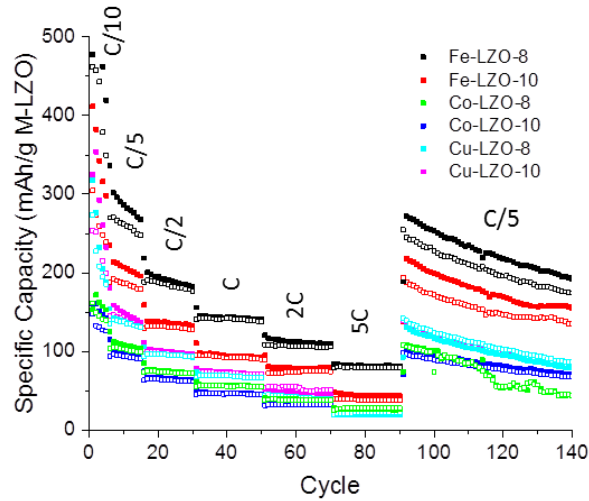
Figure 7.7. Galvanostatic cycling capacity of transition-metal-doped Li_8ZrO_6/C composites made with either 8:1 or 10:1 Li:Zr cycled at varied rates. The indicated rates are based on composite mass.

To help understand the electrochemical behavior, band calculations were carried out. The removal of Li also removes electrons from the valence band, and therefore the nature of the electronic states at and near the valence-band maximum (VBM) is important. Figure 7.8 shows the calculated total density of states (TDOS) and partial density of states (PDOS) for both $Li_{94}CoZr_{12}O_{72}$ and $Li_{93}CoZr_{12}O_{72}$. Co^{2+} doping decreases the band gap, which is further decreased during the delithiation process. At the top of the valence band, several new states appear that were not present in LZO; these new states originate mainly from the d subshell of Co with a small mixing of oxygen p states. This indicates

that charge transfer during delithiation involves a partial oxidation state change for Co, from Co^{2+} to Co^{3+}. After the delithiation, the hole is a polaron mainly localized on Co^{3+}.
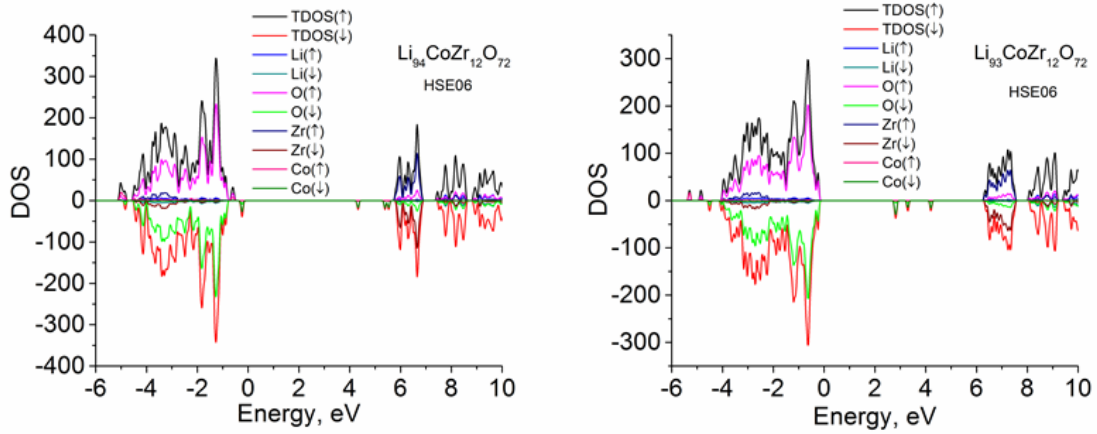
Figure 7.8. The total DOS (TDOS) and partial DOS (PDOS) of $Li_{94}CoZr_{12}O_{72}$ and $Li_{93}CoZr_{12}O_{72}$ by HSE06 calculations. The up arrows are for the majority spin; by convention, this is the α spin (spin up). The down arrows are for the minority spin; by convention, this is the β spin (spin down).

The charge redistribution of doped-LZO in the charging process can be ascertained from the integrated spin density at the spin-polarized atoms. When one Li is removed from the Mn^{2+}-doped supercell, the spin density of Mn, within a given cutoff radius, decreases from 4.50 to 3.85 μ_B, suggesting that Mn^{2+} is oxidized to Mn^{3+}. For Cu^{2+} doping, the spin density of Cu (0.69 μ_B) does not change before and after delithiation, and the oxygen atoms around Cu become oxidized in the delithiation process. For the Ce^{3+}-doped material, Ce^{3+} is oxidized to Ce^{4+} during delithiation. As the delithiation proceeds, all Ce^{3+} is oxidized to Ce^{4+}; then oxygen near the Li vacancy is oxidized. For Co^{2+} doping, during the delithiation the spin density of Co increases from 2.76 to 3.12 μ_B,

178

and the spin densities of the oxygen around the Co are about 0.11–0.23 μ_B. Both Co and the oxygen around it are oxidized in the delithiation.

For Fe^{3+} doping at a Li ion site, the magnetic moment of Fe is nearly unchanged, whereas for the doping at a Zr ion site, the energy is lower for the delithiated material in which Fe^{3+} is oxidized (the spin density of one Fe decreases from 4.12 to 3.46 μ_B). However, we know from calculations presented above that Fe prefers to occupy the Li ion site. Thus, in Fe doping, Fe is not oxidized but the oxygen is oxidized. From the DOS and partial charge density for the highest occupied orbital of $Li_{93}FeZr_{12}O_{72}$ (Figure 7.9), we can see that the top of the valence band is mainly contributed by the p orbitals of oxygen. This indicates that charge transfer will occur on oxygen, in agreement with the spin density result. For $Li_{96}Fe_2Zr_{10}O_{71}$, the d orbitals of Fe contribute to the top of valence bands,[364] which is also consistent with the spin density result. Compared with pure LZO, the doping at Li ion sites creates Li vacancies, which will benefit the Li-ion diffusion and increase conductivity.
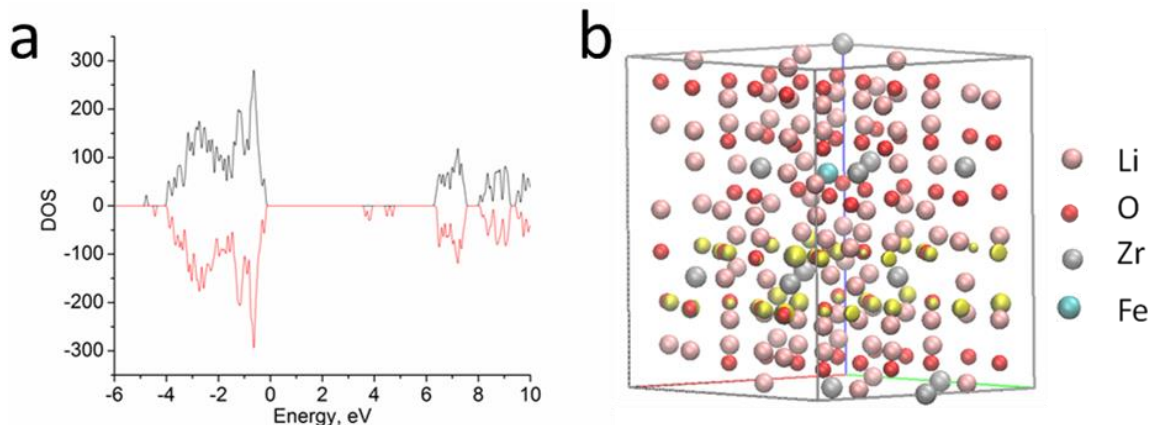
Figure 7.9. (a) The DOS of $Li_{93}FeZr_{12}O_{72}$ determined using the HSE06 functional; (b) The partial charge density of the highest occupied orbital. The isovalue is 0.02 for the yellow isosurface.

7.4 Conclusions

In this Chapter, I have presented a method for the synthesis of transition-metal-doped Li_8ZrO_6 using doped ZrO_2-nanoparticle/carbon composites as precursors. A significant improvement in the specific capacity as compared to undoped Li_8ZrO_6/C composites is shown, especially in Fe-doped samples, for which a stoichiometric precursor ratio of Li:Zr (8:1) yielded the highest capacity yet seen for this class of materials. In initial delithiation/lithiation cycles these materials exhibit a discharge capacity of over 2 Li per formula unit, and a specific capacity of 175 mAh/g is maintained after 140 cycles. This shows the viability of Li_8ZrO_6 for becoming a competitive cathode material for Li-ion batteries after additional development to decrease the large polarization during cycling. Another future challenge is to maintain this capacity and limit the capacity fading over a larger number of cycles. The doping effects of Ce^{3+}, Fe^{3+}, Mn^{2+}, Co^{2+}, Ni^{2+}, and Cu^{2+} were also investigated by density functional calculations. The calculations show that all

the studied dopants prefer to occupy octahedral Li sites rather than Zr ion sites. The doping with any of these ions leads to smaller band gaps than in the undoped material. During the charging, the spin densities of Fe^{3+} and Cu^{2+} remain nearly the same, while the spin densities of Mn^{2+}, Co^{2+}, Ni^{2+}, and Ce^{3+} change. This indicates that Mn^{2+}, Co^{2+}, Ni^{2+}, and Ce^{3+} become oxidized during delithiation while the oxidation mainly occurs on oxygen atoms for LZO doped with Fe^{3+} or Cu^{2+}. The PBE+U calculations show that deintercalation after doping with Ce^{3+}, Fe^{3+}, Mn^{2+}, or Co^{2+} at a Li site decreases the attainable cell voltage, whereas Cu^{2+} and Ni^{2+} doping at a Li site increases it. These results further show that Li_8ZrO_6 is a viable material for future use as a cathode in high energy density lithium batteries.

Chapter 8: Summary and Outlook

8.1 Summary

8.1.1 Electrochemical Double Layer Capacitors

In this thesis I have discussed the use of templated carbon materials for application in electrochemical double layer capacitors (EDLCs). I first showed an improved method for producing soft-templated carbon materials. Ordinarily, producing these materials requires a large surface area to create well-ordered films, which can be tedious and time consuming to isolate. I showed that using a sacrificial layer, such as sucrose or KCl, can be used to produce a similar final product. This significantly reduces the processing time required to make these materials, increasing their future viability as electrode materials.

Following this, I discussed my research on EDLCs by studying the physical properties and electrochemical stability of ionic liquids and relating these properties to the performance of the ionic liquids as electrolytes in porous carbon electrodes. Ionic liquids have the advantage of a generally large potential window to cycle an electrochemical cell, but had not been systematically studied to provide general guidelines for evaluating their performance. From this, I determined, through a collaboration with Dr. Maral Mousavi, that conductivity and ionic size play the largest role in the performance of the electrolyte, as compared to energy density. The smaller ions provide a larger capacitance while the higher conductivity allows for this capacitance to be maintained at higher rates. Using the results measured, I showed that 1-

ethyl-3-methylimidazolium bis(trifluoromethylsulfonyl)imide was the best electrolyte of the ionic liquids tested.

In Chapter 4, I concluded my research on EDLCs with a study of ionic liquids as a precursor to synthesize nitrogen-doped mesoporous carbon. This method has the advantage of using the same processing and synthesis steps and the original phenol-formaldehyde recipe; only changing the precursor composition. When 50 wt% of the initial precursor solution was replaced with 1-ethyl-3-methylimidazolium dicyanoamide, a mesoporous carbon material was produced that contained 7.6% nitrogen while retaining the ordered mesopores that give the high capacitance. The nitrogen content led to improved conductivity and consequently over 40% improvement in the capacitance at high cycling rates.

8.1.2 Lithium Ion Batteries

My work on LIBs began with the development of a low-cost electrochemical cell that can be used to monitor crystalline changes by in situ powder X-ray diffraction. This cell allows for a wider audience to access this characterization technique, which is important for understanding both charge storage mechanisms and failure and decomposition analysis of electrode materials. Previously, this could only be accomplished through the use of specialized equipment and expensive cells. While this cell design was tested using a known cathode material to show proof-of-concept, the design can be applied to any type of electrode material that is compatible with the polymers used in the cell body.

I also worked to develop novel cathode materials for use in LIBs. Specifically, I worked on Li_8ZrO_8, which has a high maximum theoretical capacity of 880 mAh/g,

although computation predicts structural changes when the third lithium ion is extracted per formula unit, giving a theoretical capacity of between 220 and 330 mAh/g; still higher than any other developed cathode material. My initial work focused on showing the viability of the system and comparing computational predictions (performed by Dr. Shuping Huang), such as the oxidation state of the oxygen atoms, with experimental results, such as a shift in the O_{1s} peak in the XPS spectrum. Additionally, the Li_8ZrO_6 system was improved with the addition of both a secondary carbon phase and yttria dopants within the LZO system. Both additives mitigate the effect of the low conductivity inherent to Li_8ZrO_6 by creating a conductive network through the composite and reducing the grain size of the active material. This led to initial capacities of over 200 mAh/g with over 140 mAh/g retained after 60 cycles.

This system was then further developed by the incorporation of transition metal dopants into the LZO/C composites. This was done to both improve the conductivity, as all dopants were predicted to reduce the band gap of the material, and mitigate the redox activity on the oxygen atom by providing a more favorable redox center. As expected, all dopants tested improved the specific capacity over an undoped control sample, with Fe^{3+} showing the best improvement. In the case of Fe-LZO-8, a specific capacity of over 175 mAh/g was observed after 140 cycles. This shows the viability and gives direction for future development of the system with additional dopants and different methods for dopant incorporation.

8.2 Outlook and Future Directions

8.2.1 Electrochemical Double-Layer Capacitors

My work focused on pure double-layer capacitance, as described in Chapter 1. While this can provide significant power density, it is fundamentally limited by the accessible surface area of the electrodes. Work to improve this is focused on creating hierarchical porosity, with small micropores to create the high surface area necessary for maximum capacitance and meso- and macropores for electrolyte accessibility to the micropores. One method to do this is to create composites of carbon nanotubes and graphene oxide.[378] Both forms of carbon are conductive, allowing for fast electron transport within the structure. The carbon nanotubes created pillared 3D structures, increasing the surface area and allowing for fast ion diffusion (Figure 8.1). This composite showed high electrochemical performance in an ionic liquid electrolyte.
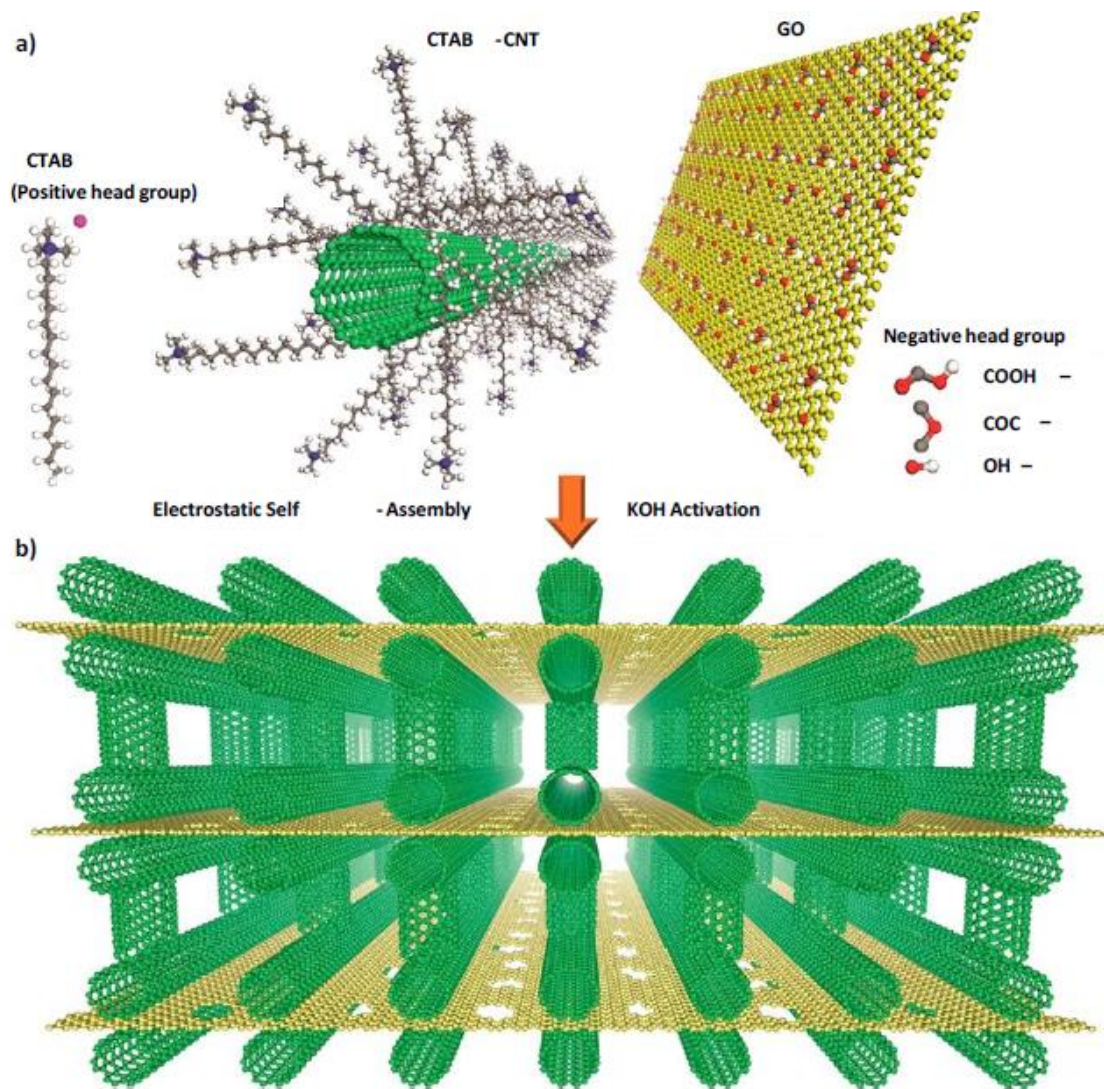
Figure 8.1. Schematic for fabricating the graphene/carbon nanotube 3D structure. The carbon nanotubes are positively charged and the graphene oxide sheets are negatively charged as a result of their respective functional groups (a) leading to the self-assembly into a 3D network (b). KOH activation creates nanoscale pores within the graphene layers to improve ion diffusion. Reprinted with permission from reference 378. Copyright 2015, American Chemical Society.

Beyond double-layer capacitance, pseudocapacitive elements can be added to improve the energy density, creating a hybrid capacitor. For instance,

186

MnO_2/graphene/carbon nanofiber ternary composites have been created through a dispersion/filtration mechanism.[379] The composite was reacted with hydrazine to create a reduced graphene oxide composite. The use of this type of hybrid capacitor could be combined with a templated carbon, such as that described in Chapters 2 and 3. The highly conductive carbon, combined with a pseudocapacitive element could improve the capacitance, allowing for higher energy density applications.

8.2.2 Lithium-Ion Batteries

The Li_8ZrO_6 system is still in its infancy. A significant amount of work remains to create a viable alternative for commercialization and replacement of existing cathode materials. One of the biggest limitations of the system described in Chapters 6 and 7 is the high carbon content. Currently, this carbon is required to both limit the grain size of the active material and to provide a conductive phase to allow for reasonable cycling rates. One method to reduce the necessary carbon content is to utilize templating, similar to the approach described in Chapter 4. However, the template should be at a larger scale to help prevent grain growth and sintering, eliminating the structure. Using poly(methyl methacrylate) sphere colloidal crystal templates has been used previously to create macroporous cathode materials out of a $LiFePO_4$/C composite.[115] Initial results using this technique has resulted in small grain sizes of less than 40 nm with carbon contents half of that needed for the published synthesis. While the final material does not predominately show the desired three-dimensionally ordered macroporous structure, it does show a high level of porosity and Li_8ZrO_6 purity (Figure 8.2). This material shows promise for future optimization for use as a higher volumetric capacity cathode material.

187
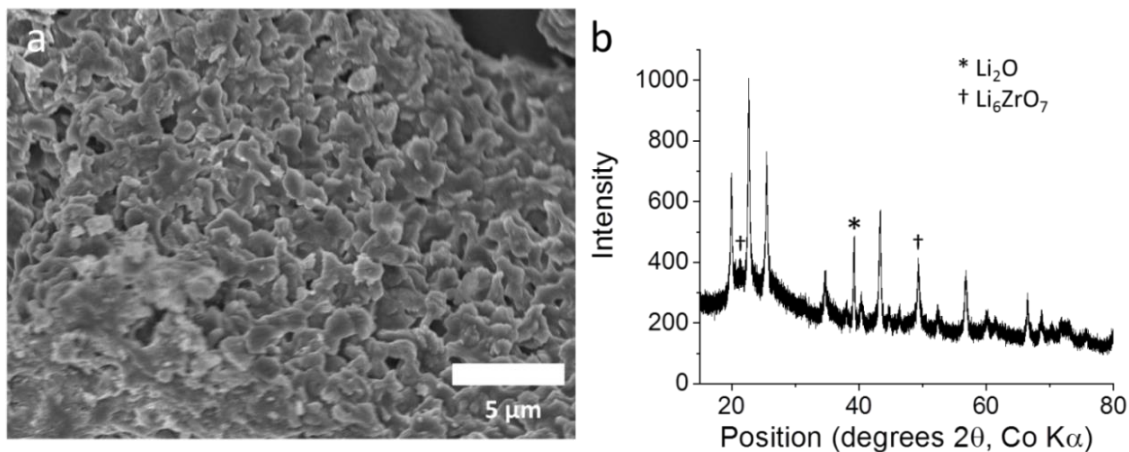
Figure 8.2. Scanning electron micrograph (a) and powder X-ray diffraction pattern (b) for Li_8ZrO_6 templated with a poly(methyl methacrylate) colloidal crystal template. Results unpublished.

As discussed in Chapter 7, transition metal dopants can be used to improve the specific capacity of Li_8ZrO_6. In the work discussed, this has only been done for six metals, at approximately 5% precursor loading, and through doping of the ZrO_2/C precursor material. This leaves a wide range of future directions to improve the final material through doping. Work has already been performed in the group to dope the final material through an ion exchange process, either with a solution exchange or though reaction at high temperatures with a secondary salt. This has shown initial promise to load the dopants into the active material with little to no impurities detected though X-ray diffraction. This procedure has the advantage of putting the dopant atom into the interstitial lithium sites, rather than potentially in the zirconium or interlayer lithium sites, as these ions are the most mobile and likely to be exchanged. Computation has predicted that by introducing defect sites into these locations, such as by introducing a multivalent cation, ionic diffusion can be increased, leading to improved capacity, especially at

higher rates. Furthermore, by introducing the dopant atoms into the structure post synthesis, additional synthetic routes could be explored, such as chemical or physical vapor deposition, that can be difficult to find appropriate precursors for the dopant atoms.

Another avenue that should be explored is the use of different atoms for doping. While all six dopant atoms chosen showed improved performance, some elements showed better improvements than others. This implies that the atom used has a large effect on the resulting performance rather than merely being a method for producing structural defects, as would be expected. Therefore, potential exists for other, yet untested, dopants to have an even greater effect on both the specific capacity and the capacity retention. A systematic study of suitable dopant atoms could yield valuable insight into the process by which the dopant atoms benefit the performance, as well as yielding higher capacity materials.

Beyond doping with transition metals, alternative dopants could be used. Initial studies into doping with sodium to replace lithium within the structure (not shown) led to reduced capacity. However, as mentioned, alternative dopants that create defects in the interlayer lithium sites could improve the ionic conductivity, and subsequently the performance, of the cathode material. Replacing one lithium ion with an alkaline earth metal, such as magnesium, would require a lithium vacancy for charge balance, and could yield the desired improvements. This might be accomplished by either initially replacing some of the lithium precursor salt with an appropriate magnesium salt or by using the ion exchange method discussed earlier. Alternatively, the oxygen atom could be replaced with a different, more redox active, element such as nitrogen or sulfur. As discussed in

Chapter 6, the redox activity in the undoped Li_8ZrO_6 is shown to be primarily focused on the oxygen atoms. By providing a more stable redox center in those locations, a more thermodynamically favorable delithiation process could be achieved, giving rise to higher capacity and verifying the role that oxygen plays in balancing the charge after removal of one lithium atom. As a more stable redox center, a higher depth of charge could be expected, and potentially a higher theoretical limit of lithium ions removed before structural changes occur, which are typically irreversible and stop further lithium cycling.

In all, there exists significant work yet to be done to fully optimize the Li_8ZrO_6 cathode system. While I have briefly described a few options in the preceding few pages, many alternatives also exist. This material shows great promise as a potential cathode material for high performance lithium ion batteries and begs for further research to reach its full potential.

8.3 A Few Final Words

Throughout this thesis, I have shown that nanostructured materials, from templated to textural porosity, can lead to improved performance in electrochemical storage devices. Beyond control over the structural morphology, control over the composition through doping can lead to further improvements while retaining the same structural control necessary for improved performance. I hope that my contributions to the electrochemical storage literature can help lead to more efficient utilization of energy in the coming years. While my work may only be a brick in the wall of science, together, with collaboration and respect, we can build a better tomorrow.

Bibliography

(1) Department of Energy, *Quadrennial Energy Review: Energy Transmission, Storage, and Distribution Infrastructure*; 2015.

(2) Camara, M. B.; Gualous, H.; Gustin, F.; Berthon, A., Design and New Control of DC/DC Converters to Share Energy Between Supercapacitors and Batteries in Hybrid Vehicles. *IEEE T. Veh. Technol.* **2008,** *57*, 2721-2735.

(3) Goodenough, J. B.; Abruna, H. D.; Buchanan, M. *Basic Research Needs for Electrical Energy Storage*; Office of Basic Energy Science, 2007.

(4) Frackowiak, E., Carbon Materials for Supercapacitor Application. *Phys. Chem. Chem. Phys.* **2007,** *9*, 1774-85.

(5) Simon, P.; Gogotsi, Y., Charge Storage Mechanism in Nanoporous Carbons and Its Consequence for Electrical Double Layer Capacitors. *Philos. Trans. R. Soc. A* **2010,** *368*, 3457-67.

(6) Conte, M., Supercapacitors Technical Requirements for New Applications. *Fuel Cells* **2010,** *10*, 806-818.

(7) Zhai, Y.; Dou, Y.; Zhao, D.; Fulvio, P. F.; Mayes, R. T.; Dai, S., Carbon materials for chemical capacitive energy storage. *Adv. Mater.* **2011,** *23*, 4828-50.

(8) Walcarius, A., Mesoporous materials and electrochemistry. *Chem. Soc. Rev.* **2013,** *42*, 4098-140.

(9) Pitchai, R.; Thavasi, V.; Mhaisalkar, S. G.; Ramakrishna, S., Nanostructured Cathode Materials: A Key for Better Performance in Li-ion Batteries. *J. Mater. Chem.* **2011,** *21*, 11040.

(10) Vetter, J.; Novák, P.; Wagner, M. R.; Veit, C.; Möller, K. C.; Besenhard, J. O.; Winter, M.; Wohlfahrt-Mehrens, M.; Vogler, C.; Hammouche, A., Ageing Mechanisms in Lithium-Ion Batteries. *J. Power Sources* **2005,** *147*, 269-281.

(11) Goodenough, J. B.; Kim, Y., Challenges for Rechargeable Li Batteries. *Chem. Mater.* **2010,** *22*, 587-603.

(12) Etacheri, V.; Marom, R.; Elazari, R.; Salitra, G.; Auerbach, D., Challenges in the Development of Advanced Li-Ion Batteries: A Review. *Energy Environ. Sci.* **2011,** *4*, 3243-3262.

(13) Simon, P.; Gogotsi, Y., Materials for Electrochemical Capacitors. *Nat. Mater.* **2008,** *7*, 845-854.

(14) Kotz, R.; Carlen, M, Principles and applications of Electrochemical Capacitors. *Electrochim. Acta* **2000,** *45*, 2483-2498.

(15) Becker, H. I. Low Voltage Electrolytic Capacitor. 2,800,616, 1954.

(16) Boos, D. L. Electrolytic Capacitor Having Carbon Paste Electrodes. 3,536,963, 1970.

(17) Liu, R.; Shi, Y.; Wan, Y.; Meng, Y.; Zhang, F.; Gu, D.; Chen, Z.; Tu, B.; Zhao, D., Triconstituent Co-assembly to Ordered Mesostructured Polymer-Silica and Carbon-Silica Nanocomposite and Large-Pore Mesoporous Carbons with High Surface Areas. *J. Am. Chem. Soc.* **2006,** *128*, 11652-11662.

(18) Gadipelli, S.; Calizo, I.; Ford, J.; Cheng, G.; Walker, A.; Yildirim, T., A Highly Practical Route for Large-Area, Single-Layer Graphene From Liquid Carbon Sources such as Benzene and Methanol. *J. Mater. Chem.* **2011,** *21*, 16057-16065.

(19) Galinski, M.; Lewandowski, A.; Stepniak, I., Ionic Liquids as Electrolytes. *Electrochim. Acta* **2006,** *51*, 5567-5580.

(20) Arbizzani, C.; Biso, M.; Cericola, D.; Lazzari, M.; Soavi, F.; Mastragostino, M., Safe, High-Energy Supercapacitors based on Solvent-Free Ionic Liquid Electrolytes. *J. Power Sources* **2008,** *185*, 1575-1579.

(21) Lee, T.; Jeagal, J.; Choi, J.; Choi, W.; Lee, M.; Oh, J.; Kim, K.; Baik, H.; Xia, Y.; Myoung, J., Binder-Free and Full Electrical-Addressing Free-Standing Nanosheets with Carbon Nanotube Fabrics for Electrochemical Applications. *Adv. Mater.* **2011,**

(22) Stoller, M. D.; Park, S.; Zhu, Y.; An, J.; Ruoff, R., Graphene-Based Ultracapacitors. *Nano Lett.* **2008,** *8*, 3498-3502.

(23) Faraji, S.; Ani, F. N, The Development of Supercapacitors from Activated Carbon by Electroless Plating - A Review. *Renew. Sustain. Energy Rev.* **2015,** *42*, 823-834.

(24) Pandolfo, T.; Ruiz, V.; Sivakkumar, S.; Nerkar, J., General Properties of Electrochemcial Capacitors. In *Supercapacitors: Materials, Systems, and Applications, First Edition*, Beguin, F.; Frackowiack, E., Eds. Wiley-VCH Verlag GmbH and Co.: 2013; pp 69-114.

(25) Gileadi, E., *Physical Electrochemistry*. Wiley-VCH: Weinheim, Germany, 2011.

(26) Huang, J.; Sumpter, B. G.; Meunier, V., A Universal Model for Nanoporous Carbon Supercapacitors Applicable to Diverse Pore Regimes, Carbon Materials, and Electrolytes. *Chem. - Eur. J.* **2008,** *14*, 6614-6626.

(27) Rouquerol, J.; Avnir, D.; Fairbridge, C. W.; Everett, D. H.; Haynes, J. M.; Pernicone, N.; Ramsay, J. D. F.; Sing, K. S. W.; Unger, K. K., Recommendations for the Characterization of Porous Solids (Technical Report). *Pure. Appl. Chem.* **1994,** *66*, 1739-1754.

(28) Huang, J.; Sumpter, B. G.; Meunier, V., A universal model for nanoporous carbon supercapacitors applicable to diverse pore regimes, carbon materials, and electrolytes. *Chemistry* **2008,** *14*, 6614-26.

(29) Varghese, J.; Wang, H.; Pilon, L., Simulating Electric Double Layer Capacitance of Mesoporous Electrodes with Cylindrical Pores. *J. Electrochem. Soc.* **2011,** *158*, A1106.

(30) Largeot, C.; Portet, C.; Chmiola, J.; Taberna, P.-L.; Gogotsi, Y.; Simon, P., Relation between the Ion Size and Pore Size for an Electric Double-Layer Capacitor. *J. Am. Chem. Soc.* **2008,** *130*, 2730-2731.

(31) Fischer, A. E.; Pettrigrew, K. A.; Rolinson, D. R.; Stroud, R. M.; Long, J. W., Incorporation of Homogenous, Nanoscale MnO_2 Within Ultraporous Carbon Structures via Self-Limiting Electroless Deposition: Implications for Electrochemical Capacitors. *Nano Lett.* **2007,** *7*, 281-286.

(32) Wu, N. -L., Nanocrystalline Oxide Supercapacitors. *Mat. Chem. Phys.* **2002,** *75*, 6-11.

(33) Zhang, L. L.; Zhou, R.; Zhao, X. S., Graphene-Based Materials as Supercapacitor Electrodes. *J. Mater. Chem.* **2010,** *20*, 5983-5992.

(34) Amade, R.; Jover, E.; Caglar, B.; Mutlu, T.; Bertran, E., Optimization of MnO2/Vertically Aligned Carbon Nanotube Composite for Supercapacitor Application. *J. Power Sources* **2011,** *196*, 5779-5783.

(35) Choi, H.; Yoon, H., Nanostructured Electrode Materials for Electrochemical Capacitor Applications. *Nanomaterials* **2015,** *5*, 906-936.

(36) Huang, J.; Qiiao, R.; Feng, G.; Sumpter, B. G.; Meunier, V., Modern Theories of Carbon-Based Electrochemical Capacitors. In *Supercapacitors: Materials, Systems, and Applications, First Edition*, Beguin, F.; Frackowiak, E., Eds. Wiley-VCH Verlag GmbH and Co: 2013; pp 167-216.

(37) Taer, E.; Deraman, M.; Talib, I. A.; Awitdrus, A.; Hashimi, S. A.; Umar, A. A., Preparation of a Highly Porous Binderless Activated Carbon Monolith from Rubber Wood Sawudust by a Multi-step Activation Process for Application in Supercapacitors. *Int. J. Electrochem. Sci.* **2011,** *6*, 3301-3315.

(38) Raymundo-Pinero, E.; Leroux, Fabrice; Beguin, F., A High-Performance Carbon for Supercapacitors Obtained by Carbonization of a Seaweed Biopolymer. *Adv. Mater.* **2006,** *18*, 1877-1882.

(39) Subramanian, V.; Luo, C.; Stephan, A. M.; Nahm, K. S.; Thomas, S.; Wei, B., Supercapacitors from Activated Carbon Derived from Banana Fibers. *J. Phys. Chem. C* **2007,** *111*, 7527-7531.

(40) Wang, R.-Q.; Fang, Q.; Deng, M.-G., Templated Synthesis of Activated Carbon for Supercapacitor. *Mater. Sci. Forum* **2011,** *663-665*, 568-571.

(41) Wang, Y.; Zheng, C.; Qi, L.; Yoshio, M.; Yoshizuka, K.; Wang, H., Utilization of (oxalato)borate-Based Organic Electrolytes in Activated Carbon/Graphite Capacitors. *J. Power Sources* **2011,** *196*, 10507-10510.

(42) Huang, C.-W.; Hsieh, C.-T.; Kuo, P.-L.; Teng, H., Electric Double Layer Capacitors Based on a Composite Electrode of Activated Mesophase Pitch and Carbon Nanotubes. *J. Mater. Chem.* **2012,** *22*, 7314-7322.

(43) Sun, G.; Li, K.; Liu, Y.; Wang, J.; He, H.; Wang, J.; Gu, J.; Li, Y., Physical and Electrochemical Characterization of Activated Carbons with High Mesoporous Ratio for Supercapacitors Based on Ionic Liquid as the Electrolyte. *J. Solid State Electrochem.* **2011,** *15*, 607-613.

(44) Tong, S.; Qin, C.; Jin, Z.; Wang, X.; Bai, X., Activated Nitrogen-Enriched Carbon/Reduced Expanded Graphite Composites for Supercapacitors. *Adv. Mater. Res.* **2011,** *211-212*, 440-444.

(45) Liu, S.-H.; Wu, M.-T.; Lai, Y.-H.; Chiang, C.-C.; Yu, N.; Liu, S.-B., Fabrication and Electrocatalytic Performance of Highly Stable and Active Platinum Nanoparticles Supported on Nitrogen-Doped Ordered Mesoporous Carbons for Oxygen Reduction Reaction. *J. Mater. Chem.* **2011,** *21*, 12489-12496.

(46) Chmiola, J.; Yushin, G.; Dash, R.; Gogotsi, Y., Effect of Pore Size and Surface Area of Carbide Derived Carbons on Specific Capacitance. *J. Power Sources* **2006,** *158*, 765-772.

(47) Jiang, D. E.; Jin, Z.; Wu, J., Oscillation of Capacitance Inside Nanopores. *Nano Lett.* **2011,** *11*, 5373-7.

(48) Barbieri, O.; Hahn, M.; Herzog, A.; Kotz, R., Capacitance Limits of High Surface Area Activated Carbons for Double Layer Capacitors. *Carbon* **2005,** *43*, 1303-1310.

(49) Deng, L.; Young, R. J.; Kinloch, J. A.; Abdelkader, A. M.; Holmes, S. M.; Rios, D. A.; Eichhorn, S. J., Supercapacitance from Cellulose and Carbon Nanotube Nanocomposite Fibers. *ACS Appl. Mater. Interfaces* **2013,** *5*, 9983-9990.

(50) Qin, Z.; Taylor, M.; Hwang, M.; Bertoldi, K.; Buehler, M. J., Effect of Wrinkles on the Surface Area of Graphene; Toward the Design of Nanoelectronics. *Nano Lett.* **2014,** *14*, 6520-6525.

(51) Matsumoto, H.; Imiazumi, S.; Konsu, Y.; Ashizawa, M.; Minagawa, M.; Tanioka, A.; Lu, W.; Tou, J. M., Electrospun Composite Nanofiber Yarns Containing Oriented Graphene Nanoribbons. *ACS Appl. Mater. Interfaces* **2013,** *5*, 6225-6231.

(52) Krishnan, D.; Raidongia, K.; Shao, J.; Huang, J., Graphene Oxide Assisted Hydrothermal Carbonization of Carbon Hydrates. *ACS Nano* **2014,** *8*, 449-457.

(53) Chen, X.; Qiu, L.; Ren, J.; Guan, G.; Lin, H.; Zhang, Z.; Chen, P.; Wang, Y.; Peng, H., Novel Electric Double-Layer Capacitor with a Coaxial Fiber Structure. *Adv. Mater.* **2013,** *25*, 6436-6441.

(54) Yang, X.; Zhang, L.; Zhang, F.; Zhang, T.; Huang, Y.; Chen, Y., A High-Performance All-Solid-State Supercapacitor with Graphene-Doped Carbon Material Electrodes and a Graphene Oxide-Doped Ion Gel Electrolyte. *Carbon* **2014,** *72*, 381-386.

(55) Lazzari, M.; Mastragostino, M. Capacitance Response of Carbons in Solvent-Free Ionic Liquid Electrolytes. *Electrochem. Comm.* **2007,** *9*, 1567-1572.

(56) Lang, J.; Yan, X.; Yuan, X.; Yang, J.; Xue, Q., Study on the Electrochemical Properties of Cubic Ordered Mesoporous Carbon for Supercapacitors. *J. Power Sources* **2011,** *196*, 10472-10478.

(57) Fuertes, A. B.; Pico, F.; Rojo, J. M., Influence of Pore Structure on Electric Double-Layer Capacitance of Template Mesoporous Carbons. *J. Power Sources* **2004,** *133*, 329-336.

(58) Simon, P.; Gogotsi, Y., Materials for Electrochemical Capacitors. *Nat. Mater.* **2008,** *7*, 845-854.

(59) Rose, M.; Korenblit, Y.; Kockrick, E.; Borchard, L.; Oschatz, M.; Kaskel, S.; Yushin, G., Heirarchical Micro- and Mesoporous Carbide-Derived Carbon as a High-Perfromance Electrode Material in Supercapacitors. *Small* **2011,** *7*, 1108-1117.

(60) Jayalashmi, M.; Balasubramanian, K., Simple Capacitors to Supercapacitors - An Overview. *Int. J. Electrochem. Sci.* **2008,** *3*, 1196-1217.

(61) Kotz, R.; Carlen, M., Principles and Applications of Electrochemical Capacitors. *Electrochim. Acta* **2000,** *45*, 2483-2498.

(62) Toupin, M.; Brousse, T.; Belanger, D., Charge Storage Mechanism of MnO_2 Electrode Used in Aqueous Electrochemical Capacitor. *Chem. Mater.* **2004,** *16*, 3184-3190.

(63) Ruiz, V.; Pandolfo, A. G., High-Frequency Carbon Supercapacitors from Polyfurfuryl Alcohol. *J. Power Sources* **2011,** *196*, 7816-7822.

(64) Wang, Y.; Zheng, C.; Qi, L.; Yoshio, M.; Yoshizuka, K.; Wang, H., Utilization of (oxalato)borate-based Organic Electrolytes in Activated Carbon/Graphite Capacitors. *J. Power Sources* **2011,** *196*, 10507-10510.

(65) Salitra, G.; Soffer, A.; Eliad, L.; Cohen, Y.; Aurbach, D., Carbon Electrodes for Double-Layer Capacitors I. Relations Between Ion and Pore Dimensions. *J. Electrochem. Soc.* **2000,** *147*, 2486-2493.

(66) Naoi, K., 'Nanohybrid Capacitor': The Next Generation Electrochemical Capacitors. *Fuel Cells* **2010,** *10*, 825-833.

(67) Liu, H.; Ping, H.; Li, Z.; Liu, Y.; Zheng, L.; Li, J., The Inherent Capacitive Behavior of Imidazolium-based Room-Temperature Ionic Liquids at Carbon Paste Electrode. *Electrochem. Solid St. Lett.* **2005,** *8*, J17-J19.

(68) Nadherna, M.; Dominko, R.; Hanzel, D.; Reiter, J.; Gaberscek, M., Electrochemical Behavior of Li_2FeSiO_4 with ionic Liquids at Elevated Temperature. *J. Electrochem. Soc.* **2009,** *156*, A619-A626.

(69) Marra, A.; Chiappe, C.; Mele, A., Sugar-Derived Ionic Liquids. *Chimia* **2011,** *65*, 76-80.

(70) Imperato, G.; Konig, B.; Chlappe, C., Ionic Green Solvents from Renewable Resources. *Eur. J. Org. Chem.* **2007,** *7*, 1049-1058.

(71)   Liu, H.; Zhu, G., The Electrochemical Capacitance of Nanoporous Carbons in Aqueous and Ionic Liquids. *J. Power Sources* **2007,** *171*, 1054-1061.

(72)   Zhou, J.; Cai, J.; Cai, S.; Zhou, X.; Mansour, A., Development of All-Solid-State Mediator-Enhanced Supercapacitors with PVDF/LiTFS Separators. *J. Power Sources* **2011,** *196*, 10479-10483.

(73)   Meng, F.; Ding, Y., Sub-Micrometer-Thick All-Solid-State Supercapacitors with High Power and Energy Densities. *Adv. Mater.* **2011,** *23*, 4098-4102.

(74)   Hu, L.; Pasta, M.; Mantia, F.; Cui, L.; Jeong, S.; Deshazer, H.; Choi, J.; Han, S.; Cui, Y., Stretchable, Porous, and Conductive Energy Textiles. *Nano Lett.* **2010,** *10*, 708-714.

(75)   Nagura, T.; Tozawa, K., Lithium Ion Rechargeable Battery. *Prog. Batter. Sol. Cells* **1990,** *9*, 209-211.

(76)   Abraham, K. M., Prospects and Limits of Energy Storage in Batteries. *J. Phys. Chem. Lett.* **2015,** *6*, 830-844.

(77)   Julien, C. M.; Mauger, A.; Zaghib, K.; Groult, H., Comparative Issues of Cathode Materials for Li-Ion Batteries. *Inorganics* **2014,** *2*, 132-154.

(78)   Ko, M.; Oh, P.; Chae, S.; Cho, W.; Cho, J., Considering Critical Factors of Li-rich Cathode and Si Anode Materials for Practical Li-ion Cell Applications. *Small* **2015,** *11*, 4058-4073.

(79)   Linden, D.; Reddy, T. R., In *Handbook of Batteries*, McGraw Hill: New York, 2011.

(80)   Mizushima, K.; Jones, P. C.; Wiseman, P. J.; Goodenough, J. B., Li_xCoO_2 ($0<x<1$): A New Cathode Material for Batteries of High Energy Density. *Mat. Res. Bull.* **1980,** *15*, 783-789.

(81)   Arroyo y de Dompablo, M. E.; Marianetti, C.; van der Ven, A.; Ceder, G., Jahn-Teller Mediated Ordering in Layered Li_xCoO_2 Compounds. *Phys. Rev. B* **2001,** *63*, 144104.

(82)   Li, X.; Liu, J.; Meng, X.; Tang, Y.; Banis, M. N.; Yang, J.; Hu, Y.; Li, R.; Cai, M.; Sun, X., Significant Impact on Cathode Performance of Lithium-Ion Batteries by Precisely Controlled Metal Oxide Nanocoatings via Atomic Layer Deposition. *J. Power Sources* **2013,** *247*, 57-69.

(83)   Li, X.; Liu, J.; Banis, M. N.; Lushington, A.; Li, R.; Caib, M.; Sun, X., Atomic Layer Deposition of Solid-State Electrolyte Coated Cathode Materials with Superieor High Voltage Cycling Behavior for Lithium Ion Battery Application. *Energy Environ. Sci.* **2014,** *7*, 768-778.

(84)   Thackeray, M. M.; David, W. I. F.; Bruce, P. G.; Goodenough, J. B., Lithium Insertion Into Manganese Spinels. *Mat. Res. Bull.* **1983,** *18*, 461-472.

(85) Thackeray, M. M.; Johnson, P. J.; de Piccioto, L. A.; Bruce, P. G.; Goodenough, J. B., Electrochemical Extraction of Lithium from $LiMn_2O_4$. *Mat. Res. Bull.* **1984,** *19*, 179-187.

(86) Padhi, A. K.; Nanjundaswamy, K. S.; Goodenough, J. B., Phospho-Olvines as Positive-Electrode Materials for Rechargeable Lithium Batteries. *J. Electrochem. Soc.* **1997,** *144*, 1188-1194.

(87) Zaghib, K.; Mauger, A.; Goodenough, J. B.; Gendron, F.; Julien, C. M., Design and Properties of $LiFePO_4$ Positive Electrode Materials for Li-ion Batteries. In *Advanced Materials and Methods for Lithium-ion Batteries*, Zhang, S. S., Ed. Transworld Research Network: Trivandrum, India, 2007; pp 115-149.

(88) Li, H.; Wang, Z.; Chen, L.; Huang, X., Research on Advanced Materials for Li-ion Batteries. *Adv. Mater.* **2009,** *21*, 4593-4607.

(89) Ritchie, A. G., Recent Developments and Likely Advances in Lithium Rechargable Batteries. *J. Power Sources* **2004,** *136*, 285-289.

(90) Terason, J. M.; Armand, M., Issues and Challenges Facing Rechargeable Lithium Batteries. *Nature* **2001,** *414*, 359-367.

(91) Li, Z.; Zhang, D.; Yang, F., Developments of Lithium-ion Batteries and Challenges of $LiFePO_4$ as One Promising Cathode Material. *J. Mater. Sci.* **2009,** *44*, 2435-2443.

(92) Ritchie, A. G.; Howard, W., Recent Development and Likely Advances in Lithium-Ion Batteries. *J. Power Sources* **2006,** *162*, 809-812.

(93) Kim, D.-H.; Kim, J., Synthesis of $LiFePO_4$ Nanoparticles in Polyol Medium andTheir Electrochemcial Properties. *Electrochem. Solid St.* **2006,** *9*, A439-442.

(94) Yada, C.; Iriyama, Y.; Jeong, S.-K.; Abe, T.; Inaba, M.; Ogumi, Z., Electrochemical Properties of $LiFePO_4$ Thin Films Prepared by Pulsed Laser Deposition. *J. Power Sources* **2005,** *146*, 559.

(95) Yamada, A.; Koizumi, H.; Nishimura, S.-I.; Sonoyama, N.; Kanno, R.; Yonemura, M.; Nakamura, T.; Kobayashi, Y., Room-Temperature Miscibiliy Gap in Li_xFePO_4. *Nat. Mater.* **2006,** *5*, 357-360.

(96) Yang, M.-R.; Teng, T.-H.; Wu, S.-H., $LiFePO_4$/Carbon Cathode Materials Prepared by Ultrasonic Spray Pyrolysis. *J. Power Sources* **2006,** *159*, 307-311.

(97) Yamada, A.; Hosoya, M.; Chung, S.-C.; Kudo, Y.; Hinokuma, K.; Liu, K.-Y.; Nishi, Y., Olvine-type Cathodes: Achievements and Problems. *J. Power Sources* **2003,** *119*, 232-238.

(98) Xia, H.; Lu, L.; Ceder, G., Li Diffusion in $LiCoO_2$ Thin Films Prepared by Pulsed Laser. *J. Power Sources* **2006,** *159*, 1422-1427.

(99) Lee, J.; Teja, A. S., Synthesis of $LiFePO_4$ Micro- and Nanoparticles in Supercritical Water. *Mat. Lett.* **2006,** *60*, 2105-2109.

(100) Yun, N. J.; Ha, H.-W.; Jeong, K. H.; Park, H.-Y.; Kim, K., Synthesis and Electrochemical Properties of Olvine-type LiFePO$_4$/C Composite Cathode Material Prepared From a Poly(vinyl alcohol)-Containing Precursor. *J. Power Sources* **2006,** *160*, 1361-1368.

(101) Zhuang, D.; Zhao, X. S.; Xie, J.; Tu, J. P.; Zhu, T.; Cao, G., One-Step Solid-State Synthesis and Electrochemical Performance of Nb-Doped LiFePO$_4$/C. *Acta Phys. Chem.* **2006,** *22*, 840-844.

(102) Melingrana, G.; Gerbaldi, C.; Tuel, A.; Bodoardo, S.; Penazzi, N., Hydrothermal Synthesis of High Surface LiFePO$_4$ Powders as Cathode for Li-Ion Cells. *J. Power Sources* **2006,** *160*, 516-522.

(103) Shin, H. C.; Cho, W. I.; Jang, H., Electrochemical Properties of the Carbon-Coated LiFePO$_4$ as a Cathode Material for Lithium-Ion Secondary Batteries. *J. Power Sources* **2006,** *159*, 1383.

(104) Ait Salan, A.; Zaghib, K.; Mauger, A.; Gendron, F.; Julien, C. M., Magnetic Studies of the Carbothermal Effect on LiFePO$_4$. *Phys. Status Solidi A* **2006,** *203*, R1-R3.

(105) Huang, Y.-H.; Park, K.-S.; Goodenough, J. B., Improving Lithium Batteries by Tethering Carbon-Coated LiFePO$_4$ to Polypyrrole. *J. Electrochem. Soc.* **2006,** *153*, A2282-A2286.

(106) Thorat, I. V.; Mathur, V.; Harb, J. N.; Wheeler, D. R., Performance of Carbon-Fiber-Containing LiFePO$_4$ Cathodes for High-Power Applications. *J. Power Sources* **2006,** *162*, 673-678.

(107) Li, W.; Gao, J.; Ying, J.; Wan, C.; Jiang, C., Preparation and Characterization of LiFePO$_4$ from Novel Precursor of NH$_4$FePO$_4 \cdot$ H$_2$O. *J. Electrochem. Soc.* **2006,** *153*, F194-F198.

(108) Liu, H.; Fu, L. J.; Zhang, H. P.; Gai, J.; Li, C.; Wu, Y. P.; Hu, H. Q., Effects of Carbon Coatings on Nanocomposite Electrodes for Lithium-Ion Batteries. *Electrochem. Solid St.* **2006,** *9*, A529-A533.

(109) Hannoyer, B.; Prince, A. A. M.; Jean, M.; Liu, R. S.; Wang, G. X., Mossbauer Study on LiFePO$_4$ Cathode Materal for Lithium Ion Batteries. *Hyperfine Interact.* **2006,** *167*, 767-772.

(110) Nakamura, T.; Miwa, Y.; Tabuchi, M.; Yamada, Y., Structural and Surface Modifications of LiFePO$_4$ Olvine Particles and Their Electrochemical Properties. *J. Electrochem. Soc.* **2006,** *153*, A1108-A1114.

(111) Xia, Y.; Yoshio, M.; Noguchi, H., Improved Electrochemical Performance of LiFePO$_4$ by increasing its Specific Surface Area. *Electrochim. Acta* **2006,** *52*, 240-245.

(112) Franger, S.; Benoit, C.; Bourbon, C.; Le Cras, F., Chemistry and Electrochemistry of Composite LiFePO$_4$ Materials for Secondary Lithium Batteries. *J. Phys. Chem. Solids* **2006,** *67*, 1338-1342.

(113) Ravet, N.; Chourinard, Y.; Magnan, J. F.; Besner, S.; Gauthier, M.; Armand, M., Electroactivity of Natural and Synthetic Triphylite. *J. Power Sources* **2001,** *97*, 503-507.

(114) Liu, H.; Li, C.; Zhang, H. P.; Fu, L. J.; Wu, Y. P.; Wu, H. Q., Kinetic Study on $LiFePO_4/C$ Nanocomposites Synthesized by Solid State Technique. *J. Power Sources* **2006,** *159*, 717-720.

(115) Vu, Anh; Stein, Andreas, Multiconstituent Synthesis of LiFePO4/C Composites with Hierarchical Porosity as Cathode Materials for Lithium Ion Batteries. *Chem. Mater.* **2011,** *23*, 3237-3245.

(116) Amine, K.; Tukamoto, H.; Yasuda, H.; Fujita, Y., Preparation and Electrochemical Investigation of $LiMn_{2-x}Me_xO_4$ (Me: Ni, Fe, and x = 0.5, 1) Cathode Materials for Secondary Lithium Batteries. *J. Power Sources* **1997,** *68*, 604-608.

(117) Wang, G. X.; Bewlay, S.; Yao, J.; Ahn, J H.; Dou, S. X.; Liu, H. K., Characterization of $LiM_xFe_{1-x}PO_4$ (M=Mg, Zr, Ti) Cathode Materials Prepared by the Sol-Gel Method. *Electrochem. Solid St.* **2004,** *7*, A503-A506.

(118) Herle, P. S.; Ellis, B.; Coombs, N.; Nazar, L. F., Nano-Network Electronic Conduction in Iron and Nickel Olivine Phosphates. *Nat. Mater.* **2004,** *3*, 147-152.

(119) Islam, M. S.; Driscoll, D. J.; Fisher, C. A> J.; Slater, P. R., Atomic-Scale Investigation of Defects, Dopants, and Lithium Transport in the $LiFePO_4$ Olvine-Type Battery Material. *Chem. Mater.* **2005,** *17*, 5085-5092.

(120) Liu, H.; Cao, Q.; Fu, L. J.; Li, C.; Wu, Y. P.; Wu, H. Q., Doping Effects of Zinc on $LiFePO_4$ Cathode Materials for Lithium Ion Batteries. *Electrochem. Comm.* **2006,** *8*, 1553-1557.

(121) Ren, M.; Zhou, Z.; Li, Y.; Gao, X. P.; Yan, J., Preparation and Electrochemical Studies of Fe-Doped $Li_3V_2(PO_4)_3$ Cathode Materials for Lithium-Ion Batteries. *J. Power Sources* **2006,** *162*, 1357-1362.

(122) Wang, G. X.; Needham, S.; Yao, J.; Wang, J. Z.; Liu, R. S.; Liu, H. K., A Study on $LiFePO_4$ and its Doped Derivatives as Cathode Materials for Lithium-Ion Batteries. *J. Power Sources* **2006,** *159*, 282-286.

(123) Yang, M.-R.; Ke, W.-H., The Doping Effect on the Electrochemical Properties of $LiFe_{0.95}M_{0.05}PO_4$ (M = Mg^{2+}, NI^{2+}, Al^{3+}, or V^{3+}) as Cathode Materials for Lithium-Ion Cells. *J. Electrochem. Soc.* **2008,** *155*, A729-A732.

(124) Lu, Y.; Shi, J.; Guo, Z.; Tong, Q.; Huang, W.; Li, B., Synthesis of $LiFe_{1-x}Ni_xPO_4/C$ Composites and Their Electrochemical Performance. *J. Power Sources* **2009,** *194*, 786-793.

(125) Chen, Y.; Zhao, Y.; An, X.; Liu, J.; Dong, Y.; Chen, L., Preparation and Electrochemical Performance Studies on Cr-Doped $Li_3V_2(PO_4)_3$ as Cathode Materials for Lithium-Ion Batteries. *Electrochim. Acta* **2009,** *54*, 5844-5850.

(126) Fergus, J. W., Recent Developments in Cathode Materials for Lithium Ion Batteries. *J. Power Sources* **2010,** *195*, 939-954.

199

(127)   Kuang, Q.; Zhao, Y.; An, X.; Jiu, J.; Dong, Y.; Chen, L., Synthesis and Electrochemical Properties of Co-Doped $Li_3V_2(PO_4)_3$ Cathode Materials for Lithium-Ion Batteries. *Electrochim. Acta* **2010,** *55*, 1575-1581.

(128)   Naoi, K.; Simon, P., New Materials and New Conficurations for Advanced Electrochemical Capacitors. *Electrochem. Soc. Interface* **2008,** *17*, 34-37.

(129)   Meng, Y.; Gu, D.; Zhang, F.; Shi, Y.; Cheng, L.; Feng, D.; Wu, Z.; Chen, Z.; Wan, Y.; Stein, A.; Zhao, D., A Family of Highly Ordered Mesoporous Polymer Resin and Carbon Structures from Organic-Organic Self-Assembly. *Chem. Mater.* **2006,** *18*, 4447-4464.

(130)   Wang, J.; Kasel, S., KOH Activation of Carbon-Based Materials for Energy Storage. *J. Mater. Chem.* **2012,** *22*, 23710-23725.

(131)   Ducrot-Boisgontier, Claire; Parmentier, Julien; Faour, Azzam; Patarin, Joël; Pirngruber, Gerhard D., FAU-Type Zeolite Nanocasted Carbon Replicas for CO2Adsorption and Hydrogen Purification. *Energ. Fuels* **2010,** *24*, 3595-3602.

(132)   Lang, Jun-Wei; Yan, Xing-Bin; Yuan, Xiao-Yan; Yang, Jie; Xue, Qun-Ji, Study on the Electrochemical Properties of Cubic Ordered Mesoporous Carbon for Supercapacitors. *J. Power Sources* **2011,** *196*, 10472-10478.

(133)   Jin, J.; Mitome, T.; Egashira, Y.; Nishiyama, N., Phase Control of Ordered Mesoporous Carbon Synthesized by a Soft-Templating Method. *Colloids Surf., A* **2011,** *384*, 58-61.

(134)   Wan, Y.; Shi, Y.; Zhao, D., Supramolecular Aggregates as Templates, Ordered Mesoporous Polymers and Carbons. *Chem. Mater.* **2008,** *20*, 932-945.

(135)   Meng, Y.; Gu, D.; Zhang, F.; Shi, Y.; Yang, H.; Li, Z.; Yu, C.; Tu, B.; Zhao, D., Ordered Mesoporous Polymers and Homologous Carbon Frameworks: Amphiphilic Surfactant Templating and Direct Transformation. *Angew. Chem. Int. Ed.* **2005,** *44*, 7053-7059.

(136)   Liu, N.; Song, H.; Chen, X., Morphology Control of Ordered Mesoporous Carbons by Changing HCl Concentration. *J. Mater. Chem.* **2011,** *21*, 5345.

(137)   Xiong, W.; Liu, M.; Gan, L.; Lv, Y.; Li, Y.; Yang, L.; Xu, Z.; Hao, Z.; Liu, H.; Chen, L., A Novel Synthesis of Mesoporous Carbon Microspheres for Supercapacitor Electrodes. *J. Power Sources* **2011,** *196*, 10461-10464.

(138)   Levario, T. J.; Dai, M.; Yuan, W.; Vogt, B. D.; Nielsen, D. R., Rapid Adsorption of Alcohol Biofuels by High Surface Area Mesoporous Carbons. *Micro. Meso. Mater.* **2012,** *148*, 107-114.

(139)   Liu, D.; Lei, J.-H.; Guo, L.-P.; Deng, K.-J., Simple Hydrothermal Synthesis of Ordered Mesoporous Carbons From Resorcinol and Hexamine. *Carbon* **2011,** *49*, 2113-2119.

(140) Wang, Z.; Kiesel, E. R.; Stein, A., Silica-Free Syntheses of Hierarchically Ordered Macroporous Polymer and Carbon Monoliths with Controllable Mesoporosity. *J. Mater. Chem.* **2008,** *18*, 2194.

(141) Florent, M.; Xue, C.; Zhao, D.; Goldfarb, D., Formation Mechanism of Cubic Mesoporous Carbon Monolith Synthesized by Evaporation-Induced Self-assembly. *Chem. Mater.* **2012,** *24*, 383-392.

(142) Patarin, J.; Lebeau, B.; Zana, D., Recent Advances in the Formation Mechanisms of Organized Mesoporous Materials. *Curr. Opin. Colloid Interface Sci.* **2008,** *7*, 107-115.

(143) Wilson, B. E.; Rudisill, S. G.; Stein, A., Use of a Sacrificial Layer for an Efficient EISA Synthesis of Mesoporous Carbon. *Micro. Meso. Mater.* **2014,** *197*, 174-179.

(144) Parmentier, J.; Valtchev, V.; Gaslain, F.; Tosheva, L.; Ducrot-Boisgontier, C.; Möller, J.; Patarin, J.; Vix-Guterl, C., Effect of the Zeolite Crystal Size on the Structure and Properties of Carbon Replicas Made by a Nanocasting Process. *Carbon* **2009,** *47*, 1066-1073.

(145) Kawashima, D.; Aihara, T.; Kobayashi, Y.; Kyotani, T.; Tomita, A., Preparation of Mesoporous Carbon from Organic Polymer/Silica Nanocomposite. *Chem. Mater.* **2000,** *12*, 3397-3401.

(146) Toupin, M.; Brousse, T.; Belanger, D., Charge Storage Mechanism if MnO_2 Electrode used in Aqueous Electrochemical Capacitor. *Chem. Mater.* **2004,** *16*, 1196-1217.

(147) Liu, Y.; Ju, M.; Wang, C.; Zhang, L.; Liu, X., Preparation of Monodisperse Mesoporous Carbon Microspheres From Poly(furfuryl alcohol)–Silica Composite Microspheres Produced in a Microfluidic Device. *J. Mater. Chem.* **2011,** *21*, 15049.

(148) Yokoi, T.; Sakamoto, Y.; Terasaki, O.; Kubota, Y.; Okubo, T.; Tatsumi, T., Periodic Arrangement of Silica Nanoparticles Assisted by Amino Acids. *J. Am. Chem. Soc.* **2006,** *128*, 13664-13665.

(149) Vu, A.; Li, X.; Phillips, J.; Han, A.; Smyrl, W. H.; Bühlmann, P.; Stein, A., Three-Dimensionally Ordered Mesoporous (3DOm) Carbon Materials as Electrodes for Electrochemical Double-Layer Capacitors with Ionic Liquid Electrolytes. *Chem. Mater.* **2013,** *25*, 4137-4148.

(150) Meng, Y.; Gu, D.; Zhang, F.; Shi, Y.; Yang, H.; Li, Z.; Yu, C.; Tu, B.; Zhao, D., Ordered Mesoporous Polymers and Homologous Carbon Frameworks: Amphiphilic Surfactant Templating and Direct Transformation. *Angew. Chem. Int. Ed.* **2005,** *44*, 7053-7059.

(151) Meng, Y.; Gu, D.; Zhang, F.; Shi, Y.; Cheng, L.; Feng, D.; Wu, Z.; Cheng, Z.; Wan, Y.; Stein, A.; Zhao, D., A Family of Highly Ordered Mesoporous Polymer Resin and Carbon Structures from Organic-Organic Self-Assembly. *Chem. Mater.* **2006,** *18*, 4447-4464.

(152)   Kim, T.-W.; Kleitz, F.; Paul, B.; Ryoo, R., MCM-48-like Large Mesoporous Silicas with Tailored Pore Structure: Facile Synthesis Domain in a Ternary Triblock Copolymer-Butanol-Water System. *J. Am. Chem. Soc.* **2006,** *127*, 7601-7610.

(153)   Brinker, C. J.; Lu, Y.; Sellinger, A.; Fan, H., Evaporation-Induced Self-Assembly: Nanostructures Made Easy. *Adv. Mater.* **1999,** *11*, 579-585.

(154)   Soler-Illia, G. J.; Crepaldi, E. L.; Grosso, D.; Sanchez, C., Block Copolymer-Templated Mesoporous Oxides. *Curr. Opin. Colloid In.* **2003,** *8*, 109-126.

(155)   Florent, M.; Xue, C.; Zhao, D.; Goldfarb, D., Formation Mechanism of Cubic Mesoporous Carbon Monolith Synthesized by Evaporation-Induced Self Assembly. *Chem. Mater.* **2012,** *24*, 383-392.

(156)   Patarin, J.; Lebeau, B.; Zana, D., Recent Advances in the Formation Mechanisms of Organized Mesoporous Materials. *Curr. Opin. Colloid Interface Sci.* **2002,** *7*, 107-115.

(157)   Deng, Y.; Liu, J.; Liu, C.; Gu, D.; Sun, Z.; Wei, J.; Zhang, J.; Zhang, L.; Tu, B.; Zhao, D., Ultra-Large-Pore Mesoporous Carbons Templated from Poly(ethylene oxide)-*b*-Polystyrene Diblock Copolymer by Adding Polystyrene Homopolymer as a Pore Expander. *Chem. Mater.* **2008,** *20*, 7281-7286.

(158)   Wang, J.; Xue, C.; Lv, Y.; Zhang, F.; Tu, B.; Zhao, D., Kilogram-Scale Synthesis of Ordered Mesoporous Carbons and Their Electrochemical Performance. *Carbon* **2011,** *49*, 4580-4588.

(159)   Tan, Y.; Steinmiller, E. M. P.; Choi, K.-S., Electrochemical Tailoring of Lamellar-Structures ZnO Films by Interfacial Surfactant Templating. *Langmuir* **2005,** *21*, 9618-9624.

(160)   Liu, N.; Song, H.; Chen, X., Morphology Control of Ordered Mesoporous Carbons by Changing HCl Concentration. *J. Mater. Chem.* **2011,** *21*, 5345-5351.

(161)   Xue, C.; Tu, B.; Zhao, D., Evaporation-Induced Coating and Self-Assembly of Ordered Mesoporous Carbon-Silica Composite Monoliths with Macroporous Architecture on Polyurethane Foams. *Adv. Funct. Mater.* **2008,** *18*, 3914-3921.

(162)   Li, N.; Zheng, M.; Feng, S.; Lu, H.; Zhao, B.; Zheng, J.; Zhang, S.; Ji, G.; Cao, J., Fabrication of Hierarchical Macroporous/Mesoporous Carbons via the Dual-Template Method and teh Restriction Effect of Hard Template on Shrinkage of Mesoporous Polymers. *J. Phys. Chem. C* **2013,** *117*, 8704-8792.

(163)   Lai, J. T.; Filla, D.; Shea, R., Functional Polymers from Novel Carboxyl-Terminated Trithiocarbonates as Highly Efficient RAFT Agents. *Macromolecules* **2002,** *35*, 6754-6756.

(164)   Hardwick, L. J.; Ruch, P. W.; Hahn, M.; Scheifele, W.; Kötz, R.; Novák, P., In Situ Raman Spectroscopy of Insertion Electrodes for Lithium-Ion Batteries and Supercapacitors: First Cycle Effects. *J. Phys. Chem. Solids* **2008,** *69*, 1232-1237.

(165)   Gor, G. Y.; Thommes, M.; Cychosz, K. A.; Neimark, A. V., Quenched Solid Density Functional Theory Method for Characterization of Mesoporous Carbons by Nitrogen Adsorption. *Carbon* **2012,** *50*, 1583-1590.

(166)   Kononenko, O. K.; Herstein, K. M., Nonaqueous Solvents for Sucrose. *Chem. Eng. Data Ser.* **1956,** *1*, 1583-1590.

(167)   McNaney, J. A.; Zimmerman, H. K.; Gross, P. H., Ternary System Phase Diagram Determinations Concerning Potassium Electrolyte Influence on Aqueous Solutions of Dioxane or Tetrahydrofuran. In *Thermodynamic Behavior of Electrolytes in Mixed Solvents*, Furter, W., Ed. American Chemical Society: Washington, DC, 1979; pp 177-188.

(168)   Kim, T.-W.; Kleitz, F.; Paul, B.; Ryoo, R., MCM-48-Like Large Mesoporous Silicas with Tailored Pore Structure: Facile Synthesis Domain in a Ternary Triblock Copolymer-Butanol-Water System. *J. Am. Chem. Soc.* **2005,** *127*, 7601-7610.

(169)   Arbizzani, Catia; Biso, Maurizio; Cericola, Dario; Lazzari, Mariachiara; Soavi, Francesca; Mastragostino, Marina, Safe, High-Energy Supercapacitors Based on Solvent-Free Ionic Liquid Electrolytes. *J. Power Sources* **2008,** *185*, 1575-1579.

(170)   Brandt, A.; Balducci, A., Theoretical and Practical Energy Limitations of Organic and Ionic Liquid-Based Electrolytes for High Voltage Electrochemical Double Layer Capacitors. *J. Power Sources* **2014,** *250*, 343-351.

(171)   Galiński, M.; Lewandowski, A.; Stępniak, I., Ionic Liquids as Electrolytes. *Electrochim. Acta* **2006,** *51*, 5567-5580.

(172)   Lazzari, M.; Soavi, F.; Mastragostino, M., Mesoporous Carbon Design for Ionic Liquid-Based, Double-Layer Supercapacitors. *Fuel Cells* **2010,** *10*, 840-847.

(173)   Ue, M.; Takeda, M.; Toriumi, A.; Kominato, A.; Hagiwara, R.; Ito, Y., Application of Low-Viscosity Ionic Liquid to the Electrolyte of Double-Layer Capacitors. *J. Electrochem. Soc.* **2003,** *150*, A499.

(174)   Xu, B.; Hou, S.; Zhang, F.; Cao, G.; Chu, M.; Yang, Y., Nitrogen-Doped Mesoporous Carbon Derived from Biopolymer as Electrode Material for Supercapacitors. *J. Electroanal. Chem.* **2014,** *712*, 146-150.

(175)   Zhong, M.; Kim, E. K.; McGann, J. P.; Chun, S. E.; Whitacre, J. F.; Jaroniec, M.; Matyjaszewski, K.; Kowalewski, T., Electrochemically Active Nitrogen-Enriched Nanocarbons With Well-Defined Morphology Synthesized by Pyrolysis of Self-Assembled Block Copolymer. *J. Am. Chem. Soc.* **2012,** *134*, 14846-57.

(176)   Candelaria, S. L.; Garcia, B. B.; Liu, D.; Cao, G., Nitrogen Modification of Highly Porous Carbon for Improved Supercapacitor Performance. *J. Mater. Chem.* **2012,** *22*, 9884-9889.

(177)   Han, J.; Xu, G.; Ding, B.; Pan, J.; Dou, H.; MacFarlane, D. R., Porous Nitrogen-Doped Hollow Carbon Spheres Derived From Polyaniline For High Performance Supercapacitors. *J. Mater. Chem. A* **2014,** *2*, 5352-5357.

(178) Sun, L.; Tian, C.; Fu, Y.; Yang, Y.; Yin, J.; Wang, L.; Fu, H., Nitrogen-Doped Porous Graphitic Carbon as an Excellent Electrode Material for Advanced Supercapacitors. *Chem. Eur. J.* **2014,** *20*, 564-74.

(179) Hulicova, D.; Yamashita, J.; Soneda, Y.; Hatori, H.; Kodama, M., Supercapacitors Prepared from Meamine-Based Carbon. *Chem. Mater.* **2005,** *17*, 1241-1247.

(180) Wang, X.; Li, X.; Zhang, L.; Yoon, Y.; Weber, P. K.; Wang, H.; Guo, J.; Dai, H., N-Doping of Graphene Through Electrothermal Reactions with Ammonia. *Science* **2009,** *324*, 768-771.

(181) Cao, B.; Zhang, B.; Jiang, X.; Zhang, Y.; Pan, C., Direct Synthesis of High Concentration N-Doped Coiled Carbon Nanofibers From Amine Flames and Its Electrochemical Properties. *J. Power Sources* **2011,** *196*, 7868-7863.

(182) Bulusheva, L. G.; Fedorovskaya, E. O.; Kurenya, A. G.; Okotrub, A. V., Supercapacitor Performance of Nitrogen-Doped Carbon Nanotube Arrays. *Phys. Status Solidi B* **2013,** *250*, 2586-2591.

(183) Yang, C.-M.; Kaneko, K., Adsorption Properties of Nitrogen-Alloyed Activated Carbon Fiber. *Carbon* **2001,** *39*, 1075-1082.

(184) Wu, D.; Li, Z.; Zhong, M.; Kowalewski, T.; Matyjaszewski, K., Templated Synthesis of Nitrogen-Enriched Nanoporous Carbon Materials From Porogenic Organic Precursors Prepared by ATRP. *Angew. Chem. Int. Ed.* **2014,** *53*, 3957-60.

(185) Liang, J.; Du, X.; Gibson, C.; Du, X. W.; Qiao, S. Z., N-Doped Graphene Natively Grown on Hierarchical Ordered Porous Carbon for Enhanced Oxygen Reduction. *Adv. Mater.* **2013,** *25*, 6226-31.

(186) Morelos-Gómez, A.; Mani-González, P. G.; Aliev, A. E.; Muñoz-Sandoval, E.; Herrera-Gómez, A.; Zakhidov, A. A.; Terrones, H.; Endo, M.; Terrones, M., Controlling the Optical, Electrical and Chemical Properties of Carbon Inverse Opal by Nitrogen Doping. *Adv. Funct. Mater.* **2014,** *24*, 2612-2619.

(187) Liu, R.; Wu, D.; Feng, X.; Mullen, K., Nitrogen-Doped Ordered Mesoporous Graphitic Arrays with High Electrocatalytic Activity for Oxygen Reduction. *Angew. Chem. Int. Ed.* **2010,** *49*, 2565-9.

(188) Wang, D.-W.; Li, F.; Yin, L.-C.; Lu, X.; Chen, Z.-G.; Gentle, I. R.; Li, G. Q.; Chen, H.-M., Nitrogen-Doped Carbon Monolith for Alkaline Supercapacitors and Understanding Nitrogen-Induced Redox Transitions. *Chem. Eur. J.* **2012,** *18*, 5345-5351.

(189) Chen, L.-F.; Zhang, X.-D.; Liang, H.-W.; Kong, M.; Guan, Q.-F.; Chen, P.; Wu, Z.-Y.; Yu, S.-H., Synthesis of Nitrogen-Doped Porous Carbon Nanofibers as an Efficient Electrode Material for Supercapacitors. *ACS Nano* **2012,** *6*, 7092-7102.

(190) Qiu, B.; Pan, C.; Qian, W.; Peng, Y.; Qiu, L.; Yan, F., Nitrogen-Doped Mesoporous Carbons Originated From Ionic Liquids as Electrode Materials for Supercapacitors. *J. Mater. Chem. A* **2013,** *1*, 6373-6378.

(191) Zhang, S.; Miran, M. S.; Ikoma, A.; Dokko, K.; Watanabe, M., Protic Ionic Liquids and Salts as Versatile Carbon Precursors. *J. Am. Chem. Soc.* **2014,** *136*, 1690-3.

(192) Paraknowitsch, J. P.; Thomas, A.; Antonietti, M., A Detailed View on the Polycondensation of Ionic Liquid Monomers Towards Nitrogen Doped Carbon Materials. *J. Mater. Chem.* **2010,** *20*, 6746-6748.

(193) Guo, D.-C.; Mi, J.; Hao, G.-P.; Dong, W.; Xiong, G.; Li, W.-C.; Lu, A.-H., Ionic Liquid C_{16}mimBF$_4$ Assisted Synthesis of Poly(benzoxazine-co-resol)-Based Hierarchically Porous Carbons with Superior Performance in Supercapacitors. *Energ. Environ. Sci.* **2013,** *6*, 652-659.

(194) Wang, X.; Dai, S., Ionic liquids as Versatile Precursors for Functionalized Porous Carbon and Carbon-Oxide Composite Materials by Confined Carbonization. *Angew. Chem. Int. Ed.* **2010,** *49*, 6664-8.

(195) Li, Y.-S.; Sun, I. W.; Chang, J.-K.; Su, C.-J.; Lee, M.-T., Doped Butylmethylpyrrolidinium–Dicyanamide Ionic Liquid as an Electrolyte for MnO_2 Supercapacitors. *J. Mater. Chem.* **2012,** *22*, 6274-6279.

(196) Imperato, G.; König, B.; Chiappe, C., Ionic Green Solvents from Renewable Resources. *Eur. J. Org. Chem.* **2007,** *2007*, 1049-1058.

(197) Gor, G. Y.; Thommes, M.; Cychosz, K. A.; Neimark, A. V., Quenched Solid Density Functional Theory Method for Characterization of Mesoporous Carbons by Nitrogen Adsorption. *Carbon* **2012,** *50*, 1583-1590.

(198) Cychosz, K. A.; Guo, X.; Fan, W.; Cimino, R.; Gor, G. Y.; Tsapatsis, M.; Neimark, A. V.; Thommes, M., Characterization of the Pore Structure of Three-Dimensionally Ordered Mesoporous Carbons Using High Resolution Gas Sorption. *Langmuir* **2012,** *28*, 12647-54.

(199) Stoller, M. D.; Ruoff, R. S., Best Practice Methods for Determining an Electrode Material's Performance for Ultracapacitors. *Energ. Environ. Sci.* **2010,** *3*, 1294-1301.

(200) Wilson, B. E.; He, S.; Buffington, K.; Smyrl, W. H; Stein, A., Utilizing Ionic Liquids for Controlled N-Doping in Hard-Templated, Mesoporous Carbon Electrodes for High-Performance Electrochemical Double-Layer Capacitors. *J. Power Sources* **2015,** *298*, 193-202.

(201) Ferrrari, A. C.; Robertson, J., Interpretation of Raman Spectra of Disordered and Amorphous Carbon. *Phys. Rev. B* **2000,** *6*, 14095-15107.

(202) Tuinstra, F.; Koenig, J. L., Raman Spectra of Graphite. *J. Chem. Phys.* **1970,** *53*, 1126-1130.

(203) Ferrrari, A. C.; Robertson, J., Interpretation of Raman Spectra of Disordered and Amorphous Carbon. *Phys. Rev. B* **2000,** *6*, 14095-15107.

(204) Doeff, M. M.; Hu, Y.; McLarnon, F.; Kostecki, R., Effect of Surface Carbon Structure on the Electrochemical Performance of $LiFePO_4$. *Electrochem. Solid St.* **2003,** *6*, A207-A209.

(205) Liu, H.; Zhang, Y.; Li, R.; Sun, X.; Desilets, S.; Abou-Rachid, H.; Jaidann, M.; Lussier, L.-S., Structural and Morphological Control of Aligned Nitrogen-Doped Nanotunes. *Carbon* **2010,** *48*, 1498-1507.

(206) Ayala, P.; Gruneis, A.; Gemming, T.; Grimm, D.; Kramberger, C.; Rummeli, M. H.; LFreire, F. L.; Kuzmany, H.; Pfeiffer, R.; Barreiro, A.; Buhchner, B.; Picher, T., Tailoring N-Doped Single and Double Wall Carbon Nanotubes from a Nondiluted Carbon/Nitrogen Feedstock. *J. Phys. Chem. C* **2007,** *111*, 2879-2884.

(207) Xu, F.; Minniti, M.; Barone, P.; Sindona, A.; Bonanno, A.; Oliva, A., Nitrogen Doping of Single Walled Carbon Nanotrubes by Low Energy N_2^+ Ion Implantation. *Carbon* **2008,** *46*, 1489-1496.

(208) Biniak, S.; Szymanski, G.; Siedlewski, J.; Swiatkowski, A., The Characterization of Activated Carbons with Oxygen and Nitrogen Surface Groups. *Carbon* **1997,** *35*, 1799-1810.

(209) Fuertes, A. B.; Lota, G.; Centeno, T. A.; Frackowiack, E., Templated Mesoporous Carbons for Supercapacitor Application. *Electrochim. Acta* **2005,** *50*, 2799-2805.

(210) Ricketts, B. W.; Ton-That, C., Self-Discharge of Carbon-Based Supercpacitors With Organic Electrolytes. *J. Power Sources* **2000,** *89*, 64-69.

(211) Jeong, H. M.; Lee, J. W.; Shin, W. H.; Choi, Y. J.; Shin, H. J.; Kang, J. K.; Choi, J. W., Nitrogen-Doped Graphene For High-Performance Ultracapacitors and The Importance of Nitrogen-Doped Sites at Basal Planes. *Nano Lett.* **2011,** *11*, 2472-2477.

(212) Lewandowski, A.; Galiński, M., Carbon–Ionic Liquid Double-Layer Capacitors. *J. Phys. Chem. Solids* **2004,** *65*, 281-286.

(213) Zhang, S.; Dokko, K.; Watanabe, M., Direct Synthesis of Nitrogen-Doped Carbon Materials from Protic Ionic Liquids and Protic Salts: Structural and Physicochemical Correlations between Precursor and Carbon. *Chem. Mater.* **2014,** *26*, 2915-2926.

(214) Walcarius, A., Mesoporous Materials and Electrochemistry. *Chem. Soc. Rev.* **2013,** *42*, 4098-4140.

(215) Zhai, Y. P.; Dou, Y. Q.; Zhao, D. Y.; Fulvio, P. F.; Mayes, R. T.; Dai, S., Carbon Materials for Chemical Capacitive Energy Storage. *Adv. Mater.* **2011,** *23*, 4828-4850.

(216) MacFarlane, D. R.; Tachikawa, N.; Forsyth, M.; Pringle, J. M.; Howlett, P. C.; Elliott, G. D.; Davis, J. H.; Watanabe, M.; Simon, P.; Angell, C. A., Energy Applications of Ionic Liquids. *Energ. Environ. Sci.* **2014,** *7*, 232-250.

(217) Stoller, M. D.; Park, S. J.; Zhu, Y. W.; An, J. H.; Ruoff, R. S., Graphene-Based Ultracapacitors. *Nano lett.* **2008,** *8*, 3498-3502.

(218) Barbieri, O.; Hahn, M.; Herzog, A.; Kotz, R., Capacitance Limits of High Surface Area Activated Carbons for Double Layer Capacitors. *Carbon* **2005,** *43*, 1303-1310.

(219) Sato, T.; Masuda, G.; Takagi, K., Electrochemical Properties of Novel Ionic Liquids for Electric Double Layer Capacitor Applications. *Electrochim. Acta* **2004,** *49*, 3603-3611.

(220) Kotz, R.; Carlen, M., Principles and Applications of Electrochemical Capacitors. *Electrochim. Acta* **2000,** *45*, 2483-2498.

(221) Lewandowski, A.; Galinski, M., Carbon-Ionic Liquid Double-Layer Capacitors. *J. Phys. Chem. Solids* **2004,** *65*, 281-286.

(222) Xing, W.; Qiao, S. Z.; Ding, R. G.; Li, F.; Lu, G. Q.; Yan, Z. F.; Cheng, H. M., Superior Electric Double Layer Capacitors Using Ordered Mesoporous Carbons. *Carbon* **2006,** *44*, 216-224.

(223) Jeong, H. M.; Lee, J. W.; Shin, W. H.; Choi, Y. J.; Shin, H. J.; Kang, J. K.; Choi, J. W., Nitrogen-Doped Graphene for High-Performance Ultracapacitors and the Importance of Nitrogen-Doped Sites at Basal Planes. *Nano Lett.* **2011,** *11*, 2472-2477.

(224) Olson, E. J.; Buhlmann, P., Unbiased Assessment of Electrochemical Windows: Minimizing Mass Transfer Effects on the Evaluation of Anodic and Cathodic Limits. *J. Electrochem. Soc.* **2013,** *160*, A320-A323.

(225) Wu, H.; Wang, X.; Jiang, L.; Wu, C.; Zhao, Q.; Liu, X.; Hu, B.; Yi, L., The Effects of Electrolyte on the Supercapacitive Performance of Activated Calcium Carbide-Derived Carbon. *J. Power Sources* **2013,** *226*, 202-209.

(226) Lewandowski, A.; Swiderska, A., Electrochemical Capacitors with Polymer Electrolytes Based on Ionic Liquids. *Solid State Ionics* **2003,** *161*, 243-249.

(227) Wei, D.; Ivaska, A., Applications of Ionic Liquids in Electrochemical Sensors. *Anal. Chim. Acta* **2008,** *607*, 126-135.

(228) De Vos, N.; Maton, C.; Stevens, C. V., Electrochemical Stability of Ionic Liquids: General Influences and Degradation Mechanisms. *ChemElectroChem* **2014,** *1*, 1258-1270.

(229) Yuyama, K.; Masuda, G.; Yoshida, H.; Sato, T., Ionic Liquids Containing the Tetrafluoroborate Anion Have the Best Performance and Stability for Electric Double Layer Capacitor Applications. *J. Power Sources* **2006,** *162*, 1401-1408.

(230) Ue, M.; Takeda, M.; Toriumi, A.; Kominato, A.; Hagiwara, R.; Ito, Y., Application of Low-Viscosity Ionic Liquid to the Electrolyte of Double-Layer Capacitors. *J. Electrochem. Soc.* **2003,** *150*, A499-A502.

(231) Montanino, M.; Carewska, M.; Alessandrini, F.; Passerini, S.; Appetecchi, G. B., The Role of the Cation Aliphatic Side Chain Length in Piperidinium Bis(trifluoromethansulfonyl)imide Ionic Liquids. *Electrochim. Acta* **2011,** *57*, 153-159.

(232) Lang, C. M.; Kim, K.; Guerra, L.; Kohl, P. A., Cation Electrochemical Stability in Chloroaluminate Ionic Liquids. *J. Phys. Chem. B* **2005,** *109*, 19454-19462.

(233)   Fitchett, B. D.; Knepp, T. N.; Conboy, J. C., 1-Alkyl-3-methylimidazolium Bis(perfluoroalkylsulfonyl)imide Water-Immiscible Ionic Liquids - The Effect of Water on Electrochemical and Physical Properties. *J. Electrochem. Soc.* **2004,** *151*, E219-E225.

(234)   Appetecchi, G. B.; Montanino, M.; Zane, D.; Carewska, M.; Alessandrini, F.; Passerini, S., Effect of the Alkyl Group on the Synthesis and the Electrochemical Properties of N-alkyl-N-methyl-pyrrolidinium Bis(trifluoromethanesulfonyl)imide Ionic Liquids. *Electrochim. Acta* **2009,** *54*, 1325-1332.

(235)   Lockett, V.; Sedev, R.; Ralston, J.; Horne, M.; Rodopoulos, T., Differential Capacitance of the Electrical Double Layer in Imidazolium-Based Ionic Liquids: Influence of Potential, Cation Size, and Temperature. *J. Phys. Chem. C* **2008,** *112*, 7486-7495.

(236)   Yoshimura, M.; Honda, K.; Kondo, T.; Uchikado, R.; Einaga, Y.; Rao, T. N.; Tryk, D. A.; Fujishima, A., Factors Controlling the Electrochemical Potential Window for Diamond Electrodes in Non-Aqueous Electrolytes. *Diamond Relat. Mater.* **2002,** *11*, 67-74.

(237)   Liu, H.; Zhu, G., The Electrochemical Capacitance of Nanoporous Carbons in Aqueous and Ionic Liquids. *J. Power Sources* **2007,** *171*, 1054-1061.

(238)   Bedrov, D.; Vatamanu, J.; Hu, Z., Ionic Liquids at Charged Surfaces: Insight From Molecular Simulations. *J. Non-Cryst. Solids* **2015,** *407*, 339-348.

(239)   Gryglewicz, G.; Machnikowski, J.; Lorenc-Grabowska, E.; Lota, G.; Frackowiak, E., Effect of Pore Size Distribution of Coal-Based Activated Carbons on Double Layer Capacitance. *Electrochim. Acta* **2005,** *50*, 1197-1206.

(240)   Largeot, C.; Portet, C.; Chmiola, J.; Taberna, P. L.; Gogotsi, Y.; Simon, P., Relation Between the Ion Size and Pore Size for an Electric Double-Layer Capacitor. *J. Am. Chem. Soc.* **2008,** *130*, 2730-2731.

(241)   Mousavi, M. P. S.; Wilson, B. E.; Hu, J.; Stein, A.; Bühlmann, P., Unbiased Quantification of the Electrochemical Stability Limits of Electrolytes and Ionic Liquids. *J. Electrochem. Soc.* **2015,** *162*, A2250-A2258.

(242)   Vu, A.; Li, X. Y.; Phillips, J.; Han, A. J.; Smyrl, W. H.; Buhlmann, P.; Stein, A., Three-Dimensionally Ordered Mesoporous (3DOm) Carbon Materials as Electrodes for Electrochemical Double-Layer Capacitors with Ionic Liquid Electrolytes. *Chem. Mater.* **2013,** *25*, 4137-4148.

(243)   Mousavi, M. P. S.; Buhlmann, P., Reference Electrodes with Salt Bridges Contained in Nanoporous Glass: An Underappreciated Source of Error. *Anal. Chem.* **2013,** *85*, 8895-8901.

(244)   Becke, A. D., Density-Functional Exchange-Energy Approximation with Correct Asymptotic-Behavior. *Phy.s Rev. A* **1988,** *38*, 3098-3100.

(245) Lee, C.; Yang, W.; Parr, R. G., Development of the Colle-Salvetti Correlation-Energy Formula Into a Functional of the Electron Density. *Phys. Rev. B* **1988,** *37*, 785-789.

(246) Becke, A. D., Density-Functional Thermochemistry 3. The Role of Exact Exchange. *J Chem Phys* **1993,** *98*, 5648-5652.

(247) Frisch, M. J.; Trucks, G. W.; Schlegel, H. B.; Scuseria, G. E.; Robb, M. A.; Cheeseman, J. R.; Montgomery, Jr., J. A.; Vreven, T.; Kudin, K. N.; Burant, J. C.; Millam, J. M.; Iyengar, S. S.; Tomasi, J.; Barone, V.; Mennucci, B.; Cossi, M.; Scalmani, G.; Rega, N.; Petersson, G. A.; Nakatsuji, H.; Hada, M.; Ehara, M.; Toyota, K.; Fukuda, R.; Hasegawa, J.; Ishida, M.; Nakajima, T.; Honda, Y.; Kitao, O.; Nakai, H.; Klene, M.; Li, X.; Knox, J. E.; Hratchian, H. P.; Cross, J. B.; Bakken, V.; Adamo, C.; Jaramillo, J.; Gomperts, R.; Stratmann, R. E.; Yazyev, O.; Austin, A. J.; Cammi, R.; Pomelli, C.; Ochterski, J. W.; Ayala, P. Y.; Morokuma, K.; Voth, G. A.; Salvador, P.; Dannenberg, J. J.; Zakrzewski, V. G.; Dapprich, S.; Daniels, A. D.; Strain, M. C.; Farkas, O.; Malick, D. K.; Rabuck, A. D.; Raghavachari, K.; Foresman, J. B.; Ortiz, J. V.; Cui, Q.; Baboul, A. G.; Clifford, S.; Cioslowski, J.; Stefanov, B. B.; Liu, G.; Liashenko, A.; Piskorz, P.; Komaromi, I.; Martin, R. L.; Fox, D. J.; Keith, T.; Al-Laham, M. A.; Peng, C. Y.; Nanayakkara, A.; Challacombe, M.; Gill, P. M. W.; Johnson, B.; Chen, W.; Wong, M. W.; Gonzalez, C.; Pople, J. A. *Gaussian 03, Revision C.02*, Gaussian 03, Revision C.02, Gaussian Inc.: Wallingford CT, 2004.

(248) Stephens, P. J.; Devlin, F. J.; Chabalowski, C. F.; Frisch, M. J., Ab Initio Calculation of Vibrational Absorption and Circular Dichroism Spectra Using Density Functional Force Fields. *J. Phys. Chem.* **1994,** *98*, 11623-11627.

(249) Lu, T.; Chen, F., Multiwfn: A Multifunctional Wavefunction Analyzer. *J. Computat. Chem.* **2012,** *33*, 580-592.

(250) Xu, K.; Ding, M. S.; Jow, T. R., Quaternary Onium Salts as Nonaqueous Electrolytes for Electrochemical Capacitors. *J. Electrochem. Soc.* **2001,** *148*, A267.

(251) Zhou, Z. B.; Matsumoto, H.; Tatsumi, K., Low-Melting, Low-Viscous, Hydrophobic Ionic Liquids: Aliphatic Quaternary Ammonium Salts With Perfluoroalkyltrifluoroborates. *Chemistry* **2005,** *11*, 752-66.

(252) Liu, C.; Xu, F.; Feng, S.; Zheng, L.; Zhang, H.; Feng, W.; Huang, X.; Armand, M.; Nie, J.; Zhou, Z., New Hydrophobic Ionic Liquids Based on (fluorosulfonyl)(polyfluorooxaalkanesulfonyl)imides With Various Oniums. *Electrochim. Acta* **2013,** *99*, 262-272.

(253) Fang, S.; Jin, Y.; Yang, L.; Hirano, S.; Tachibana, K.; Katayama, S., Functionalized Ionic Liquids Based on Quaternary Ammonium Cations With Three or Four Ether Groups as New Electrolytes for Lithium Battery. *Electrochim. Acta* **2011,** *56*, 4663-4671.

(254) Zhou, Z. B.; Matsumoto, H.; Tatsumi, K., Cyclic Quaternary Ammonium Ionic Liquids with Perfluoroalkyltrifluoroborates: Synthesis, Characterization, and Properties. *Chemistry* **2006,** *12*, 2196-212.

(255)   Lang, C. M.; Kohl, P. A., Investigation of Ether-Substituted Quaternary Ammonium Ionic Liquids. *J. Electrochem. Soc.* **2007,** *154*, F106.

(256) Mousavi, M. P. S.; Kashefolgheta, S.; Stein, A.; Bühlmann, P., Electrochemical Stability of Quaternary Ammonium Cations: An Experimental and Computational Study. *J. Electrochem. Soc.* **2016,** *163*, H1-H7.

(257) Mousavi, M. P. S.; Wilson, B. E.; Kashefolgheta, S.; Anderson, E.; He, S.; Bühlmann, P.; Stein, A., Ionic Liquids as Electrolytes for Electrochemical Double-Layer Capacitors: Structures that Optimize Specific Energy. *ACS Appl. Mater. Interfaces*, DOI: 10.1021/acsami.5b11353.

(258) Wilson, B. E.; He, S. Y.; Buffington, K.; Rudisill, S.; Smyrl, W. H.; Stein, A., Utilizing Ionic Liquids for Controlled N-Doping in Hard-Templated, Mesoporous Carbon Electrodes for High-Performance Electrochemical Double-Layer Capacitors. *J. Power Sources* **2015,** *298*, 193-202.

(259) McLin, M. G.; Angell, C. A., Ion-Pairing Effects on Viscosity/Conductance Relations in Raman-Characterized Polymer Electrolytes: $LiClO_4$ and $NaCF_3SO_3$ in PPG(4000). *J. Phys. Chem.* **1991,** *95*, 9464-9469.

(260) Fierke, M. A.; Lai, C. Z.; Buhlmann, P.; Stein, A., Effects of Architecture and Surface Chemistry of Three-Dimensional Ordered Macroporous Carbon Solid Contacts on Performance of Ion-Selective Electrodes. *Anal. Chem.* **2010,** *82*, 680-688.

(261) Thackeray, M. M.; Vaughey, J. T.; Johnson, C. S.; Kropf, A. J.; Benedek, R.; Fransson, L. M. L.; Edstrom, K., Structrual Considerations of Intermetallic Electrodes for Lithium Batteries. *J. Power Sources* **2003,** *113*, 124-130.

(262) Novak, P.; Panitz, J.-C.; Joho, F.; Lanz, M.; Imhof, R.; Coluccia, M., Advanced In Situ Methods for the Characterization of Practical Electrodes in Lithium-Ion Batteries. *J. Power Sources* **2000,** *90*, 52-58.

(263) Arakawa, M.; Tobishima, S.; Nemoto, Y.; Ichimura, M., Lithium Electrode Cycleability and Morphology Dependence on Current Density. *J. Power Sources* **1993,** *43-44*, 27-35.

(264) Rosso, M.; Brissot, C.; Teyssot, A.; Dolle, M.; Sannier, L.; Tarascon, J.-M.; Bouchet, R.; Lascaud, S., Dentrite Short-Circuit and Fuse Effect on Li/Polymer/Li Cells. *Electrochim. Acta* **2006,** *51*, 5334-5340.

(265) Baudry, P.; Armand, M.; Gauthier, M.; Masoinave, J., In Situ Observation By SEM of Positive Composite Electrodes During Discharge of Polymer Lithium Batteries. *Solid State Ionics* **1988,** *28-30*, 1567-1571.

(266) Raimann, P. R.; Hochgatterer, N. S.; Korepp, C.; Moeller, K. C.; Winter, M.; Schroettner, H.; Hofer, F.; Besenhard, J. O., Monitoring Dynamics of Electrode Reactions in Li-ion Batteries by In Situ ESEM. *Ionics* **2006,** *12*, 253-255.

(267) Chen, D.; Indris, S.; Schulz, M.; Gamer, B.; Moenig, R., In Situ Scanning Electron Microscopy on Lithium-Ion Battery Electrodes Using an Ionic Liquid. *J. Power Sources* **2011,** *196*, 6382-6387.

(268) Liu, X. H.; Huang, J. Y., In Situ TEM Electrochemistry of Anode Materials in Lithium Ion Batteries. *Energ. Environ. Sci.* **2011,** *4*, 3844-3860.

(269) Hirasawa, K. A.; Sato, T.; Asahina, H.; Yamaguchi, S.; Mori, S., In Situ Electrochemical Atomic Force Microscope Study on Graphite Electrodes. *J. Electrochem. Soc.* **1997,** *144*, L81-L84.

(270) Orikasa, Y.; Maeda, T.; Koyama, Y.; Minato, T>; Murayama, H.; Fukada, K.; Tanida, H.; Arai, H.; Matsubara, E.; Uchimoto, Y.; Ogumi, Z., Phase Transition Analysis between $LiFePO_4$ and $FePO_4$ by In-Situ Time-Resolved X-ray Absoruption and X-ray Diffraction. *J. Electrochem. Soc.* **2013,** *160*, A3061-A3065.

(271) Balasubramanian, M.; Sun, X.; Yang, X. Q.; McBreen, J., In Situ X-ray Diffraction and X-ray Absorption Studies of High-Rate Lithium-Ion Batteries. *J. Power Sources* **2001,** *92*, 1-8.

(272) Nakai, I.; Nakagome, T., In Situ Transmission X-Ray Absorption Fine Structure Analysis of the Li Deintercalation Process in $Li(Ni_{0.5}Co_{0.5})O_2$. *Electrochem. Solid-State Lett.* **1998,** *1*, 259-261.

(273) Hardwick, L. J.; Ruch, P. W.; Hahn, M.; Scheifele, W.; Koetz, R.; Novak, P., In Situ Raman Spectroscopy of Insertion Electrodes for Lithium-Ion Batteries and Supercapacitors: First Cycle Effects. *J. Phys. Chem. Solids* **2008,** *69*, 1232-1237.

(274) Kong, F.; Kostecki, R.; Nadeau, G.; Song, X.; Zaghib, K.; Kinoshita, K.; McLarnon, F., In Situ Studies of SEI Formation. *J. Power Sources* **2001,** *97-98*, 58-66.

(275) Wuersig, A.; Scheifele, W.; Novak, P., CO_2 Gas Evolution on Cathode Materials for Lithium-Ion Batteries. *J. Electrochem. Soc.* **2007,** *154*, A449-A454.

(276) Lee, S. H.; Jung, J.-M.; Ok, J. .; Park, C.-H., Thermal Studies of Charged Cathode Material (Li_xCoO_2) with Temperature-Programmed Decomposition-Mass Spectrometry. *J. Power Sources* **2010,** *195*, 5049-5051.

(277) Gachot, G.; Ribiere, P.; Mathiron, D.; Grugeon, S.; Armand, M.; Leriche, J. B.; Pilard, S.; Laruelle, S., Gas Chromatography/Mass Spectrometry As a Suitable Tool for the Li-Ion Battery Electrolyte Degradation Mechanisms Study. *Anal. Chem.* **2011,** *89*, 478-485.

(278) Key, B.; Bhattacharyya, R.; Morcrette, M.; Seznec, V.; Tarascon, J.-M.; Grey, C. P., Real-Time NMR Investigations of Structural Changes In Silicon Electrodes for Lithium-Ion Batteries. *J. Am. Chem. Soc.* **2009,** *131*, 9239-9249.

(279) Bhattacharyya, R.; Key, B.; Chen, H.; Best, A. S.; Hollenkamp, A. F.; Grey, C. P., In Situ NMR Observation of the Formation of Metallic Lithium Microstructures in Lithium Batteries. *Nat. Mater.* **2010,** *9*, 504-510.

(280) Rhodes, K.; Kirkham, M.; Meisner, R.; Parish, C. M.; Dudney, N.; Daniel, C., Novel Cell Design for Combined In Situ Acoustic Emission and X-ray Diffraction Study During Electrochemical Cycling of Batteries. *Rev. Sci. Instrum.* **2011,** *82*, 075107.

(281) Morcrette, M.; Chabre, Y.; Vaughan, G.; Amatucci, G.; Leriche, J.-B.; Patoux, S.; Masquelier, C.; Tarascon, J.-M., In Situ X-ray Diffraction Techniques as a Powerful Tool to Study Battery Electrode Materials. *Electrochim. Acta* **2002,** *47*, 3137-3149.

(282) Chianelli, R. R.; Scanlon, J. C.; Rao, B. M. L., Dynamic X-Ray Diffraction. *J. Electrochem. Soc.* **1978,** *125*, 1563-1566.

(283) Dahn, J. R.; Py, M. A.; Haering, R. R., In situ X-ray Diffraction Experiments on Lithium Intercalaction Compounds. *Can. J. Phys.* **1982,** *60*, 307-313.

(284) Roberts, G. A.; Stewart, K. D., Reflection-Mode X-ray Powder Diffraction Cell for In Situ Studies of Electrochemical Reactions. *Rev. Sci. Instrum.* **2004,** *75*, 1251-1254.

(285) Richard, M. N.; Koetschau, I.; Dahn, J. R., A Cell for In Situ X-Ray Diffraction Based on Coin Cell Hardware and Bellcore Plastic Electrode Technology. *J. Electrochem. Soc.* **1997,** *144*, 554-557.

(286) Li, J.; Dahn, J. R., An In Situ X-Ray Diffraction Study of the Reaction of Li with Crystalline Si. *J. Electrochem. Soc.* **2007,** *154*, A156-A161.

(287) Braun, A.; Shrout, S; Fowlks, A. C.; Osaisai, B. A.; Seifert, S.; Granlund, E.; Caims, E. J., Electrochemical In Situ Reaction Cell for X-ray Scattering, Diffraction and Spectroscopy. *J. Synchrotron Rad.* **2003,** *10*, 320-325.

(288) Leriche, J. B.; Hamelet, S.; Shu, J.; Morcrette, M.; Masquelier, C.; Ouvrard, G.; Zerrouki, M.; Soudan, P.; Belin, S.; Elkaim, E.; Baudelet, An Electrochemical Cell of Perando Study of Lithium Batteries Using Synchrotron Radiation. *J. Electrochem. Soc.* **2010,** *157*, A606-A610.

(289) Zhao, H.; Einarsrud, M.-A.; Vullum-Bruer, F., In Situ X-ray Diffraction and Electrochemical Impedance Spectroscopy of a Nanoporous Li_2FeSiO_4/C Cathode During Initial Charge/Discharge Cycle of a Li-Ion Battery. *J. Power Sources* **2013,** *238*, 478-484.

(290) Aurbach, D.; Ein-Eli, Y., The Study of Li-Graphite Intercalation Processes in Several Electrolyte Systems Using In Situ X-Ray Diffraction. *J. Electrochem. Soc.* **1995,** *142*, 1746-1752.

(291) Shin, H. C.; Park, S. B.; Jang, H.; Chung, K. Y.; Cho, W. I.; Kim, C. S.; Cho, B. W., Rate Performance and Structrual Change of Cr-Doped $LiFePO_4$/C During Cycling. *Electrochim. Acta* **2008,** *53*, 7946-7951.

(292) Meulenkamp, E. A., An Electrochemical Cell for Simultaneous In Situ X-Ray Diffraction and Optical Measurements. *J. Electrochem. Soc.* **1998,** *145*, 2759-2762.

(293) Bergstrom, O.; Gustafsson, T.; Thomas, J. O., An X-ray Powder Diffraction Attachment for In Situ Studies of Ion Insertion Processes in Electrode Materials. *J. Appl. Crystallogr.* **1998,** *31*, 103-105.

(294)   Shin, H. C.; Chung, K. Y.; Min, W. S.; Byun, D. J.; Jang, H.; Cho, B. W., Asymmetry Between Charge and Discharge During High Rate Cycling in LiFePO$_4$ - In Situ X-ray Diffraction Study. *Electrochem. Commun.* **2008,** *10*, 536-540.

(295)   Yang, X.-Q.; Sun, X.; Lee, S. J.; McBreen, J.; Mukerjee, S.; Daroux, M. L.; Xing, X. K., In Situ Synchrotron X-Ray Diffraction Studies of the Phase Transitions in Li$_x$Mn$_2$O$_4$ Cathode Materials. *Electrochem. Solid-State Lett.* **1999,** *2*, 157-160.

(296)   Levi, E.; Levi, M. D.; Salitra, G.; Aurbach, D.; Oesten, R.; Heider, U.; Heider, L., Electrochemical and In-Situ XRD Characterization of LiNiO$_2$ and LiCo$_{0.2}$Ni$_{0.8}$O$_2$ Electrodes for Rechargeable Lithium Cells. *Solid State Ionics* **1999,** *126*, 97-108.

(297)   Andersson, A. S.; Thomas, J. O., The Source of First-Cycle Capacity Loss in LiFePO$_4$. *J. Power Sources* **2001,** *97-98*, 498-502.

(298)   Andersson, A. S.; Kalska, B.; Haggstrom, L.; Thomas, J. O., Lithium Extraction/Insertion in LiFePO$_4$: and X-ray Diffraction and Mossbauer Spectroscopy Study. *Solid State Ionics* **2000,** *130*, 41-52.

(299)   Chang, H.-H.; Chang, C.-C.; Wu, H.-C.; Yang, M.-H.; Sheu, H.-S.; Wu, N.-L., Study on Dynamics of Structrual Transformation During Charge/Discharge of LiFePO$_4$ Cathode. *Electrochem. Commun.* **2008,** *10*, 335-339.

(300)   Wheldon, J.; Lee, W.-J.; Lim, D.-H.; Broste, A. B.; Bollinger, M.; Smyrl, W. H., High-Performance Flexible Miniature Fuel Cell. *Electrochem. Solid-State Lett.* **2009,** *12*, B86-B89.

(301)   Wakihara, M.; Yamamoto, O., *Lithium Ion Batteries: Fundamentals and Performance*. Wiley: New York: Kodansha, Tokyo, 1998.

(302)   Huggins, R. A., *Advanced Batteries: Materials Science Aspects*. Springer: New York: 2009.

(303)   *Lithium-Ion Batteries: Advanced Materials and Technologies*. CRC Press: Boca Raton, FL, 2011.

(304)   Zheng, J. M.; Xiao, J.; Yu, X. Q.; Kovarik, L.; Gu, M.; Omenya, F.; Chen, X. L.; Yang, X. Q.; Liu, J.; Graff, G. L.; Whittingham, M. S.; Zhang, J. G., Enhanced Li$^+$ Ion Transport in LiNi$_{0/5}$Mn$_{1.5}$O$_4$ Through Control of Site Disorder. *Phys. Chem. Chem. Phys.* **2012,** *14*, 13515-13521.

(305)   Manthiram, A.; Murugan, A. V.; Sarkar, A.; Muraliganth, T., Nanostructured Electrode Materials for Electrochemical Energy Storage and Conversion. *Energy Environ. Sci.* **2008,** *1*, 621-638.

(306)   Vu, A.; Qian, Y. Q.; Stein, A., Porous Electrode Materials for Lithium-Ion Batteries - How to Prepare Them and What Makes Them Special. *Adv. Energy Mater.* **2012,** *2*, 1056-1085.

(307)   Cho, Y. J.; Kim, C. H.; Im, H. S.; Myung, Y.; Kim, H. S.; Back, S. H.; Lim, Y. R.; Jung, C. S.; Jang, D. M.; Park, J.; Lim, S. H.; Cha, E. H.; Bae, K. Y.; Song, M. S.; Cho,

W. I. , Germanium-Tin Alloy nanocrystals for High Performance Lithium Ion Batteries. *Phys. Chem. Chem. Phys.* **2013,** *15*, 11691-11695.

(308) Fisher, C. A. J.; Islam, M. S., Surface Structures and Crystal Morphologies of $LiFePO_4$: Relevance to Electrochemical Behaviour. *J. Mater. Chem.* **2008,** *18*, 1209-1215.

(309) Kuganathan, N.; Islam, M. S., Li_2MnSiO_4 Lithium Battery Material: Atomic-Scale Study of Defects, Lithium Mobility, and Trivalent Dopants. *Chem. Mater.* **2009,** *21*, 5196-5202.

(310) Adams, S.; Rao, R. P., Ion Transport and Phase Transition in $Li_{7-x}La_3(Zr_{2-x}M_x)O_{12}$ ($M = Ta^{5+}$, Nb^{5+}, x = 0, 0.25). *J. Mater. Chem.* **2012,** *22*, 1426-1434.

(311) Meng, Y. S.; Arroyo-de Dompablo, M. E., First Principles Computational Materials Design for Energy Storage Materials in Lithium Ion Batteries. *Energy Environ. Sci.* **2009,** *2*, 589-609.

(312) Ceder, G., Opportunities and Challenges for First-Principles Materials Design and Applications to Li Battery Materials. *MRS Bull.* **2010,** *35*, 693-701.

(313) Ceder, G.; Hautier, G.; Jain, A.; Ong, S. P., Recharging Lithium Battery Research With First-Principles Methods. *MRS Bull.* **2011,** *36*, 185-191.

(314) Tang, Q.; Zhou, Z.; Shen, P., Are MXenes Promising Anode Materials for Li Ion Batteries? Computational Studies on Electronic Properties and Li Storage Capability of Ti_3C_2 and $Ti_3C_2X_2$ (X = F, OH) Monolayer. *J. Am. Chem. Soc.* **2012,** *134*, 16909-16916.

(315) Li, Y.; Wu, D.; Zhou, Z.; Cabrera, C. R.; Chen, Z., Enhanced Li Adsorption and Diffusion on MoS_2 Zigzag Nanoribbons by Edge Effects: A Computational Study. *J. Phys. Chem. Lett.* **2012,** *3*, 2221-2227.

(316) Yu, J.; Zhou, Z.; Cabrera, C. R.; Chen, Z., Metallic VS_2 Monolayer: A Promising 2D Anode Material for Lithium Ion Batteries. *J. Phys. Chem. C* **2013,** *117*, 25409-15413.

(317) Bao, J.; Wu, D.; Tang, Q.; Ma, Z.; Zhou, Z., First-Principles Investigations on Delithiation of Li_4NiTeO_6. *Phys. Chem. Chem. Phys.* **2014,** *16*, 16145-16149.

(318) Van der Ven, A.; K., Aydinol. M.; Ceder, G.; Kresse, G.; Hafner, J., First-Principles Investigation of Phase Stability in Li_xCoO_2. *Phys. Rev. B* **1998,** *58*, 2975-2987.

(319) Ceder, G.; Van der Ven, A., Phase Diagrams of Lithium Transition Metal Oxides: Investigations from First Principles. *Electrochim. Acta* **1999,** *45*, 131-150.

(320) Van der Ven, A.; Ceder, G., Lithium Diffusion Mechanisms in Layered Intercalation Compounds. *J. Power Sources* **2001,** *97-8*, 529-531.

(321) Bhattacharya, J.; Van der Ven, A., Phase Stability and Nondilute Li Diffusion in Spinel $Li_{1+x}Ti_2O_4$. *Phys. Rev. B* **2010,** *81*, 104304.

(322) Van der Ven, A.; Marianetti, C.; Morgan, D.; Ceder, G., Phase Transformations and Volume Changes in Spinel $Li_xMn_2O_4$. *Solid State Ionics* **2000,** *135*, 21-32.

(323) Van der Ven, A.; Thomas, J. C.; Xu, Q. C.; Swoboda, B.; Morgan, D., Nondilute Diffusion From First Principles: Li Diffusion in Li_xTiS_2. *Phys. Rev. B* **2008,** *78*, 104306.

(324) Yu, J. G.; Rosso, K. M.; Zhang, J. G.; Liu, J., *Ab Initio* Study of Lithium Transition Metal Fluorophosphate Cathodes for Rechargeable Batteries. *J. Mater. Chem.* **2011,** *21*, 12054-12058.

(325) Arroyo-de Dompablo, M. E.; Dominko, R.; Gallardo-Amores, J. M.; Dupont, L.; Mali, G.; Ehrenberg, H.; Jamnik, J.; Moran, E., On the Energetic Stability and Electrochemistry of Li_2MnSiO_4 Polymorphs. *Chem. Mater.* **2008,** *20*, 5574-5584.

(326) Eames, C.; Armstrong, A. R.; Bruce, P. G.; Islam, M. S., Insights into Changes in Voltage and Structure of Li_2FeSiO_4 Polymorphs for Lithium-Ion Batteries. *Chem. Mater.* **2012,** *24*, 2155-2161.

(327) Saracibar, A.; Van der Ven, A.; Arroyo-de Dompablo, M. E., Crystal Structure, Energetics, And Electrochemistry of Li_2FeSiO_4 Polymorphs from First Principles Calculations. *Chem. Mater.* **2012,** *24*, 495-503.

(328) Santamaria-Perez, D.; Amador, U.; Tortajada, J.; Dominko, R.; Arroyo-de Dompablo, M. E., High-Pressure Investigation of Li_2MnSiO_4 and Li_2CoSiO_4 Electrode Materials for Lithium-Ion Batteries. *Inorg. Chem.* **2012,** *51*, 5779-5786.

(329) Longo, R. C.; Xiong, K.; Cho, K., Multicomponent Silicate Cathode Materials for Rechargeable Li-Ion Batteries: An *Ab Initio* Study. *J. Electrochem. Soc.* **2013,** *160*, A60-A65.

(330) Kohn, W.; L., Sham., Self-Consistent Equations Including Exchange and Correlation Effects. *Phys. Rev.* **1965,** *140*, A1133-A1138.

(331) Zou, Y.; Petric, A., Thermodynamic Stability of the Lithium Zirconates and Lithium Yttrate. *J. Phys. Chem. Solids* **1994,** *55*, 493-499.

(332) Duan, Y., Structural and Electronic Properties of Li_8ZrO_6 and its CO_2 Capture Capabilities: An *Ab Initio* Thermodynamic Approach. *Phys. Chem. Chem. Phys.* **2013,** *15*, 9752-9760.

(333) Duan, Y., Electronic Structural and Electrochemical Properties of Lithium Zirconates and Their Capabilities of CO_2 Capture: A First-Principles Density-Functional Theory and Phonon Dynamics Approach. *J. Renew. Sust. Energy* **2011,** *3*, 013102.

(334) Yin, X.-S.; Zhang, Q.-H.; Yu, J.-G., Three-Step Calcination Synthesis of High-Purity Li_8ZrO_6 with CO_2 Absorption Properties. *Inorg. Chem.* **2011,** *50*, 2844-2850.

(335) Jiang, S.; Stangle, G. C.; Amarakoon, V. R. W.; Schulze, W. A., Synthesis of Yttria-Stabilized Zirconia Nanoparticles by Decomposition of Metal Nitrates Coated on Carbon Powder. *J. Mater. Res.* **1996,** *11*, 2318-2324.

(336) Gobapalan, R.; Chang, C.-H.; Lin, Y. S., Thermal Stability Improvement on Pore and Phase Structure of Sol-Gel Derived Zirconia. *J. Mater. Sci.* **1995,** *30*, 3075.

215

(337) Kubelka, P.; Munk, F. Z., A Contribution to the Optics of Pigments. *Tech. Phys.* **1931,** *12*, 593-601.

(338) López, R.; Gómez, R., Band-Dap Energy Estimation From Diffuse Reflectance Measurements on Sol–Gel and Commercial TiO_2: A Comparative Study. *J. Sol-Gel Sci. Technol.* **2012,** *61*, 1-7.

(339) Tauc, J.; Grigorovici, R.; Vancu, A., Optical Properties and Electronic Structure of Amorphous Germanium. *Phys. Status Solidi B* **1966,** *15*, 627-637.

(340) Huang, S.; Wilson, B. E.; Wang, B.; Fang, Y.; Buffington, K.; Stein, A.; Truhlar, D. G., Y-Doped Li_8ZrO_6: A Li-Ion Battery Cathode Material with High Capacity. *J. Am. Chem. Soc.* **2015,** *137*, 10992-11003.

(341) Adamo, C.; Barone, V., Toward Reliable Density Functional Methods Without Adjustable Parameters: The PBE0 Model. *J. Chem. Phys.* **1999,** *110*, 6158-6170.

(342) Mühle, C.; Dinnebier, R. E.; van Wüllen, L.; Schwering, G.; Jansen, M. , New Insights into the Structural and Dynamical Features of Lithium Hexaoxometalates Li_7MO_6 (M = Nb, Ta, Sb, Bi). *Inorg. Chem.* **2004,** *43*, 874-881.

(343) Delmas, C.; Maazaz, A.; Guillen, F.; Fauassier, C.; Réau, J. M.; Hagenmuller, P., Des Conducteurs Ioniques Pseudo-Bidimensionnels: Li_8MO_6 (M = Zr, Sn), Li_7LO_6 (L = Nb, Ta) et $Li_6In_2O_6$. *Mater. Res. Bull.* **1974,** *14*, 619-625.

(344) Scholder, R.; Gläser, H., Über Lithium- und Natriumuranate(V) und Über Strukturelle Beziehungen Zwischen den Verbindungstypen Li_7AO_6 und Li_8AO_6. *Anorg. Allg. Chem.* **1964,** *327*, 15-27.

(345) Bogicevic, A.; Wolverton, C.; Crosbie, G. M.; Stechel, E. B. , Defect Ordering in Aliovalently Doped Cubic Zirconia From First Principles. *Phys. Rev. B* **2001,** *64*, 014106.

(346) Emeline, A.; Kataeva, G.; Litke, A.; Rudakova, A.; Ryabchuk, V.; Serpone, N., Spectroscopic and Photoluminescence Studies of a Wide Band Gap Insulating Material: Powdered and Colloidal ZrO_2 Sols. *Langmuir* **1998,** *14*, 5011-5022.

(347) Zhao, Y.; Truhlar, D. G., Calculation of Semiconductor Band Gaps with the M06-L Density Functional. *J. Chem. Phys.* **2009,** *130*, 074103.

(348) Peverati, R.; Truhlar, D. G., Performance of the M11-L Density Functional for Bandgaps and Lattice Constants of Unary and Binary Semiconductors. *J. Chem. Phys.* **2012,** *136*, 134704.

(349) Peverati, R.; Truhlar, D. G., Quest for a Universal Density Functional: The Accuracy of Density Functionals Across a Broad Spectrum of Databases in Chemistry and Physics. *Phil. Trans. Roy. Soc. A* **2014,** *372*, 20120476.

(350) Hoang, K., Defect Physics, Delithiation Mechanism, and Electronic and Ionic Conduction in Layered Lithium Manganese Oxide Cathode Materials. *Phys. Rev. Applied* **2015,** *3*, 024013.

(351) Kang, S. H.; Mo, Y.; Ong, S. P.; Ceder, G., A Facile Mechanism for Recharging Li_2O_2 in $Li-O_2$ Batteries. *Chem. Mater.* **2013,** *25*, 3328-3336.

(352) Ong, S. P.; Wang, L.; Kang, B.; Ceder, G., $Li-Fe-P-O_2$ Phase Diagram from First Principles Calculations. *Chem. Mater.* **2008,** *20*, 1798-1807.

(353) Petkovich, N. D.; Rudisill, S. G.; Wilson, B. E.; Mukherjee, A.; Stein, A., Control of TiO2 Grain Size and Positioning in Three-Dimensionally Ordered Macroporous TiO2/C Composite Anodes for Lithium Ion Batteries. *Inorg. Chem.* **2014,** *53*, 1100-12.

(354) Arico, A. S.; Bruce, P.; Scrosati, B.; Tarascon, J.-M.; van Schalkwijk, W., Nanostructured Materials for Advanced Energy Conversion and Storage Devices. *Nat. Mater.* **2005,** *4*, 366-377.

(355) Dai, Y.; Manthiram, A.; Campion, A.; Goodenough, J. B., X-Ray-Photoelectron-Spectroscopy Evidence for Peroxide in 1:2:3 Copper Oxides Containing Disordered or Excess Oxygen. *Phys. Rev. B* **1988,** *38*, 5091(R).

(356) Merino, N. A.; Barbero, B. P.; Eloy, P.; Cadús, L. E., $La_{1-x}Ca_xCoO_3$ Perovskite-Type Oxides: Identification of the Surface Oxygen Species by XPS. *Appl. Surf. Sci.* **2006,** *253*, 1489-1493.

(357) Chen, Y.; Li, X.; Park, K.; Song, J.; Hong, J.; Zhou, L.; Mai, Y.-M.; Huang, H.; Goodenough, J. B., Hollow Carbon-Nanotube/Carbon-Nanofiber Hybrid Anodes for Li-ion Batteries. *J. Am. Chem. Soc.* **2013,** *135*, 16280-16283.

(358) Kannan, A. M.; Rabenberg, L.; Manthiram, A., High Capacity Surface-Modified $LiCoO_2$ Cathodes for Lithium-Ion Batteries. *Electrochem. Solid St.* **2003,** *6*, A16-A18.

(359) Vu, A.; Stein, A., Lithium Iron Phosphate Spheres as Cathode Materials for High Power Lithium Ion Batteries. *J. Power Sources* **2014,** *245*, 48-58.

(360) Zhou, W.; He, W.; Li, Z.; Zhao, H., Biosynthesis and Electrochemical Characteristics of $LiFePO_4$/C by Microwave Processing. *J. Solid State Electrochem.* **2009,** *13*, 1819-1823.

(361) Chaing, C.-Y.; Su, H.-C.; Wu, P.-J.; Liu, H.-J.; Hu, C.-W.; Sharma, N.; Peterson, V. K.; Hsieh, H.-W.; Lin, Y.-F.; Chou, W.-C.; Lee, C.-H.; Lee, J.-F.; Shew, B.-Y., Vanadium Subsition of $LiFePO_4$ Cathode Materials To Enhance the Capacity of $LiFePO_4$-Based Lithium-Ion Batteries. *J. Phys. Chem. C* **2012,** *116*, 24424-24429.

(362) Whittingham, M. S., Lithium Batteries and Cathode Materials. *Chem. Rev.* **2004,** *104*, 4271-4302.

(363) Doeff, M. M., Battery Cathodes. In *Batteries for Sustainability: Selected Entries from the Encyclopedia of Sustainability Science and Technology*, Brodd, R. J., Ed. Springer Science + Business Media: New York, 2013.

(364) Huang, S.; Wilson, B. E.; Smyrl, W. H; Truhlar, D. G.; Stein, A., Transition-Metal-Doped $M-Li_8ZrO_6$ (M = Mn, Fe, Co, Ni, Cu, Ce) as High-Specific-Capacity Li-Ion Battery Cathode Materials: Synthesis, Electrochemistry, and Quantum Mechanical Characterization. *Chem. Mater.* **2016**, DOI: 10.1021/acs.chemmater.5b03554

(365) Patterson, A., The Scherrer Formula for X-Ray Particle Size Determination. *Phys. Rev.* **1939,** *56*, 978-982.

(366) Jiang, J. Z.; Poulsen, F. W.; Morup, S., Structure and Thermal Stability of Nanostructures Iron-Doped Zirconia Prepared by High-Energy Ball Milling. *J. Mater. Res.* **1999,** *14*, 1343-1352.

(367) Clavel, G.; Willinger, M.-G.; Zitoun, D.; Pinna, N., Manganese-Doped Zirconia Nanocrystals. *Eur. J. Inorg. Chem.* **2008,** *2008*, 863-868.

(368) Harmanova, M.; Hanic, F.; Tunega, D.; Putyera, K., Structural and Electro-Optical Properties of C-Doped Yttria-Stabalized Zirconia. *Chem. Papers* **1998,** *52*, 12-15.

(369) Debernardi, A.; Sangalli, D.; Lamperti, A.; Cianci, E.; Lupo, P.; Casoli, F.; Albertini, F.; Nasi, L.; Ciprian, R.; Torelli, P., Electronic and Magnetic Properties of Iron Doped Zirconia: Theory and Experiment. *J. Appl. Phys.* **2014,** *115*, 17D718.

(370) Gurushantha, K.; Anatharaju, K. S.; Nagabhushana, H.; Sharma, S. C.; Vidya, Y. S.; Shivakumara, C.; Nagaswarupa, H. P.; Prashantha, S. C.; Anilkumar, M. R., Facile Green Fabrication of Iron-Doped Cubic ZrO_2 Nanoparticles by *Phyllanthus acidus*: Structural, Photocatalytic, and Photoluminescent Properties. *J. Mol. Catal. A: Chem.* **2015,** *397*, 36-47.

(371) Shannon, R. D.; Prewitt, C. T., Effective Ionic Radii in Oxides and Fluorides. *Acta Crystalogr.* **1969,** *25*, 925-946.

(372) Shannon, R. D., Revised Ionic Radii and Systematic Studies of Interatomic Distances in Halides and Chalcogenides. *Acta Crystalogr.* **1976,** *32*, 751-767.

(373) Berlin, I. J.; Iekshmy, S. S.; Ganesan, V.; Thomas, P. V.; Joy, K., Effect of Mn doping on the Structural and Optical Properties of ZrO_2 Thin Films Prepared by Sol-Gel Method. *Thin Solid Films* **2014,** *550*, 199-205.

(374) Steel, J. A.; Dahn, J. R., Electrochemical Intercalation of PF_6 into Graphite. *J. Electrochem. Soc.* **2000,** *147*, 892-898.

(375) Ishihara, T.; Yokoyama, Y.; Konzo, F.; Hayashi, H., Intercalation of PF_6^- Anion into Graphitic Carbon with Nano Pore for Dual Carbon Cell with High Capacity. *J. Power Sources* **2011,** *196*, 6955-6959.

(376) Farley, T. W. D.; Hayes, W.; Hull, S.; Hutchings, M. T.; Vrtis, M., Investigation of Thermally Induced Li^+ Ion Disorder in Li_2O Using Neutron Diffraction. *J. Phys. Condens. Matter* **1991,** *3*, 4761-4781.

(377) Caekalla, R.; Jeitschko, W., Preparation and Crystal Structure of $Li_6Zr_2O_7$ and $Li_6Hf_2O_7$. *Chem. Ber.* **1993,** *619*, 2038-2042.

(378) Pham, D. T.; Lee, T. H.; Luong, D. H.; Yao, F.; Ghosh, A.; Le, V. T.; Kim, T. H.; Li, B.; Chang, J.; Lee, Y. H., Carbon Nanotune-Bridged Graphene 3D Building Blocks for Ultrafast Compact Supercapacitors. *ACS Nano* **2015,** *9*, 2018-2027.

(379) Kwon, O. S.; Kim, T.; Lee, J. S.; Park, S. J.; Park, H.-W.; Kang, M.; Lee, J. E.; Jang, J.; Yoon, H., Fabrication of Graphene Sheets Intercalated with Manganese Oxide/Carbon Nanofibers: Toward High-Capacity Energy Storage. *Small* **2013,** *9*, 248-254.